

Experimental and Theoretical Studies of Corrosion Fatigue in a High Strength Steel

By

Xiao Dong Wu

Thesis submitted to the University of Sheffield for the Degree of Doctor of Philosophy
in the Faculty of Engineering

University of Sheffield

Department of Mechanical and Process Engineering

March 1995

To my parents

Preface

This thesis is based on the findings of research carried out in the Department of Mechanical and Process Engineering at the University of Sheffield.

The content of this thesis is original except where specific references are made to other work.

No part of this thesis has been submitted to any other University for a degree.

Xiao Dong Wu

Acknowledgements

I wish to express my hearty gratitude to my supervisor Prof. K. J. Miller for providing the funds, and for his invaluable guidance, kind help, and encouragement during my study in the department. I am also very grateful to Dr. R. Akid for his supervision, advice and help.

I would like to express particular appreciation to Dr. E. R. de los Rios for his helpful advice and beneficial discussion.

I am thankful to the Head of the Department of Mechanical and Process Engineering, University of Sheffield, for the use of the laboratory facilities, and Pandrol International Ltd for providing the test material.

My thanks are extended to Mr. J. Smith for manufacturing the specimens, Mr. D. Hallford for help with the photographic skills and Mr. J. Goodliff for help with the electronic control system.

I would also like to thank Dr. X. J. Xin for his discussion.

Abstract

The present work consists of both experimental and theoretical aspects of corrosion fatigue in a high strength steel.

Fatigue tests were conducted under fully reversed shear loading in an aerated 0.6M NaCl solution at pH6, for a silico-manganese spring steel (BS251A58) having a yield strength around 1400 MPa. The fatigue crack evolution process can be defined sequentially in terms of a pit, a short crack in stage I and a crack in stage II. It was observed that in the early stages pits developed at Mn-rich sulphide inclusions, from which short cracks developed and propagated in stage I; the crack growth rate of such cracks was dominated by microstructural features. Stage II, microstructure-independent crack growth was observed following a transition from stage I crack growth. In addition consideration was given to the influences of cyclic frequency, the effect of cathodic polarisation and the effect of electrolyte compositions on corrosion fatigue lifetime and crack growth behaviour. Mechanical properties, metallurgical and electro-chemical properties of the material used were also investigated. The failed specimens were examined using SEM and X-ray spectra analysis in order to study the failure mechanism.

Using a dislocation based Navarro-de los Rios model to represent the crack and its associated plastic zone, the crack growth process is characterised by the interaction of dislocations associated with micro-cracks, or local damage, and microstructural barriers (grain boundaries, precipitates, dispersed particles, phase interfaces, *etc.*). Some modifications to the model were made to incorporate the corrosive effect on the early stages of crack initiation (i.e. pit growth), the transition of stage I crack growth to stage II crack growth, and strain hardening of a parabolic form in order to achieve a more accurate

prediction. The validity of the model was justified by the good agreement achieved between predictions based on the model and the experimental results.

Based on the present study the following conclusions were made:

1. The fatigue strength of BS251A58 steel, subjected to 10^7 cycles in a 0.6M NaCl solution, at pH6 and at a frequency of 5Hz, is 98 MPa, and is significantly lower than the value of the fatigue limit in air, i.e. 457.5 MPa.
2. Corrosion fatigue crack propagation in the high strength BS251A58 steel can be described sequentially in terms of corrosion-induced pits, microcracks from pits, cracks in stage I (shear type cracks), and cracks in stage II (tensile cracks).
3. The number of cycles in the stage I-to-stage II transition, in relation to the whole fatigue life, varies from 20% to 60%, increasing as the applied load decreases.
4. Crack coalescence may occur in both the stage I and stage II regimes. In the stage I regime, microcracks with an effective tip-to-tip distance less than 1 to 2 prior austenite grains will coalesce, while those with distances greater than 2 to 3 prior austenite grains will change to stage II propagation. In the stage II regime, crack coalescence occurs after about 70% of the fatigue life N_f .
5. The lower the cycling frequency, the shorter will be the corrosion fatigue life. The combination of a high stress level and a low frequency can eliminate the in-air-fatigue microstructural barrier effect.
6. Cathodic polarisation ($E=-1280\text{mv (SCE)}$) can prevent the surface of the specimen from pitting, delay the stage I-to-stage II transition, and decelerate the early stage II crack

growth rate. However, as a stage II crack grows, cathodic polarisation will accelerate the crack growth rate.

7. In a 0.6M NaCl solution, the final stage I crack length increases from 50 μ m to 300 μ m with increasing cyclic shear stress range (from 224 MPa to 926 MPa). This distance equals approximately 2 to 10 prior austenite grain diameters. The final stage I crack length is much longer under cathodic polarisation than for a free corrosion potential under the same stress range. There is no significant frequency effect on the final stage I crack length when the frequency is in the range of 2Hz to 12.5Hz.

8. The dislocation based Navarro-de los Rios model was employed in the present study to describe crack growth behaviour and to predict fatigue life. The pit growth behaviour, the crack transition from stage I-to-stage II, and a parabolic strain hardening law, were incorporated into the model to reflect more closely the actual fatigue behaviour of the material. The validity of the model was justified by the good agreement achieved between predictions based on the model and the experimental results.

Introduction

In modern engineering practice, static or quasistatic loading is rarely observed. By far the majority of machinery and structural components are subjected to fluctuating or cyclic loads. Such loading induces fluctuating or cyclic stresses that often result in failure by *fatigue*.

Corrosion, a rather broad term, is generally defined as the undesired deterioration of the material through chemical or electro-chemical interaction with the environment. Corrosion, when interacting synergistically with fatigue, will produce an even more serious combined failure mode:- *corrosion fatigue*.

Corrosion process often forms pits and surface discontinuities that act as stress raisers which in turn accelerate fatigue failure process; microcracks in the usually brittle corrosion layer act as fatigue crack nuclei that propagate into the base material. On the other hand, the cyclic stresses or strains cause cracking and flaking of the corrosion layer, which exposes fresh metal to the corrosive medium. Thus, each process accelerates the other, often making the result disproportionately serious.

The complexity of the corrosion fatigue process can be appreciated by recognising the fact that many variables are involved, including environmental, electro-chemical, mechanical, and metallurgical aspects. The subject of corrosion fatigue is therefore indeed a task for not only engineers and mechanists, but also chemists, materials scientists, and metallurgists.

In the present project, experimental work and theoretical analysis were carried out to study the corrosion fatigue of a high strength steel. Instead of taking an exhaustive view on the subject, attention was focused on the central question as to how an aggressive environment triggers fatigue crack initiation, accelerates crack growth, and eventually eliminates the in-air fatigue limit of the material. Knowledge in electro-chemistry, metallurgy and mechanics (more specifically, micro-mechanics) provided the theoretical basis to explain the experimental observations, to analyse the test data, to model fatigue crack growth behaviour and to predict fatigue lifetime.

The main structure of this thesis is comprised of seven chapters.

Chapter 1 presents a brief review of metal fatigue, corrosion and corrosion fatigue. The importance of studies on the corrosion fatigue of metals is highlighted, this arising from the ever-increasing industrial requirement to use metallic components and structures in aggressive environments and adverse circumstances and also from research interest to understand thoroughly deformation and fracture behaviour of materials in the presence of environmental attack. Some existing theories and models about corrosion or corrosion fatigue are reviewed. Finally the scope of the present work is outlined to set a clear scene for all subsequent chapters.

Details of the experimental program are described in chapter 2.

In chapter 3, results of initial tests studying the electro-chemical and general mechanical properties prior to the fatigue tests are reported. These properties are important in the sense that they provide the basic material parameters to describe the corrosion fatigue process, and to help in the understanding the general processes that occur during corrosion fatigue.

The results of corrosion fatigue and in-air fatigue tests are reported and discussed in chapter 4. A number of aspects relevant to corrosion fatigue crack growth, such as pitting, crack coalescence, stage I to stage II transition, frequency effects, cathodic polarisation effects and electrolyte composition effects, have been examined.

In chapter 5, a microstructurally-sensitive crack propagation model based on the dislocation representation of a crack is used to provide the theoretical basis to understand the underlying principles of the supposed 'anomalous' short fatigue crack behaviour, to analyse the experimental data, and to predict the fatigue lifetime. Modifications to the model are made to incorporate the corrosive effect on the early stage of crack initiation, stage I to stage II transition, and strain hardening of a parabolic form in order to achieve a more accurate prediction.

Chapter 6 highlights a few final points which are central to the question as to why corrosion fatigue cracks can grow under a stress level well below the "in-air" fatigue limit and cause failure.

Conclusions are then drawn in chapter 7 together with some suggestions about further work.

Contents

Preface	i
Acknowledgements	ii
Abstract	iii
Introduction	vi
Chapter 1 Literature Review	1
1.1 Fatigue	1
1.1.1 A historical review	1
1.1.2 The S-N curve	3
1.1.3 Fatigue crack initiation	3
1.1.4 Fatigue crack propagation	4
1.1.5 Long crack growth behaviour	6
1.1.6 Short fatigue cracks	11
1.2 Corrosion	15
1.2.1 Categorisation of corrosion	15
1.2.2 Hydrogen embrittlement (HE)	16
1.2.3 Stress corrosion cracking (SCC)	17
1.3 Corrosion Fatigue	18
1.3.1 Anodic dissolution and hydrogen embrittlement	19
1.3.2 Environment induced stress concentrations	20
1.3.3 Yield stress effect	21
1.3.4 Frequency effect	21
1.3.5 Short cracks in corrosion fatigue	22

1.3.6 Corrosion fatigue of pre-cracked specimens	23
1.3.7 Corrosion fatigue modelling	24
1.3.8 The scope of the present work	27
References	28
Figures	34
Chapter 2 Experiment Work	42
2.1 Introduction	42
2.2 Test material	43
2.1.1. Material and in-service condition	43
2.1.2 Chemical composition	43
2.1.3 Heat treatment	43
2.3 Test facilities	44
2.3.1 Test machine for torsional fatigue test	44
2.3.2 Environment circulation system	44
2.4 Calibration of torque and twist angle	45
2.4.1 Calibration of torque	45
2.4.2 Calibration of twist angle	45
2.5 Preparation of the specimens	47
2.6 Metallographic studies	47
2.7 Mechanical tests	48
2.7.1 Hardness	48
2.8 Cyclic torsion tests	48
2.9 Electro-chemical studies	49
2.9.1 The apparatus	49
2.9.2 Determination of i_{corr}	50
2.9.3 Potentiodynamic curve	52
2.9.4 Corrosion tests	53
2.10 Crack growth monitoring	54

2.10.1 The surface replication technique	54
2.10.2 The image analysis system	55
2.11 Fatigue test in air	56
2.12 Corrosion fatigue	56
2.12.1 Corrosion fatigue	57
2.12.2 The frequency effect	58
2.12.3 The effect of electrolyte composition	58
2.12.4 The cathodic polarisation effect	59
References	62
Tables	63
Figures	66
Chapter 3 Initial experimental results	75
3.1 Metallographic studies	75
3.1.1 Microstructures	75
3.1.2 Inclusions	76
3.1.3 Discussion	77
3.1.4 Grain boundaries	80
3.2 General mechanical tests	81
3.2.1 Monotonic stress-strain relationship	81
3.2.2 Hardness	81
3.3 The calibration of the torsion test machine and specimen	82
3.3.1 Torque-stress relation	82
3.3.2 Twist angle-strain relation	83
3.3.3 Strain calibration	84
3.4 Cyclic torsional test	86
3.5 Electro-chemical tests	87
3.5.1 Polarisation Parameters	87
3.5.2 'Rest potential', E_{rest} , and 'true corrosion potential', E_{corr}	88

3.5.3 Discussion	90
3.6 Corrosion tests	94
3.7 Discussion	97
References	101
Tables	103
Figures	109
Chapter 4 Corrosion Fatigue and In-Air Fatigue	131
4.1 Torsion fatigue tests in 0.6M NaCl solution	131
4.1.1 S-N endurance curve	132
4.1.2 Pitting	133
4.1.3 Stage I crack initiation	138
4.1.4 Stage I crack propagation	139
4.1.5. Stage I crack coalescence	140
4.1.6 Stage I-Stage II crack transition	141
4.1.7 Stage II crack propagation	147
4.1.8 Stage II crack coalescence	149
4.1.9 Crack aspect ratio λ	151
4.1.10 pH value in the crack tip	156
4.2 Frequency effect	158
4.3 Cathodic polarisation effects	166
4.4 Solution composition effect	177
4.5 Torsion fatigue tests in air	180
References	182
Tables	187
Figures	195
Chapter 5 Modelling	252
5.1 The microstructurally-sensitive crack growth model	252

5.2 Pit initiation and propagation	254
5.3 Stress concentration around an inclusion or a pit	257
5.4 Continuous distribution function of dislocation pile-up	258
5.5 Critical equilibrium condition	259
5.6 Crack transition from stage I to stage II	263
5.7 The effect of grain orientation	266
5.8 Strain hardening effect	267
5.9 Crack propagation	271
5.10 The transition and instability of crack growth	273
5.11 Lifetime prediction	274
5.12 Concluding remarks	276
References	277
Appendix A	281
Tables	286
Figures	290
Chapter 6 Discussion	297
6.1. Pit initiation time, t_0	297
6.2. Effective size of the stress concentration around a pit	300
6.3. The effect of crack blunting	303
6.4. The effect of triaxial stress	305
6.5. Corrosion fatigue resistance of a high strength steel	307
6.6. Fatigue strength	308
References	311
Chapter 7 Conclusions	312
7.1 Conclusions	312
7.2 Suggestions for future work	314

Chapter 1 Literature Review

A brief review of metal fatigue, corrosion and corrosion fatigue is presented in this chapter. Corrosion fatigue has an interdisciplinary nature, and so attention is drawn to the principles that are of concern to both material scientists and mechanical engineers. The importance of studies on the corrosion fatigue of metals is highlighted, this arising from the ever-increasing industrial requirement to use metallic components and structures in aggressive environments and adverse circumstances and also from research interest to understand thoroughly deformation and fracture behaviour of materials in the presence of environmental attack. Some existing theories and models about corrosion or corrosion fatigue are reviewed. Finally the scope of the present work is outlined to set a clear scene for all subsequent chapters.

1.1 Fatigue

Fatigue is the progressive, localised, permanent structural change that occurs in materials subjected to fluctuating stresses and strains that may result in cracks or fracture after a sufficient number of fluctuations.

1.1.1 A historical review

Fatigue of metals has been recognised as a failure process for more than 150 years.

During the 1850s and 1860s, Wohler [1] conducted numerous fatigue tests in order to determine the cause of railway axles failures. From his first systematic investigation, Wohler formulated two fundamental laws of fatigue:

1. The fatigue life is determined by the applied stress states from which a stress versus life (S-N) diagram can be introduced to describe fatigue behaviour.
2. No matter how many times the stress is repeated, failure will not occur if the range of stress is less than a certain limiting value, which leads to the concept of a fatigue limit.

So far both the S-N diagram and the fatigue limit, remain the most important concepts in any fatigue investigation.

Griffith's pioneering theory [2] about the brittle fracture of glass in 1920s set a milestone in the investigation of material failure processes and marked the birth of the subject of fracture mechanics.

In the 1950s Irwin [3] introduced the stress intensity factor K , which has been accepted as the basis of linear elastic fracture mechanics (LEFM), the characterization of fatigue crack growth, and fatigue life prediction.

In the early 1960s, the Coffin-Manson [4, 5] relationship between plastic strain amplitude and fatigue life was proposed, which provides one basis for current notch strain fatigue analysis.

It was in 1963 that Paris [6] correlated the fatigue crack growth rate, da/dN , with the stress intensity factor range ΔK_I by his now famous formula, and successfully described the fatigue crack propagation (FCP) phase within the so-called intermediate stress intensity factor range.

Rapid developments in fracture mechanics analyses (i.e. LEFM, and elastic-plastic fracture mechanics to fatigue crack growth analysis) and lately development of microstructural fracture mechanics (short crack phase) has led to a far better understanding of fatigue failure behaviour which can be translated into a quantitative prediction.

1.1.2 The S-N curve

In laboratory fatigue testing, specimens or components are subjected to the number of stress cycles required for a fatigue crack to initiate and then to grow large enough to produce failure. The results are usually plotted as stress amplitude, S , versus the number of cycles to failure, N , using a logarithmic scale for the number of cycles. This diagram is called an S-N curve. Three typical S-N curves (in-air fatigue) are shown in Figure 1.1 [7]

The number of stress cycles that a metal can endure before failure, increases with decreasing stress level. The horizontal portion of an S-N curve represents the maximum stress that the metal can withstand for an infinitely large number of cycles without failure and is known as the fatigue (endurance) limit. Most non-ferrous metals do not exhibit a fatigue limit; nor do ferrous metals in an aggressive environment. Instead, their S-N curves continue to drop at a slow rate at large number of cycles, as shown by the curve for the aluminium alloy 7075-T6 in Figure 1.1. In this case, fatigue strength rather than the fatigue limit is reported, which is the stress to which the metal can be subjected for a specified number of cycles without failure.

1.1.3 Fatigue crack initiation

On a microscope scale, the most important feature of the fatigue cracking process is the nucleation of one or more crack sites subjected to stress reversals exceeding the local flow yield stress. These sites may be at persistent slip bands, within grains, or at grain boundaries. The development of the microcrack, at the nucleation site, to a detectable fatigue crack is called the crack initiation phase. The demarcation between initiation and propagation is somewhat arbitrary. Proposals for the definition of crack length at so-called initiation vary from zero to several millimetres [8]. Material scientists usually consider the detectable fatigue crack size a_0 , to be as small as 2 or 3 μm . Some investigators assume

a_0 to be zero, since the growth of a crack from 0 to 3 μm makes little difference to the life time.

Fatigue cracks initiate at points of maximum local stress and minimum local strength. The local stress pattern is determined by the geometry of the component, the type and magnitude of the loading, and the material texture. In addition to geometric factors, features such as surface and metallurgical imperfections can add to the local stress concentration. Local surface imperfections such as scratches, dents, burrs, cuts and other manufacturing flaws are the favourite sites at which fatigue cracks can initiate. The minimum local strength may occur at relatively weak grain boundaries, twin boundaries, interfaces between inclusions and the matrix, and interfaces between second phases and the matrix; all these being possible crack initiation sites. Except for those instances where internal defects or surface-hardening treatments are involved, fatigue cracks usually initiate at the surface. In commercial materials, inclusions often act as crack initiation sites.

In addition, the aggressive environment could have a significant influence on the fatigue crack initiation process, by increasing the local maximum stress (due to the growth of pits), and by decreasing the local strength (e.g. by hydrogen diffusion and subsequent embrittlement of the metal).

1.1.4 Fatigue crack propagation

The whole fatigue life is the sum of the number of stress (strain) cycles for crack initiation and the number of cycles for crack propagation, and is a function of many variables, including stress level, stress state, cyclic wave form, fatigue environment and metallurgical condition of the material.

Crack growth behaviour has been observed to be governed by different propagation laws for the short and the long crack regimes.

Miller [9] proposed a scheme to describe the microstructurally-short fatigue crack, the physically-short fatigue crack, and the microstructure-independent long crack, based on a physical understanding of the crack growth behaviour in relation to the plastic zone size in front of the crack tip which in turn depends on the material microstructure and applied load.

Following Miller [9], the three categories of crack growth and their physical significance are illustrated in Figure 1.2 and Figure 1.3. In the well-documented linear elastic fracture mechanics (LEFM) regime, cracks are long and require a small stress range to propagate them. For such cracks the crack tip plasticity is negligible and hence an elastic analysis of the crack tip stress-strain field is sufficiently accurate to characterise their behaviour; such a crack will propagate in a cyclic tension type test as a Mode I, stage II crack. In summary form, the LEFM type of crack is strongly dependent on both crack length and stress level while microstructure plays an insignificant role.

Conversely, when the starter crack is very small, e.g. comparable to the grain size, d , of the material, a totally different situation exists. In most pure metals and ductile alloys the initial crack will grow by a shear micro-mechanism and is exceedingly difficult to observe in comparison to the plasticity which drives it, i.e. a crack surface area of a few square microns which is small compared to the surface area of a grain. Under these circumstances microstructure fracture mechanics (MFM) is required to characterise the propagation behaviour of the stage I (Mode II and/or Mode III) crack.

An intermediate condition between LEFM and MFM will occur when the starter crack length a is such that $a_{th} < a < d$. This intermediate regime is usually for cracks of a few grain lengths in size and for cracks which are changing from a shear growth mechanism to a tensile (opening growth) mechanism. Not surprisingly, the microstructure texture has an effect, but is of an intermediate nature between the MFM regime (where microstructure is

very important) and the LEFM regime (where microstructure is not so important). To characterise growth in this regime, elastic-plastic fracture mechanics (EPFM) is required.

1.1.5 Long crack growth behaviour

Linear elastic fracture mechanics is based on an analytical procedure that relates the stress-field magnitude and distribution in the vicinity of a crack tip to the nominal stress applied to the structure, to the size, shape, and orientation of the crack or crack-like imperfection, and to the material properties. The stress field equations show that the magnitude of the elastic stress field can be described by a single parameter, K , which is known as the stress-intensity factor.

All stress systems in the vicinity of a crack tip may be derived from three modes of loading: **Mode I** (*opening* mode) - where the crack surfaces move apart from each other in a direction normal to the crack face; **Mode II** (*sliding* mode) - where the crack surfaces slide over each other in a direction perpendicular to the leading edge of the crack; **Mode III** (*tearing* mode) - where the crack surfaces slide relatively to each other parallel to the leading edge of the crack. In many practical cases, mode I loading is the predominant situation.

In the 1950s, Irwin [3] showed that the stresses in the vicinity of a crack tip whatever the mode, take the form:

$$\sigma_{ij} = \frac{K}{\sqrt{2\pi r}} f_{ij}(\theta) + \begin{matrix} \text{high order} \\ \text{terms of } r \end{matrix} \quad (1.1)$$

where r and θ are the cylindrical polar co-ordinates of a point with respect to the crack tip, $f_{ij}(\theta)$ is a dimensionless function of θ , and

$$K = \sigma \sqrt{\pi a} f\left(\frac{a}{w}\right) \quad (1.2)$$

Here the term K is a constant factor which controls the magnitude of the elastic stress field, and is therefore called the stress intensity factor, while $f(a/w)$ is a dimensionless factor that depends on the geometry of the cracked specimen and the loading system.

Small scale yielding

The most significant application of LEFM, is when K can correlate the crack growth and fracture behaviour of materials, i.e. when the crack tip stress field remains predominately elastic.

The characteristic sigmoidal shape of a da/dN versus ΔK , the fatigue crack growth rate curve, is shown in Figure 1.4 [10]. The curve can be divided into three regions where different crack growth mechanisms will operate and different phenomena can be observed.

In region I there is a threshold value, ΔK_{th} , below which cracks do not propagate. Above this value the crack growth rate increases relatively rapidly with increasing ΔK . In region II there is often a linear log-log relation between da/dN and ΔK . Finally, in region III the crack growth rate rises to an asymptotic value where ΔK approaches the critical stress intensity factor, K_C , at which instant unstable crack growth would occur.

At intermediate ΔK values, a straight line is usually obtained to give the power-law relationship, referred to as the Paris' law [6],

$$da/dN = C(\Delta K)^n \quad (1.3)$$

where C and n are constants for a given material and stress ratio.

The ability of ΔK to correlate crack growth rate data depends to a large extent on the fact that the alternating stress, $\Delta\sigma$, causing crack growth is small compared to the cyclic yield

strength, $\Delta\sigma_{cy}$, i.e. $\Delta\sigma < 2/3 \Delta\sigma_{cy}$, therefore, crack tip plastic zones are small compared to the crack length.

Irwin [11] considered a circular plastic zone to exist at the crack tip under tensile loading, this of diameter $2r_y$, where

$$r_y = \frac{1}{2\pi} \left(\frac{K_I}{\sigma_y} \right)^2 \quad \text{for plane stress} \quad (1.4a)$$

$$\text{and } r_y = \frac{1}{2\pi} \left(\frac{K_I}{C\sigma_y} \right)^2 \quad \text{for plane strain} \quad (1.4b)$$

where σ_y is the yield stress, and C is usually estimated to be about 1.7.

In cyclic loading, following the analysis by Rice [12], the cyclic plastic zone size is approximately:

$$r_y \approx \frac{1}{2\pi} \left(\frac{\Delta K}{2\sigma_{cy}} \right)^2 \quad (1.5)$$

where σ_{cy} is the cyclic yield stress. The above relation is best understood in the way a material behaves, nominally elastically, between two stress reversing points of distance of $2\sigma_{cy}$ (unless the stress changes direction). This makes $2\sigma_{cy}$ the equivalent yield stress as compared with σ_y in monotonic loading, while the effect of the larger plastic zone during the first cycle of loading (given by Equation (1.4)) will decrease as the crack propagates through the initial stress field.

The small-scale-yielding situation occurs only when r_y is less than, or equal to, one fiftieth of the crack length, or the remaining ligament, which is a limit on applicability of LEFM; otherwise the problem has to be treated by elastic-plastic analyses. So far, the most promising concepts of elastic-plastic fracture mechanics (EPFM) are the crack opening

displacement (COD) approach (based on the crack tip strain), and the J-integral energy balance concept.

J-integral

The J-integral was first introduced by Rice [13] for non-linear elastic behaviour. He defined an integral along an open curve Γ surrounding the crack tip, travelling from the lower crack surface to the upper one, as:

$$J = \int_{\Gamma} w dy - \int_{\Gamma} T_i \frac{\partial u_i}{\partial x} ds \quad (1.6)$$

where $w = w(\varepsilon_{ij})$ is the recoverable strain energy density of the non-linear elastic material, T_i is the traction acting on the contour, u_i is the displacement and s is the distance travelled along the contour. Rice [13] showed that the value of J is independent of the contour Γ . The uniqueness of the integral implies that J is a crack tip characterization parameter.

The integral of Equation (1.6) can be evaluated numerically, by means of finite element analyses for example, but it is difficult to determine by experimental measurement. An alternative definition was later provided by Hutchinson [14] and also by Rice and Rosengren [15], usually referred to as the *Deformation J*, i.e.

$$J = -\frac{1}{B} \frac{\partial U}{\partial a} \quad (1.7)$$

where U is the potential energy and B is the thickness of the specimen. It has been proved that the two definitions given by Equations (1.6) and (1.7) are equivalent. Equation (1.7), however, relates J to measurable quantities such as load and displacement, and is therefore more useful for experimental evaluations.

For an elastic-plastic material, w in Equation (1.6) should be replaced by the density of stress work. The assumption of non-linear elasticity is compatible with actual (elastic-

plastic) deformation behaviour only if no unloading occurs in any part of the material. Such conditions only hold for a stationary crack under monotonic loading. Therefore strictly speaking, J is applicable only up to the beginning of crack growth and should be taken as an initiation criterion. However, theoretical analyses and experimental results [16-19] have confirmed that the actual conditions for the applicability of the J-integral concept can be relaxed:- for a limited amount of crack growth (compared with the current crack length and remaining ligament) J is still valid for characterising the crack growth. The indication is that J can then be used to predict the initiation of crack growth, and characterize a limited amount of ductile crack growth.

COD

The COD (crack opening displacement) approach was introduced by Wells in 1961 [20]. At crack tips the stresses will always reach the yield strength and plastic deformation will occur. Thus failure is brought about by stresses and plastic strains exceeding certain respective limits.

In 1966, Burdekin and Stone [21] used the Dugdale strip yield model to find an expression for COD. The result is:

$$\delta_t = \frac{8\sigma_{ys}a}{\pi E} \ln \sec \left(\frac{\pi\sigma}{2\sigma_{ys}} \right) \quad (1.8)$$

For $\sigma \ll \sigma_{ys}$, under LEFM conditions, there is a direct relation between δ_t and K_I : i.e.

$$\delta_t = \frac{K_I^2}{E\sigma_{ys}} \quad (1.9)$$

Currently, methods of analysis associated with the J-integral are used to support and improve crack tip opening displacement test procedure. The following equivalence

$$J = \sigma_y \delta \quad (1.10)$$

with an allowance for a suitable σ_y value, has been verified by experimental comparison for various loading conditions beyond general yielding.

1.1.6 Short fatigue cracks

Short cracks are observed to grow at stress intensities below the long crack threshold, some extend with decelerating growth rates until arrest, while others propagate quite rapidly and tend towards long crack behaviour. Short cracks have practical significance noting that at present, damage tolerant fatigue lifetime computations are invariably based on long crack data. Since overall life is greatly influenced by low growth rate behaviour, the accelerated and sub-threshold extension of small flaws can lead to the potentially dangerous over-prediction of lifetime.

Broadly speaking, there are several ways to define a 'short' crack. The categories given by Miller [9] for the MFM and EPFM short cracks (as quoted in section 1.1.4), are well-defined and relevant to short crack modelling, and are therefore used in the present work. In addition, differences in local crack tip environment provide the further category of a chemically-short crack, as described by Gangloff and Wei [22]. The chemically-short crack may propagate 1.5 to several hundred times faster than long cracks subjected to the same mechanical driving force.

All short crack problems are in essence created because of a breakdown in the continuum similitude concept of long cracks.

Two models, that take account of short and long crack behaviour, have been developed over the past few years, one due to Brown and Hobson [23], which is empirically based on experimental results, and one due to Navarro and de los Rios, which is theoretical and based on a dislocation representation of a crack [24-27].

The Brown-Hobson model

For the microstructurally short crack growth regime, Hobson [23] examined a medium carbon steel under push-pull tests and derived an equation to describe growth rate:

$$\frac{da}{dN} = A(\Delta\gamma_p)^\alpha (d - a) \quad (a < d) \quad (1.11)$$

Here A and α are material constants, $\Delta\gamma_p$ is the plastic shear strain range, d is the distance to the strongest barrier, and a is the crack length.

For the physically small crack growth regime, the growth rate is described by:

$$\frac{da}{dN} = (\Delta\gamma_p)^\beta (Ba - C) \quad (a > a_{th} = \frac{C}{B}) \quad (1.12)$$

where B and β are material constants and C is the long crack threshold condition [23].

The above empirical equations indicate that microstructurally short crack growth is a function of a characteristic dimension (d) of the microstructure, as well as the crack length.

The characteristic dimension is dependent on stress state, microstructural features (grain diameter, inclusions, precipitates) and environment. The life time prediction can be obtained by the sum of the time spent in the following three regions of integration: 1. the initial period when $a < a_{th}$; 2. the transition period when $a_{th} \leq a < d$; and 3. the final period when $a \geq d$.

The Brown-Hobson model is simple and easy to use. The short crack retards or arrests when it approaches the strongest barrier. The influence of microstructure is clearly described by the model. Because it is a 'best-fit' of the experimental data, the model gives good life time predictions.

The Navarro-de los Rios model

To further understand the complex nature of short crack behaviour and the relatively large scatter in experimental data, Navarro and de los Rios [24-27] proposed a model based on a dislocation representation of cracks.

For a constant applied stress τ , when a crack initiates within a grain, the plastic zone ahead of the crack tip extends to the barrier (normally the grain boundary) and is blocked there. The crack and the plastic zone ahead of the crack tip is presented by an array of dislocation pile-ups (Figure 1.5) [24], first proposed by Bilby et al [28]. The stress concentration ahead of the plastic zone is considered as the driving parameter for the transfer of slip across a grain boundary, and is found to be dependent on the parameter $n_i = a_i / c_i$ defining the position of the crack tip relative to the grain boundary. Here a_i is the half crack length with the subscript i indicating the number of half grains being penetrated by plastic slip, $c_i = iD / 2$ is the half crack length plus the plastic zone size, and D is the grain diameter.

It has been shown in [24] that the stress concentration ahead of the plastic zone can be expressed by:

$$\frac{S(\zeta_0, n_i)}{\tau} = \frac{1}{\sqrt{2}} \frac{1}{(\zeta_0 - 1)^{1/2}} \left(1 - \frac{2\tau_0}{\pi\tau} \cos^{-1} n_i \right) + \frac{\tau_0}{\tau} \quad (1.13)$$

In the above equation τ is the applied stress, τ_0 is the internal friction stress to the movement of a single dislocation on the slip plane, $\zeta_0 = (r_0 + c_i)/c_i$, r_0 is the distance from the grain boundary where the dislocation source is activated. The condition for operating the dislocation source in the next grain is given by:

$$S = \frac{1}{2} m^* \tau_c \quad (1.14)$$

where m^* is an orientation factor of the Sachs type, τ_c is the critical stress to bow out a dislocation link or to unlock a pinned dislocation.

Once the crack tip has reached a position close to the grain boundary and a critical value of n_i is achieved:

$$n_i = n_i^c \quad (1.15)$$

the critical stress ($0.5 m^* \tau_c$ in Equation (1.14)) is attained, and slip will take place and the plastic zone will extend into the next grain. Therefore the parameter n_i decreases to a new value $n_i^s = a_i / (c_i + D)$.

The crack tip plastic displacement ϕ_i is considered to be a function of n_i , and can be expressed as:

$$\phi_i = \frac{2b}{\pi^2 A} \tau_o c_i \left[n_i \ln \left(\frac{1}{n_i} \right) + \sqrt{1 - n_i^2} \left(\frac{\pi \tau}{2 \tau_o} - \cos^{-1} n_i \right) \right] \quad (1.16)$$

where b is the Burgers vector, and $A = Gb/2\pi$ for screw dislocation, or $A = Gb/2\pi(1-\nu)$ for edge dislocation, G is the shear modulus and ν is the Poisson's ratio. The crack growth rate is considered to be proportional to the crack tip displacement ϕ_i in a power law form i.e.

$$\frac{da_i}{dN} = \alpha (\phi_i)^m \quad (1.17)$$

When the crack grows through each grain, the value of n_i changes from n_i^s to n_i^c , the crack growth rate, given by Equation (1.17), varies in an intermittent, oscillating pattern, as shown in Figure 1.6 [24]. With the N-R model, the intermittent pattern of decelerating and accelerating behaviour of short cracks is explained successfully. The fatigue limit is equated to the stress below which a crack is unable to transfer slip to the next grain.

It is evident that the large scatter of data observed in the short crack growth regime, should lie between the upper and lower bounds of growth rate behaviour corresponding to $n_i = n_i^s$ and $n_i = n_i^c$. The upper and lower limit will come together when the crack growth is less affected by microstructural features. A development of this model shows that crack growth behaviour becomes less influenced by the microstructures when the crack length is larger than 8 to 10 grain diameters [29].

The above discussion so far pertains to fatigue in an inert environment. However, a number of engineering structures and components in service are subjected to aggressive environments. The interaction between the mechanical fatigue mechanism and the electro-chemical effect will severely reduce fatigue life of a material. This highlights the processes leading to corrosion fatigue.

1.2 Corrosion

Corrosion is the chemical or electro-chemical reaction between a material, usually a metal, and its environment which jointly can cause a large deterioration in the material properties.

1.2.1 Categorisation of corrosion

A general categorisation is to classify corrosion process as either *general* corrosion or *localised* corrosion.

General corrosion is defined as a corrosive attack dominated by uniform thinning, e.g. atmospheric corrosion, high temperature corrosion etc. Since all areas of the metal corrode at a similar rate, it is possible to apply the results obtained from polarisation studies to predict the rate of metal loss over a given period of time.

Localised corrosion concerns damage which is localised rather than spreads uniformly over the exposed metal surface, and includes pitting and crevices and biological corrosion. Instead of a slow, relatively uniform loss of metal thickness, high rates of metal penetration occur at specific sites, while the remainder of the metal goes largely unaffected. The attack can also be harder to detect because much of the damage may occur subsurface, with only a small opening visible to the eye on the metal surface. Moreover, these forms of attack are economically important and dangerous because they can lead to premature failure of a structure by rapid penetration.

In many instances corrosion problems are exacerbated by synergistic effects caused by the conjoint action of mechanical stresses and chemical reactions. There are two major processes by which the integrity of a component may be affected:

1. stress corrosion cracking (SCC, static stress);
2. corrosion fatigue (CF, cyclic stress).

In both cases, hydrogen embrittlement (HE) may play an important role. These processes are briefly discussed in the following sections.

1.2.2 Hydrogen embrittlement (HE)

HE is a process that results in a decrease of toughness or ductility of a metal due to the presence of atomic hydrogen. It has been recognised as being of two types. The first, internal hydrogen embrittlement, occurs when the hydrogen enters molten metal which becomes supersaturated with hydrogen immediately after solidification. The second type, environment hydrogen embrittlement, results from hydrogen being adsorbed by solid metals; this can occur during an elevated-temperature thermal treatment and in service during, for example, electroplating contact with maintenance chemicals, corrosion reactions, cathodic protection, and plant operation in high pressure hydrogen.

1.2.3 Stress corrosion cracking (SCC)

SCC is a term given to the intergranular or transgranular cracking of a metal by the conjoint action of a static tensile stress and a specific environment. Experiments on steels in sea water have shown that the threshold stress intensity of SCC, K_{ISCC} decreases as yield stress increases, from which it can be deduced that SCC is much more of a problem in high strength materials.

The Initiation phase:

SCC is observed in metal/environment pairs where, conjoint effects of stress and corrosion interact. The most fundamental possibility of SCC initiation is when a tensile stress on a crystal lattice (which is otherwise in equilibrium), results in the raising of the thermodynamic energy of the atomic bonds. If this effect is localised at a surface, anodes will be formed, even though the material is being stressed below its elastic limit.

There are many weak 'spots' on a metal surface for the creation of a tiny concentration cell in the metal such as, for example, grain boundaries, non-metallic inclusions, phase interfaces and particles. Under the tensile stress, the movement of dislocations along active slip planes will be halted when they reach either the surface of the metal or a grain boundary, resulting in formation of slip steps. The 'pile-up' of dislocations at grain boundaries results in the anodic polarisation of these regions because of the increased irregularities in the crystal structure. The slip steps break the thin protective oxide film within a microscopic quantity of bare metal, which is highly anodic compared to the surrounding surface.

Crack propagation:

Many mechanisms have been proposed for the propagation of cracks in environment-sensitive cracking [30]. They include:

1. Pre-existing active paths. Propagation is believed to occur preferentially along active grain boundary regions. Grain boundaries may be anodically polarised for a variety of metallurgical reasons, such as the segregation of alloying elements.
2. Strain-generated active paths. This mechanism is based upon the idea of a strain-induced rupture of the film, following by metal dissolution at rupture. The propagation rate is governed by three criteria: - (a) rate of film rupture, determined by the applied strain rate, or, in the case of static loading, by the creep rate. (b) solution renewal and removal rates at the crack tip, a diffusion controlled process governed by the accessibility of the crack tip to the aggressive species, and (c) passivation rate.
3. Adsorption-related mechanism. A hydrogen adsorption-related mechanism proposes that active species in the electrolyte degrade the mechanical integrity of the crack tip region, thus facilitating fracture of bonds at energies much lower than would be expected.

It is worth mentioning that no single mechanism can account for all the experimental observations concerning instances of corrosion fatigue. As is usually the case where more than one mechanism can be operating, it is likely that each is applicable under different service conditions.

1.3 Corrosion Fatigue

Corrosion fatigue is the process in which a metal fractures prematurely under conditions of simultaneous corrosion and repeated cyclic loading at lower stress levels or fewer cycles than would be required in the absence of a corrosive environment. This makes corrosion fatigue a common and dangerous forms of corrosion.

Figure 1.7 illustrates the interrelationship between stress corrosion, corrosion fatigue, and hydrogen embrittlement [30]. The most serious practical situations involving ductile alloy/environment systems are in the cross-hatched regions, which indicate the

combination of any two failure mechanisms, and especially in the centre, where all three phenomena interact. Although much research [7] has been carried out in recent years, many unanswered questions remain.

There are many similarities between corrosion fatigue and stress-corrosion cracking, but the most significant difference is that corrosion fatigue is extremely non-specific. One of the main features of stress-corrosion cracking is that cracking of a particular metal is observed only for relatively few chemical species [31], while corrosion fatigue occurs in a much wider range of material/environment systems.

1.3.1 Anodic dissolution and hydrogen embrittlement

For alloy/aqueous environment systems subjected to cyclic loads, interpretations of embrittlement can involve electrochemical reactions at freshly formed slip steps around the crack tip. The process includes two principal possible mechanisms of environmental damage: anodic dissolution or hydrogen embrittlement.

The advance of fracture by dissolution occurs by:

1. the diffusion of the active species (such as water molecules or halide anions).
2. the rupture of the protective oxide film at a slip step or in the immediate wake of a crack tip by strain concentration or fretting contact between the crack faces, respectively.
3. the dissolution of the exposed surface.
4. the nucleation and growth of oxide on the bared surface.

For the alternative mechanism of hydrogen embrittlement in an aqueous media, the critical steps involve:

1. the diffusion of water molecules or hydrogen ions between the crack walls towards the crack tip.

2. the reduction of these species to create adsorbed hydrogen atoms at the crack tip surface.
3. the surface diffusion of adsorbed atoms to preferential surface locations.
4. the adsorption of the atoms to a critical location (e.g., grain boundary, the region of high triaxiality ahead of a crack tip, or a void).

1.3.2 Environment induced stress concentrations

The environment affects the probability of early fatigue crack initiation, fast crack growth rate or both. For many materials, the stress range required to cause fatigue failure diminishes progressively with increasing time and with the number of cycles of applied stress. A corrosive environment can substantially reduce the crack initiation time by any form of localised attack to form a stress concentration. Corrosion attack would be favoured at newly unfiled metal surfaces formed at a persistent slip band.

A clear example of the importance of stress concentrations due to corrosion is illustrated in Figure 1.8 which shows fatigue endurance results for plain and notched specimens of a 13% Cr ferritic steel in distilled water and salt water [32]. These environments are seen to cause a massive reduction in the endurance limit of the smooth specimen but only a relatively modest effect on notched specimens. From this it was concluded that the main effect of the environment in plain specimens is to introduce stress concentrations with virtually the same effect as a machined notch.

Such results highlight the fact that preservation of a good surface finish by an effective corrosion protection measure is an effective way of reducing the susceptibility of materials to corrosion fatigue.

1.3.3 Yield stress effect

Data obtained by Markfield [33] suggested that for freely-corroding HY80 (a relatively low strength steel) in 3.5% NaCl solution, the crack velocity due to dissolution is only significant for crack lengths of the order of 50 μm or less. This work was performed at a relatively high frequency and a high stress.

For relatively high strength steels, such as spring steel, however, there is increasing evidence that the effect of hydrogen on fatigue crack growth in the low ΔK regime is relatively large and sensitive to the amount of hydrogen supplied. Under these conditions it is possible that dissolution effects can be detected for longer cracks when the time available for hydrogen diffusion is greater, or the stress is less.

In cycle-time-dependent corrosion fatigue in the steel-chloride system, the magnitude of the short crack effect decreases substantially with decreasing steel yield strength of a steel [22]. It was observed that for low strength steels, the small crack growth rate was increased by between 1.5 to 2 fold; for moderate-strength steels such as HY130, small cracks grew up to four times faster than long cracks [22, 34]; while for high-strength steels, small corrosion fatigue cracks grow at unpredictably high rates, varying (from long crack data) by one to two orders of magnitude.

1.3.4 Frequency effect

Under cyclic conditions, fretting contact between the mating crack faces, pumping of the aqueous environment to the crack tip by the crack walls, and continual blunting and re-sharpening of the crack tip by reversed loads will influence the rate of anodic dissolution and crack growth behaviour. Therefore, both cyclic frequency and stress wave form are known to strongly influence crack growth.

The effect of frequency is really a deformation strain rate effect. At low strain rates, repassivation is fast and plays an important role while the straining is slow enough to have little effect upon the specimen failure. Conversely, at high strain rates, the mechanical effect predominates over the corrosion processes while the environment does not have enough contact time with the specimen, and failure occurs by mechanical means only. At intermediate strain rates, usually about 0^{-4} to 0^{-6} /s, the environment effect is the greatest.

1.3.5 Short cracks in corrosion fatigue

Recent research has highlighted the short crack problem because the early growth phase of cracks often dominates the fatigue life of components and so errors in growth rates of short cracks have a large adverse effect on life prediction. Aggressive environment-chemical effects, which are unique to the small crack geometry, are an important aspect of corrosion fatigue behaviour. Obviously, the short crack problem induces the break-down of the continuum similitude principle (i.e. crack size and applied stress effects on growth kinetics cannot be uniquely described by a single parameter (such as ΔK)), and short cracks propagate at stress-intensity ranges well below the long-crack threshold and at unpredictable high rates compared to the growth rates of long cracks. One such good example was provided by the corrosion fatigue crack growth in the weld of a pipe carrying H_2S -contaminated oil [35]. 80% of the fatigue life was spent on crack growth from 0.5mm to 1.0 mm; cracking from 1.0 mm to failure occupied only 20 % of lifetime.

For either hydrogen embrittlement or anodic dissolution mechanisms to be applied to the short crack growth model, a great deal of phenomena must be addressed through careful experimental studies before the exact nature of hydrogen/short crack or dissolution/short crack interactions can be understood. This is because at the crack tip, the chemical reaction and the mechanical effect are complex and difficult to measure. What is clear is

that a straight-forward application of long-crack fracture mechanics data to the prediction of corrosion-fatigue S-N behaviour of smooth specimens is inappropriate.

1.3.6 Corrosion fatigue of pre-cracked specimens

In precrack specimen fatigue tests, fracture mechanics methods are used to describe the crack growth rates of the pre-existing cracks under cyclic loading. The growth of a fatigue crack under cyclic loading is principally controlled by the maximum load and the stress ratio. Most corrosion fatigue crack growth investigations attempt to follow the general provisions of the standard test method presented in ASTM E647.

However, as there is a number of additional factors that may exert a strong influence in the presence of an aggressive environment, the corrosion fatigue crack growth rates for many metallic structural materials are different from those of 'pure' fatigue. Referring to the da/dN versus ΔK curves in an inert environment (Figure 1.9 [36]), the rate of crack growth in 'pure' fatigue depends strongly on K at levels approaching K_C or K_{IC} at the high end (region III) and also at levels approaching the threshold, ΔK_{th} , at the lower end (region I), with an intermediate region II that is described usually by some power-law relationship, as described in Equation (1.3). In an aggressive environment, the corrosion fatigue crack growth curves can be quite different, depending on the sensitivity of the material to the given environment, and the occurrence of various static-stress fracture mechanisms. The environmental effect is quite strong above some threshold for SCC (K_{ISSC}); certain loading factors, such as cyclic frequency, stress ratio, and stress wave form, can have marked effects on the crack growth curves. Therefore, a variety of curves can be expected from the broad range of materials-environment-loading systems that will produce various corrosion fatigue crack processes. Such an example is illustrated in Figure 1.9.

1.3.7 Corrosion fatigue modelling

Crack initiation

Models for the initiation of fatigue cracks in aqueous media have generally been based on the following events:

1. stress concentration at the roots of corrosion pits serving as crack nucleation sites.
2. preferential electrochemical attack at regions (such as PSBs) where plastic deformation is localised, with relatively less deformed surrounding regions acting as cathodes.
3. preferential electrochemical attack at locations on the surfaces of a fatigued metal where the protective oxide film is ruptured.
4. a reduction in the surface energy of the alloy as a consequence of the adsorption of the environmental species, and a consequential increase in the rates of microcrack growth.

Crack propagation (long crack regime)

The rates of environmental attack and their effect on fatigue lives are influenced by the electrochemistry of the medium as well as by the specific mechanical loading conditions. Several models have been proposed to describe the effect of mechanical fatigue under a chemical environment. They are reviewed briefly below.

'The superposition model'

Corrosion fatigue crack propagation was first described by a superposition concept proposed by Wei and co-workers [37-39].

Considering da/dN versus ΔK data for an alloy in an aggressive environment, the total crack growth rate is considered to be the superposition of two parts:

$$\left(\frac{da}{dN}\right)_e = \left(\frac{da}{dN}\right)_m + \left(\frac{da}{dN}\right)_{cf} \quad (1.18)$$

where $(da/dN)_e$ is the growth rate in the aggressive environment; $(da/dN)_m$ is the rate of plasticity-driven fatigue crack propagation in an inert environment; $(da/dN)_{cf}$ is the difference between the total growth rate and the 'pure' fatigue growth rate and represents the effect of interaction between the cyclic plastic deformation and the chemical reactions.

'The competition model'

This model was proposed by Austen and Walker [40]. The measured environmental crack growth rate $(da/dN)_e$ is determined by the dominant mechanism (the faster of two processes, either mechanical fatigue or cycle-time dependent corrosion fatigue).

$$\left(\frac{da}{dN}\right)_e = \left(\frac{da}{dN}\right)_m (\theta) + \left(\frac{da}{dN}\right)_{cf} (\phi) \quad (1.19)$$

Here θ and ϕ are measured by fractographic analysis and $\theta = 1 - \phi$. Considering environment-dominant fatigue cracking, $\phi = 1$ and $(da/dN)_m \ll (da/dN)_{cf}$, therefore $(da/dN)_e = (da/dN)_{cf}$.

'Time (frequency) dependent models'

Several models [41, 42] of corrosion fatigue propagation begin with the following assumption:

$$\left(\frac{da}{dN}\right)_{cf} = \frac{da}{dt} \left(\frac{1}{f}\right) \quad (1.20)$$

where f is the cyclic loading frequency and da/dt is the average time-based growth rate per loading cycle.

The frequency and the mean stress effects on the crack growth rate could be assumed in a form in accordance with the modified Paris law:

$$\frac{da}{dN} = C\Delta K^m + \phi \quad (1.21)$$

The fatigue endurance limits can be calculated, for different initial and final crack lengths, a_i and a_f respectively (based upon a typical low value threshold stress intensity for crack propagation of the order of $2\text{MPa}\sqrt{\text{m}}$), by means of the equation:

$$N = \int_{a_i}^{a_f} \frac{da}{(C\Delta K^m + \phi)} \quad (1.22)$$

where $\Delta K = \Delta\sigma\sqrt{\pi a} f(a/w)$.

Unified model considering short and long crack regime

'The modified Hobson-Brown model and the Navarro-de los Rios model'

Akid and Miller [43, 44], modifying both the H-B model and the N-R model, proposed corresponding versions for short corrosion fatigue crack growth. The crack extension rate is controlled by both the metal dissolution and the mechanical growth processes. Subject to the superposition rule, the fatigue crack growth rate is expressed by the sum of two terms, the growth rate in air and the dissolution rate in the environment, i.e.

$$\left(\frac{da}{dN}\right)_{\text{env}} = \left(\frac{da}{dN}\right)_{\text{air}} + \left(\frac{da}{dN}\right)_{\text{diss}} \quad (1.23)$$

with

$$\left(\frac{da}{dN}\right)_{\text{diss}} = \left(\frac{Mi_a}{ZF\rho}\right) \frac{1}{w} \quad (1.24)$$

where M is the atomic weight of the corroding metal (i.e. Fe), i_a is the anodic dissolution current, Z is the charge on the cation (i.e. Fe^{2+}), F is the Faraday's constant, ρ is the metal density and w is the cyclic frequency.

The equations given above gave agreement with the experimental results for low carbon steel, when calculating crack growth rates and fatigue lifetimes based on the Hobson-Brown and the Navarro-de los Rios models.

Sun [45] observed a large reduction in fatigue strength of an Al-Li alloy in 3.5% NaCl solution and suggested that hydrogen embrittlement resulting from hydrogen diffusion was its main cause. He assumed that hydrogen diffused to the PSB where it lowered the friction stress along crack growth plane, and subsequently improved the Navarro-de los Rios model to consider the corrosion effect. A reasonable agreement between experimental and predicted fatigue lifetime was obtained.

1.3.8 The scope of the present work

The present work focuses on the corrosion fatigue crack growth behaviour of a high strength steel BS251A58, especially in the short fatigue crack regime. Additional consideration is given to the effect of frequency, cathodic polarisation, and electrolyte composition on the corrosion fatigue lifetime and crack growth behaviour.

The microstructurally-sensitive N-R model is used to analyse the experimental data and to predict the fatigue life in air and in a 0.6 M NaCl solution. Some modifications to the model are made to incorporate the corrosive effect on the early stages of crack initiation (i.e. pit growth), stage I to stage II transition, and strain hardening of a parabolic form in order to achieve a more accurate prediction.

References

- [1] A. Wohler (1871), Tests to determine the forces acting on railway carriage axles and capacity of resistance of the axles, *Engineering*, Vol. 11, pp.199-200.
- [2] A. A. Griffith (1920) The phenomena of rupture and flow in solids, *Trans. R. Soc. Lond.*, **A221**, pp.163-197.
- [3] G. R. Irwin (1957) Analysis of stresses and strains near the end of a crack traversing a plate, *Trans. ASME, J. Appl. Mech.*, **24**, pp.361-364.
- [4] S. S. Manson, Discussion of Ref. [5] (1962) *Trans. ASME, J. Basic Eng.*, **84**, pp.537-538.
- [5] J. F. Tavernelli and L. F. Coffin (1962) Experimental support for generalised equation predicting low cycle fatigue, *Trans. ASME, J. Basic Eng.*, **84**, pp.533-536.
- [6] P. C. Paris and F. Erdogan (1963) A critical analysis of crack propagation law, *Trans. ASME, J. Basic Eng.*, **85**, pp.528-534.
- [7] D. O. Sprowls (1989) Evaluation of corrosion fatigue, In *Metal Handbook*, 9th ed., pp.291-302.
- [8] F. C. Smith (1986) Applying fatigue research to engineering design, *The behaviour of short fatigue cracks*, ed. K. J. Miller and E. R. de los Rios, EGF Publication **1**, pp.15-26.
- [9] K. J. Miller (1993) Two thresholds of fatigue behaviour, *Fatigue Frac. Engng. Mater. Struct.* **16**, No. 9, pp.931-939.

- [10] R. O. Ritchie (1977) Influence of microstructure on near-threshold fatigue-crack propagation in ultra-high strength steel, *Metal Science*, pp.368-381, Aug./Sept.
- [11] G. R. Irwin (1960) Plastic zone near a crack and fracture toughness, in *Proceedings 7th Sagamore Ordnance Mater. Conf.*, Vol. IV, pp.63-78, New York: Syracuse University.
- [12] J. R. Rice (1967) Mechanics of crack tip deformation and extension by fatigue, In *Fatigue Crack Propagation*, ASTM STP 415, pp.247-309.
- [13] J. R. Rice (1968), A path independent integral and the approximate analysis of strain concentration by notches and cracks, *J. Appl. Mech.*, **35**, pp.379-386.
- [14] J. W. Hutchinson (1968) Singular behaviour at the end of a tensile crack in a hardening material, *J. Mech. Phys. Solids*, **16**, pp.13-31.
- [15] J. R. Rice and G. F. Rosengren (1968) Plane strain deformation near a crack tip in a power law hardening material, *J. Mech. Phys. Solids*, **16**, pp.1-12.
- [16] J. W. Hutchinson and P. C. Paris (1979) The theory of stability analysis of J-controlled crack growth, *ASTM STP 668*, pp.37-64.
- [17] P. C. Paris, H. Tada, A. Zahoor and H. Ernst (1979) An initial experimental investigation of the tearing instability, *ASTM STP 668*, pp.251-265.
- [18] A. Zahoor and M. F. Kannien (1981) A plastic fracture mechanics prediction of fracture instability in a circumferentially cracked pipe in bending - part I: J-integral analysis, *J. Press. Vessel Tech.*, **103**, pp.352-358.

- [19] G. M. Wilkowski, A. Zahoor and M. F. Kannien (1981) A plastic fracture mechanics prediction of fracture instability in a circumferentially cracked pipe in bending - part II: experimental verification on a type 304 stainless steel pipe, *J. Press. Vessel Tech.*, **103**, pp.352-358.
- [20] A. A. Wells (1961) Unstable crack propagation in metals: damage and fast fracture, *Proceedings of the Crack Propagation Symposium Cranfield*, The College of Aeronautics, Cranfield, England, Vol. **1**, pp.210-230.
- [21] F. M. Burdekin and D. E. W. Stone (1966) The crack opening displacement approach to fracture mechanics in yielding, *J. Strain Analysis*, **1**, pp.145-153.
- [22] R. P. Gangloff and R. P. Wei (1986) In *Small fatigue cracks*, ed. R. O. Ritchie and J. Lankford, Warrendale, PA. TMS-AIME, pp.239-264.
- [23] P. D. Hobson (1985) The growth of short fatigue cracks in a medium carbon steel, *Ph.D thesis*, University of Sheffield.
- [24] A. Navarro and de los Rios (1988) Short and long fatigue crack growth: a unified model, *Phil. Mag.*, **57**, pp.15-36.
- [25] A. Navarro and de los Rios (1988) An alternative model for the blocking of dislocations at grain boundaries, *Phil. Mag.*, **57**, pp.37-42.
- [26] A. Navarro and de los Rios (1988) Compact solution for multizone BCS crack with bounded or unbounded end conditions, *Phil. Mag.*, **57**, pp.43-50.
- [27] A. Navarro and de los Rios (1992) Fatigue crack growth modelling by successive blocking of dislocations, *Proc. R. Soc. Lond.*, **A 437**, pp.375-390.

[28] B. A. Bilby, A. H. Cottrell and K. H. Swinden (1963) The spread of plastic yield from a notch, *Proc. R. Soc. Lond.*, A **272**, pp.304-314.

[29] X. J. Xin, E. R. de los Rios and A. Navarro (1992) Modelling strain hardening at short fatigue cracks, in *Short Fatigue Cracks*, ed. K. J. Miller & E. R. de los Rios, Mechanical Engineering Publications, pp.369-389.

[30] F. P. Ford (1984) Current understanding of mechanisms of stress corrosion and corrosion fatigue, edited by S W Dean, E. N. Pugh and G. M. Ugiansky, *Environment-Sensitive Fracture*, ASTM STP **821**, pp32-51.

[31] B. F. Brown (1972) A preface to the problem of stress corrosion cracking, *Stress-corrosion cracking of metals - a state of the art*. edited by H. L. Jr Craig, ASTM STP 518, pp3-15.

[32] M. O. Speidel (1977) Corrosion fatigue in Fe-Ni-Cr-Alloys, in Proceedings of the International Conference on Stress Corrosion and Hydrogen Embrittlement of Iron-Base Alloys, Unieux-Firminy. France, June 1973, National Association of Corrosion Engineers, pp.1071-1094.

[33] A. Markfield (1986), The role of inclusion in the corrosion fatigue of a marine structure steel, *PhD Thesis*, UMIST.

[34] K. Tanaka and R. P Wei (1985), Growth of short fatigue cracks in hy130 steel in 3.5% NaCl solution, *Eng. Frac. Mech.*, **21**, pp.293-305.

[35] O. Vosikovskiy and R. J. Cooke (1978) *Int. J. Press. Ves. & Piping*, **6**, pp.113-129.

- [36] P. M. Scott (1983) Chemistry effects in corrosion fatigue, *In Corrosion Fatigue: Mechanics, Metallurgy, Electrochemistry and Engineering*, ASTM STP 801, ed. Crooker and B. N. Leis, pp.319-350.
- [37] R. P. Wei (1979) Fatigue mechanisms, ASTM STP 675, ed. J. T. Fong , Philadelphia PA ASTM, pp.816-840.
- [38] R. P. Wei and J. D. Landes (1970). Correlation between sustained-load and fatigue crack growth in high strength steels. *Materials Research and Standards*, 9, pp.25-27.
- [39] R. P. Wei and M. Gao (1983), Reconsideration of superposition model for environmentally assisted fatigue crack growth, *Scripta Metall.*, 17, pp.959-962.
- [40] I. M. Austen and E. F. Walker(1984), Corrosion fatigue crack propagation in steels under simulated offshore condition, *Fatigue 84*, pp.1457-1469.
- [41] F. P. Ford (1988) Status of research on environmentally-assisted cracking in LWR pressure vessel steels, *Journal of Pressure Vessel Technology-Transactions of ASME*, Vol.110, No.2, pp.113-128.1988.
- [42] F. P. Ford (1988) Crack-Tip Chemistry, *Proceedings of the First International Conference on Environment-Induced Cracking of Metals*, Eds. R.P.Gangloff and M. B. Ives, Octobre 2-7, 1988, The American Club, Koler, Wisconsin, USA, NACE.
- [43] R Akid and K. J. Miller (1990) The initiation and growth of short fatigue cracks in an aqueous saline environment, *Environmental Assisted Fatigue*, EGF7, ed. P. Scott, Mechanical Engineering Publication, London, pp.415-434.

[44] R. Akid and K. J. Miller (1991) Short fatigue crack growth behaviour of a low carbon steel under corrosion fatigue conditions, *Fatigue Fract. Engng. Mater. Struct.*, **14**, pp.637-649.

[45] Z. Y. Sun (1991) Long life corrosion fatigue in an Aluminium-Lithium alloy, *Ph.D Thesis*, University of Sheffield.

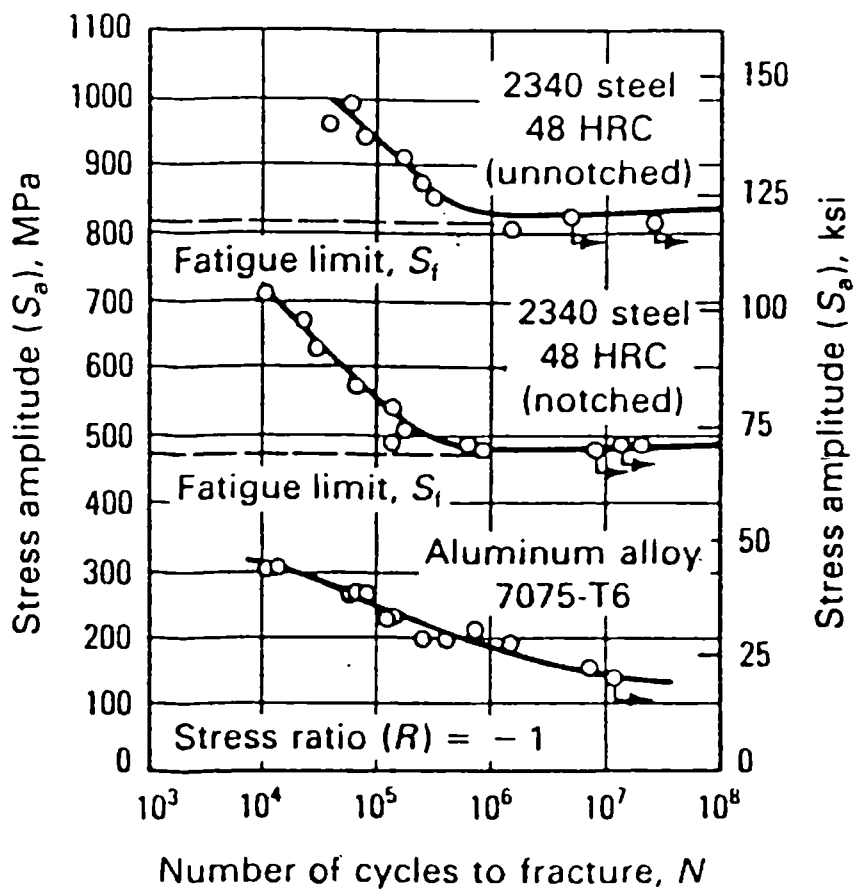


Figure 1.1 Typical S-N curves for constant amplitude and sinusoidal loading [7].

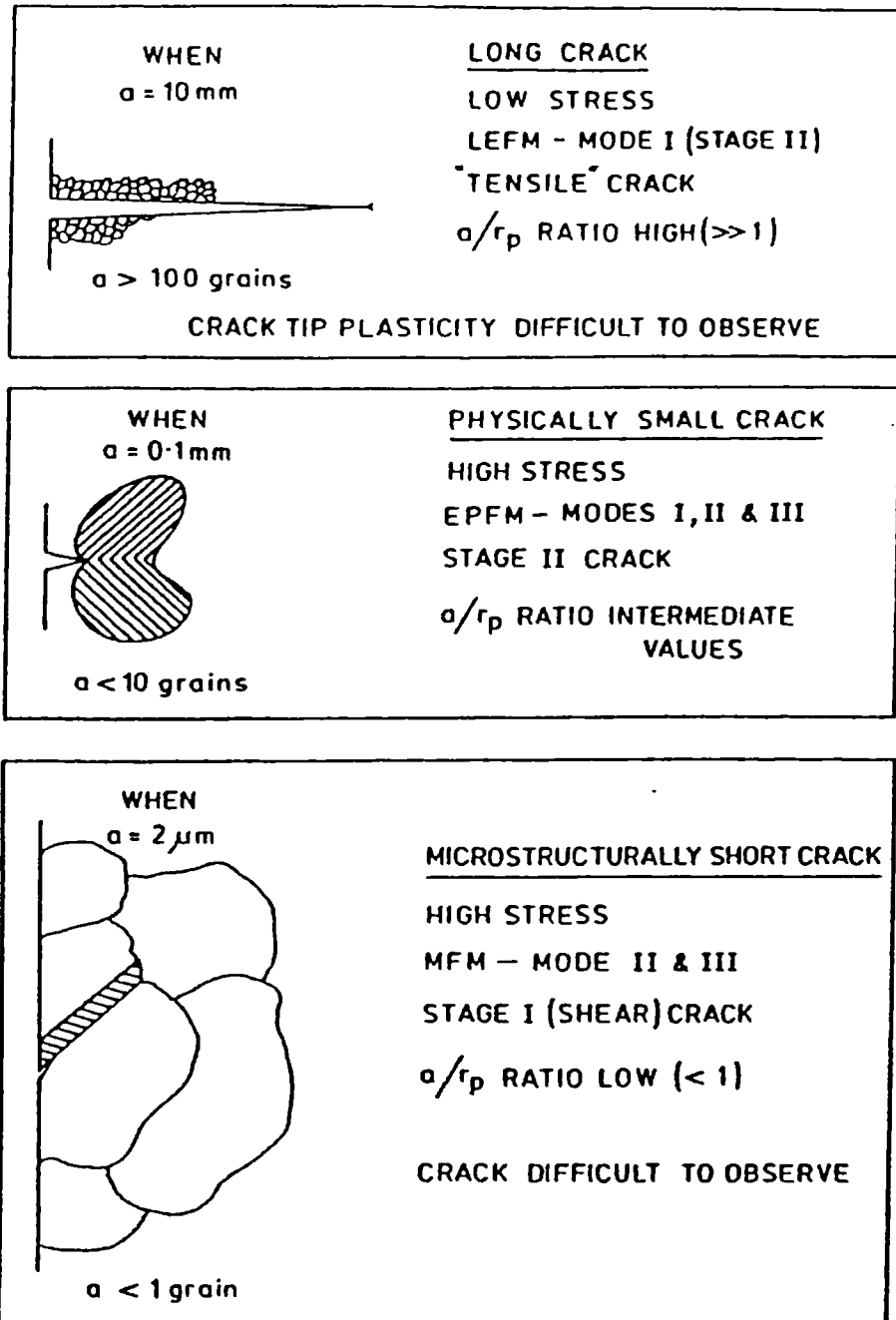


Figure 1.2 The three distinct regimes of long cracks, physically small cracks and microstructurally short cracks. Here a =crack length and r_p =plastic zone size [9].

The two thresholds of fatigue behaviour

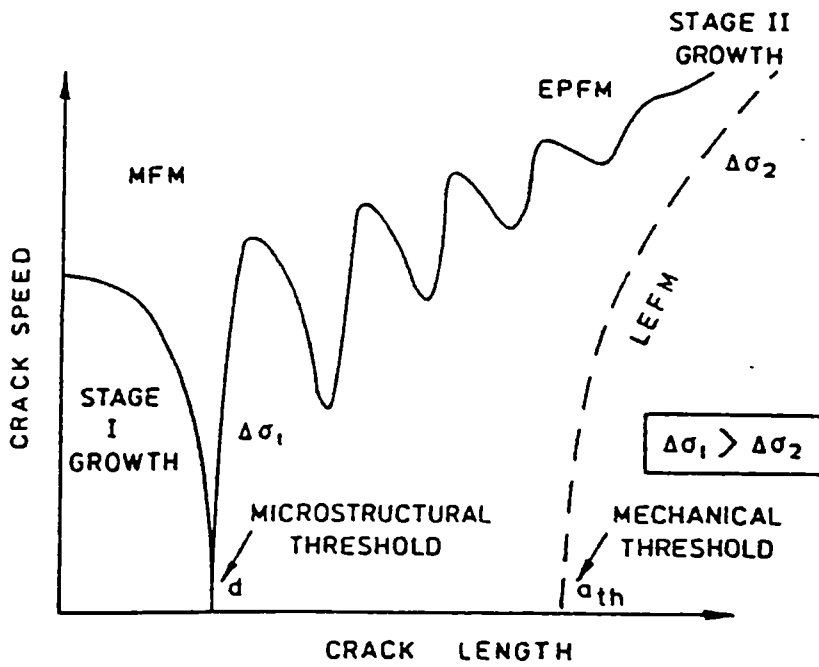


Figure 1.3 The two fundamentally different fatigue thresholds, d and a_{th} [9].

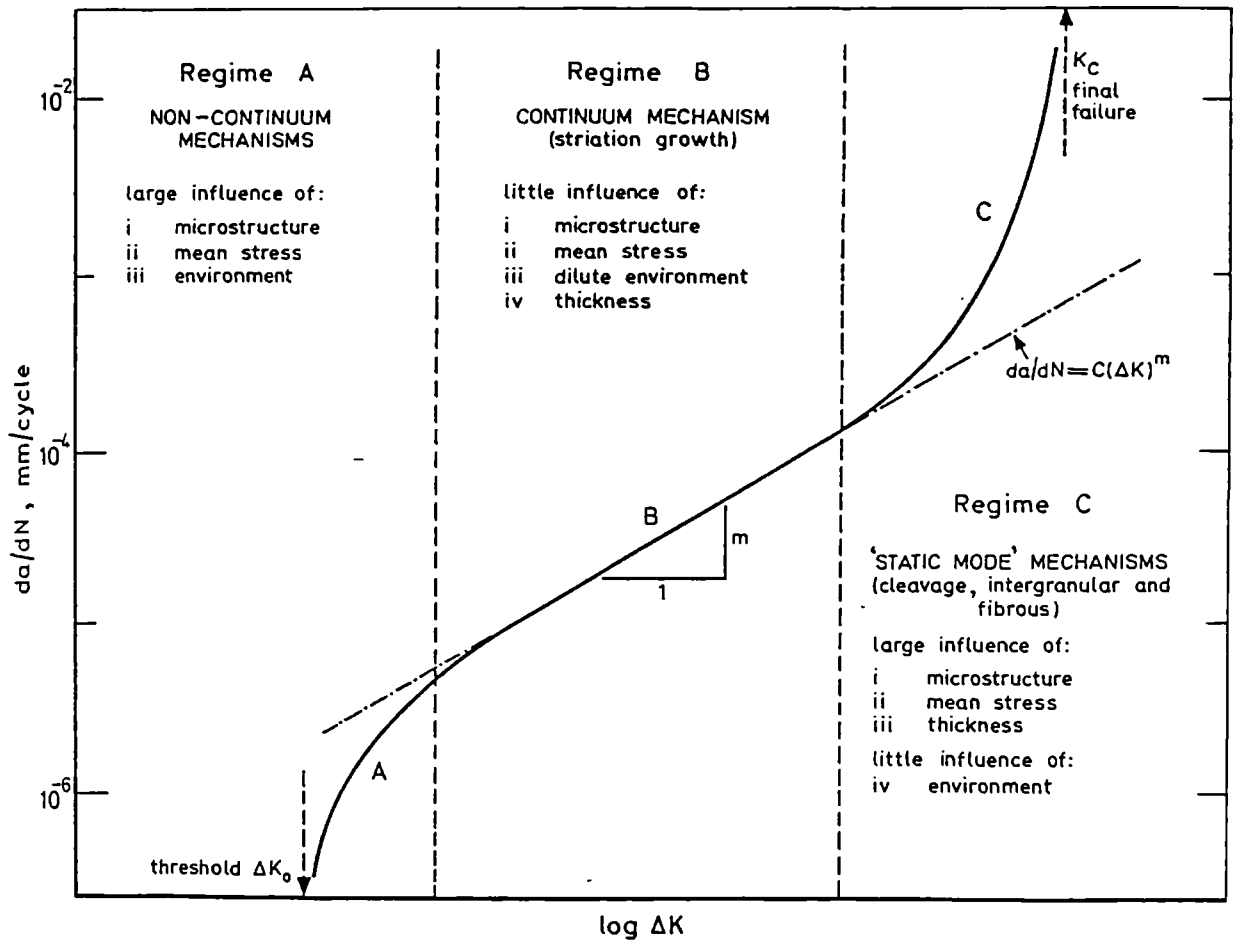


Figure 1.4 Primary fracture mechanisms in steels associated with a sigmoidal variation of fatigue crack propagation rate (da/dN) when plotted as a function of the alternating stress intensity factor (ΔK) [10].

A. Navarro and E. R. de los Rios

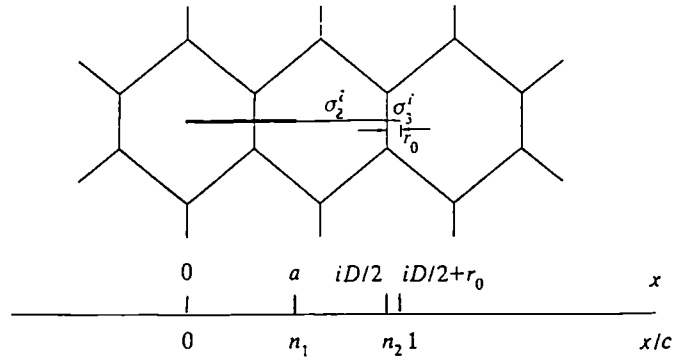


Figure 1.5 Schematic representation of a crack, slip band and a zone simulating the locked dislocation across the grain boundary; σ_2 , σ_3 , are friction stresses [24].

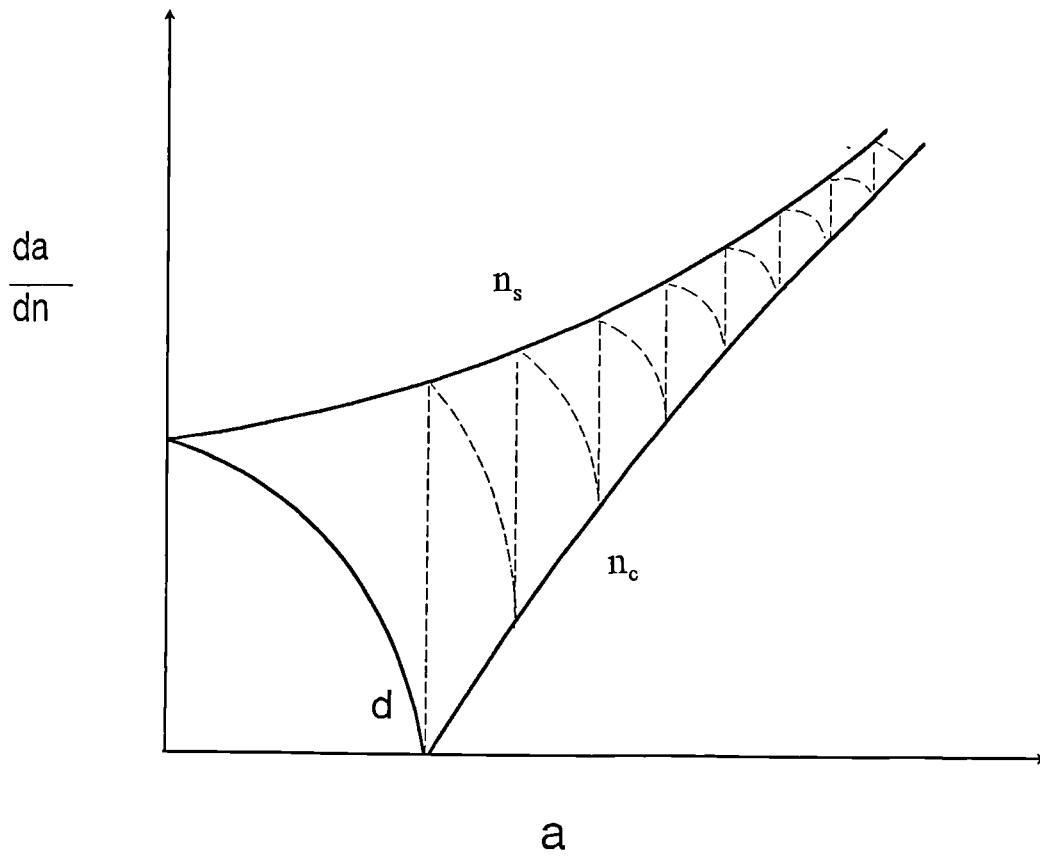


Figure 1.6 Oscillating pattern of crack growth rate as predicted from the Navarro-de los Rios model [24].

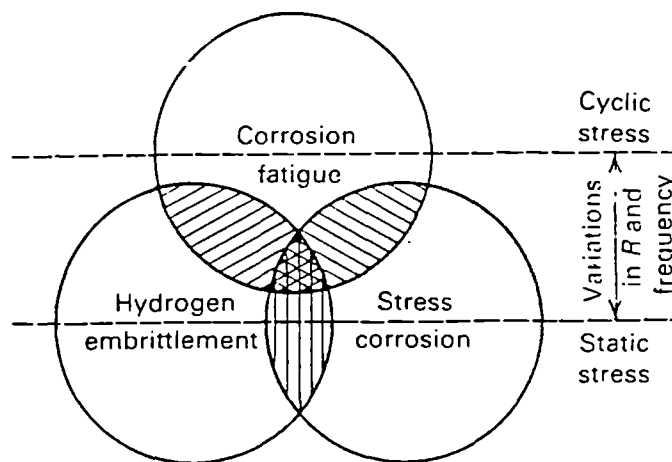


Figure 1.7 Venn diagram illustrating the inter-relationship among stress corrosion, corrosion fatigue, and hydrogen embrittlement [30].

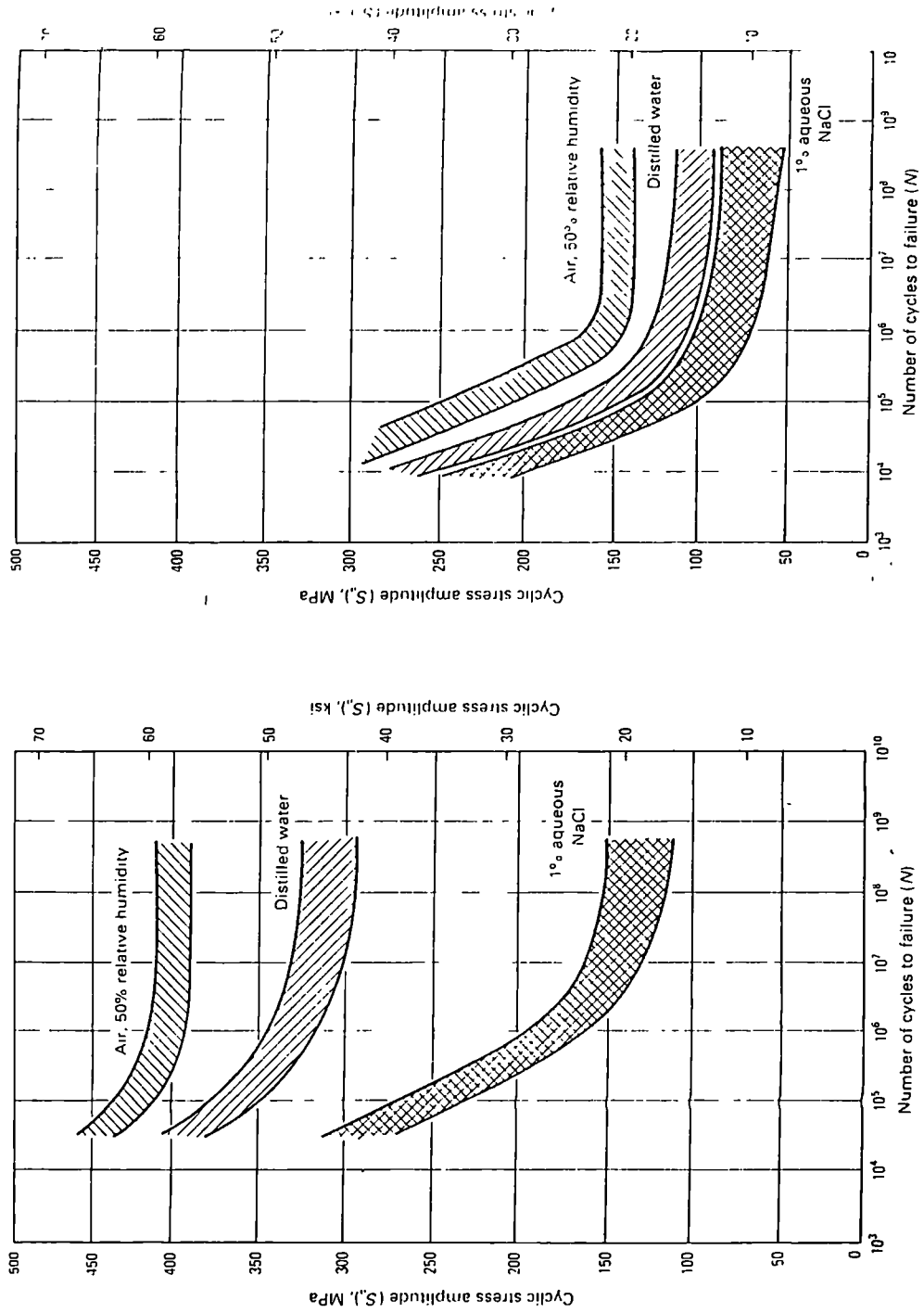


Figure 1.8 Corrosion fatigue endurance data for specimens of 13% Cr steel. Rotating bending tests (mean load zero) at a frequency of 50Hz and a temperature of 23 degree C [31].

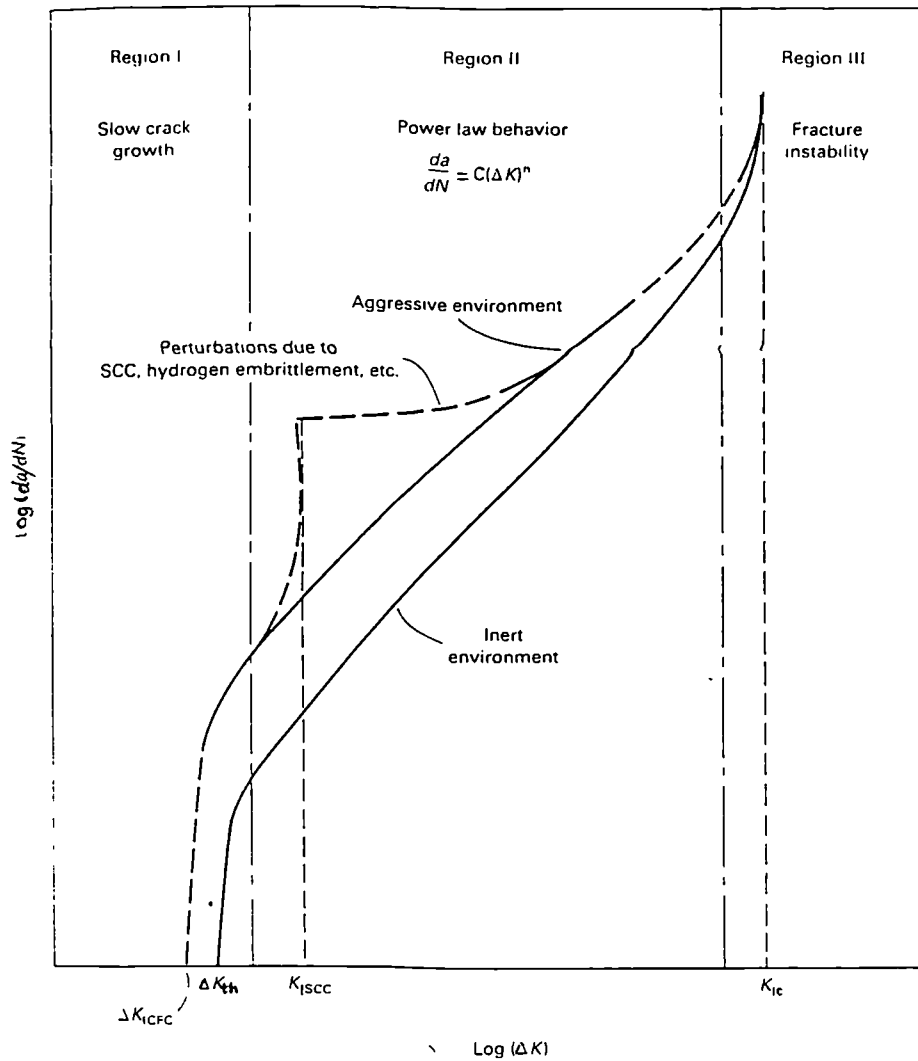


Figure 1.9 Inert atmosphere and corrosion fatigue crack propagation rates as a function of the cyclic crack tip stress intensity factor [36].

Chapter 2 Experiment Work

2.1 Introduction

The present project concerns fatigue crack growth of a high strength spring steel (BS251A58) subject to fully reversed shear loading in an aerated 0.6M NaCl solution. In addition consideration has been given to the influence of cyclic frequency, and the effect of cathodic potential and electrolyte composition on crack growth behaviour. The experimental work is described in this chapter while preliminary experimental results, i.e. basic mechanical and chemical properties of the test material, are reported in Chapter 3. The experimental results for fatigue tests are presented in Chapter 4, and the modelling and prediction analyses are described in Chapter 5.

The experimental work includes following aspects:

- Test machine calibration,

- Preparation of specimens,

- Metallographic studies,

- Mechanical tests and hardness measurements,

- Cyclic torsion tests,

- Electro-chemical property studies,

- SEM and X-ray spectrum analyses,

- Fatigue tests in air,

- Corrosion fatigue in a 0.6M NaCl solution, at pH 6, and a frequency of 5Hz, at room temperature,

- The influence of cyclic frequency on corrosion fatigue crack growth behaviour,

- The effect of cathodic potential on corrosion fatigue crack growth behaviour, and

The effect of electrolyte composition on corrosion fatigue lifetime.

2.2 Test material

2.1.1. Material and in-service condition

The material to be tested is a silico-manganese spring steel, BS251A58, which is heat treated to a quenched and tempered condition to provide a high yield strength. Such a material is used in railway track fastener, see Figure 2.1. The test material was provided by Pandrol International Ltd, a company specialising in the manufacture of railway components which are subjected to a variety of environmental conditions due to exposure all forms of weather. These fastening devices are subjected to both torsion and bending either statically or, when a train passes over, dynamically.

2.1.2 Chemical composition

The chemical composition of this material is (%wt): 0.56 C, 1.89 Si, 0.93 Mn, 0.24 Cr, 0.032 Mo, 0.026 Ni, remainder Iron.

2.1.3 Heat treatment

The heat-treatment for the first batch material to be studied (Groupe A) was as follows:

Austenitised at 920° C for 15 minutes followed by an oil quench, then tempered at 475° C for 30 minutes followed by an oil quench.

The heat-treatment for the second batch of material (Group B) was as follows:

Austenitised at 950° C for 15 minutes followed by an oil quench, then tempered at 495° C for 30-40 minutes followed by an oil quench.

2.3 Test facilities

2.3.1 Test machine for torsional fatigue test

Fatigue tests were conducted under fully reversed torsion loading. Detailed descriptions of the torsion machine can be found in reference [1]. The torsion machine is illustrated in Figure 2.2 (a), (b), (c) and (d)

A D.C. motor drives a variable throw crank and a connecting rod, generating a sinusoidal wave form at frequencies between 0.4 and 20 Hz. The connecting rod is attached to one specimen holder via a fine control link. The two ends of the specimen are fixed with a pair of cotter-pins through the torsion grips. The applied torque is measured by a load cell. The twist angle of the specimen following the application of torque, is measured by cams operating Linear Variable Displacement Transducers (LVDT), see Figure 2.2 (d). Two cams are fixed on the specimen at a gauge length of 25 mm and these drive the two LVDTs. The recorded information, such as torque range, mean torque, twist angle, number of loading cycles, frequency and temperature can be logged at pre-set periods during the test, in a BBC computer which can provide a print out through an Epson-80x printer. The computer controlled program facilitates the automatic switch-off of the motor and solution circulation pump at a pre-set number of cycles or at any number of cycles during corrosion fatigue tests. In addition, the computer can stop the test machine automatically when the torque range decreases by 20 percent of the original stabilised torque range. This decrease is the failure criteria in the corrosion test programme.

2.3.2 Environment circulation system

The corrosion solution from a tank is pumped to a corrosion cell fitted onto the specimen, see Figure 2.2 (b).

The corrosion cell is specially designed for the cathodic potential charge on the centre section of the specimen surface, see Figure 2.2 (c). The applied potential can be controlled and recorded by a Viglen PC computer via a polarisation instrument.

2.4 Calibration of torque and twist angle

2.4.1 Calibration of torque

The applied torque is proportional to the mean value of the out-put signal from four resistance strain gauges adhered to the load cell surface. The load cell was calibrated by hanging dead weights on to a load arm and recording the output from a strain gauge bridge indicator. The results of the calibration is expressed as

$$T = 9.974932v + 0.024937 \quad (2.1)$$

where T is the applied torque in N.m., v is the output in volts of the strain gauge bridge indicator. The calibration results are also shown in Figure 2.3 and Table 2.1.

Figure 2.3 (b) indicates that the applied torque is independent of the loading frequencies in the range 2.5Hz to 5Hz, when the torque is within ± 50 N.m. However the applied torque increases slightly when the frequency is higher than 6Hz (see Figure 2.3(c)).

2.4.2 Calibration of twist angle

The twist angle is measured by a pair of LVDTs. The independent moving spindles of two transducers (A and B) resting on the two cams, move vertically, when the two cams rotate in the plane vertical to the axis of the specimen over the gauge zone of the specimen. The output of the two transducers is proportional to the angular movement of the two cams. During the calibration process, the twist angle of the cams was produced by rotating the input shaft via a gear box which had a reduction ratio of 3000:1. The calibration results of

the LVDTs versus twist angle measurements are shown in Figure 2.4 and Table 2.2, and can be expressed by the following equation:

$$\Delta\theta = \frac{\Delta S + 0.038}{0.742} = \frac{(S_B - S_A) + 0.038}{0.742} \quad (2.2)$$

where S_A and S_B are the output of the transducer A and B in volts respectively, and $\Delta\theta$ is the twist angle in degrees.

From the torque and twist angle in torsional tests, the stress and strain on the surface of a specimen can be calculated from Brown's equation detailed in Chapter 3.

In order to confirm the calibration of the output of the LVDTs, two cylindrical solid specimens of 8mm diameter were used. A strain gauge was adhered on the surface of the centre section of one specimen at a 45° to both the specimen axis and the torsional axis. Meanwhile, the cams were also fixed onto the specimen over a gauge length of 25mm, and the twist angle was measured by the LVDTs, and the torque by the load cell. The output of the strain gauge, which is directly proportional to the strain on the surface of specimen, was shown in a indicator and found to give the same result derived from the LVDT calibration.

For the second specimen, which had the same geometry as the first specimen, four strain gauges were so arranged that the bending effect, if any, was eliminated and gave a higher sensitivity to the torsional signal. The results obtained from the four strain gauges were again in good agreement to those from the LVDTs, indicating the high precision of the LVDT calibration.

The calibration was carried out for both monotonic and cyclic torsional tests (using the multiple step method in the elastic region). The results of the strain calibration are given in Chapter 3.

2.5 Preparation of the specimens

The hour-glass shaped specimen was used for torsional fatigue tests in order to facilitate an easy detection of crack initiation in the central section of the specimen. The specimen configuration is shown in Figure 2.5. It should be noticed that specimens for corrosion fatigue have a minimum diameter of 8mm in the central section, and those for the tests in air have a minimum diameter of 7.3mm in the central section.

All gauge length sections of the specimens were polished with a wet polish, using increasingly finer grit, 240, 400, 800, and 1200 SiC paper, prior to the final polishing by cloth using diamond pastes of 30, 15, 6, 1 and 0.25 μm grits receptively, finally to a mirror image surface finish. After polishing, there are no surface scratches appreciable under an optical microscope at 400X magnification.

Indentation reference marks were made within the gauge length of the as-polished specimen in order to aid the identification of the position of cracks, especially in the short crack regime. These marks were made using a Vicker's micro-hardness indenter on four locations, i.e. top, bottom, front and rear side of the specimen circumference, located at a distance 9 to 10mm each side of the minimum diameter of the specimen. During experiments it was found that those indentation marks have little influence on the initiation of short fatigue cracks since no crack was observed to initiate from those marks.

2.6 Metallographic studies

The microstructure of the BS251A58 steel under the given heat treatment was investigated by metallographic studies (etching with a 2% Nital solution).

Scanning Electron Microscopy and X-ray spectrum analyses were also used to study the microstructure and chemical element compositions for the present material.

The distribution of the non-metallic inclusions, in three dimensions, has been investigated under optical microscopy.

2.7 Mechanical tests

Monotonic tensile tests were carried out using a MAYES servo-hydraulic test machine according to the British Standard 18 [1]. The configuration of the specimen is shown in Figure 2.6

2.7.1 Hardness

The hardness of both batches of materials, under different as-received heat treatments, was measured along the longitudinal and transverse directions relative to the torsion specimen axis using a Vicker's micro-hardness indicator.

2.8 Cyclic torsion tests

Cyclic torsion tests were conducted in a torsion machine at a frequency of 5Hz, at room temperature, using multiple-step load increasing method to obtain a cyclic stress-strain curve. Two hour glass type specimens (C and D) were used having a minimum diameter in the central section of 7.3mm and 8mm respectively. The applied torque was increased step by step. At every torque level, the stabilised torque and twist angle were recorded by a BBC computer after a few hundred cycles. The stabilised cyclic torque and angular displacement (in degrees) at every applied torque level is plotted on a log-log co-ordinate system, and their relationship is in the following form:

$$\Delta T = A(\Delta\theta)^n \quad (2.3)$$

where ΔT is the torque in N.m, and $\Delta\theta$ is the twist angle in degrees.

2.9 Electro-chemical studies

2.9.1 The apparatus

The electro-chemical test cell is constructed to allow the following items to be inserted into the solution chamber: the test electrode (working electrode), two platinum auxiliary electrodes, a capillary with salt-bridge connection to the reference electrode (calomel electrode), inlet and outlet for an inert gas, and a thermometer. The cell is shown in Figure 2.7(a) and (b).

A one-litre round-bottom flask has been modified by the addition of various necks to permit the introduction of the working electrode (working electrode is the name given to the electrode being investigated), two platinum auxiliary electrodes, a luggin capillary with salt-bridge connection to the reference electrode, gas inert and outlet tubes, and a thermometer. The lugging probe-salt bridge separates the bulk solution from the saturated calomel reference electrode, and the probe tip can be easily adjusted to bring it in close proximity with the working electrode.

A "Teflon" holder is required for mounting thin discs of the test material. A 5mm diameter rod, 20cm long, made from stainless steel was used for an electrical connection. A leak-proof assembly was obtained by a compression fit between the electrode, the "Teflon" gasket, an "O" ring and the "Teflon" specimen holder. The test material is the BS251A58 high strength spring steel. The sample of this material was cut as thin discs of approximately 11.85mm in diameter and 2.8mm in thickness, polished with 1200-grit Sic

paper, cleaned with acetone and dried, and then mounted onto the electrode holder. The sample surface area exposed to the bulk solution was measured to be 0.95cm^2 .

For comparison, the stainless steel type AISI316 was also used in tests with the same size of specimen and test procedures.

A schematic potentiostatic anodic polarisation wiring diagram is illustrated in Figure 2.8 [7]. The potentiodynamic polarisation resistance measurements were conducted according to the ASTM standards G59-78 [2] and the potentiodynamic anodic polarisation measurements were carried out following the procedures described in ASTM standard G5-82 [3].

The electrochemical polarisation resistance measurements and curve-plotting were determined using software "AUTOSTAT" installed in a PC via a Thompson Electrochem Potentiostat connected to the polarisation cell. The results of corrosion potential and corrosion current were recorded and analysed by the computer.

2.9.2 Determination of i_{corr}

In order to determine the i_{corr} value of the test material, the anodic and cathodic Tafel slopes (b_a , b_c) and the polarisation resistance, R_p , need to be measured.

The measurement of anodic and cathodic Tafel slopes (b_a , b_c)

The test sample was first fitted into the test cell, and the corrosion potential was recorded by a computer. When the sample had been immersed in the 0.6M NaCl solution (pH=6) for approximately 30 minutes, a relative stable corrosion potential value, called the rest corrosion potential (E_{rest}), was achieved.

Once E_{rest} was reached, a potential initially set to be 100 mv *negative* to the stable rest corrosion potential E_{rest} was applied to the sample which scanned at a sweep rate of 20 mv/min. The corrosion potential and corrosion current on the sample surface were recorded by a computer continuously. As the applied potential increased to the rest potential E_{rest} , the corrosion potential versus corrosion current density curve, was plotted on semi-logarithmic co-ordinates; and cathodic Tafel slope, b_c , is determined as the tangent of this curve.

The anodic Tafel slope, b_a , was also measured following the same procedure, but the potential scan began at a pre-set applied potential of 100 mv *positive* to the rest potential E_{rest} .

The measurement of polarisation resistance R_p

The polarisation resistance R_p of a corroding electrode is defined as the slope of the graph of potential E against current density i at the rest corrosion potential E_{rest} , i.e.

$$R_p = \left(\frac{\partial \Delta E}{\partial i} \right)_{\Delta E=0} \quad (2.4)$$

The potentiodynamic polarisation curve was recorded throughout the polarisation process. The applied potential started from -10 mv relative to the rest potential, continuously increased to +10 mv relative to the rest potential at a sweep rate of 60 mv/min, and then dropped back to -10 mv. When a linear potential-current density plot was obtained, the polarisation resistance, R_p , was derived graphically from the tangent of the curve at the origin of the plot ($\Delta E=0$).

From the polarisation resistance R_p , the corrosion current density i_{corr} can be calculated as follows:

$$i_{\text{corr}} = \frac{B}{R_p} \quad (2.5)$$

where B is a combination of the anodic and cathodic Tafel slopes (b_a, b_c) expressed by:

$$B = \frac{b_a b_c}{2.303(b_a + b_c)} \quad (2.6)$$

The anodic and cathodic Tafel slope, b_a and b_c , the polarisation resistance, R_p , and the corrosion current density, i_{corr} , for the present test material in 0.6M NaCl solution at pH=6, were obtained (for results see Chapter 3).

2.9.3 Potentiodynamic curve

After immersing a sample (cut from the BS251A58 spring steel bar) in 0.6M NaCl solution for 30 minutes, the rest potential E_{rest} state was achieved and then the applied potential started from a value negative to the rest potential to several hundred micro volts positive to the rest potential, at a slow scanning sweep rate (such as 60 mv/min), or a fast scanning sweep rate (such as 1200 mv/min). From these tests the potentiodynamic curves were obtained.

In order to study the influence of aggressive ion and inhibitors on the electrochemical characteristics of the high strength steel BS251A58 steel, another four electrolyte concentration solutions were made, namely:

aggressive ion solutions:

- (1) 2M NaCl
- (2) 0.6M NaCl + 0.1M Na₂SO₄

inhibitor solutions:

- (3) 0.6M NaCl + 0.2 M NaNO₂
- (4) 0.6M NaCl + 0.5 M NaNO₂

The first and second kind of solutions listed above were used to investigate the effect of aggressive ion, and the third and fourth to investigate the effect of inhibitors.

Seven samples were cut from the BS251A58 spring steel bar, and used in different solutions, see Table 2.3. The applied potential started from a value negative to the rest potential for each test (after immersion of the sample in the solution for 30 minutes), to several hundred micro volts positive to the rest potential, at slow-scanning sweep rates ranging from 20, 60, and 120 mv/min, or fast scanning sweep rates ranging from 1200, 1600, and 2000 mv/min.

The anodic polarisation curve was obtained in the presence of an aggressive ion, or an inhibitor for each test. Comparisons with results obtained from a 0.6M NaCl solution are detailed in Chapter 3.

The application of different potential sweep rates allowed an assessment of the possible susceptibility of a material to stress corrosion cracking where active/passive corrosion mechanisms prevail. From the potentiodynamic polarisation curves, the test materials can be assessed as either a weakly passivating metal or a strongly passivating metal in a particular metal/environment system, in order to understand the different mechanisms of environment-sensitive cracking which arise from different polarised potentials in various kinds of solutions.

2.9.4 Corrosion tests

In addition to the fatigue tests, further samples were polished to the same surface finish as the fatigue test specimens and then exposed to corrosive solution or pitting solution in the absence of stress. The table below lists the electrolyte concentrations in the corrosion or pitting solution. The development of pits was studied as a function of time in the various solutions. The number of pits and the sites of pitting were noted.

- (1) 2M NaCl
- (2) 1M NaCl
- (3) 0.6M NaCl
- (4) 0.6M NaCl + 0.1 M Na₂HCO₃
- (5) 0.6M NaCl + 0.1 M Na₂CO₃
- (6) 0.6M NaCl + 0.1 M Na₂SO₄
- (7) 0.6M NaCl + 0.2 M NaNO₂
- (8) 0.6M NaCl + 0.5 M NaNO₂

2.10 Crack growth monitoring

2.10.1 The surface replication technique

A number of methods are commonly used for monitoring long crack growth of pre-cracked specimens, and include optical, acoustic microscopy and electrical potential drop methods.

So far, however, only a few methods are available for studying short crack growth behaviour on smooth specimen surfaces. For example, acoustic microscopy, video camera monitoring, and the plastic replication technique.

The surface plastic replication technique was applied here in the present tests to detect crack initiation and propagation during fatigue cycling. At a pre-set time of replication, the corrosion products had to be cleaned by gently swabbing the specimen surface with cotton wool soaked in acetone and then a piece of acetate sheet having of length 22 mm and width 12 mm was placed on the front surface of the specimen at which time a few drops of acetone were sprayed onto it. This helps in wrapping the remaining part of the tape onto the surface of the specimen. After drying for 5 minutes, the piece is removed from the

specimen surface, and fixed onto a microscope glass slide for subsequent microscopical examination using an in-house Image Analysis System. Another piece of acetate sheet was placed onto the rear side of the specimen surface in order to obtain details over the whole circumferential surface area.

The advantage of this technique as applied in this study on short crack growth behaviour, is its effectiveness and its economy. It can record pits and cracks of a few microns in length during the early phase and cracks up to the point of failure. However, all the information recorded only illustrates crack growth behaviour on the surface of the specimen and it is difficult to detect crack growth in the depth direction.

Consequently a few specimens in the corrosion fatigue test series were removed from the test machine at a pre-set number of cycles, and examined directly under the optical microscope. The crack depth on the specimen surface could be obtained from a change in the focus length of the microscope. The crack profile aspect ratio, $\lambda = a / c$, where c is the half crack length on the surface, a is the crack depth, can be obtained. After completion of the tests, the circumferential and fracture surfaces of specimens were cleaned and dried and examined using a Scanning Electron Microscope. The depth of cracks at the stage I to stage II transition was measured from SEM photographs, and the depth of stable growth of the final stage-II cracks was obtained by post-examination.

2.10.2 The image analysis system

This system consists of an optical microscope, an image capturing monitor, a video camera mounted on the microscope all of which is connected to a personnel computer fitted with a digital image analysis board.

Before the measurement of cracks, the measuring monitor screen has to be calibrated using calibration slides for different magnifications of the optical microscope.

Features of the image from a replica, such as pit size, inclusion size, and crack length etc. are displayed on the monitor and can be measured with a high resolution, stored and analysed by the REPAN software that is installed in the computer.

In addition, the microscope provides a facility for auto-exposure photography. This requires the replacement of the video camera by a photographic camera.

2.11 Fatigue test in air

Seven hour-glass specimens were used to carry out fully reversed torsion fatigue tests in air, see Table 2.4, under stress ranges from 980 MPa to 1285 MPa. Some specimens had a minimum diameter of 8mm in the central section (these were used in low stress range tests), some of them had a minimum diameter of 7.3 mm (these were used in high stress range tests).

The results of fatigue life for various stress levels are presented in Chapter 4, together with the S-N curve obtained by Murtaza and Rehman [4, 5].

2.12 Corrosion fatigue

Tests were carried out to examine the following aspects:

1. Corrosion fatigue behaviour in 0.6M NaCl solution at a frequency of 5Hz
2. The effect of frequency
3. The effect of cathodic polarisation
4. The effect of electrolyte composition

2.12.1 Corrosion fatigue

Ten smooth hour-glass shaped fatigue specimens, polished to a mirror-image finish ($R_a=0.25\ \mu\text{m}$), were tested under fully reversed shear loading conditions in an aerated 0.6M NaCl sodium chloride solution at pH6, at room temperature and at a frequency of 5Hz, see Table 2.5. Stress ranges from approximately 200 MPa to 920 MPa were applied, these levels being lower than the fatigue endurance in air for the same material.

A surface replication technique was applied to detect crack initiation and propagation during fatigue cycling. The failure criterion used for all tests was the instant when a 20% reduction in the stabilised cyclic load occurred. After completion of the tests, specimens were cleaned and dried and then examined using a Scanning Electron Microscope.

The S-N curve in 0.6M NaCl solution at 5Hz, room temperature was determined. The pit growth and crack growth behaviour was investigated. When crack growth changed from stage-I to stage-II, the final stage-I crack length and number of cycles at the transition stage for various stress levels were studied.

The free corrosion potential and corrosion current of the specimen surface as a function of time were recorded for two specimens TC10, TC7, exposed to the 0.6M NaCl solution, at pH=6, and room temperature.

pH value in the crack tip zone

The approximate pH value of the solution within the crack tip zone at the final stage of crack growth, was measured by freezing the fatigued specimen (TC11) in-situ in liquid nitrogen followed by pressing-on pH indicator papers.

2.12.2 The frequency effect

Time-dependent corrosion fatigue is affected by cyclic frequency. The present torsion fatigue testing was conducted at frequencies of 2.5, 5 and 12.5Hz under two different applied shear stress ranges of approximately 400 MPa and 600 MPa (see Table 2.6). Due to equipment limitations, frequencies lower than 2 Hz or higher than 12.5 Hz were difficult to attain, and the applied shear stress range could not exceed 600 MPa at the high frequency of 12.5Hz.

The fatigue life and crack growth behaviour under different loading frequencies were investigated; for results see Chapter 4.

2.12.3 The effect of electrolyte composition

The most aggressive electrolyte commonly known is chloride, which provokes pitting in iron, nickel, aluminium, titanium, zirconium and in their alloys with other metals. There are a few other aggressive ions, such as perchlorate ions, halide ions and sulphate ions, which generate pitting of iron, aluminium and other metals. However, it is well known that the severity of pitting depends not only on the concentration of aggressive ions in the solution, but also on the concentration of non-aggressive species. Many compounds may act as inhibitors when present in chloride-containing solutions. For example, the following chemicals would all act as inhibitors for irons and carbon steel:- sulphates, nitrates, sodium carbonate, sodium carbonate+sodium phosphate, hydroxyl ions, nitrites, and ammonia.

For corrosion fatigue testes, as shown in Table 2.7, another five kinds of different electrolyte composition solutions were made for the purpose of comparison with the results obtained in 0.6M NaCl solution. They were:

- (1) 0.01M NaNO₂ +0.6M NaCl
- (2) 0.1M NaNO₂ +0.6M NaCl
- (3) 0.001M NaNO₂ +0.6M NaCl
- (4) 0.1M Na₂SO₄ +0.6M NaCl
- (5) 0.02M Na₂SO₄ +0.6M NaCl
- (6) 2M NaCl

The fatigue lifetimes in various electrolyte composition solutions and under different applied stress levels are discussed in Chapter 4.

2.12.4 The cathodic polarisation effect

A special corrosion cell was designed for cathodic polarisation of the surface of a corrosion fatigue specimen. The test cell was modified to include a platinum counter electrode which lined the inner wall of the cell, and a gasket-sealed glass capillary made contact with a saturated calomel reference electrode. A flexible tygon-tube filled with electrolyte served as a salt bridge. The glass capillary within the cell was adjusted to a uniform distance of 2mm from the minimum radius of the specimen surface. Potentials were reported on the standard Saturated Calomel Electrode (SCE). All tests were carried out at room temperature, and at a frequency of 5Hz, see Table 2.8.

The central section of the hour glass specimen, with a length of 10mm, was exposed to the 0.6M NaCl solution and was charged by cathodic polarisation. The remaining part of the specimen was wrapped in PTEF tape in order to prevent cracks initiating from outside the central section.

Under a stress range of 750 MPa, two specimens, C1 and C2, were subjected to torsional corrosion-fatigue tests in 0.6M NaCl solution, at pH=6, a frequency of 5Hz, and room temperature. A cathodic potential of -1280 mv (SCE) was applied onto the surface of the specimen throughout the whole process of the corrosion fatigue test. Specimen C1 was tested without replication, and specimen C2 was tested with replication. Results of fatigue life and crack growth rate are discussed in Chapter 4.

In order to understand the difference in the cathodic potential effects on stage-I and stage-II crack growth behaviour, a third test was carried out using specimen C3. Initially the test was conducted in the bulk solution, 0.6M NaCl solution, at pH=6, frequency 5Hz, room temperature, and under free corrosion potential of approximately -650 mv (SCE). The stress range was 750 MPa . The replication technique was applied to detect crack initiation and the transition from stage-I crack to stage-II crack growth. After 45000 cycles, several cracks were found in the transition from stage-I to stage-II. In other words, cracks changed their original path direction, from along the shear stress plane to that perpendicular to the maximum tensile stress. And then a cathodic potential of -1280 mv (SCE) was applied onto the central section surface of the specimen which was exposed to the bulk solution while the remaining area was prevented from cathodic polarisation by the PTEF tape. The test was carried out continuously under the same stress level and replication was undertaken at pre-set cycle intervals. This test thus provided experimental data to study crack growth behaviour for stage-II growth under cathodic polarisation.

Obviously, it was necessary to do an extra corrosion fatigue test using specimen C4, under free corrosion potential, in 0.6M NaCl solution, at approximately the same stress level with replication, in order to provide a reference base to study the effect of cathodic polarisation on corrosion fatigue crack growth behaviour.

During tests, the corrosion current and corrosion potential between the specimen and the saturated calomel reference electrode via the logging probe-salt bridge, was measured by a voltmeter, for specimens C1, C2, C3, TC7 and TC10.

All test specimens were cleaned and dried and examined by SEM after failure.

References

- [1] BS18 (1990) British Standard, Tensile Testing of Metallic Materials, Part 1. Method of test at ambient temperature, BSEN 10002-1.
- [2] G5-82 (1982) Standard practice for standard reference method for making potentiostatic and potentiodynamic anodic polarisation measurements, *Annual Book of ASTM Standards*, Vol. 03.02.
- [3] G59-78 (reproved 1984) Standard practice for conducting potentiodynamic polarisation resistance measurements, *Annual Book of ASTM Standards* Vol. 03.02.
- [4] Ghulam Murtaza (1992) Corrosion fatigue short crack growth behaviour in a high strength steel. *Ph.D thesis*, University of Sheffield.
- [5] Hafeez Ur Rehman (1991) The influence of microstructural variables on the growth of short fatigue cracks in a high strength steel. *Ph.D thesis*, University of Sheffield.
- [6] N. D. Greene (1965) Experimental electrode kinetics, Rensselaer Polytechnic Institute, Troy, N. Y.
- [7] D. W. France, Jr. (1969) Controlled potential corrosion tests, their applications and limitations, *Materials Research and standards*, Vol 9, No. 8, P21.

Table 2.1 Calibration of torque

Applied torque N.m	Load arm (left) Volts	Load arm (right) Volts
63.54	6.37	-6.37
52.96	5.31	-5.32
42.37	4.25	-4.25
31.77	3.18	-3.18
21.18	2.11	-2.12
10.59	1.05	-1.06

Table 2.2 Calibration of twist angle

Degree	Transducer A Volts	Transducer B Volts
2.4	1.795	1.726
1.2	0.881	0.873
0.0	-0.003	0.002
-1.2	-0.822	-0.909
-2.4	-1.812	-1.856
0.0	-0.085	-0.091
2.4	1.77	1.71

Table 2.3 Polarisation tests at various scan sweep rates in different solutions

Sample	Solution composition	Scan sweep rate mv/min	Potential range mv
A1	0.6M NaCl	60	-2000~+100
B1	2M NaCl	60	-1500~+1000
C1	0.1M Na ₂ SO ₄ + 0.6M NaCl	60	-1500~+1000
A2	0.6M NaCl	1200	-2000~+1000
B2	2M NaCl	1200	-1500~+1000
C2	0.1MNa ₂ SO ₄ + 0.6M NaCl	1200	-1500~+1000
D	0.02M Na ₂ SO ₄ + 0.6M NaCl	1200	-1500~+1000
E	0.5M NaNO ₂ +0.6M NaCl	2000	-2000~+1000
F	0.2M NaNO ₂ +0.6M NaCl	20	-2000~+1000

Table 2.4 Fatigue tests in air

Specimen	$\Delta\tau$ MPa	Frequency Hz
A4	1285	5
A6	1176	5
A1	1020	5
A2	1020	5
B5	1012	5
B16	1006	5
B14	980	5

Table 2.5 Corrosion fatigue tests in a 0.6 M NaCl solution, at pH=6

Specimen	$\Delta\tau$ MPa	Environment	Frequency Hz
TC6	926	0.6M NaCl solution	5
TC5	728	ditto	5
TC10	613	ditto	5
TC18	612	ditto	5
TC2	609	ditto	5
TC3	547	ditto	5
TC7	504	ditto	5
TC11	433	ditto	5
TC13	415	ditto	5
B10	224	ditto	5

Table 2.6 Corrosion fatigue tests in a 0.6 M NaCl solution,
at various frequencies

Specimen	$\Delta\tau$ MPa	Environment	Frequency Hz
FC1	613	0.6M NaCl solution	2
FC2	616	ditto	2
TC18	613	ditto	5
FC3	621	ditto	12.5
FC4	400	ditto	12.5
TC13	415	ditto	5
FC5	399	ditto	2

Table 2.7 Corrosion fatigue tests in different electrolyte solutions

Specimen	$\Delta\tau$ MPa	Environment	Frequency Hz
CN1	912	0.6M NaCl + 0.01M NaNO ₂	5
CN2	637	0.6M NaCl + 0.1M NaNO ₂	5
CN3	613	0.6M NaCl + 0.001M NaNO ₂	5
S1	630	0.6M NaCl + 0.02M Na ₂ SO ₄	5
S2	649	0.6M NaCl + 0.1M Na ₂ SO ₄	5
S3	626	2M NaCl	5

Table 2.8 Cathodic polarisation details in corrosion fatigue tests in a 0.6 M NaCl solution and at a frequency of 5Hz

Specimen	$\Delta\tau$ MPa	Cathodic polarisation
C1	750	E=-1280 mv
C2	750	E=-1280 mv
C3	750	initially at free corrosion potential, followed by cathodic polarisation E=-1280 mv after 45000 cycles
C4	742	free corrosion potential

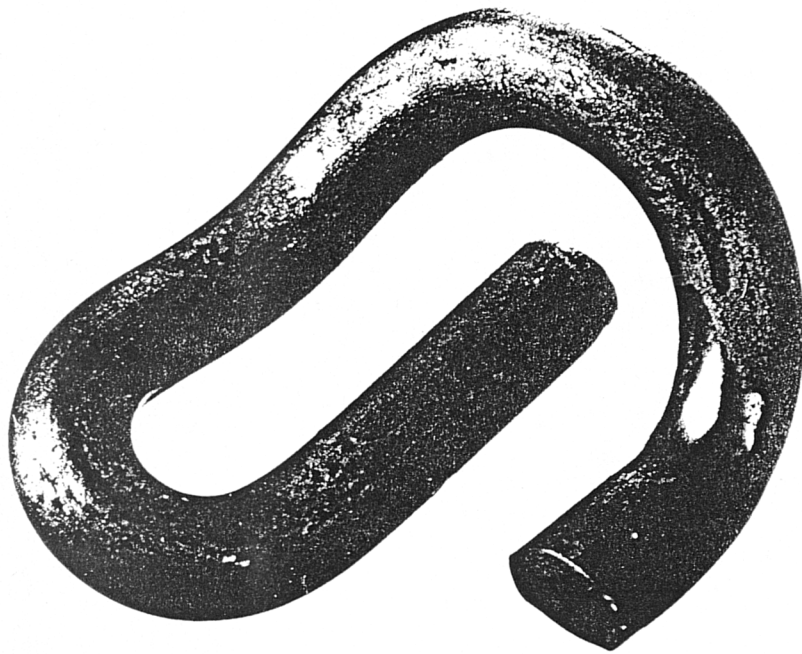


Figure 2.1 A typical rail clip

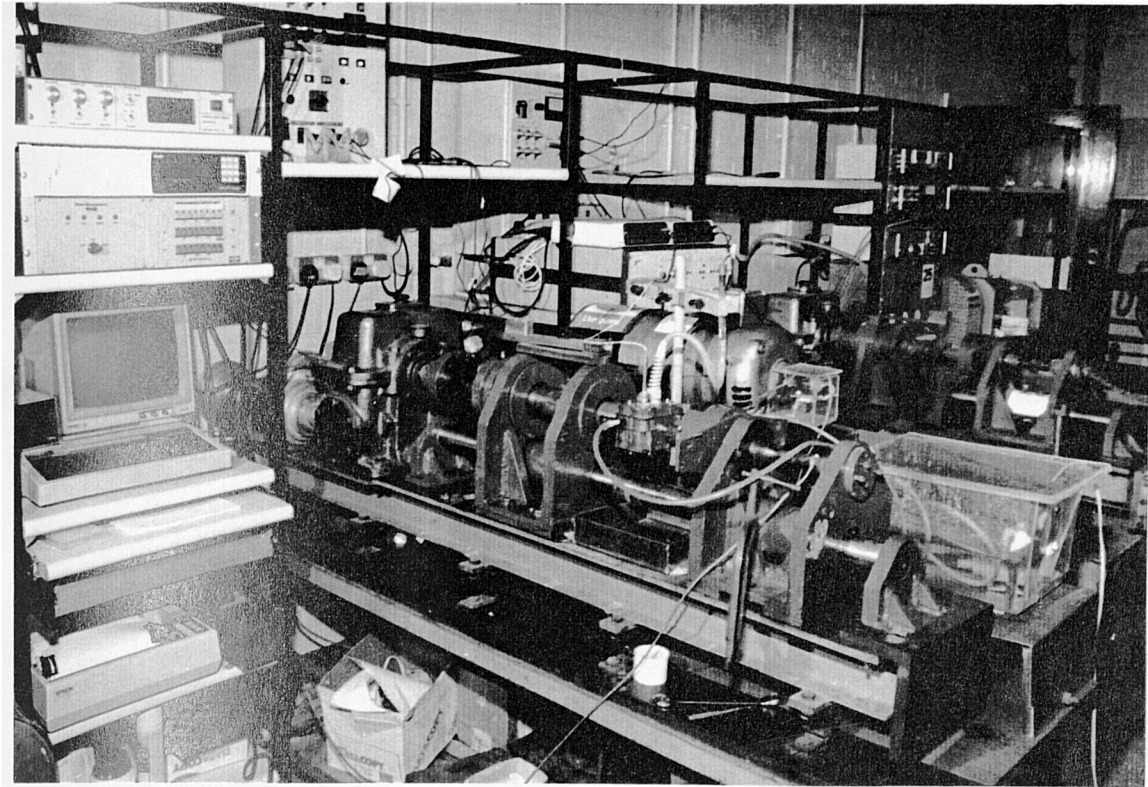


Figure 2.2 (a) Torsion machine and computer-control system

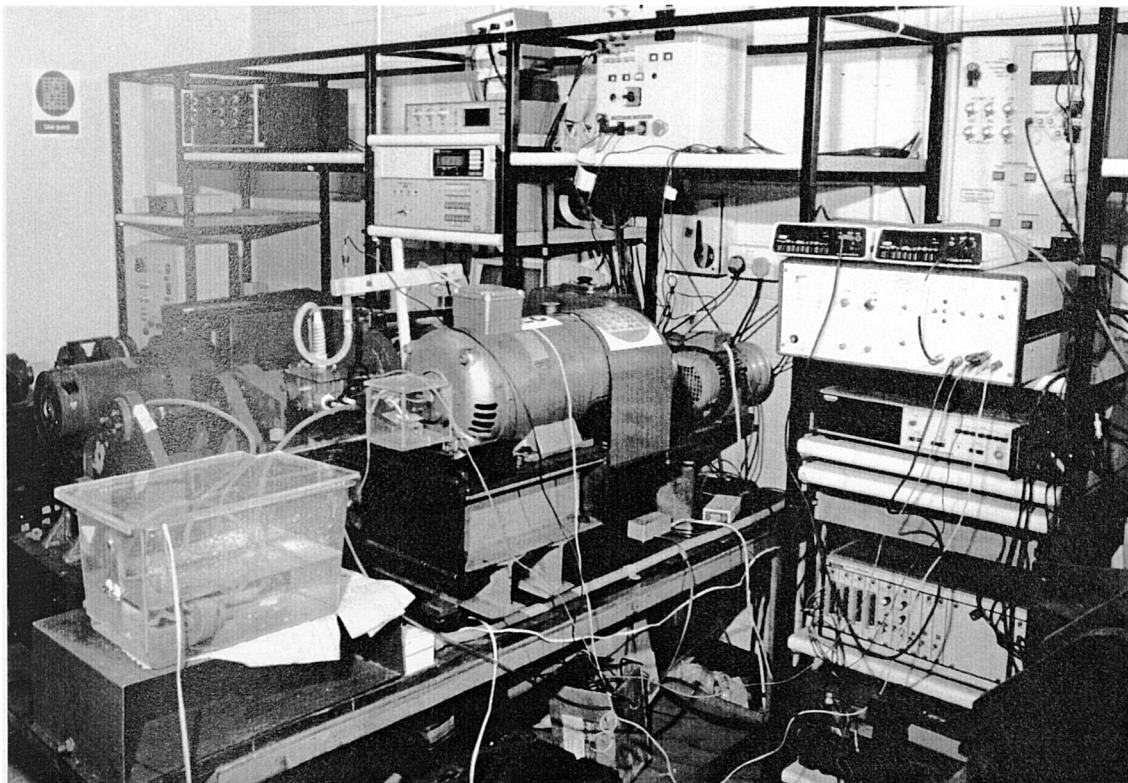


Figure 2.2 (b) Environment circulation system and polarisation facility

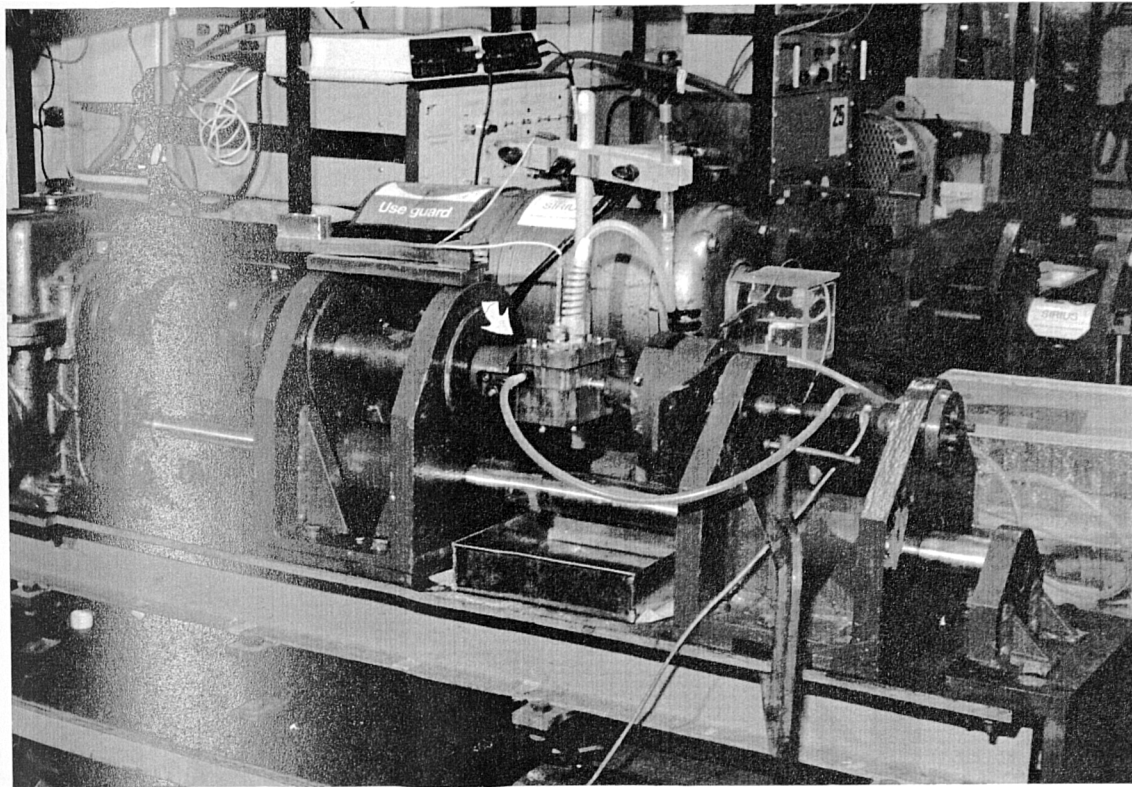


Figure 2.2 (c) Corrosion cell

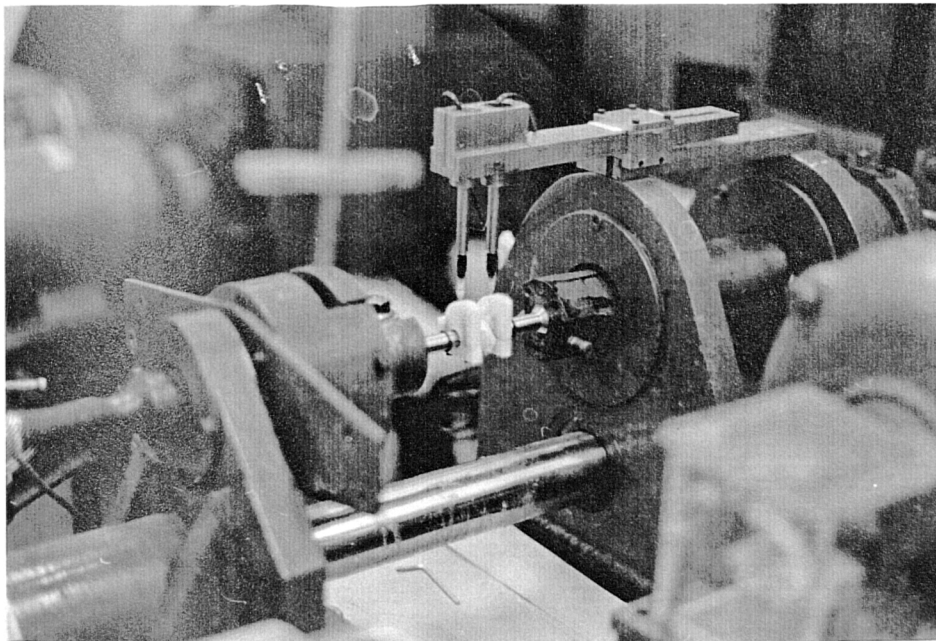


Figure 2.2 (d) Twist angle measurement device

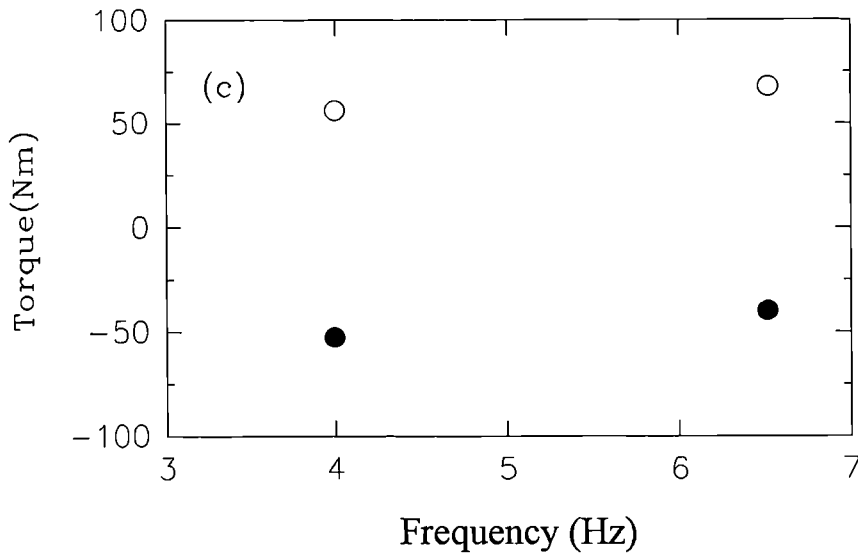
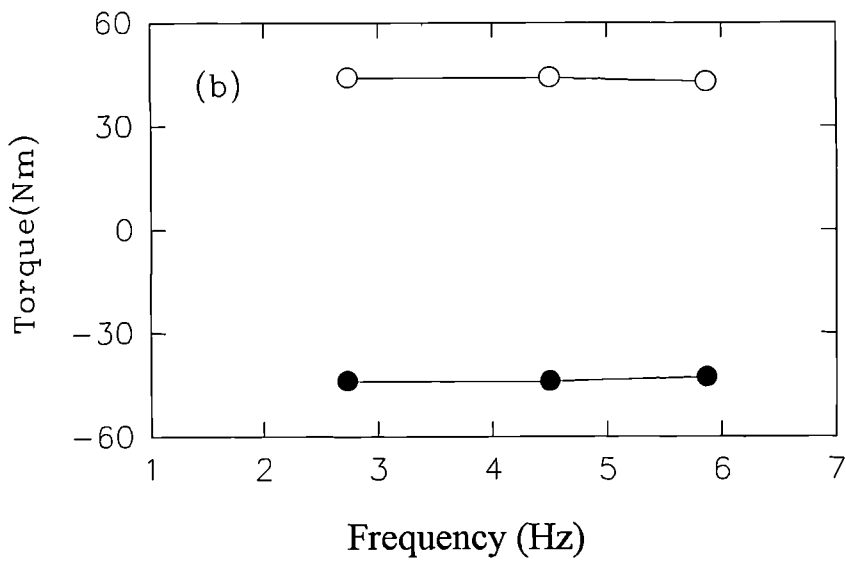
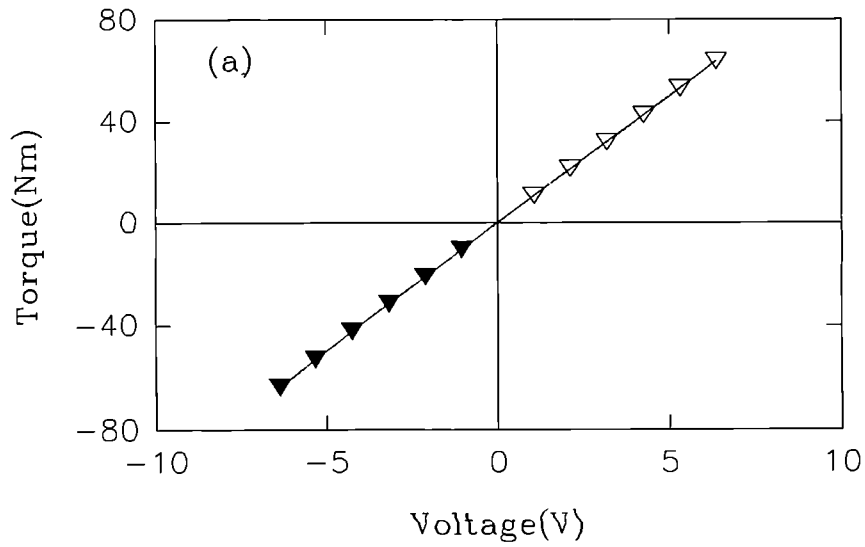


Figure 2.3 (a) Torque calibration (b) Torque at frequencies in the range 2.5 to 6 Hz (c) Torque when frequency exceeds 6 Hz

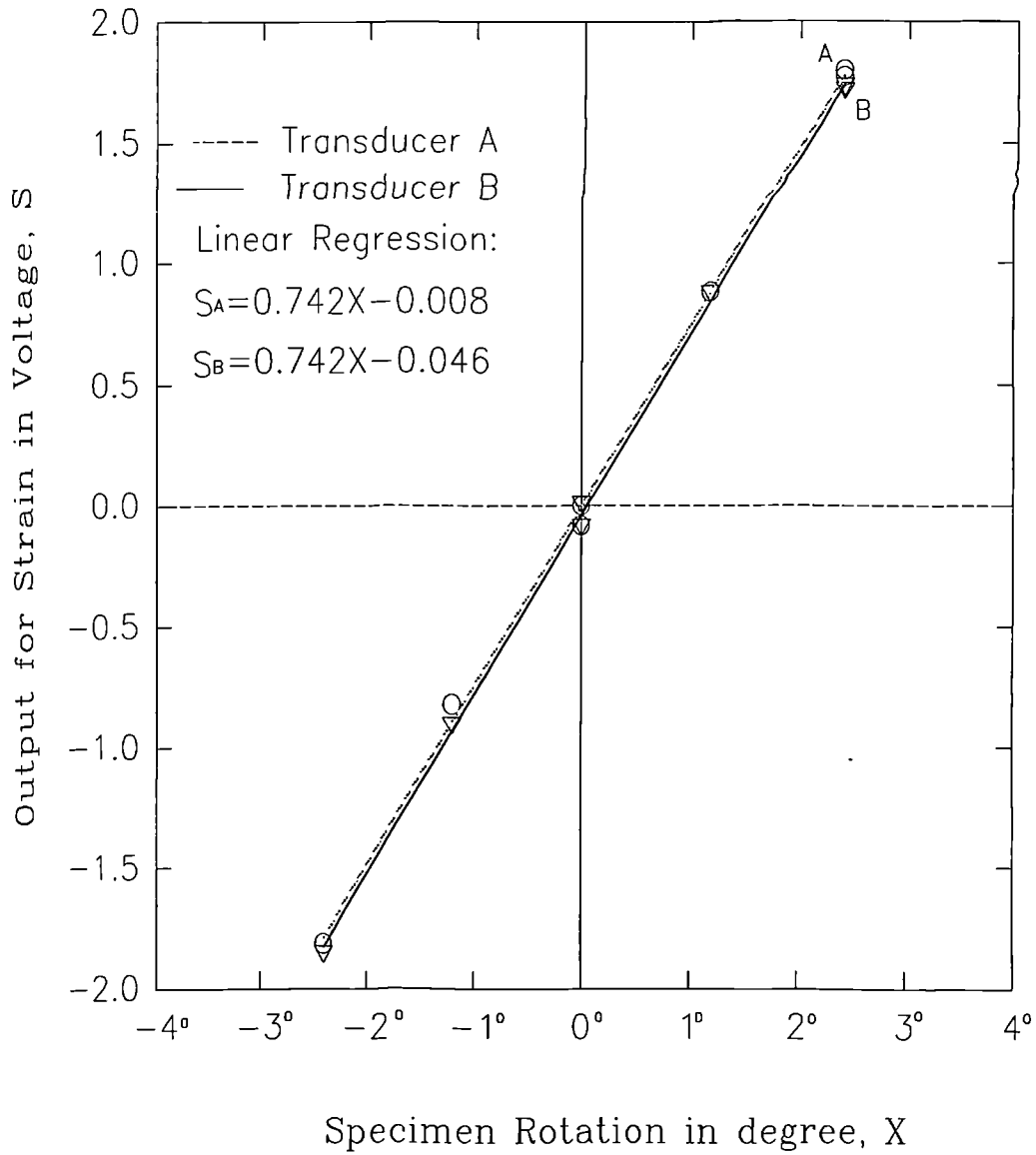
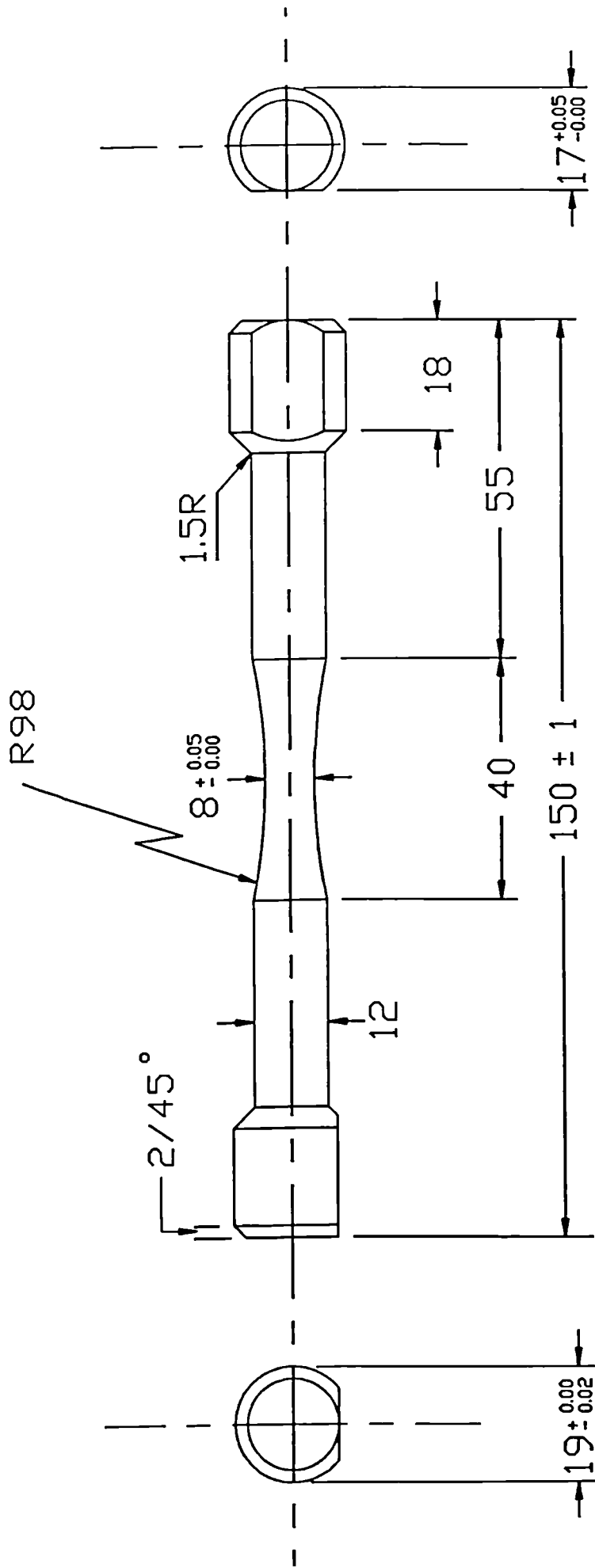


Figure 2.4 Calibration of twist angle



All dimensions in millimeters
 Tolerances ± 0.2 unless stated

Figure 2.5 Configuration of the hour-glass specimen

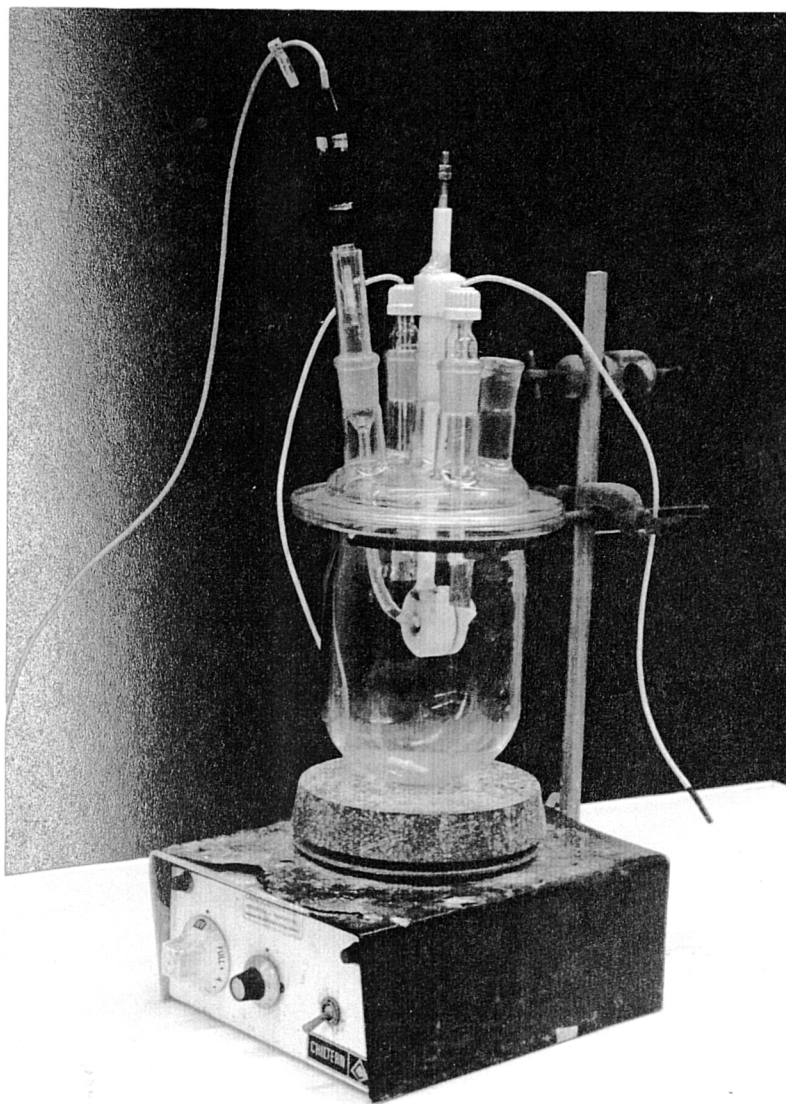


Figure 2.7 (a) Apparatus for the electrochemical studies

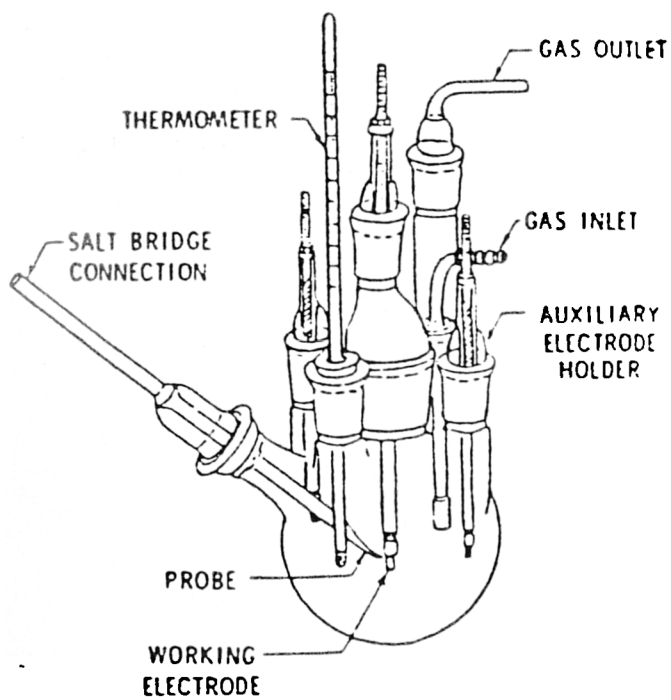
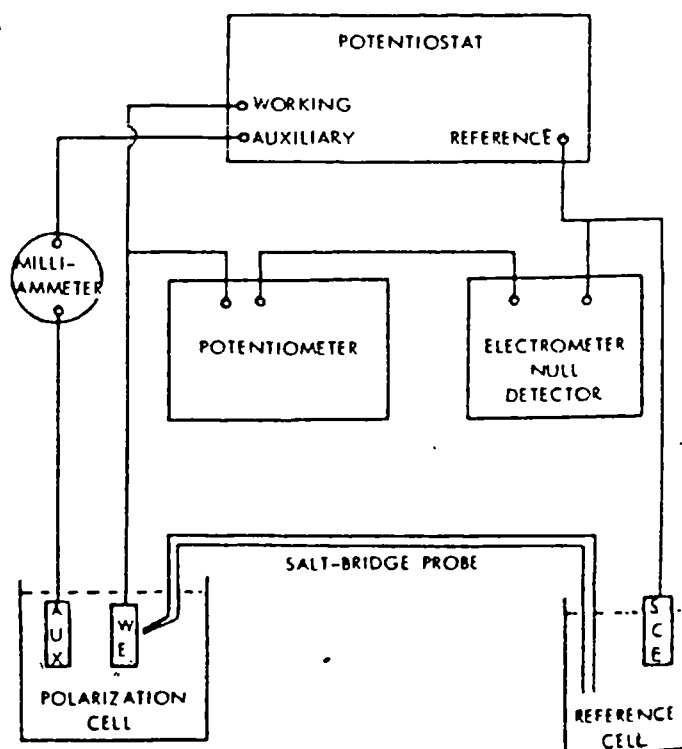


Figure 2.7 (b) Schematic diagram of the polarisation cell [6]



WE: Working Electrode
 AUE: Auxiliary Electrode
 SCE: Saturated Calomel reference Electrode

Figure 2.8 Schematic potentiostatic anodic polarisation wiring diagram [7].

Chapter 3 Initial experimental results

In this chapter, results of initial tests studying the electro-chemical and general mechanical properties prior to the fatigue tests are reported. These properties are important in the sense that they provide the basic material parameters to describe the corrosion fatigue process, and to help in the understanding the general processes that occur during corrosion fatigue.

3.1 Metallographic studies

3.1.1 Microstructures

Metallographic studies revealed that the microstructure of BS251A58 steel without a heat treatment consists of a fine pearlite together with some ferrite (see Figure 3.1), and the microstructure following a heat treatment of austenitising at 920° C for 15 min followed by an oil quench and finally tempering at 475° C for 30 minutes followed by an oil quench to provide a tempered martensite structure, see Figure 3.2

From Figure 3.3 (a) and (b), Scanning Electron Microscopy reveals that the microstructure of this material after heat-treatment is indeed tempered martensite. The average size of the prior austenite is about 30 μm .

The principal form of martensite is lath martensite (regions marked L in Figure 3.4). The laths are grouped into large packets and there are 3 or 5 such packets in a prior austenite grain; the average size of the packets is about 10 μm . Some individual, lenticular, plate

shape martensite units, sometimes referred to as plate martensite (regions marked P in Figure 3.4), are witnessed along the prior austenite grain boundaries.

The lath martensite possesses of a high density of dislocations, some of which form cells. The martensite laths may be separated by small-angle boundaries in an individual packet, or by large angle boundaries between the packets or prior austenite grains. The plate martensite consists of fine, internal twins. The crystal structure of the lath martensite is usually BCC in low-carbon steels and iron-based alloys.

3.1.2 Inclusions

Inclusions are also identified from the metallographic study. Figure 3.5 (a) shows the duplex type non-metallic inclusions where the dark region is iron oxide; and the grey region surrounding the dark region is manganese sulphide of irregular-shape.

SEM pictures clearly reveal the presence of a number of non-metallic inclusions, see regions marked in the square of Figure 3.5 (b), these inclusions lying in a matrix of tempered martensite and along prior austenite grain boundaries. The size of non-metallic inclusions is about 10 μm in length, and 3 μm in width.

Further investigations identified the non-metallic inclusions to be MnS using X-ray spectra analysis. The results of the chemical element analysis both in the matrix and in the marked regions are shown in Figure 3.6 (a) and (b) respectively. The X-ray spectra analysis of inclusions marked in the white square (in Figure 3.5(b)) indicates the presence of sulphur, manganese, iron and chromium, compared with the area in matrix where the absence of sulphur and low energy level of manganese are noted.

The distribution of non-metallic inclusions in three dimension has been investigated under optical microscope, see Figure 3.7. The inclusion has an elongated shape in the rolling direction on the surface of the specimen, and has a circular shape in the transverse section.

3.1.3 Discussion

The sulphide inclusion has a high index of deformability at elevated temperature and is always deformed to ellipsoids and becomes elongated along the hot rolling direction. It has an irregular-shape, like a tail, with a length of about 10 μm , and width and depth of 3 to 8 μm . Along the hot rolling direction on the surface of the specimen there apparently exist several parallel sulphide inclusions aligned on the same plane, see Figure 3.7, which are the typical band structures of sulphide inclusions due to the manufacturing process.

Conversely, the oxide inclusion has a low index of deformability and has the tendency to maintain an undeformed geometry. It is found that some oxide inclusions are surrounded by sulphide inclusions in the present material, i.e. a duplex inclusion structure.

It is well known that slip band cracking is promoted by high applied stresses and higher alloy purity. Inclusions have different elastic/plastic properties from the surrounding matrix, giving rise to cracking under fatigue loading. Commercial materials generally contain many inclusions and these can provide the sites for crack initiation in both conventional fatigue and corrosion fatigue. The period of stage-I crack growth is often reduced or eliminated when microcracks are initiated at inclusions.

Melander and Larsson [1] investigated the effect of stress amplitude on the cause of fatigue crack initiation in air of a spring steel with hardness 50 HRc. The fatigue tests were conducted under fully reversed load control at five different stress amplitudes between 800 and 1200 MPa, and the failure causes were established by fractographic studies. It was found at high stress amplitude the specimen failure was caused by inclusions situated at the

specimen surface. However, at the lower stress amplitude of 800 MPa, it was found that near-surface inclusions caused the failure for the low-life part of the Weibull diagram while inclusions situated well inside the specimen caused the failure for the long-life part of the Weibull diagram. The inclusions causing failure were of the duplex type and calcium-aluminide oxide.

Miller [2] has indicated that inclusions which are smaller than the grain size are not too harmful, whilst inclusions that are large in comparison to grain size can dramatically reduce fatigue resistance by two mechanisms: (a) by permitting an easy bridge between the stage I to stage II crack growth phase and (b) by themselves cracking in a manner that permits the immediate growth of a stage II crack in the bulk material.

The role of non-metallic inclusions is very important in corrosion fatigue even though the size of the inclusions is less than the grain size. This is especially true at low stress levels and long-life fatigue.

Because inclusions are also electro-chemically different from the matrix they suffer chemical attack in the presence of an aggressive environment. Corrosion attack at inclusions can promote pitting. Figure 3.8 [3] shows the profound effect of such pits on fatigue strength. Corrosion pits 1/4 mm deep in the rotor steel, reduced the fatigue strength to about one-third of that for smooth specimens.

For short cracks under certain low applied stress levels, no crack growth will occur in air, as the stress amplitude is insufficient to drive any cracks (which may have nucleated in slip bands) across the appropriate microstructural barrier. In an aggressive environment, however, defects may still grow by means of a pitting corrosion process. The role of the sulphide inclusion as a favourable site for intensive corrosion attack in a carbon steel, and a stainless steel, was recognised long ago. It has also been established that if a metal contains sulphide inclusions in addition to other inhomogeneities, the inclusions will

primarily act as pit nucleation sites. In the present study an examination of fatigued specimens confirmed the important role of pitting and its association with the sulphide inclusions which are more chemically active in a corrosion environment.

Although the interpretations proposed in literature of the role of a sulphide in pit nucleation are different, each interpretation leads to the conclusion that pitting is a special form of crevice corrosion which initiates and develops a micro cavity at the sulphide/metal boundary or is formed by sulphide dissolution. The most significant findings are summarised from a review [4], as follows:

1. The highest susceptibility to corrosion is exhibited by certain complex sulphide-oxide inclusions.
2. The presence of inclusions may produce stress fields and generate dislocations in the surrounding metal.
3. Microvoids may develop with cooling at sulphide/steel interfaces.
4. During the initial stage of corrosion, the metal surrounding an inclusion can be attacked locally, and crevices can form.
5. The presence of H_2S in an acid solution will accelerate the corrosive attack on iron and steel, thus hampering passivation.
6. Surface films on non-metallic inclusions are often thicker but less protective than those on the rest of the metal surface.
7. Crevices often form at Mn-rich sulphide inclusions, and both the inclusion and matrix are attacked, while in the case of Fe-rich sulphides, the adjacent metal is attacked. It can be concluded that pits form predominantly at Mn-rich sulphide inclusions. Pits do not necessarily nucleate at all sulphide inclusions emerging on the steel surface. Depending on their geometry and chemical composition, certain inclusions are more efficient in nucleating pits than others.
8. Spheroidized particles are less susceptible to corrosion than elongated, particulate deformed ones.

9. The pitting potential has been found to depend on the grinding direction. Transverse grinding, which cuts through inclusions, increases the effective interfacial area and creates a more negative pitting potential compared with longitudinal grinding.

The results from present tests indicated that pitting developed quickly at Mn-rich sulphide inclusions in 0.6M NaCl solution. The interface between the matrix and non-metallic inclusion (where differences in coefficients of thermal expansion (e.g. MnS in a martensitic matrix) and differences in chemical composition exist), is thought to induce the formation of a pit in a corrosion environment. The microcrack can initiate from the root of such pits at a very early stage. As a result the transition from stage-I to stage-II crack growth will occur earlier, and the fatigue life is shortened.

The density and distribution of non-metallic inclusions affect not only crack initiation, but also crack propagation, because, if the inclusion lies on the path of crack advance, the specimen will quickly cleave when the crack approaches the inclusion. This unstable fracture event could occur even in the stable crack growth regime of some ductile materials (e.g. A508 III steel) [5].

3.1.4 Grain boundaries

Quite often the grain boundaries are considered responsible for pitting. Different impurities may segregate to the grain boundaries in metals, and this is thought to be the main reason for the higher reactivity of grain boundaries relative to grain interiors. Not all grain boundaries are susceptible to localised attack, which suggests that 'pure' grain boundaries are in fact immune and that susceptibility of real grain boundaries to pitting is due to the presence of segregated impurities and/or precipitated particles.

It was observed [4] that pits which formed between differently oriented grains developed at different rates. A more prolonged corrosion environment or the application of a higher anodic potential also led to pitting on grain boundaries.

3.2 General mechanical tests

3.2.1 Monotonic stress-strain relationship

The mechanical properties of the material used were obtained and were as follows: 0.2% proof stress = 1380 MPa, tensile strength = 1588 MPa, elongation = 10.6%, reduction in area = 30.6%, and Young's Modulus = 206 GPa; see also Table 3.1.

From the monotonic tensile tests, the following equations are obtained:

True stress-strain

$$\sigma^T = 1543(\varepsilon_p^T)^{0.0568} \quad (\varepsilon_p > 0.2\%) \quad (3.1)$$

Engineering stress-strain

$$\sigma^E = 1508(\varepsilon_p^E)^{0.0424} \quad (\varepsilon_p > 0.2\%) \quad (3.2)$$

The engineering stress-strain curve and true stress-strain curve are illustrated in Figure 3.9.

3.2.2 Hardness

Results of hardness tests are shown in Table 3.2 for Batch A specimens. There is slight difference of Vicker's micro hardness between the longitudinal direction and the transverse direction of the specimen. The micro hardness in the longitudinal direction is higher than in the transverse direction. The average value of hardness for Batch A specimens is about 480Hv, i.e. approximately 47HRc, see conversion table, Table 3.4.

The Vicker's micro hardnesses measured from Batch B specimens (subjected to a slightly different heat treatment), are higher than those measured from Brach A specimens, see Table 3.3. The range of Vicker's micro hardness is from 480Hv to 510 Hv, i.e. approximately 47HRc to 49HRc.

3.3 The calibration of the torsion test machine and specimen

3.3.1 Torque-stress relation

The applied torque and the twist angle are related by an exponential law:

$$\Delta T = A(\Delta\theta)^n \quad (3.3)$$

where $\Delta\theta$ is the twist angle between the two cams, each located at one end of the gauge length of 25mm, A is a constant, and n is the exponent and can be derived from the slop of the Torque-twist angle curve in double log co-ordinates, see Figure 3.10.

For a cylindrical solid specimen, Brown [6] has proposed a simplified expression using Nadai's theory,

$$\Delta\tau = \frac{3+n}{2\pi r_0^3} \Delta T \quad (3.4)$$

where ΔT is the range of applied torque, r_0 is the radius of the cylindrical specimen.

In the elastic stress region $n \approx 1$, while in the elastic-plastic region n is obtained by a best-fit line passing through the transition point of the torque-twist angle curve i.e. between the linear relation and the power law relation.

In the present study, for the hour-glass shaped specimen with its minimum diameter of 8mm in the central section, the relationship between torque and twist angle was found to be:

$$\Delta T = 26.2(\Delta\theta)^{0.99} \quad (3.5)$$

For the hour-glass shaped specimens used in the present fatigue tests, Carbonell and Brown [7] analysed the accuracy in the calculation of the shear stress range on the surface of the minimum section of the specimen. Using the equation (3.4), the error is found to be within 0.3-0.4%.

3.3.2 Twist angle-strain relation

In addition, Carbonell and Brown [7] also proposed an expression to describe the relationship between surface shear strain and twist angle under fully-reversed cyclic loading for the hour-glass shaped fatigue specimen:

$$\Delta\theta = A \frac{\Delta\gamma_{oe}}{r_o} + B \frac{\Delta\gamma_{op}}{r_o} \quad (3.6)$$

with

$$A = \int_{-L}^L \frac{dL}{[1 + R/r_o - \sqrt{(R/r_o)^2 - (L/r_o)^2}]^4}$$

$$B = \int_{-L}^L \frac{dL}{[1 + R/r_o - \sqrt{(R/r_o)^2 - (L/r_o)^2}]^{(3+p)/p}} \quad (3.7)$$

$$\Delta\gamma_{oe} = \frac{\Delta\tau}{G} \quad (3.8)$$

$$\Delta\tau = \frac{3+n}{2\pi r_o^3} \Delta T$$

where $2L$ is the gauge length of 25 mm between the two cams, r_o is the radius in the minimum section of the hour-glass shaped specimen, R is the radius of the cambered surface of the hour-glass shaped specimen (98mm), $\Delta\theta$ is the twist angle in radians between the two adjacent transverse planes of the two cams, $\Delta\gamma_{oe}$ is the range of surface elastic shear strain, $\Delta\gamma_{op}$ is the range of surface plastic shear strain, and G is the shear modulus. The values of A and B are determined numerically by integrating over the gauge length $2L = 25$ mm, according to equation (3.7), while n is the exponent and can be

derived from the slope of the Torque-twist curve in double log co-ordinates. Assuming that, in the plastic region, the shear stress and strain relation has a power law form, then

$$\Delta\tau = H(\Delta\gamma_{op})^{\rho} \quad (3.9)$$

where ρ is the work hardening exponent from the cyclic shear stress-shear plastic strain curve.

From Figure 3.13 the following equation is derived:

$$\Delta\tau = 643(\Delta\gamma_{op})^{0.0252} \quad (3.10)$$

Substituting the two integrals, values of A and B, and $\Delta\gamma_{oe}$ into Equation (3.6), the plastic shear strain range, $\Delta\gamma_{op}$ can be obtained as:

$$\Delta\gamma_{op} = \frac{\Delta\theta r_o - A\Delta\gamma_{oe}}{B} \quad (3.11)$$

3.3.3 Strain calibration

Two cylindrical specimens with a radius of 4mm were used in a shear test within the elastic region, using both the strain gauge calibration and LVDTs (cam-Linear Variable Displacement Transducers).

Tables 3.5 (a) and (b) show the calibration results for strain of specimens A and B respectively. In the elastic region, the tensile strain on the outer surface of the specimen was directly obtained from the strain gauge indicator via a strain gauge stuck on the surface of the central section of the specimen at 45 degrees to the specimen axis. The shear strains, marked as γ and γ' in Table 3.5 (a) and (b) respectively, can be determined by the LVDTs and also calculated from the tensile strain of the strain gauge for the purpose of comparison.

For pure torsion in the elastic region, the stress system is illustrated in Figure 3.11 for the cylindrical specimen. Here

$$\begin{aligned}
\sigma_1 &= -\sigma_2, \sigma_3 = 0, \tau_1 = \tau_2 \\
\varepsilon_1 &= \frac{1}{E} \{ \sigma_1 - \nu(\sigma_2 + \sigma_3) \} = \frac{1}{E} (1 + \nu) \sigma_1 \\
\sigma_1 &= -\tau_1 = -G\gamma_1 \\
\varepsilon_1 &= \frac{1}{E} (1 + \nu) (-G\gamma_1) = -\frac{(1 + \nu)G}{E} \gamma \\
\gamma_1 &= -\frac{\varepsilon_1 E}{(1 + \nu)G}
\end{aligned} \tag{3.12}$$

The value, γ' , in Table 3.5 (a) represents the shear strain derived from Equation (3.12), with $\nu=0.3$, $G=81.5$ GPa, and $E=206$ GPa. The tensile strain, ε_1 , is obtained by the strain gauge indicator during the test. The shear strain γ is determined by means of LVDT signals in mv through the strain-twist angle calibration which is described below.

For cylindrical specimens, the shear strain on the specimen surface is proportional to the twist angle of the two cams over the distance of the gauge length, i.e.

$$\begin{aligned}
r \cdot \Delta\theta &= 2L \cdot \gamma \\
\gamma &= \Delta\theta \cdot \frac{r}{2L}
\end{aligned} \tag{3.13}$$

where r is the radius of the specimen section (4.0mm for specimen A and 4.01mm for specimen B), $2L$ is the gauge length (25 mm), $\Delta\theta$ is the relative twist angle of two cams which is calculated from Equation (2.2) in Chapter 2.

In comparison, the following equations can be obtained from Table 3.5 (a) and (b), and Figure 3.12 (a) and (b).

For specimen A

$$\gamma = 1.025\gamma' - 0.00408 \tag{3.14}$$

For specimen B

$$\gamma = 1.011\gamma' - 0.00448 \tag{3.15}$$

For the whole range of γ and γ' , the discrepancy between them, $\gamma - \gamma'$, is less than 0.031% for specimen A and 0.017% for specimen B respectively. The result verifies that the use of the strain-twist angle relation Equation (2.2) provides sufficient accuracy to calculate the shear strain range on the surface of a fatigue specimen.

3.4 Cyclic torsional test

Two hour-glass shaped specimens (C and D), having a diameter of 7.3mm and 8 mm in the minimum section respectively, were subjected to fully-reversed torsional test by means of multiple step load from a low stress level to a high stress level. The cyclic shear stress-strain data were obtained for both specimens by the application of Brown's Equation, shown in Table 3.6 (a) and (b). Cyclic stress-strain curves are plotted in Figure 3.14. A monotonic shear stress-strain curve and another cyclic shear stress-strain curve plotted by other research workers [8, 9] are shown together in Figure 3.14.

Combining the data for cyclic shear stress-strain on the present material, a Ramberg-Osgood relation is obtained for the cyclic shear stress-strain behaviour of the present material:

$$\gamma(\%) = \left(\frac{\tau}{815} \right) + \left(\frac{\tau}{643} \right)^{1/0.04} \quad (3.16)$$

The cyclic 0.2% proof yield shear stress is 625 MPa, whereas the monotonic 0.2% proof yield shear stress is 757 MPa for this material.

It is expected that the BS251A58 high strength spring steel undergoes cyclic softening within the shear strain of 4%, see Figure 3.14. For specimen C having the diameter of 7.3mm at its minimum section, the cyclic shear stress-strain curve is below that for specimen D (having the diameter of 8 mm at its minimum section). This phenomenon indicates that, under the same shear stress level, the smaller the diameter of the specimen, more cyclic softening would occur in the deformed material.

To summarise all the results of microstructure examinations, mechanical properties and cyclic shear stress-strain tests, the present material has a microstructure of a tempered martensite with an average prior austenite grain size of 30 μ m, non-metallic inclusions with

mixed Mn-Fe rich sulphide in the matrix along the prior austenite grain boundaries and of size about $10\mu\text{m}$ in the longitudinal direction and 3 or $5\mu\text{m}$ in the transverse direction.

This material, under the given heat-treatment, has a high monotonic 0.2% proof tensile stress around 1400 MPa, a high ratio of yield stress to fracture stress of 0.88 together with a high hardness around 47-49 HRc. The monotonic 0.2% proof shear stress is 757MPa, and the cyclic 0.2% proof shear stress is 625 MPa. Under a cyclic shear stress, work softening behaviour was observed.

A clarification is noted here between the softening due to stress cycling and the hardening due to increasing straining. When the monotonic stress-strain curve and the stabilised cyclic stress-strain curve are plotted together on the same scale, the cyclic softening at a given strain refers to the reduction in the stress level from the monotonic curve to the cyclic one; after stabilisation, the cyclic softened material undergoes *strain hardening* with increasing straining, as long as the material instability point, i.e. the maximum in the cyclic stress-strain curve, is not reached.

3.5 Electro-chemical tests

3.5.1 Polarisation Parameters

Table 3.7 shows the polarisation parameters R_p , b_a , b_c , B and i_{corr} for the BS251A58 steel in different solutions such as 0.6M NaCl, 2M NaCl, and 0.6M NaCl + 0.02M Na_2SO_4 , where R_p is the polarisation resistance, b_a is the anodic Tafel Slope, b_c is the cathodic Tafel Slope, B is a combination of the anodic and cathodic Tafel Slope, and i_{corr} is the corrosion current density. It can be found that the corrosion current density i_{corr} is $2.75\ \mu\text{A}/\text{cm}^2$ in 0.6M NaCl solution for BS251A58 steel, $3.06\ \mu\text{A}/\text{cm}^2$ in 2M NaCl solution, and $2.68\ \mu\text{A}/\text{cm}^2$ in 0.6M NaCl + 0.02M Na_2SO_4 solution. For the three different solutions the corrosion current densities are approximately the same.

Lee and Uhlig [10] reported that the average critical corrosion density for 4140 steel of Rc 20 to 44 was $2.3 \pm 0.5 \mu\text{A} / \text{cm}^2$, which was very close to the value obtained in the present tests.

Measured current densities were then translated into corrosion rates employing Faraday's law such that $0.40 \mu\text{A} / \text{cm}^2 = 1 \text{mg} / \text{dm}^2 / \text{day}$ (mdd) corresponding to $\text{Fe} \rightarrow \text{Fe}^{++} + 2\text{e}^-$. For the present material in 0.6M NaCl solution, the corrosion rate is 6.9 mdd.

In comparison, for stainless steel type AISI306 in 1N H_2SO_4 solution at room temperature, Table 3.8 shows the polarisation parameters R_p , b_a , b_c , B and i_{corr} . The corrosion current density is $2.82 \text{mA} / \text{cm}^2$. The Tafel plot and polarisation resistance R_p measurement are illustrated in Figure 3.15 (a) and (b) respectively, and the potentiodynamic polarisation curves at two scan sweep rates are shown in Figure 3.16.

For BS251A58 steel tested in 0.6M NaCl solution, the Tafel plot and polarisation resistance R_p are shown in Figure 3.17 and Figure 3.18 respectively; In 2M NaCl solution, the Tafel plot and polarisation resistance R_p are shown in Figure 3.19 and Figure 3.20 respectively; In 0.6M NaCl + 0.02M Na_2SO_4 solution, the Tafel plot and polarisation resistance R_p are shown in Figure 3.21 and Figure 3.22 respectively. The potentiodynamic polarisation curves in different solutions and at various scan sweep rates are plotted in Figure 3.23 (a) and (b).

3.5.2 'Rest potential', E_{rest} , and 'true corrosion potential', E_{corr}

The rest potential, E_{rest}

The rest potential, E_{rest} , represents the natural free corrosion potential which was observed to gradually decrease as the immersion time increases for the sample and to

eventually arrive at a relatively stable value after approximately half hour for the present study, see Figure 3.24.

The rest potential values E_{rest} in mv (SCE), for BS251A58 steel in different solutions, which decreases with increasing time, are given in Table 3.9 and Figure 3.24 .

From the test results, i.e. potentiodynamic curves at different solutions, it was observed that the rest potential E_{rest} was approximately the same (after 25 min immersion), see Table 3.10, ranging from -680 mv (SCE) to -633 mv (SCE), for the aggressive ion solutions, such as 0.6M NaCl, 2M NaCl, 0.1M Na₂SO₄ + 0.6M NaCl, and 0.02M Na₂SO₄ + 0.6M NaCl solutions. However, E_{rest} increased to a value of -390 mv (SCE) in the presence of an inhibitor, such as 0.2M NaNO₂ or 0.5M NaNO₂ in 0.6M NaCl solution.

It could be suggested that the aggressive ions, Cl⁻, SO₄²⁻, were responsible for attacking the surface film and thus reducing the rest potential, E_{rest} . Conversely, the inhibitor, NO₂⁻, present in a chloride-containing solution, was adsorbed onto the metal surface and/or formed a protective 3-dimensional surface film. When a passive film forms on the metal surface it will improve the protective properties and the pitting potential is thereby usually shifted to more positive values [4].

True corrosion potential: E_{corr} , the potential at zero current density on the polarisation curve

The true corrosion potential at minimum current density, which is approximately zero on the polarisation curve, is called *true corrosion potential*, in order to distinguish it from the rest potential.

The true corrosion potential at zero current density, E_{corr} , which was obtained from the potentiodynamic polarisation curves (Figure 3.23), is demonstrated in Figure 3.25. Also illustrated in Figure 3.23 is the rest potential, E_{rest} , for BS251A58 steel in various solutions.

For the material used in different solutions, i.e. 0.6M NaCl, 2M NaCl, 0.1M Na₂SO₄ + 0.6M NaCl, 0.02M Na₂SO₄ + 0.6M NaCl, the true corrosion potentials were observed to be -1052 mv, -1082 mv, -1046 mv and -1020 mv respectively at a fast scan rate (1200 mv/min) from the anodic polarisation curves, see Figure 3.25. At a slow scan rate (60 mv/min) the true corrosion potentials were -902 mv, -1015 mv and -1037 mv respectively in the corresponding solutions. For all tests, the initial applied potential in the different solutions mentioned above were approximately the same, being -1500 mv to the rest potential. The test results showed that, the true corrosion potential depends on the aggressive properties of various electrolyte compositions, the applied potential scanning sweep rate, the initially applied potential to its rest potential, and the surface film on the metal. In an aerated solution, this value could be further affected by the oxide ion.

3.5.3 Discussion

Rest potential and true corrosion potential

The question may arise as why the 'rest potential' E_{rest} is different from the 'true corrosion potential' E_{corr} for the present test material in the same solution. As we know, the surface of the metal is covered by a thin oxidation film whenever it is exposed in air or in solution. The rest potential is the potential of a corroding surface in an electrolyte, relative to a reference electrode.

For a given alloy in a chloride environment, the rest corrosion potential is affected by the surface condition of the specimen including the scan rate, the initially applied potential and

the composition of the electrolyte. The surface oxidation film of the test sample could be attacked by the chloride solution after the sample is immersed in an electrolyte, and consequently, the rest potential will decrease until it reaches a relatively stable value, i.e. the rest corrosion potential. This indicates that the surface of the specimen covered by the oxidation film at this stage is under less attack by the chloride solution due to the formation of the re-passivated film, and so represents a dynamic balance stage.

From Table 3.9 the rest potentials for the same metal tested in various electrolytes show different values at the initial stage and display a decreasing trend with different rates until they arrive at the stabilised value.

In 0.6M NaCl solution, the rest potential was -501 mv soon after the sample was immersed in the solution, decreased towards -675 mv after 30 min, and continuously decreased very slowly afterwards. The value of -675 mv was recorded as the rest potential. In the presence of 0.5M NaNO₂ in the 0.6M NaCl solution, the rest potential was -315 mv initially, and decreased towards the value of -390 mv after 20 minutes.

Inhibitors

The potential decrease means that the surface film on the metal is attacked by the corroding electrolyte. The faster the rest potential is decreasing, the more severely the surface film on the metal is attacked. If some compounds, acting as inhibitors, are present in a chloride-containing solution (such as nitrites) the inhibitor could be adsorbed on the surface film and/or produce a further oxidation film on the surface of the metal, resulting in the inhibition of further corrosion of the metal. As a result there will be a smaller and more gradual drop in the rest potential which eventually arrives at a more positive value compared to that in a 0.6M NaCl solution.

Thermo-dynamic process

The corrosion process is a thermo-dynamic process, which depends on the difference of energy between the metal surface and the solution. The difference of energy is proportional to the difference of the potential between the surface of the metal and the solution relative to an electrode. If the difference of energy equals zero, there is no further reaction between the metal and the solution. If the applied potential could fill the energy valley between the metal and the solution, there is no driving force for the chemical reaction between the metal and the solution. Consequently there is no further corrosion.

The potential at the minimum current density during the potentiodynamic test, which starts from the cathodic potential regime, represents an electrochemical dynamic balance state for the particular metal/solution system. As the corrosion current is nearly zero, there will be no further attack on the surface of the metal at this potential. This value of potential should be the true corrosion potential for the particular metal/solution system, at which there exists a thermo-dynamic balance state between the solution and the metal without an oxidation film covering the surface of the metal, and there is no further chemical reaction occurring at this particular potential.

Potentials higher, or lower than the true corrosion potential will induce anodic polarisation, or cathodic polarisation respectively. At a higher potential, the metal could be attacked by the corroding electrolyte and the oxidation reaction could occur. At a lower potential, where the metal would experience cathodic polarisation, the reduction reaction would occur. In other words, the metal is free from corroding only at this particular potential.

The difference of the 'rest potential' and the 'true corrosion potential' is due to the different surface conditions of the metal. For the rest potential, the surface of the metal is covered by an oxidation film. However, for the true corrosion potential, the surface of the metal is

initially undergoing cathodic polarisation, and there is no further oxidation film covering the surface at this potential i.e. the surface of the metal is directly exposed in the solution. Perhaps it is possible that the thermal equilibrium for iron in the electrolyte could occur at the 'true corrosion potential' without a further oxidation film.

Suppose the fatigue specimen of BS251A58 steel is experiencing cathodic polarisation at the 'true corrosion potential' throughout the corrosion fatigue process, the fatigue limit could be retrieved when the applied stress is below the fatigue limit in air.

Cathodic potential effect

A complete set of data of cathodic potential effects on corrosion fatigue for 4140 steel was obtained by Lee and Uhlig [10]. The corrosion fatigue life was continuously improved with cathodic protection to -1.0 V (SCE), but then underwent a reversal at -1.1V (SCE), see Figure 3.26.

The steel may be subjected to hydrogen damage in the endurance limit range if a cathodic overpotential occurs.

The corrosion rate has a minimum value for iron in 3% NaCl solution with a cathodic potential of -850 mv to -1000 mv (SCE), see Figure 3.26 [10]. This is consistent with the present test results, where the 'true corrosion potential' was found to be around -1000 mv for both the fast and slow scan rates for the BS251A58 steel in a 0.6M NaCl solution.

Change of the corrosion potential due to the inhibitor

It was observed that the 'true corrosion potential' for 0.6M NaCl, 2M NaCl, 0.1M Na₂SO₄ + 0.6M NaCl and 0.02M Na₂SO₄ + 0.6M NaCl solutions at a slow scan rate and a fast scan rate, is around -1000 mv (SCE). However, for 0.2M NaNO₂ + 0.6M NaCl and

0.5 M NaNO₂ + 0.6M NaCl solutions, the true corrosion potential attains higher values of -740 mv (SCE) and 28.6 mv (SCE) respectively, because of the presence of passive ion in 0.6M NaCl solution. So the value of the true corrosion potential can depend upon the inhibitor concentration in the chloride solution; the higher the concentration of the inhibitor, the more positive is the value of the true corrosion potential.

It was noted that the 'true corrosion potential' was negative to the rest potential for most solutions in the present study. However, for the 0.5M NaNO₂ + 0.6M NaCl solution, the 'true corrosion potential' was positive to the rest potential. This illustrates that the test material in 0.5M NaNO₂ + 0.6M NaCl solution might be free from corroding due to the fact that the 'true corrosion potential' is always higher than the rest potential, indicating the material undergoes cathodic protection and the anodic reaction is stopped and there is no further dissolution of the metal.

From the potentiodynamic polarisation curves, the test material can be assessed as a weakly passivating metal in 0.6M NaCl, 2M NaCl, 0.1M Na₂SO₄ + 0.6M NaCl, 0.02M Na₂SO₄ + 0.6M NaCl solutions, whereas it could be free from corrosion in 0.5M NaNO₂ + 0.6M NaCl solution and partly attacked in 0.2M NaNO₂ + 0.6M NaCl solution.

3.6 Corrosion tests

Samples were cut from the ends of failed fatigue specimens, along the specimen axis parallel to the rolling direction, and polished to the same finish as the fatigue test specimens and then exposed to the corrosion solution in the absence of stress. The development of pits was studied as a function of time, and the sites of pitting noted.

The corrosion tests were carried out for three series for the BS251A58 steel:

- (1) Corrosion tests in a 0.6M NaCl solution, and a pitting solution of different concentrations of nitrite in 0.6M NaCl solution, 0.2M NaNO₂ + 0.6M NaCl solution and 0.5M NaNO₂ + 0.6M NaCl solution.
- (2) Corrosion tests in different concentrations of chloride solutions, 2M NaCl, 1M NaCl, and 0.6M NaCl solutions, and these compared with the results from the other two solutions, i.e. 0.1M NaHCO₃ + 0.6M NaCl and 0.1M Na₂CO₃ + 0.6M NaCl solutions.
- (3) The effect of sulphate anions present in 0.6M NaCl solution on pitting density of BS251A58 steel, compared with the results in 0.6M NaCl solution and 2M NaCl solution.

The test results are shown in Tables 3.11(a), (b) and (c).

In the series 1 corrosion tests, after having been immersed in different solutions for 66 hours, samples PA1, PA2, PA3 and PA4 were examined. Sample PA1 was still bright without any sign of corrosion in 0.5M NaNO₂ + 0.6M NaCl solution while sample PA2, in a low concentrations of NaNO₂ solution (0.2M NaNO₂ + 0.6M NaCl solution), displayed a partly rusted surface with laths along the rolling direction. However, Sample PA3 and PA4 in the 0.6 M NaCl solution were completely corroded, exhibiting a dark colour and covered with corrosion products.

The results illustrated that BS251A58 steel was attacked in 0.6M NaCl solution, but that the presence of NaNO₂ in 0.6M NaCl solution can prevent the surface of BS251A58 steel from corroding. The inhibiting effect of NaNO₂ depended on its concentration in the particular 0.6M NaCl solution. The higher the concentration of the inhibitor NaNO₂, the more the protection from the corroding of the surface of the metal. This result provides evidence for the analysis from the polarisation curves obtained from the used material

immersed in 0.5M NaNO₂ + 0.6M NaCl solution and 0.2M NaNO₂ + 0.6M NaCl solution.

In test series 2 and series 3, the development of pits was studied as a function of time in different solutions.

Samples PB1 and PC3 were exposed in 2M NaCl solution, sample PB2 exposed in 1M NaCl solution, sample PB3 and PC2 exposed in 0.6M NaCl solution, sample PC1 exposed in 0.1M Na₂SO₄ + 0.6M NaCl solution, sample PB4 exposed in 0.1M NaHCO₃ + 0.6M NaCl solution, and sample PB5 exposed in 0.1M Na₂CO₃ + 0.6M NaCl solution.

For BS251A58 high strength steel, pitting occurred in 0.6M NaCl solution, 1M NaCl solution, and 2M NaCl solution, and the number of pits increased with increasing chloride ion concentration in the solution after the same duration, see Tables 3.11(b) and (c) and Figure 3.27.

It was also found that the number of pits on the surface of sample PC1 in 0.1M Na₂SO₄ + 0.6M NaCl solution was almost the same as those on the surface of sample PC3 in 2M NaCl solution, and was much more than those on the surface of sample PC2 in 0.6M NaCl solution.

Conversely, pit density decreased on sample PB4 in 0.1M NaHCO₃ + 0.6M NaCl solution. Furthermore, there were no pits on the surface of sample PB5 in 0.1M Na₂CO₃ + 0.6M NaCl solution and its surface was still bright after having been exposed for more than two days, which illustrated that the test material was not corroded in the solution.

From the corrosion tests, pitting was observed shortly after 5 minute's immersion in the different aggressive solutions of 0.6M NaCl, 1M NaCl, 2M NaCl and 0.1M Na₂SO₄ + 0.6M NaCl. Both processes, i.e. the nucleation of new pits and the development of existing

pits on the sample surface occurred at the same time, and the number of pits increased with time. After a few hours, the nucleation of pits stopped, because pits that had already formed prevented further pitting in the surrounding area. The formed pits enlarged themselves either by propagating on the surrounding surface or by growing in the depth of the metal; some of them joined together. Eventually, general corrosion took the place of local damage (pitting) and the metal surface was rusted completely exhibiting a black colour. There were no pits left on the sample surface at the final stage.

3.7 Discussion

Pitting corrosion can be caused by different anions, and the type of anion responsible for pitting depends on the type of metal involved. The most aggressive ion is chloride, which produces pits in iron, nickel, aluminium, titanium and in their alloys with other metals. Other anions may act similarly under special experimental conditions and for certain metals. For example, sulphate anions have been found to cause pitting of iron and low carbon steel [11].

For iron, a minimum concentration of Cl^- exists, which is 0.0003M, below which pitting does not occur [12-14].

From the study of the dependence of characteristic pitting potentials of Ni on Cl^- concentration in 1M K_2SO_4 solution [14], it was found that pit nucleation potential (E_{np}) was a logarithmic function of Cl^- concentration, and that the protection potential (E_{pp}) was independent of Cl^- concentration, see Figure 3.28.

This observation indicates that the higher the Cl^- concentration in the solution, the easier the metal is attacked by pitting, and the more the pits nucleate on the surface of the metal. From the present study, the number of pits increased with increasing Cl^- concentration in

the solution. However, it has also been observed that the severity of pitting depends not only on the concentration of aggressive ions in the solution, but also on the concentration of non-aggressive species. Many compounds in a chloride-containing solution, for example, sodium carbonate, sodium nitrite, sodium hydrogen carbonate, and sulphate, have been reported to act as inhibitors.

Usually the same compound that inhibits general corrosion of a metal or alloy also restrains pitting corrosion. The inhibitive efficiency of an inhibitor was evaluated by determining the minimum concentration ratio of the compounds to that of chloride [15].

The influence of different concentrations of NaNO_2 with NaCl solution was investigated on iron by Matsuda and Uhlig [16]. The results are shown in Figure 3.29.

In the present tests, it was observed that there were no pits on the surface of sample PA1 exposed in $0.5\text{M NaNO}_2 + 0.6\text{M NaCl}$ solution for 66 hours while there were some pits on the surface of sample PA2 exposed in $0.2\text{M NaNO}_2 + 0.6\text{M NaCl}$ solution. However, extensive pitting was found on the surface of samples PA3 and PA4 which were exposed in the 0.6M NaCl solution in the absence of NaNO_2 .

Similarly no pits were observed for sample PB5 exposed in $0.1\text{M Na}_2\text{CO}_3 + 0.6\text{M NaCl}$ solution after 10 days. However two pits were found on the surface of sample PB4 exposed in $0.1\text{M NaHCO}_3 + 0.6\text{M NaCl}$ solution after 170 minutes, 5 pits on the surface of sample PB3 exposed in 0.6M NaCl solution after 170 minutes, 10 pits on the surface of sample PB2 exposed in 1M NaCl solution and 13 pits on the surface of sample PB1 exposed in 2M NaCl solution after 170 minutes.

In contrast, in $0.1\text{M Na}_2\text{SO}_4 + 0.6\text{M NaCl}$ solution, extensive pitting occurred on the surface of sample PC1 after 20 minutes, as compared with the result of sample PC2 exposed in 0.6M NaCl solution after 20 minutes where there were a few pits. This is to be

expected since there was not a sufficient concentration of inhibitors present in the aggressive medium, and the SO_4^{2-} ion belongs to the group of the so-called dangerous inhibitors which, when present in an insufficient concentration in an aggressive medium, surprisingly increases the intensity of localised attack on a metal.

The mechanism of passivating inhibitors when present in the Cl^- solution, such as SO_4^{2-} , was studied by Maitra [17]. The amount of Cl^- comes into play in the outer layer of the oxide film with increasing concentration of SO_4^{2-} in the solution, and the passivating inhibitors form a three-dimensional protective surface film, preventing pit nucleation.

Another group of inhibitors, called non-aggressive inhibitors, such as NaHPO_4 , NaOH , NaNO_3 , NaNO_2 etc., form insoluble salts with metal cations on the metal surface.

The pitting inhibition mechanism might be different for different inhibitors and metals. But in general two mechanisms can be distinguished [4]:

- (1) competitive adsorption
- (2) repairing of a protection film on the metal surface

Non-passivating and passivating inhibitors are thought to act in one of the aforementioned manners, or both. Non-passivating inhibitors can not only inhibit pitting nucleation but also inhibit pitting propagation. However, passivating inhibitors just inhibit pitting nucleation.

Meanwhile, from the corrosion series test 1, the phenomenon of no pitting on the surface of sample PA1 exposed in 0.5M NaNO_2 + 0.6M NaCl solution, provides evidence for the hypothesis of potentiodynamic polarisation in the same solution where the 'true corrosion potential' was shifted to a more positive value to the rest potential for the BS251A58 steel in the same solution, eliminating the possibility of pitting, and therefore inhibiting further general corrosion.

All these corrosion tests provided a clear picture of the nature of localised corrosion and general corrosion behaviour of BS251A58 steel in different electrolytes, which proved to be useful in further studies on corrosion fatigue behaviour of BS251A58 steel in various solutions, i.e. pitting solutions or much more aggressive mediums.

References

- [1] A. Melander and M. Larsson (1993) Study the effect of stress amplitude on the cause of fatigue crack initiation in a spring steel, *Int. J. Fatigue*, March.
- [2] K. J. Miller (1993) The two thresholds of fatigue behaviour, *Fatigue Fract. Engng Mater. Struct.* **16**, pp.931-939.
- [3] Effect of environment on fatigue crack initiation, Short Course on Corrosion, held in the Dept. of Mech. Process Eng., Univ. of Sheffield, Sept. 1992.
- [4] Z Szklarska-Simalowska (1986), *Pitting corrosion of metals*, pp.70-76.
- [5] X. D. Wu, Y. P. Wang and X. H. Zhang (1990), An investigation on fracture toughness and fatigue crack growth behaviour for nuclear vessel steel A508-III, *Pressure Vessel Technology* (in Chinese), **6**, No.5, pp.10-16.
- [6] M. W. Brown (1978) Torsional stresses in tubular specimens, *J. Strain Analysis*, **13**, pp.23-28.
- [7] E. P. Carbonell and M. W. Brown (1986) A study of short crack growth in torsional low cycle fatigue for a medium carbon steel, *Fatigue. Fract. Engng. Mater. Struct.* **9**, pp.15-33.
- [8] R. Akid (1988) 250A53: the influence of physical and electrochemical variables on fatigue, Corrosion Fatigue and Stress Corrosion Crack growth. First Report.
- [9] Hafeez Ur Rehman (1991) The influence of microstructural variables on the growth of short fatigue cracks in a high strength steel. *Ph.D thesis*, September 1991.

[10] H. H. Lee and H. H. Uhlig (1972) Corrosion fatigue of Type 4140 High Strength steel, *Met. Trans.*, **3**, pp.2949-2959.

[11] Z. Szklarska-Smialowska (1978) *Corrosion Sci.* **18**, p.97.

[12] N. D. Stolica (1969), Pitting corrosion on Fe-Cr and Fe-Cr-Ni alloys, *Corrosion Sci.* **9**, pp.455-470.

[13] K. E. Heusler, L. Fischer (1976), *Werkst. Korros.*, Vol.27, p. 551.

[14] G. Sussek and M. Kesten (1975), Characterization of pitting corrosion in Nickel - 1. Determination of pitting potentials in neutral and alkaline solutions, *Corrosion. Sci.*, **15**, p.225-238.

[15] K. Schwabe, Le Dang Ank (1973), *Zashchita Metallov*, Vol.9, p.541.

[16] S. Matsuda and H. H. Uhlig (1964) *J. Electrochem. Soc.*, Vol. 111, p.156.

[17] S. Maitra (1974) *Ph.D thesis*, University of Florida.

Table 3.1 General mechanical properties of BS251A58 steel

$\sigma_{0.2}$ MPa	σ_u MPa	δ_5 %	ψ %	E GPa	$\sigma_{0.2} / \sigma_u$
1380	1588	10.6	30.6	206	0.88

Table 3.2 Vickers Hardness of BS251A58 steel in the longitudinal and transverse direction, Hv, for the specimens of Batch A

Specimen	direction	1 Hv	2 Hv	3 Hv	4 Hv	5 Hv	average Hv
TC2	Transverse	466	480	470	466	473	471
	Longitudinal	468	468	468	470	466	468
TC3	Transverse	483	480	494	476	494	485.4
	Longitudinal	476	487	487	473	480	480.6

Table 3.3 Vickers Hardness of BS 251A58 steel , Hv, for the specimens of Batch B, all in the longitudinal direction

Specimen	1 Hv	2 Hv	3 Hv	average Hv
B2	490	490	487	489
B3	481	481	480	480.7
B4	490	490	460	480
B5	470	467	464	467
B14	502	468	502	490.7
C1	442	460	467	456.3
C3	516	479	468	487.6
C4	509	539	483	510.3

Table 3.4 Conversion Table for Hardness Values

Hv	HB	HRc
460	430	45
470	438	46
480	445	47
490	453	47.5
500	460	48
510	468	48.5
520	475	49
530	483	49.5
540	490	50

Table 3.5(a) Calibration of strain gauges for the torsion machine, specimen A,
 $r=4.0$ mm, $E=206$ GPa, $G=81.5$ GPa, monotonic torsion test *

T N.m	τ MPa	$\Delta\theta$ mv	$\Delta\theta$ degree	γ %	ϵ $\mu\epsilon$	γ' %	$\gamma - \gamma'$ %
13.5	134	448.5	0.656	0.183	-894	0.174	0.00923
25.0	248	827	1.166	0.325	-1610	0.313	0.01227
33.2	329	1082	1.509	0.422	-2122	0.413	0.00922
37.5	372	1194.4	1.661	0.463	-2400	0.467	-0.00304
45.0	446.5	1438	1.989	0.555	-2862	0.556	-0.00134
51.7	513	1659	2.287	0.638	-3280	0.638	0.00951
59.8	593	1947	2.675	0.747	-3788	0.738	0.010617
59.6	591	1938	2.663	0.744	-3799	0.737	0.005494
60.3	598.3	1963	2.696	0.752	-3841	0.747	0.00529
65.7	651.9	2181	2.991	0.835	-4178	0.812	0.022335
69.5	689.6	2295	3.144	0.878	-4418	0.859	0.019444
75.5	749	2531	3.462	0.967	-4871	0.947	0.019907
77.5	769	2644	3.615	1.010	-5054	0.983	0.027104
78.8	781.8	2712	3.706	1.035	-5180	1.007	0.027477
80.8	801.7	2827	3.861	1.078	-5389	1.0478	0.030614

Table 3.5(b) Calibration of strain gauges for the torsion machine, specimen B,
 $r=4.01$ mm, $E=206$ GPa, $G=81.5$ GPa, monotonic torsion test *

T N.m	τ MPa	$\Delta\theta$ mv	γ %	$4 \cdot \epsilon$ %	ϵ %	γ' %	$\gamma - \gamma'$ %
11.06	109.7	332.5	0.1395	0.2778	0.06945	0.1350	0.00442
17.69	175.5	522.5	0.2110	0.4424	0.1106	0.2150	-0.00406
27.28	270.7	840	0.3305	0.679	0.1698	0.3301	0.00043
37.4	371.1	1125	0.4378	0.9291	0.2323	0.4516	-0.01385
47.14	467.7	1445	0.5591	1.174	0.2935	0.5706	-0.01151
58.69	582.3	1867.5	0.7152	1.457	0.3642	0.7081	0.00722
66.97	664.4	2125	0.8236	1.6578	0.4144	0.8057	0.01784

* r is the radius of the specimen, $\Delta\theta$ is the relative twist angle of two cams, γ is the shear strain determined from $\Delta\theta$, ϵ is the tensile strain calculated from the strain gauge, γ' is the shear strain derived from ϵ , $\gamma - \gamma'$ is the discrepancy between γ and γ' , G is the shear Modulus, and E is the Young's Modulus.

Table 3.6 (a) Cyclic stress-strain data for specimen C,
 $d=7.28$ mm, $2L=25$ mm, $A=19.512$, $B=8.5991$, $G=81.5$ GPa *

ΔT N.m	$\Delta \theta$ mv	n	$\Delta \tau$ MPa	$\Delta \gamma_{ot}$ %	$\Delta \gamma_{oe}$ %	$\Delta \gamma_{op}$ %
32.4	1230	1.000	440.5	0.548	0.548	0
47.3	1820	1.000	643.1	0.807	0.807	0
63.6	2450	1.000	864.7	1.074	1.074	0
71.4	2760	1.000	970.8	1.211	1.211	0
79.1	3090	0.898	1047.9	1.419	1.339	0.079
80.9	3160	0.876	1065.7	1.460	1.362	0.098
83.5	3290	0.836	1088.7	1.555	1.391	0.164
88.5	3540	0.764	1132.3	1.738	1.447	0.291
92.5	3680	0.726	1171.5	1.815	1.497	0.318
96.3	3960	0.654	1196.0	2.063	1.528	0.535
106.0	4680	0.490	1257.3	2.702	1.607	1.096
109.8	5200	0.386	1263.8	3.23	1.615	1.615
116	5900	0.262	1286.2	3.917	1.643	2.273

Table 3.6 (b) Cyclic stress-strain data for specimen D
 $d=7.92$ m, $2L=25$ mm, $A=19.851$, $B=8.9658$, $G=81.5$ GPa *

ΔT N.m	$\Delta \theta$ mv	n	$\Delta \tau$ MPa	$\Delta \gamma_{ot}$ %	$\Delta \gamma_{oe}$ %	$\Delta \gamma_{op}$ %
14.1	360	0.960	147.4	0.185	0.185	0
19.9	550	0.960	207.9	0.289	0.289	0
33.5	930	0.960	350.2	0.463	0.463	0
41.2	1150	0.960	430.7	0.566	0.566	0
51.6	1430	0.960	539.4	0.688	0.688	0
65.0	1820	0.960	679.5	0.877	0.864	0.0083
73.6	2060	0.960	769.4	0.986	0.983	0.0031
84.6	2390	0.960	884.4	1.152	1.130	0.0214
91.8	2600	0.960	959.7	1.253	1.226	0.0269
98.8	2780	0.960	1032.8	1.326	1.281	0.0350
103.6	2900	0.920	1072.1	1.390	1.355	0.0450
112.7	3170	0.896	1159.1	1.537	1.481	0.0561
118.8	3370	0.831	1201.4	1.683	1.535	0.1479

* d is the diameter in the minimum section of the hour-glass shaped specimen, $\Delta \theta$ is the relative twist angle of two cams, $2L$ is the gauge length, A and B are constants determined by Equation (3.7), G is the shear modulus, $\Delta \gamma_{oe}$ is the range of surface elastic shear strain, $\Delta \gamma_{op}$ is the range of surface plastic shear strain, $\Delta \gamma_{ot}$ is the total range of surface shear strain, and n is the exponent determined from cyclic shear stress-shear strain curve.

Table 3.7 Polarisation parameters, BS251A58 steel, 25° C
 B is a combination of the anodic and cathodic Tafel slope (see Equation (2.6))

Solution	polarisation resistance R_p ohm·cm ²	anodic Tafel slope b_a mv	cathodic Tafel slope b_c mv	B mv	corrosion current density i_{corr} μA / cm ²
0.6M NaCl	5440	54	96	15.0	2.75
2M NaCl	3889	58	52	11.9	3.06
0.6M NaCl+ 0.02M Na ₂ SO ₄	6974	65	128	18.7	2.68

Table 3.8 Polarisation parameters, stainless steel type AISI316, 25° C
 B is a combination of the anodic and cathodic Tafel slope (see Equation (2.6))

Solution	polarisation resistance R_p ohm·cm ²	anodic Tafel slope b_a mv	cathodic Tafel slope b_c mv	B mv	corrosion current density i_{corr} mA / cm ²
1N H ₂ SO ₄	8.0	95	115	22.6	2.82

Table 3.9 Rest potential, E_{rest} , as a function of time
 in different solutions for BS251A58 steel

Solution	E_{rest} in mv (SCE)				
	0 min	10 min	15 min	20 min	30 min
0.6M NaCl	-501	-620			-675
0.6M NaCl + 0.5M NaNO ₂	-315		-388	-390	
0.6M NaCl + 0.2M NaNO ₂	-386				-407

Table 3.10 Rest potential, E_{rest} , and the true corrosion potential E_{corr} of BS251A58 steel in different solutions and at different scan sweep rates

Sample	Solution composition	Scan sweep rate mv/min	E_{rest} mv (SCE)	E_{corr} mv (SCE)
A1	0.6M NaCl	60	-634	-902
B1	2M NaCl	60	-648	-1015
C1	0.1M Na ₂ SO ₄ + 0.6M NaCl	60	-661	-1037
A2	0.6M NaCl	1200	-633	-1052
B2	2M NaCl	1200	-657	-1082
C2	0.1M Na ₂ SO ₄ + 0.6M NaCl	1200	-660	-1046
D	0.02M Na ₂ SO ₄ + 0.6M NaCl	1200	-680	-1020
E	0.2M NaNO ₂ + 0.6M NaCl	20	-394	-740.3
F	0.5M NaNO ₂ + 0.6M NaCl	2000	-390	28.6

Table 3.11 Corrosion test for BS251A58 steel in different solutions,
(a) Test series 1, Sample area=3 mm²





Sample	solution	duration 66 hours	comments
PA1	0.5M NaNO ₂ + 0.6M NaCl	 shining	non-corrosion
PA2	0.2M NaNO ₂ + 0.6M NaCl	 partly rusted with laths	slight corrosion
PA3	0.6M NaCl	 dark	general corrosion
PA4	0.6M NaCl	 dark	general corrosion

Table 3.11 (b) Test series 2, sample area=4mm²











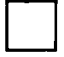


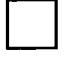
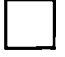



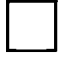





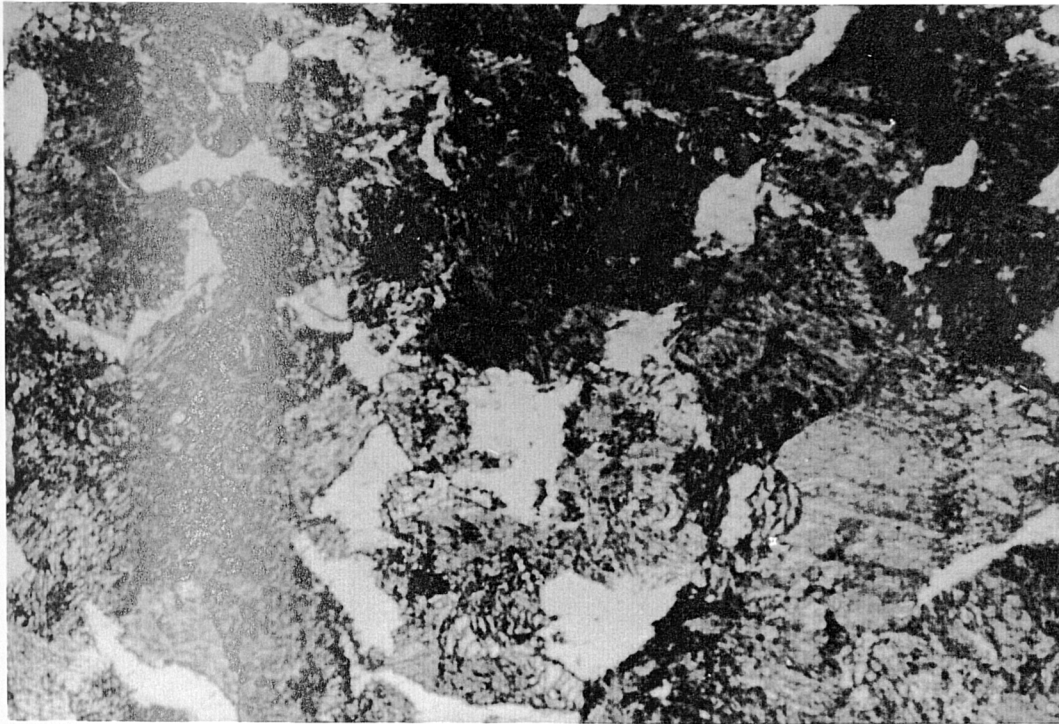
Sample	solution	15 min	170 min	10 days	comments
PB1	2M NaCl	 15 pits	 13 pits	 dark	general corrosion
PB2	1M NaCl	 10 pits	 10 pits	 dark	general corrosion
PB3	0.6M NaCl	 2 pits	 5 pits	 dark	general corrosion
PB4	0.6M NaCl + 0.1 M	 1 pit	 2 pits	 dark	general corrosion
PB5	0.6M NaCl + 0.1 M	 no pit	 no pit	 shining	no corrosion

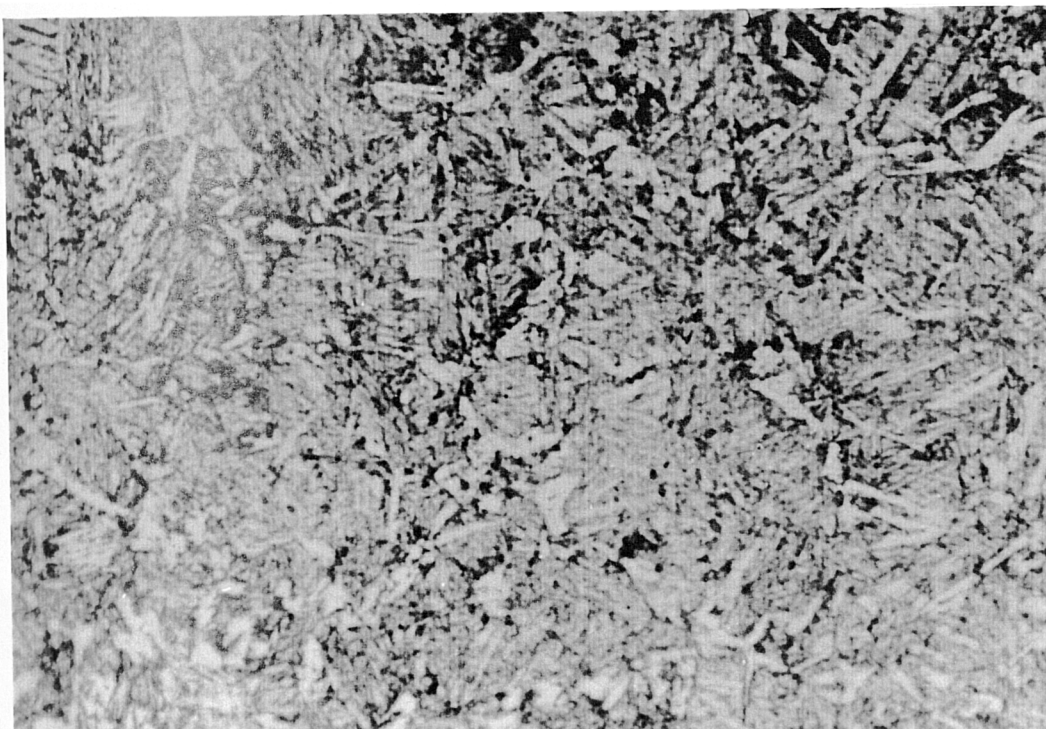
Table 3.11 (c) Test series 3, sample area=10.

Sample	solution	5 min	20 min	1 day	comments
PC1	0.6M NaCl + 0.1 M	 15 pits	 18 pits	 dark	general corrosion
PC2	0.6M NaCl	 5 pits	 9 pits	 dark	general corrosion
PC3	2M NaCl	 10 pits	 16 pits	 dark	general corrosion



10 μm

Figure 3.1 Microstructure of the sample machined from 'Normalised' BS251A58 steel, hot rolled bar. White: ferrite; Grey: fine pearlite. 2% Nital etched.



10 μm

Figure 3.2 Microstructure of heat-treated BS251A58 steel, mainly tempered martensite. 2% Nital etched.

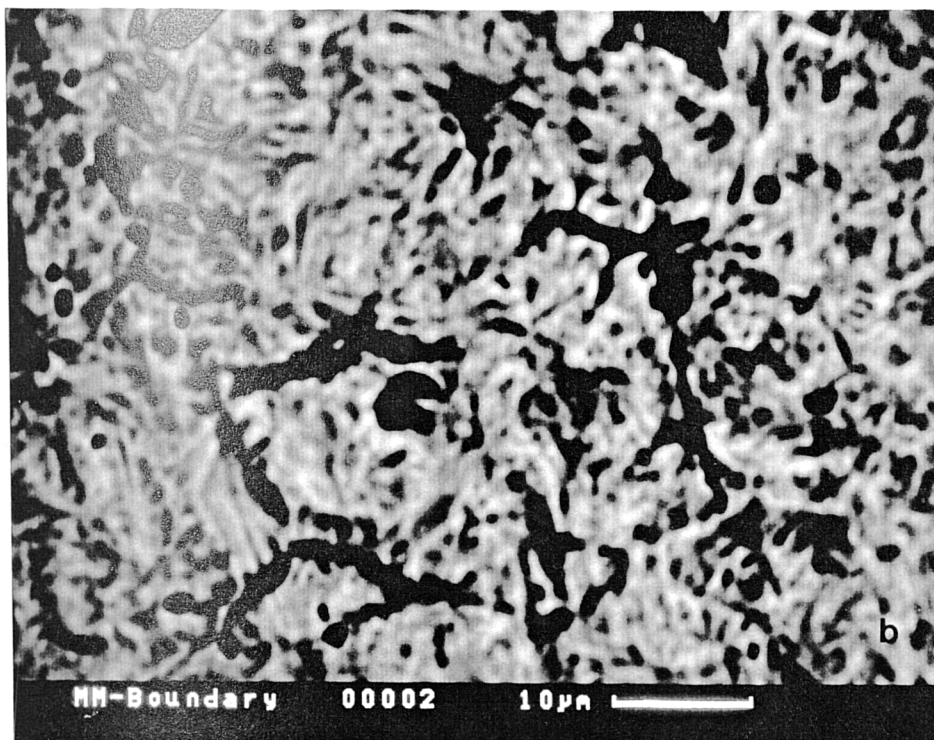
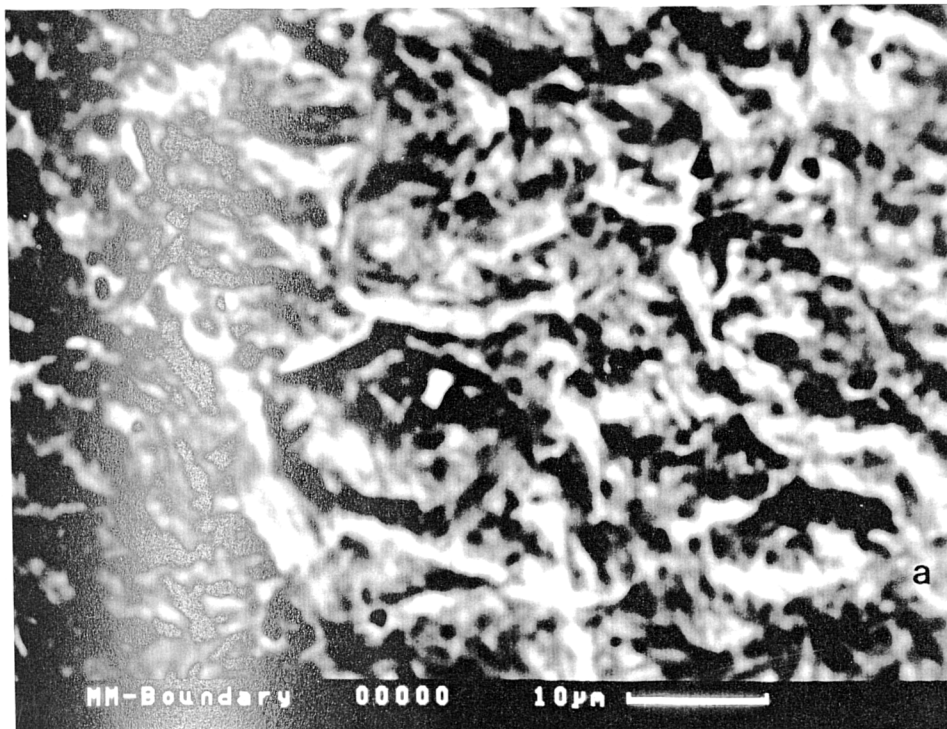
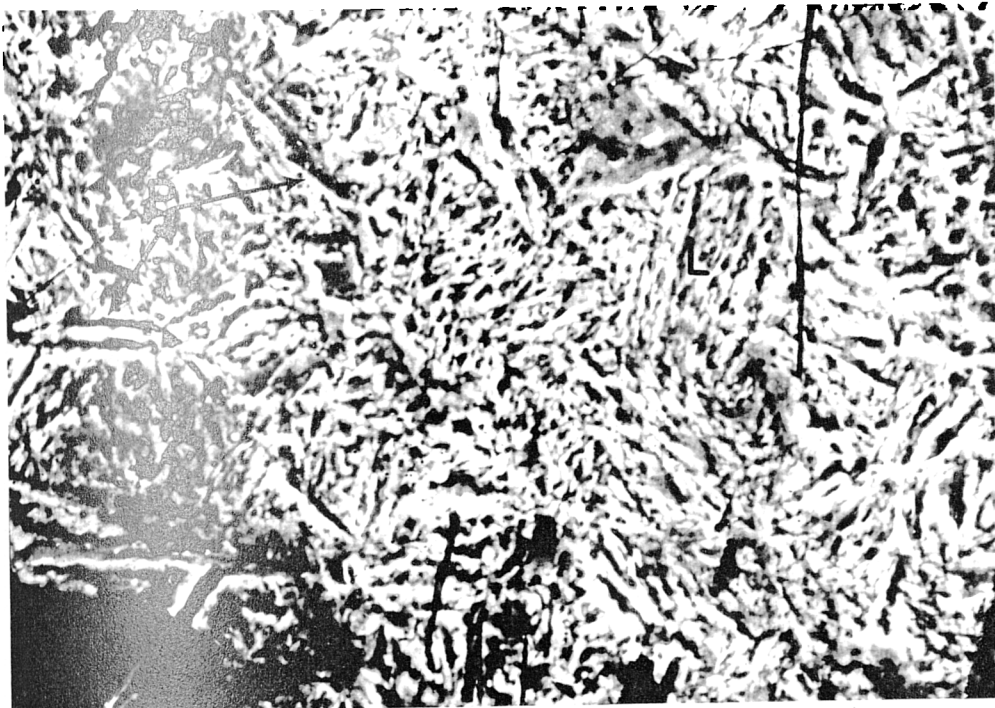


Figure 3.3 (a) SEM of the microstructure of heat-treated BS251A58 steel. (b) the same area as (a) but showing prior austenite grain boundary due to the difference in chemical composition using a different SEM mode.



10 μ m

Figure 3.4 Morphology of the microstructure as seen by SEM of a heat-treated BS251A58 steel. Each prior austenite grain consists of three to five packets of martensite laths; the packet size of the martensite laths is about 10 μ m.



Figure 3.5 (a) Duplex type inclusion. grey: Manganese sulphide (MnS); Dark: Iron oxide (FeO).

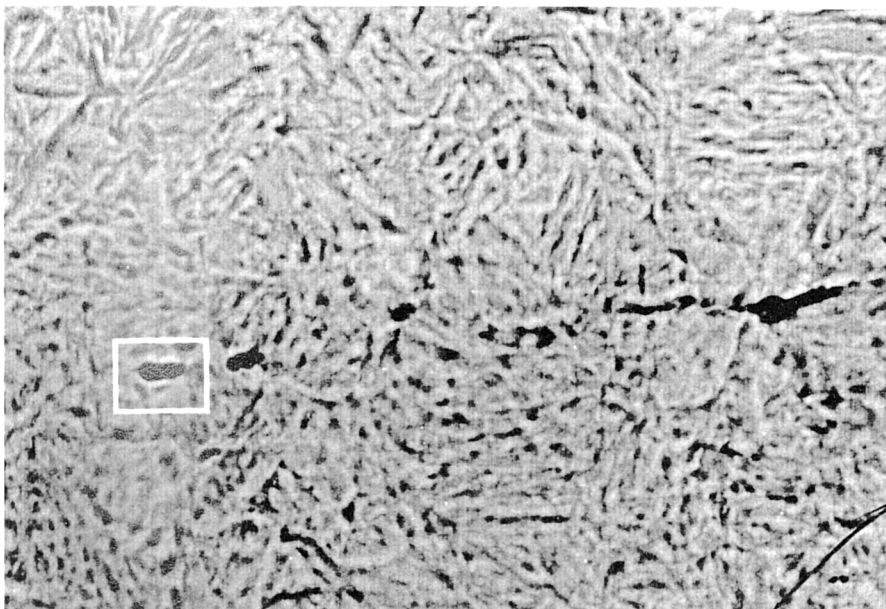


Figure 3.5 (b) A SEM micrograph of BS251A58 steel heat-treated with a non-metallic inclusion (white square) lying in the matrix of the tempered martensite and along the prior austenite grain boundary.

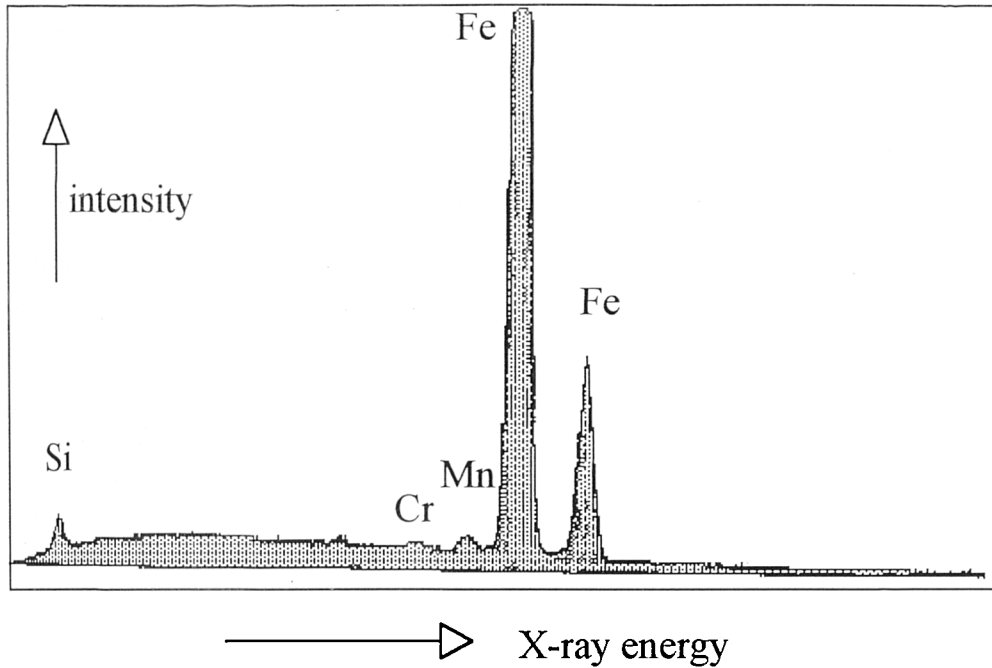


Figure 3.6 (a), The x-ray spectrum analysis of chemical element levels in the metal matrix, showing the absence of S and low energy level of Mn, compared with the energy level of Mn on Figure 3.6(b).

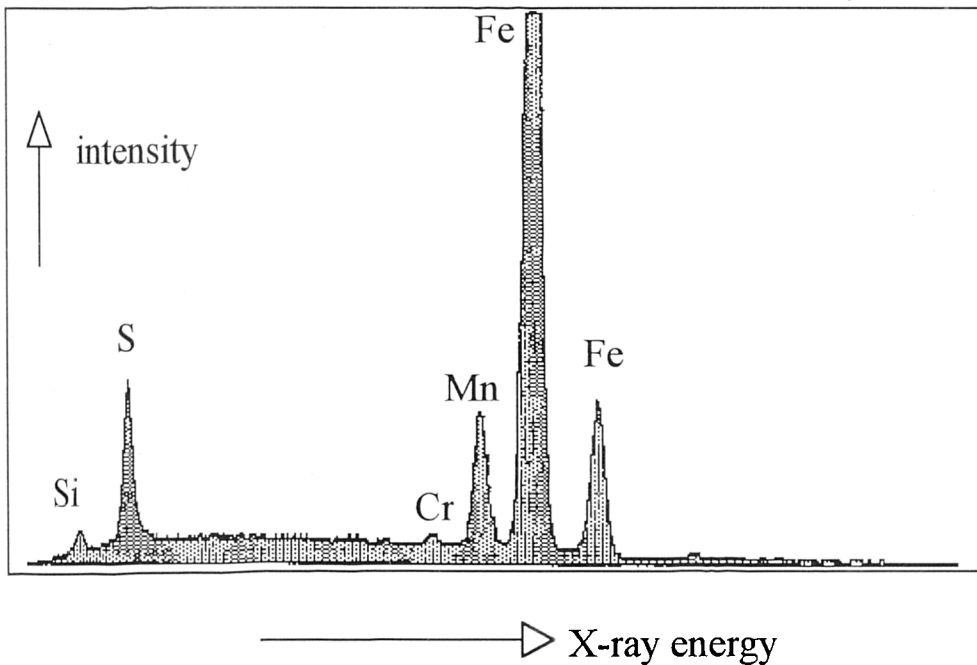
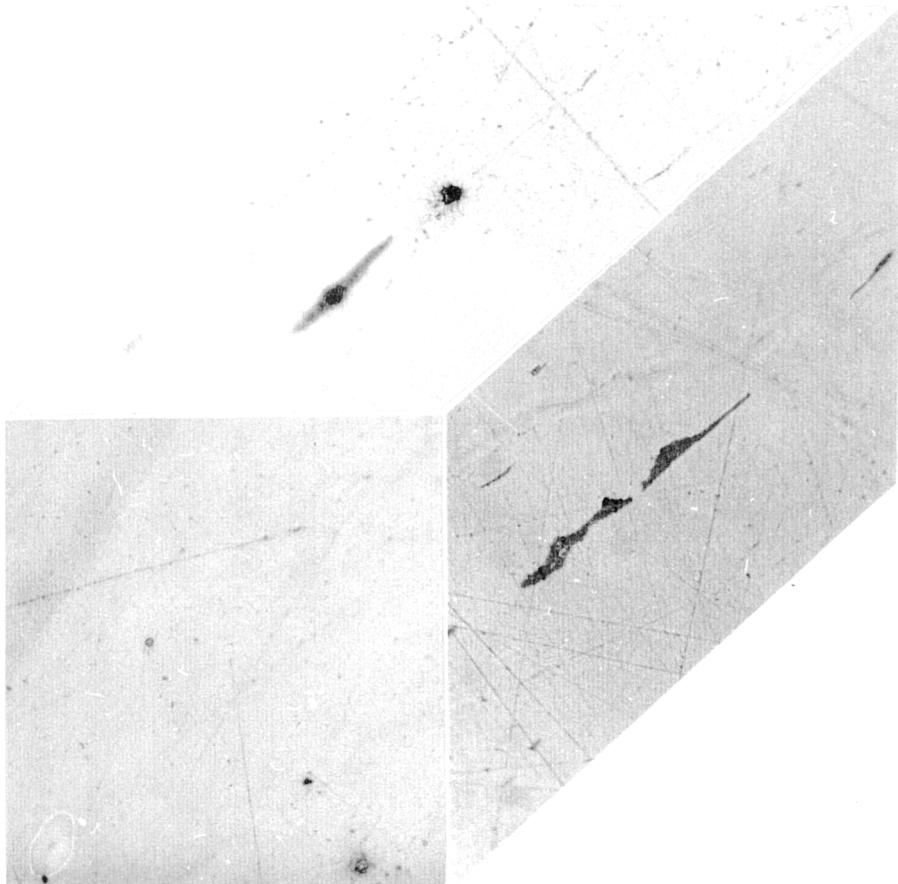


Figure 3.6 (b), The X-ray spectrum analysis of chemical element levels in the marked region (white square) shown in Figure 3.4 showing the presence of S, Cr, Mn and Fe.



20 μm

Figure 3.7 Three dimensional diagram to show the form and size of inclusions.

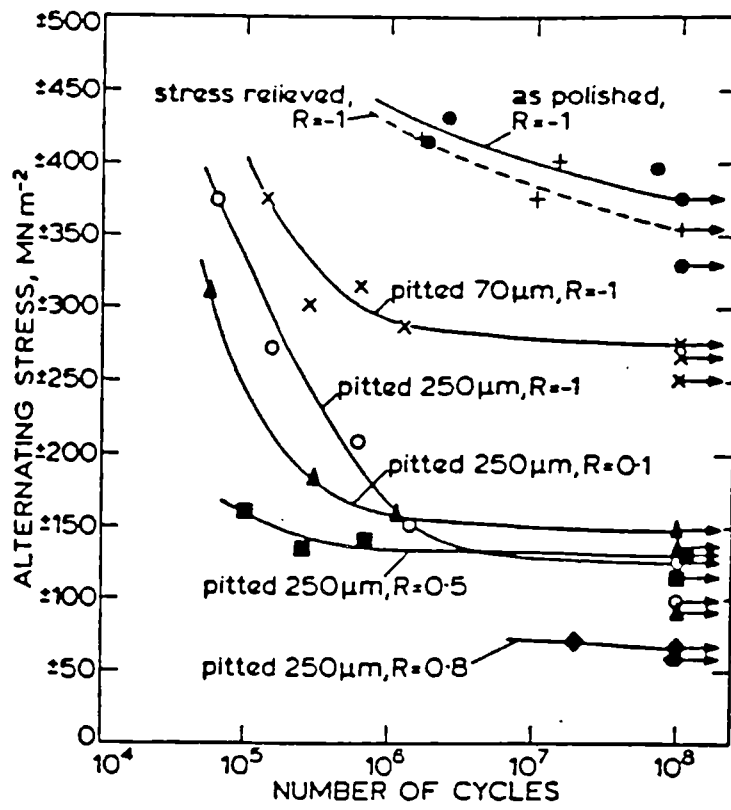


Figure 3.8 Endurance fatigue data for an as-polished and a pre-pitted push-pull specimen [3].

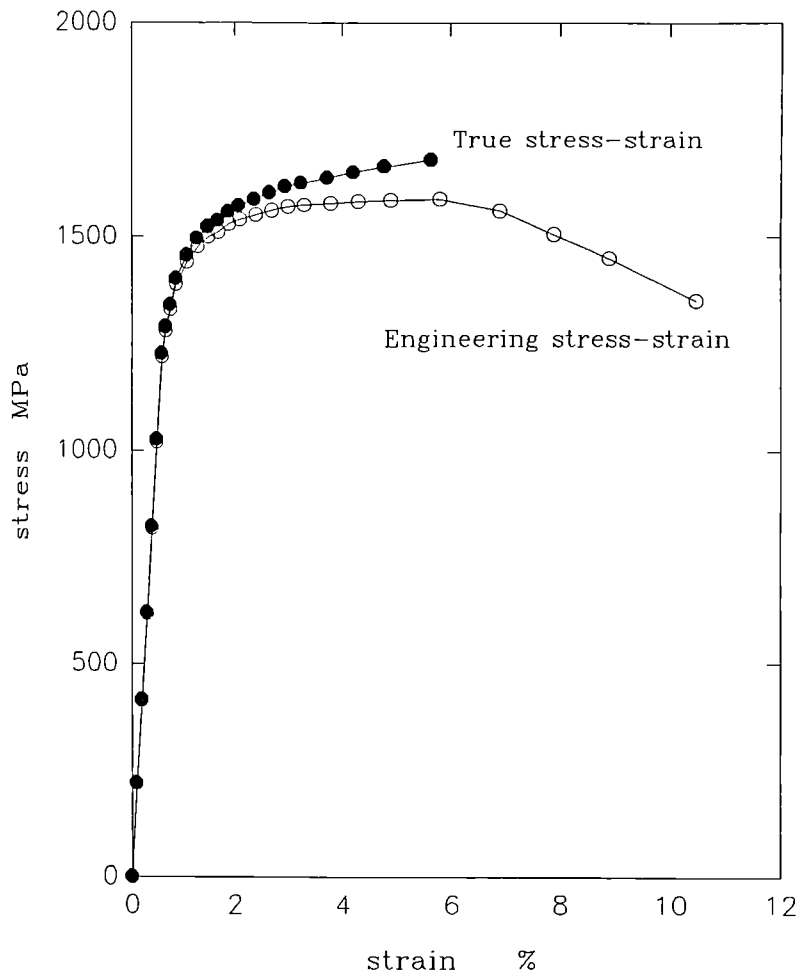


Figure 3.9 Monotonic tensile stress-strain curve.

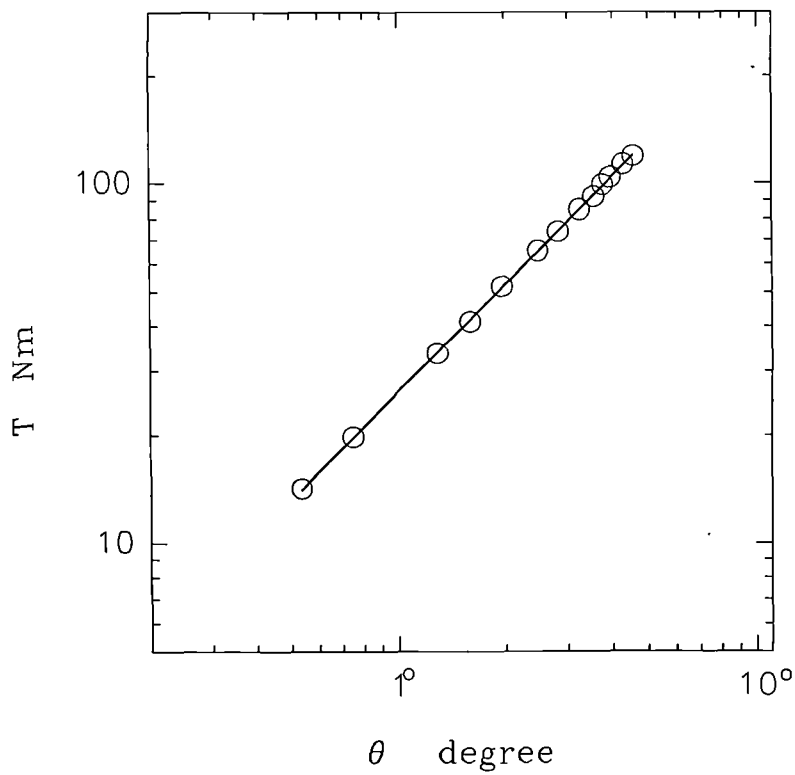
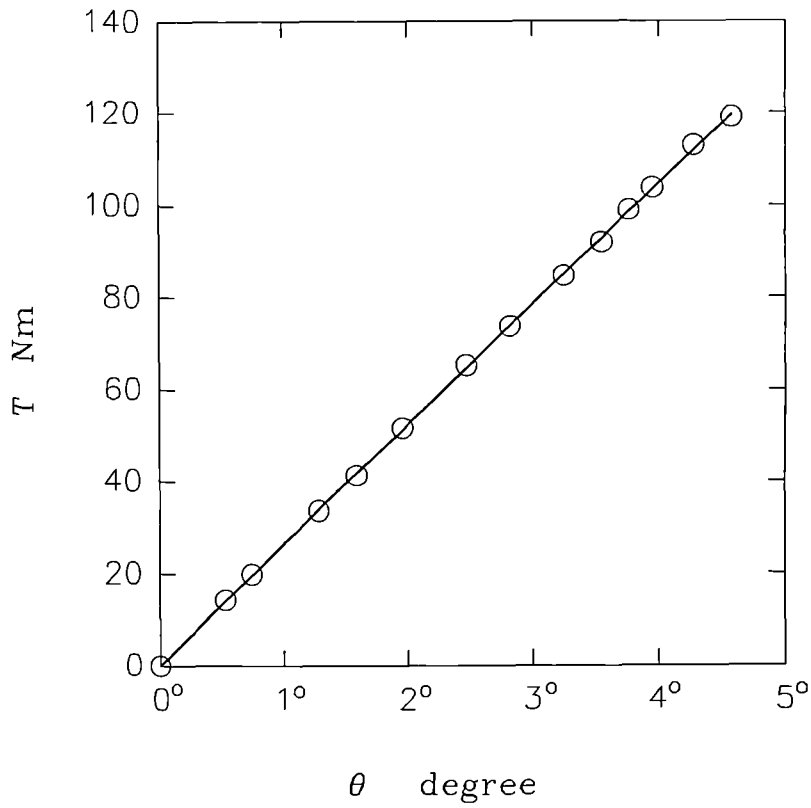


Figure 3.10 Cyclic torque versus twist angle curve for the hour-glass specimen D having a minimum diameter of 7.92 mm in the central section.

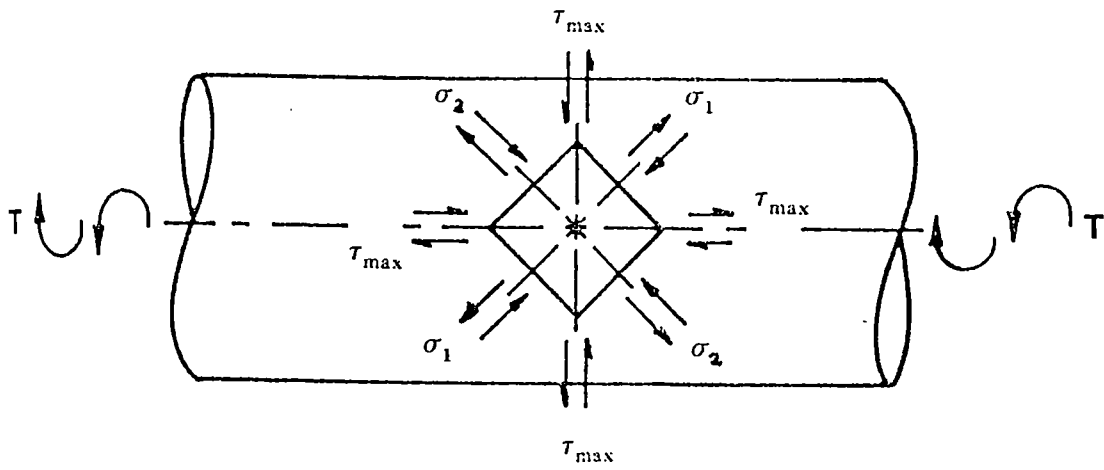
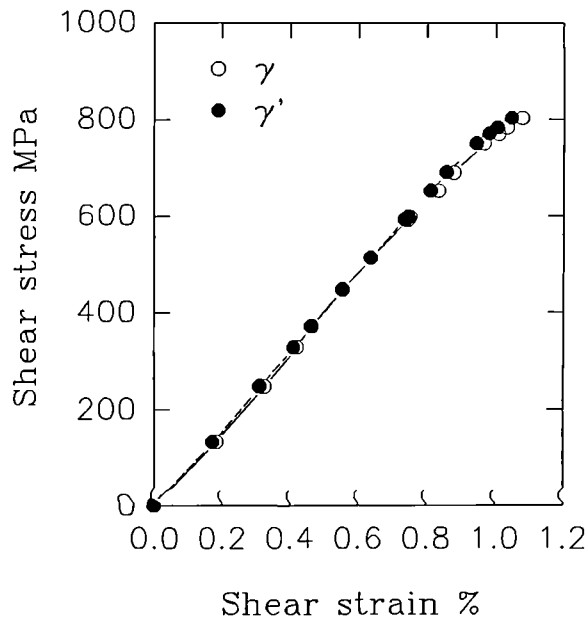
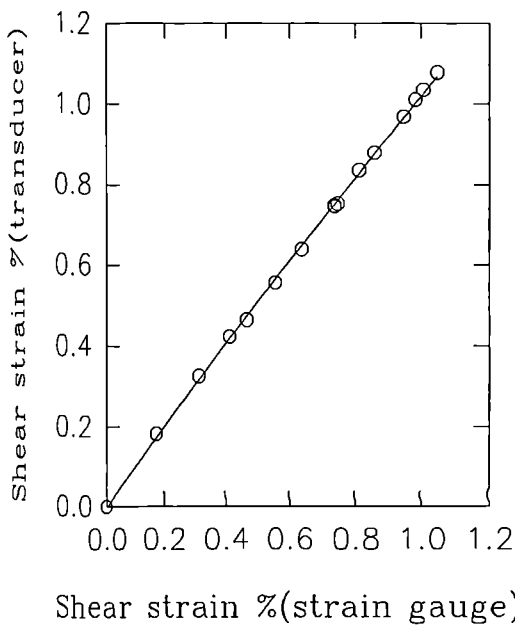
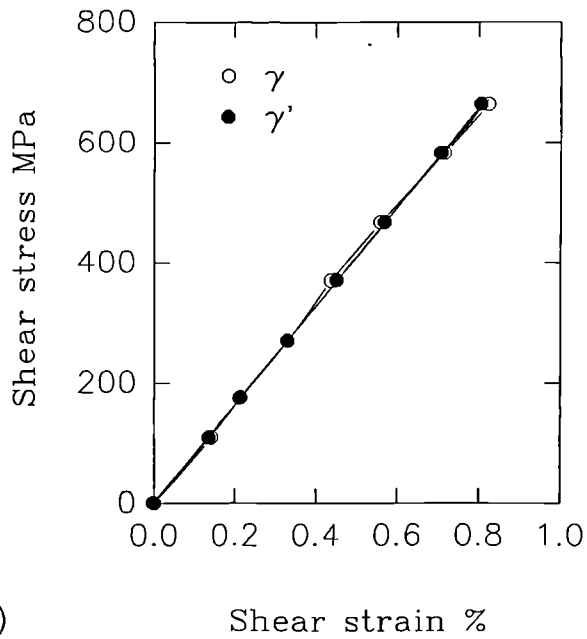
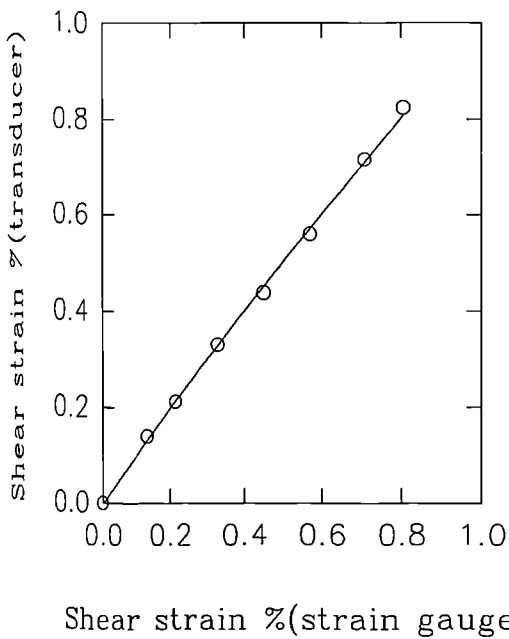


Figure 3.11 Schematic view of the stress system on the surface of a specimen subjected to reversed torsion T .



Specimen A



Specimen B

Figure 3.12 Shear strain calibration for the torsion cell during a monotonic torsion test; γ is the shear strain determined by the LVDTs and γ' is the shear strain calculated from strain gauge. (a) cylindrical specimen A, $r=4.00$ mm; (b) cylindrical specimen B, $r=4.01$ mm.

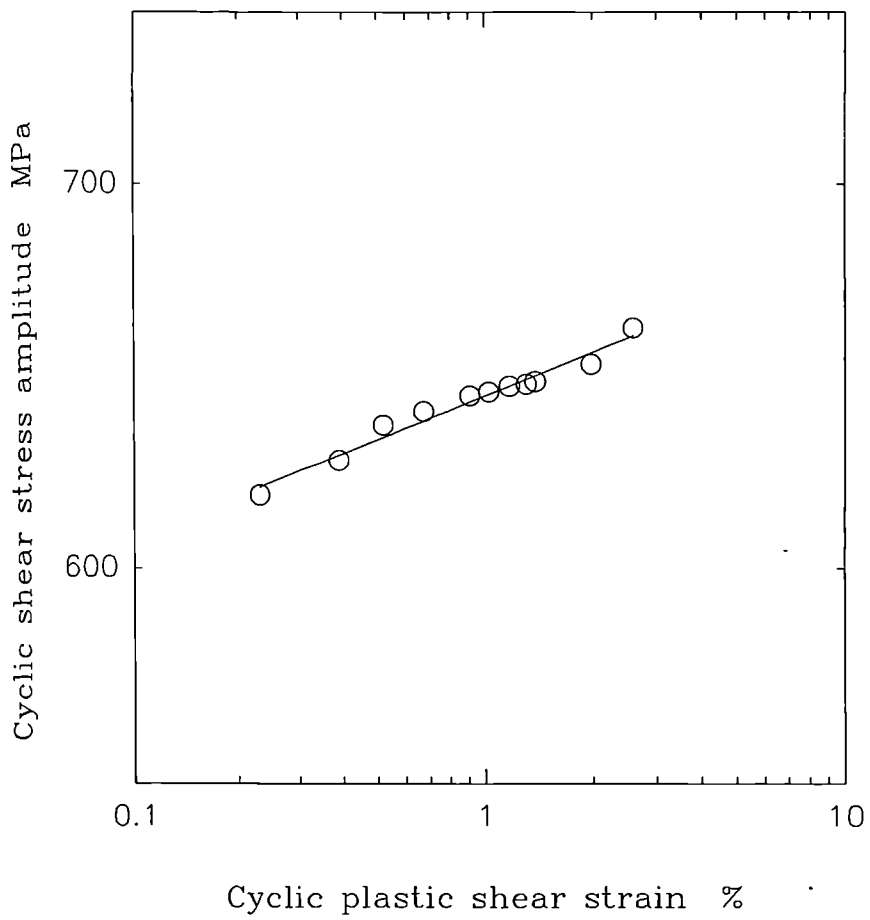


Figure 3.13 Cyclic shear stress-shear plastic strain curve.

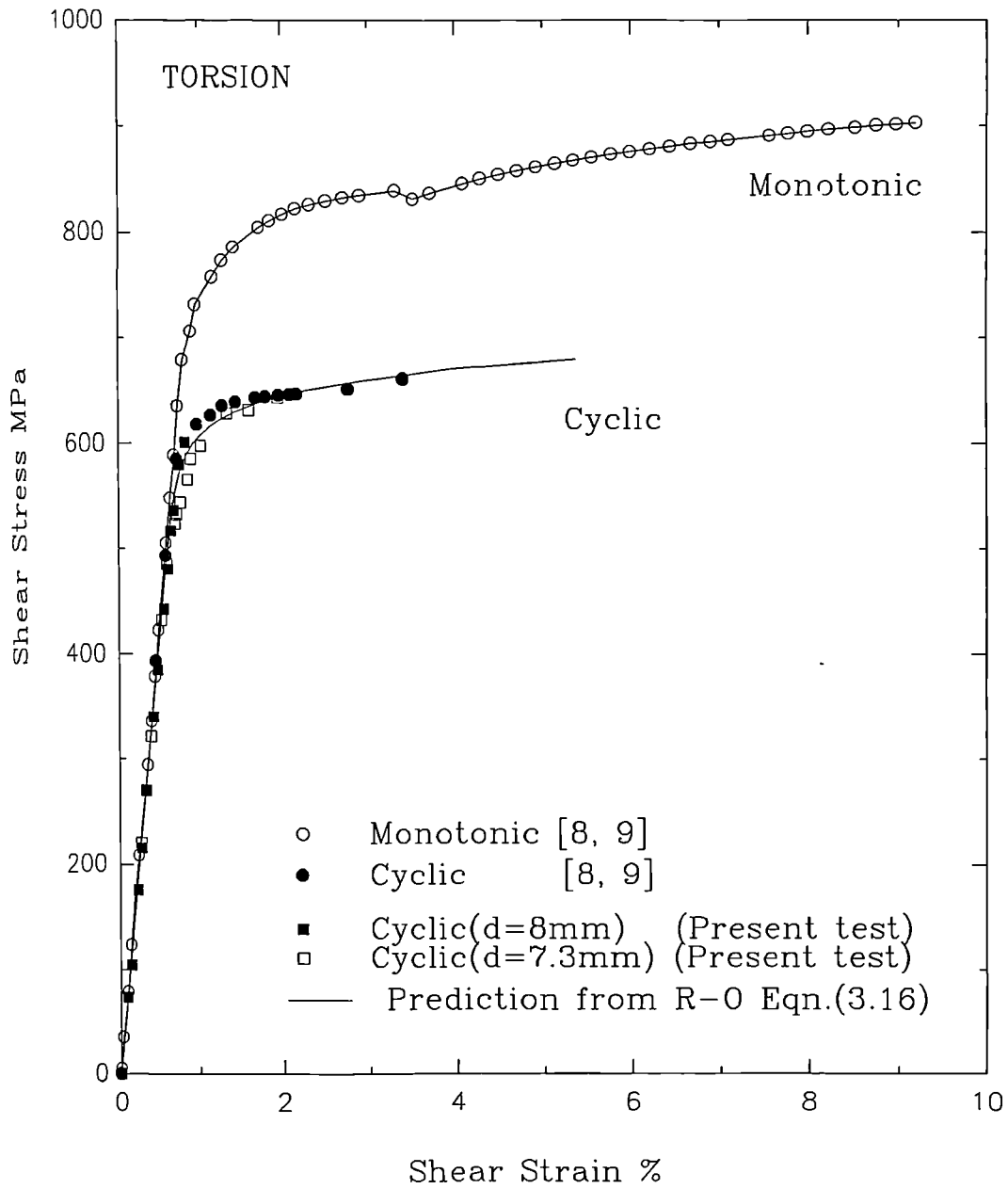


Figure 3.14 Monotonic and cyclic torsion shear stress-shear strain curves for BS251A58 steel. R-O equation is shown as:

$$\gamma(\%) = \left(\frac{\tau}{815} \right) + \left(\frac{\tau}{643} \right)^{\frac{1}{0.04}}$$

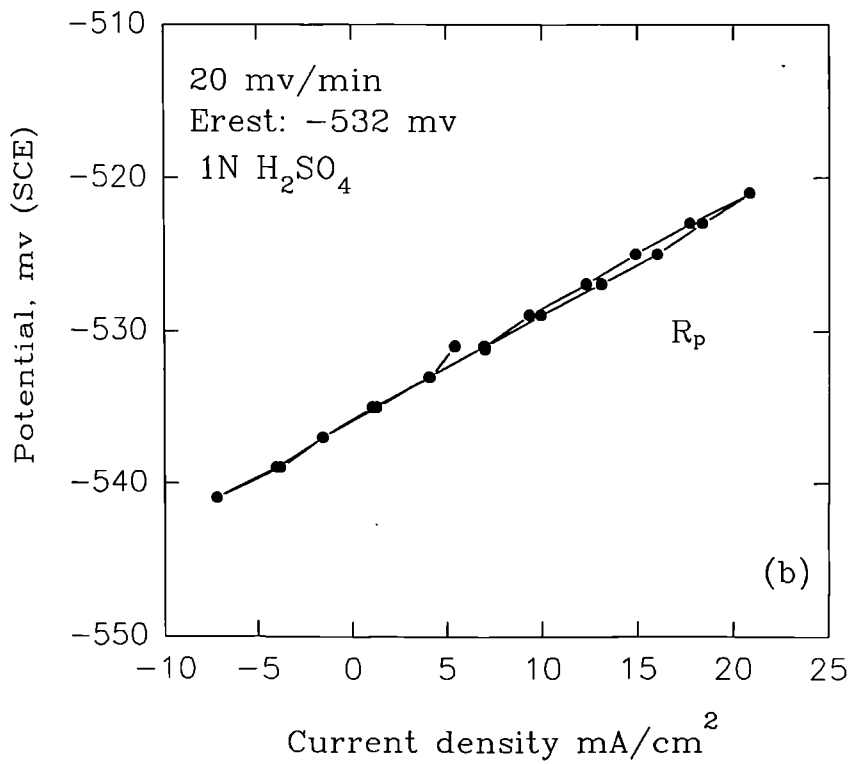
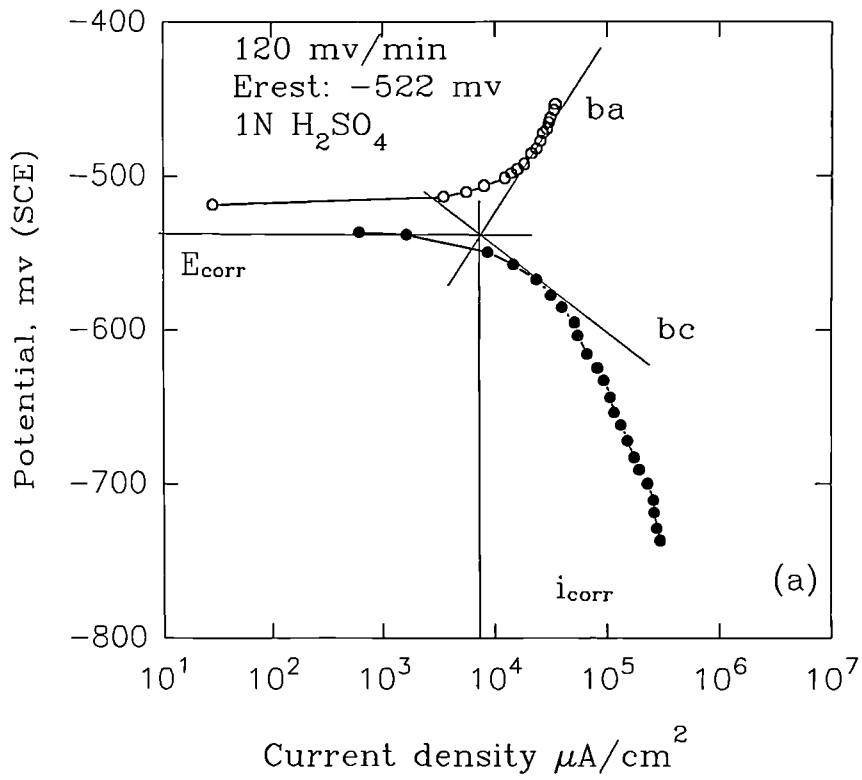


Figure 3.15 (a) Tafel plot for stainless steel type AISI316 in 1N H_2SO_4 solution at room temperature (b) Polarisation resistance, R_p .

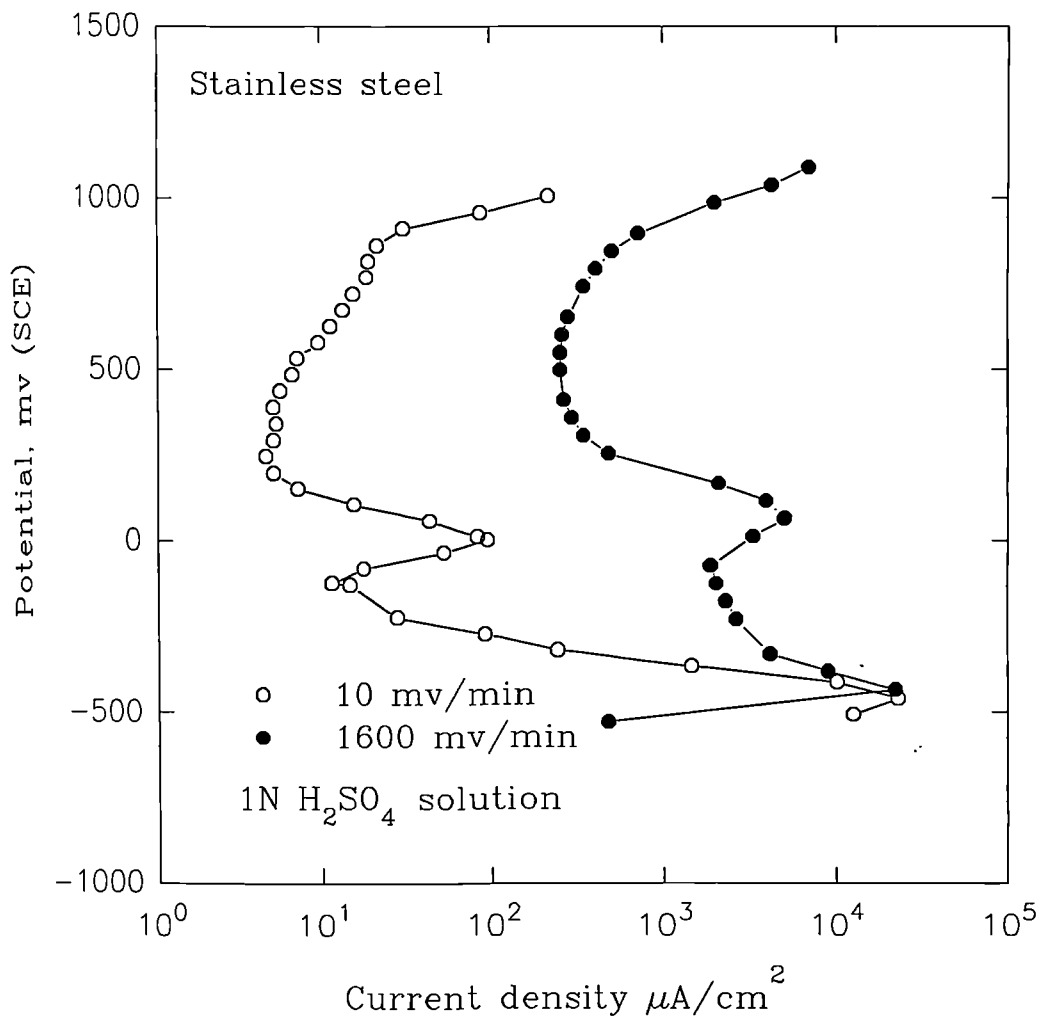


Figure 3.16 Potentiodynamic polarisation curves for stainless steel type AISI316 in 1N H₂SO₄ solution at two scan sweep rates and at room temperature.

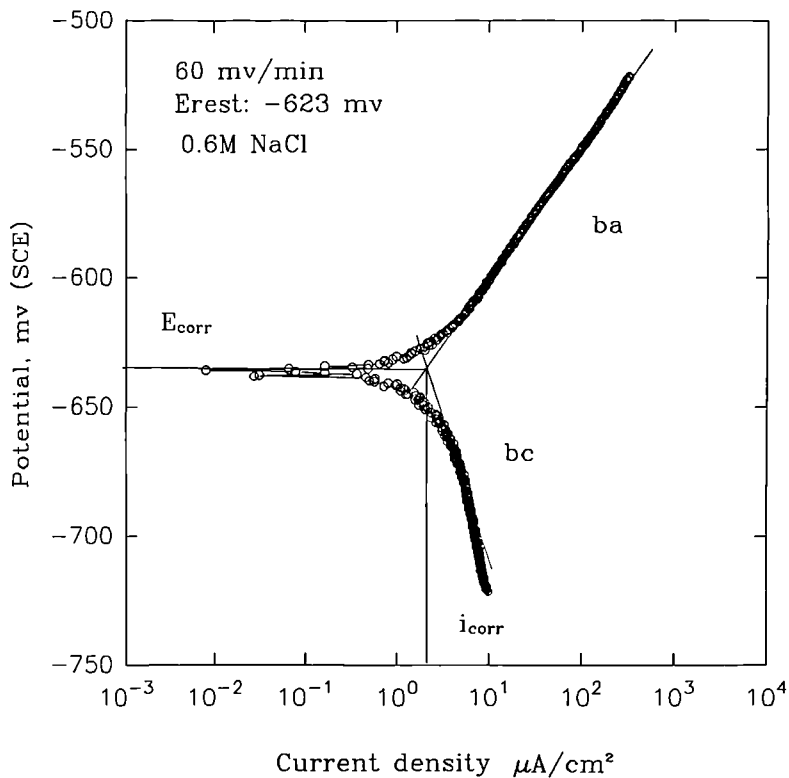


Figure 3.17 Tafel plot for BS251A58 steel in 0.6M NaCl solution at room temperature.

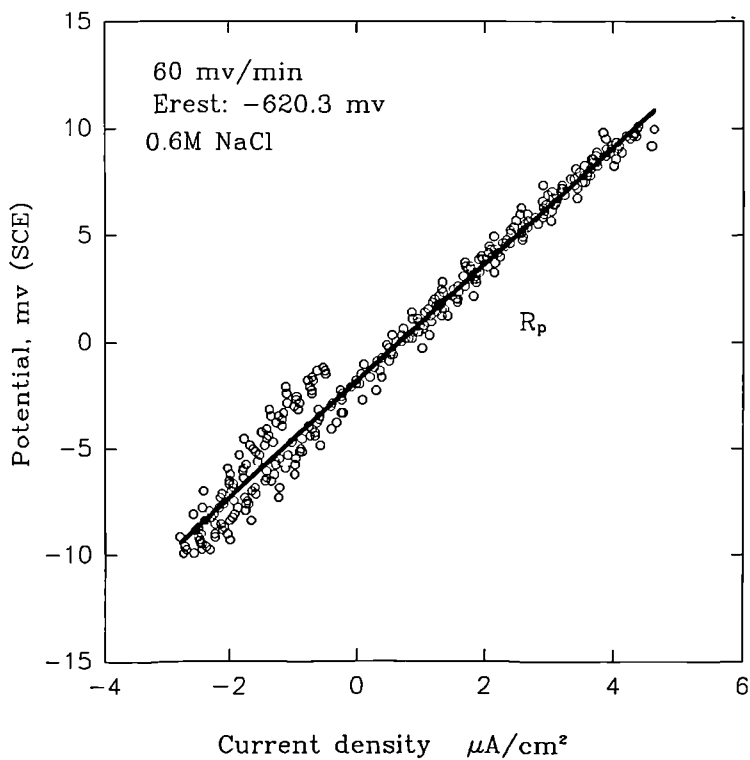


Figure 3.18 Polarisation resistance, R_p , for BS251A58 steel in 0.6M NaCl solution at room temperature.

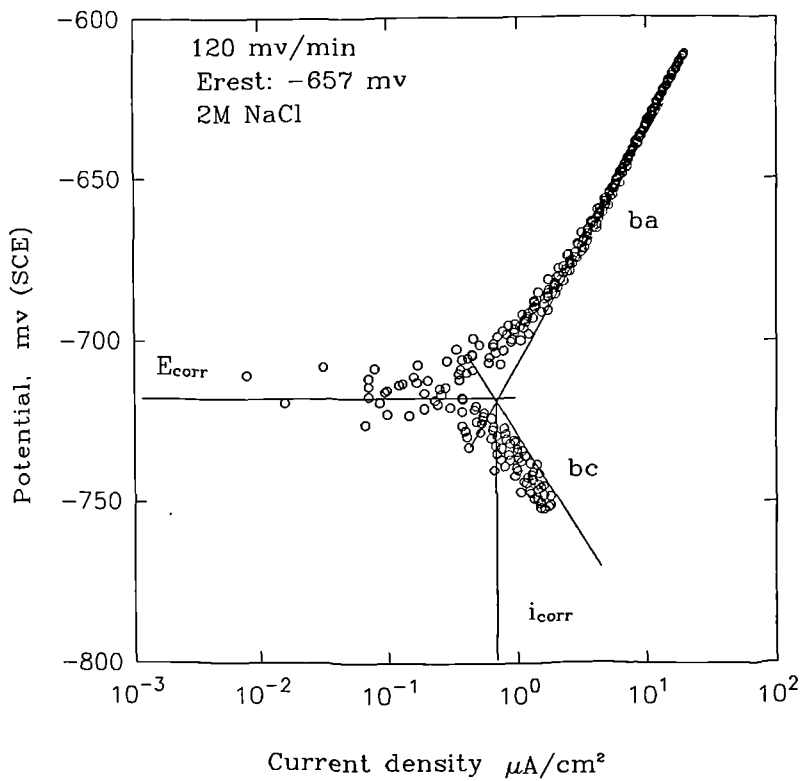


Figure 3.19 Tafel plot for BS251A58 steel in 2M NaCl solution at room temperature.

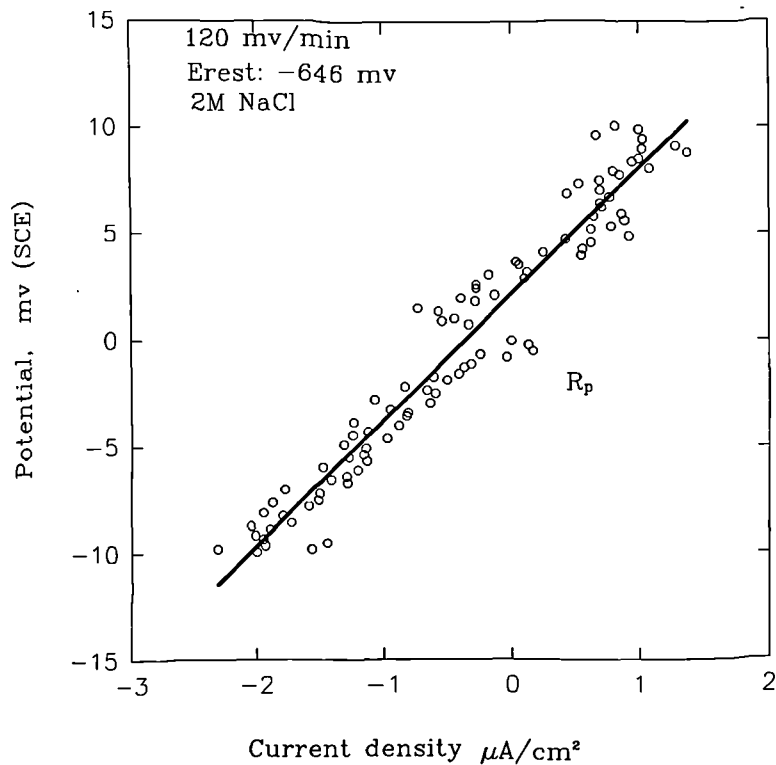


Figure 3.20 Polarisation resistance, R_p , for BS251A58 steel in 2M NaCl solution at room temperature.

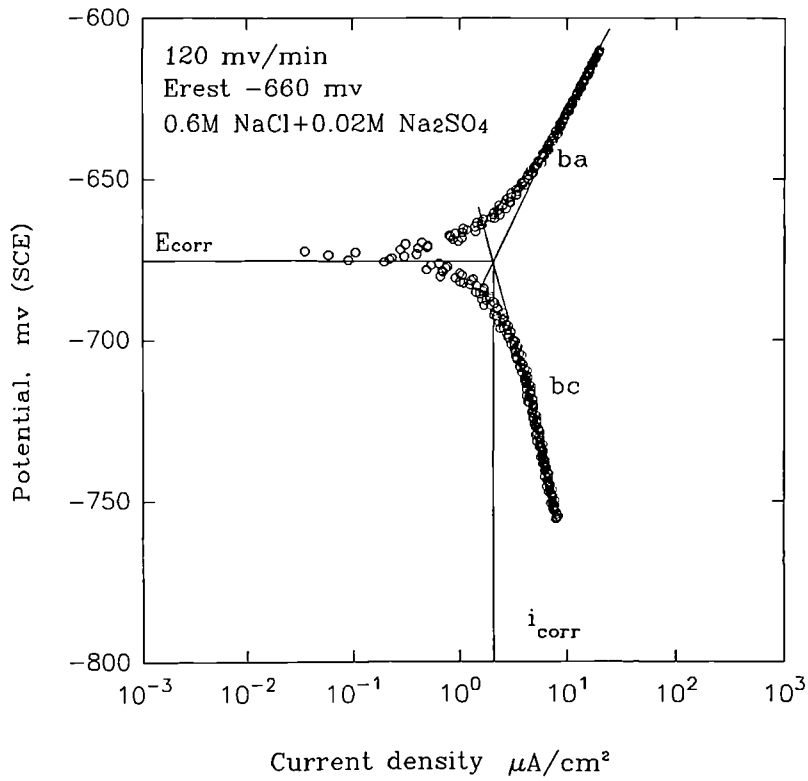


Figure 3.21 Tafel plot for BS251A58 steel in 0.6M NaCl+0.02 Na₂SO₄ solution at room temperature.

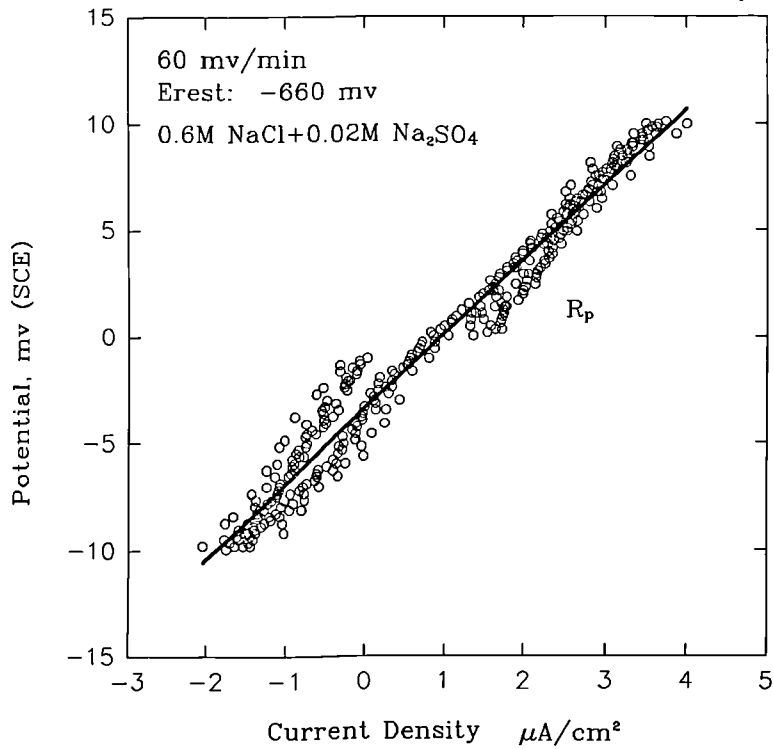


Figure 3.22 Polarisation resistance, R_p , for BS251A58 steel in 0.6M NaCl+0.02 Na₂SO₄ solution at room temperature.

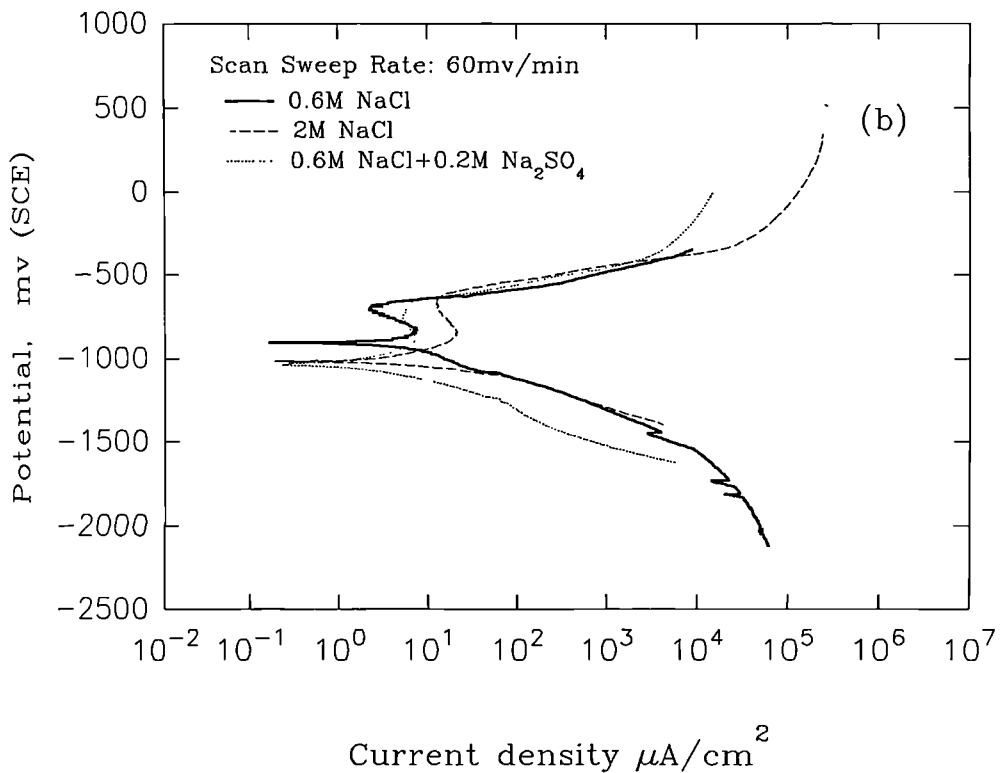
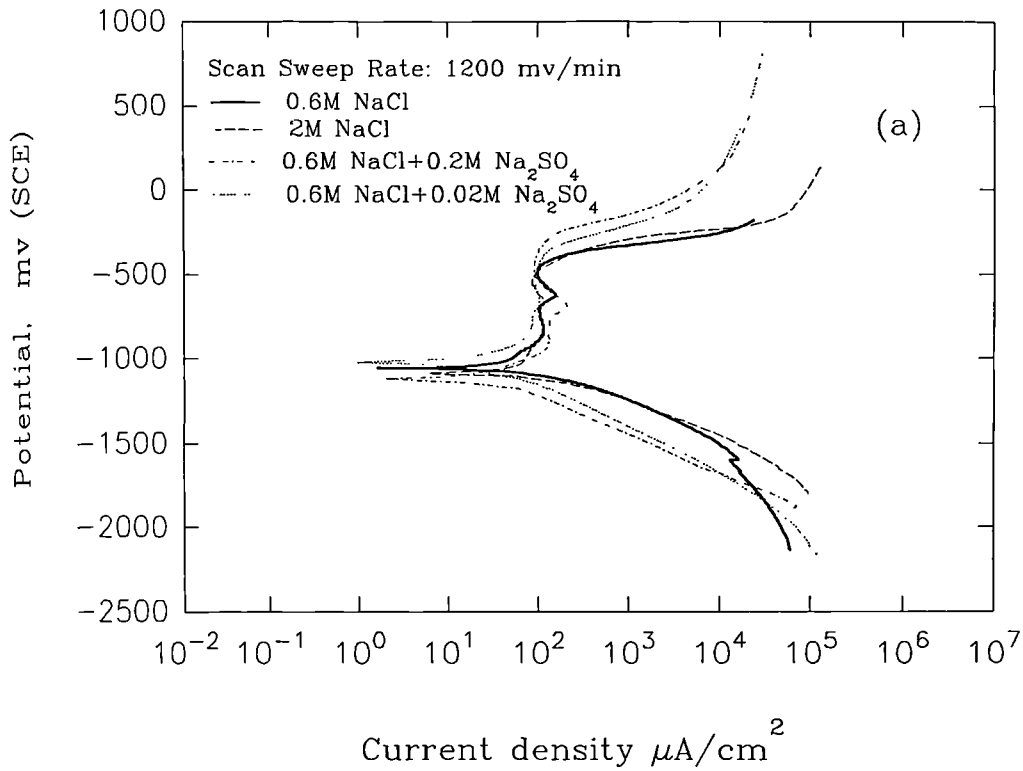


Figure 3.23 Potentiodynamic polarisation plots for BS251A58 steel in different solutions (a) at a fast scan sweep rate (b) at a slow scan sweep rate.

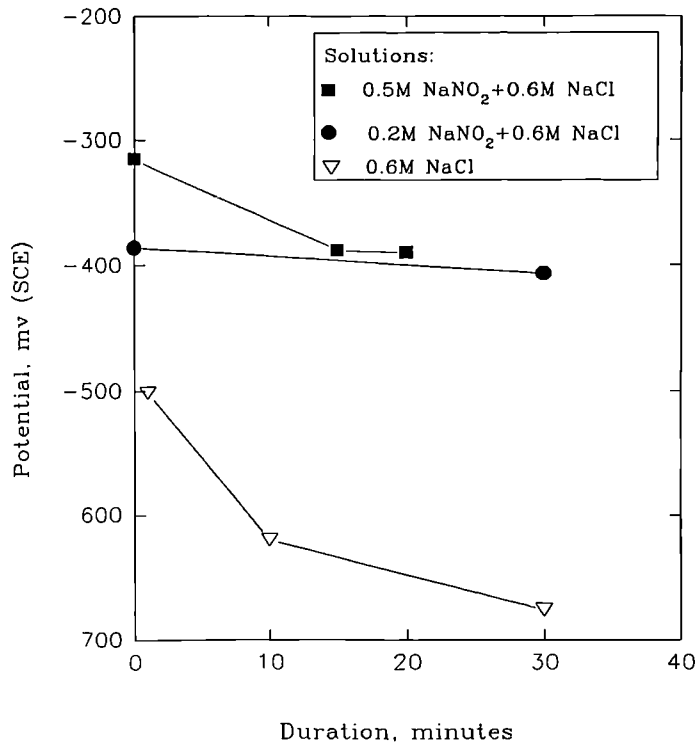


Figure 3.24 The rest potential, E_{rest} , decreasing with increasing time for BS251A58 steel in different solutions.

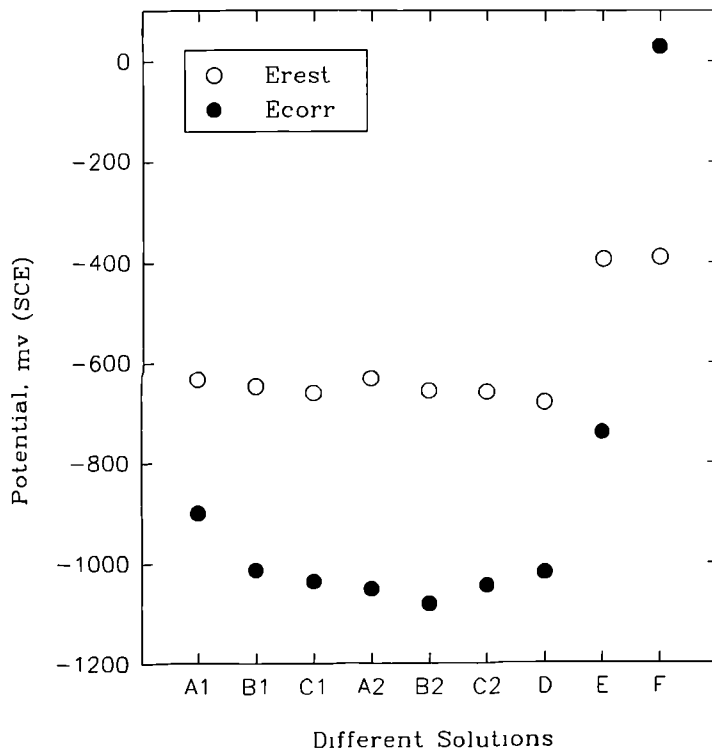


Figure 3.25 Rest potential, E_{rest} , and true corrosion potential at zero current density, E_{corr} , for BS251A58 steel in various solutions.

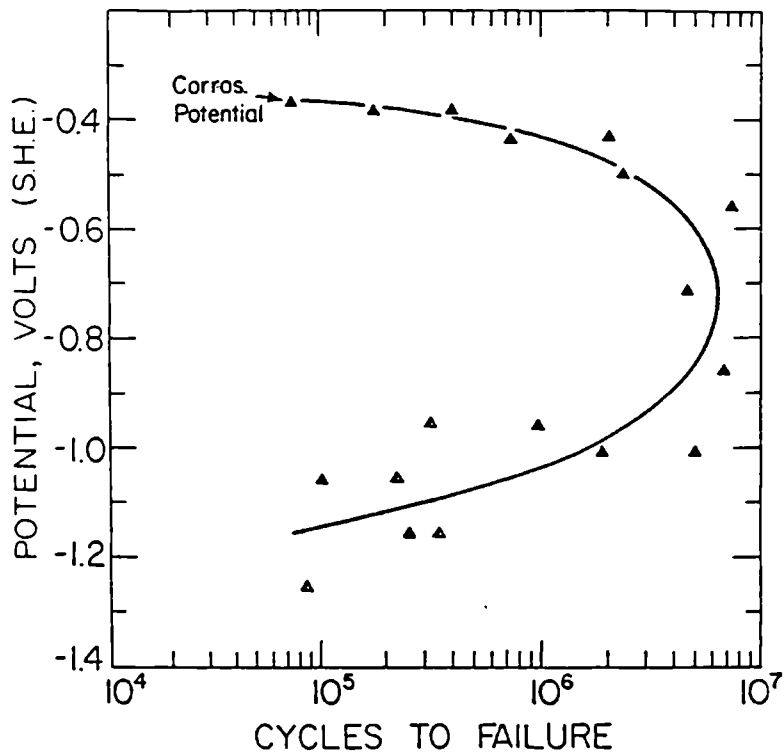


Figure 3.26 The effect of cathodic polarisation on the fatigue life of 4140 steel (HRc 52) tested in 3% NaCl solution at a stress below the fatigue limit in air [10]. SHE : Standard Hydrogen Electrode

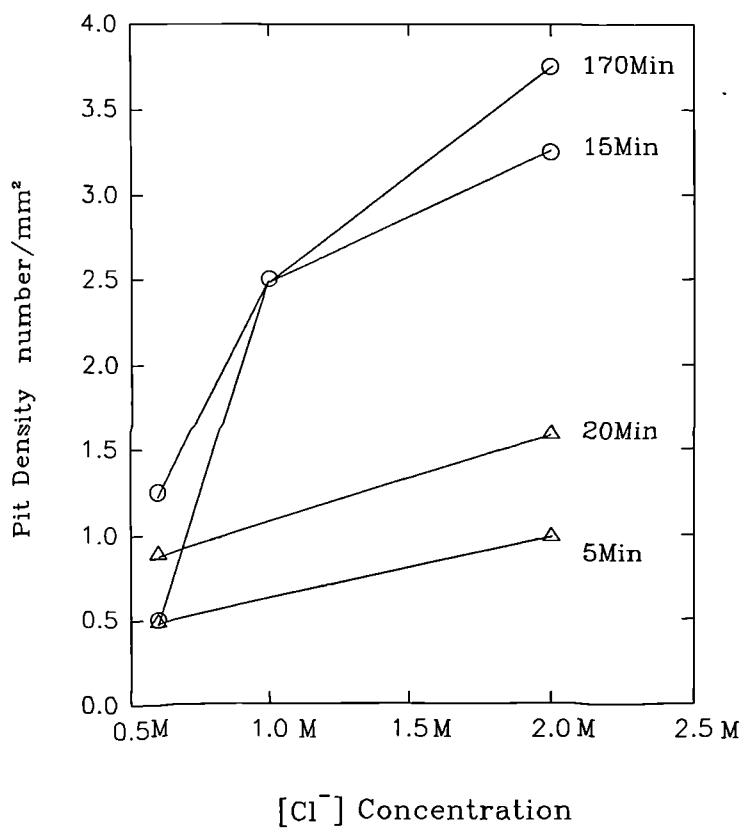


Figure 3.27 The number of pits as a function of Cl⁻ concentration in a solution of sodium chloride for BS251A58 steel.

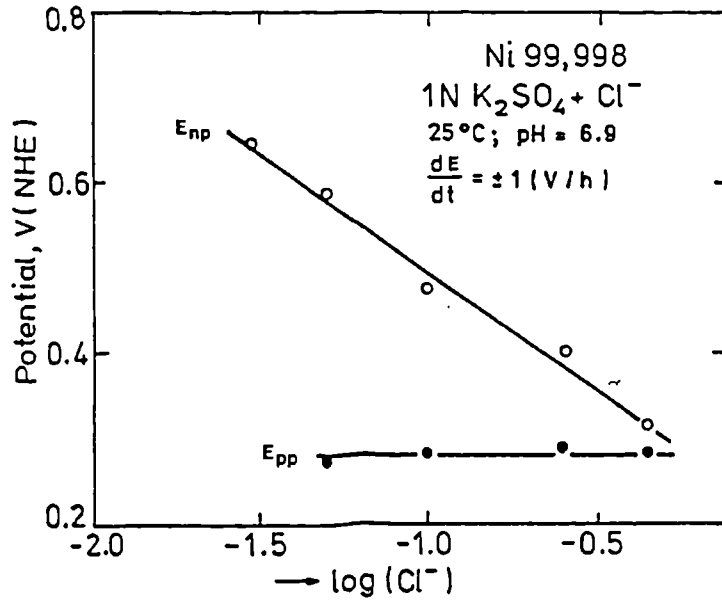


Figure 3.28 The effect of Cl⁻ concentration on the characteristic pitting potentials of pure Nickel [14].

E_{pp} = pit protection potential, E_{np} = pit nucleation potential.

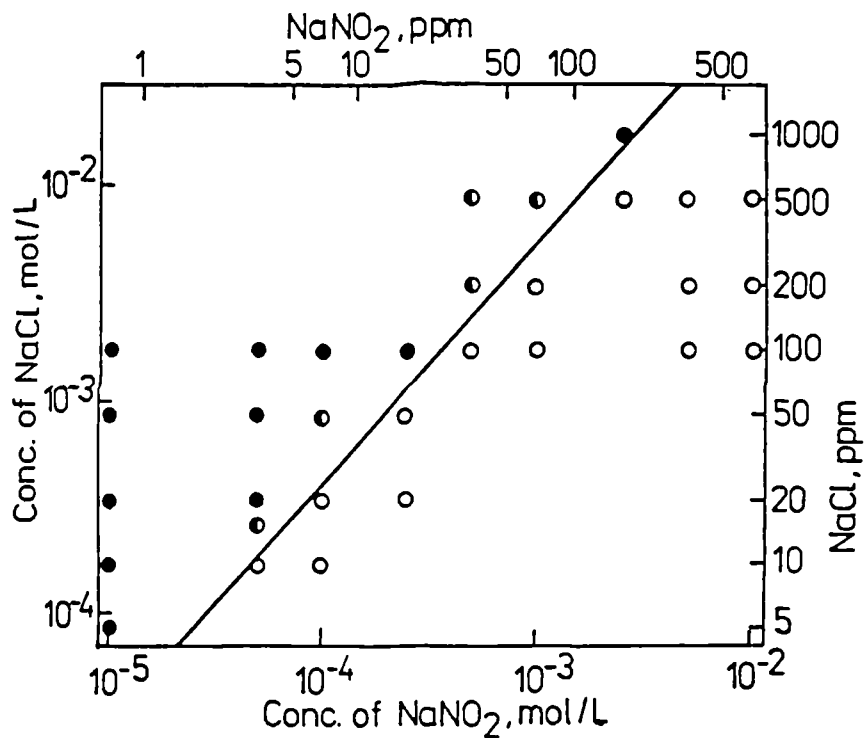


Figure 3.29 The effect of NaCl addition on the corrosion of iron in air-saturated NaNO₂ solution at 25°C. Open circles=no pitting, weight loss for 5 days immersion 1 mdd; half-dark circles=some pitting <10 mdd; dark circles=extensive pitting or general corrosion >10 mdd [16]. 1 mdd = 1mg/dm²/day

Chapter 4 Corrosion Fatigue and In-Air Fatigue

The results of corrosion fatigue and in-air fatigue tests are reported and discussed in this chapter. A number of aspects relevant to corrosion fatigue crack growth, such as pitting, crack coalescence, stage I to stage II transition, frequency effects, cathodic polarisation effects and electrolyte composition effects, have been examined. The contents are arranged such that each section focuses on a specific topic of interest, although cross-reference is often inevitable.

4.1 Torsion fatigue tests in 0.6M NaCl solution

Smooth hour-glass profiled fatigue specimens, polished to a mirror image surface finish ($R_a=0.25$), were tested under fully reversed shear loading in an aerated 0.6M sodium chloride solution of pH 6 at room temperature and at a loading frequency of 5Hz. A surface replication technique was applied to detect crack initiation and propagation during fatigue cycling.

The failure criterion used for all tests was a 20% reduction in the stabilised cyclic load. After completion of the tests, the specimens were cleaned, dried and examined using a scanning electron microscope.

The effect of test environment can be generally understood by reference to the corrosion fatigue endurance (S-N) curve, shown in Figure 4.1 and listed in Table 4.1. Clearly the loss of the fatigue limit, when compared to the in-air fatigue data, is the major feature of these curves and an understanding of this requires detailed analysis. The relationship between the

fatigue life and shear stress amplitude (in MPa) was obtained for BS251A58 steel in 0.6M NaCl solution at a frequency of 5Hz, as shown as:

$$\tau = 13708 (N_f)^{-0.306} \quad (4.1)$$

From the results of corrosion fatigue tests, the usual sequence of events leading to failure included the development of a micro pit which in turn enhanced the growth of a shear stage I crack which eventually transformed to that of a stage II crack leading to final failure. The extent of each phase in the failure process depends upon several factors some of which are discussed below.

4.1.1 S-N endurance curve

For ease of description a number of parameters are introduced here which define different stages in the life of fatigue cycling, a defect developed during:- N_p : *major pit nucleation*; N_i : *microcrack initiation from such pits*; N_t : *the crack transition from stage I to stage II*; and N_f : *the final fracture* (valid both in air and in 0.6M NaCl solution). Experimental results obtained for these parameters are shown together in Figure 4.2 and Table 4.2. The number of cycles for the initiation of a pit was 5000 cycles or less for stress ranges of 926, 728 and 613 MPa. However, the number of cycles for the initiation of a pit, which eventually developed into a microcrack, was 271300 cycles at the stress range of 415MPa. It should be noted that although there were a few pits which initiated earlier these did not develop into cracks.

For the corrosion fatigue of the high strength steel, it is evident from Figure 4.2 that early defect development, i.e. pitting, can enhance the initial crack development stage when shear stress ranges are larger than 600 MPa. However, when the shear stress range was equal to 415 MPa (for specimen TC13) the major crack, observed after 319000 cycles, was still at a length of 37 μ m. There existed a non-propagating crack with a length of 200 μ m, which initiated after 27000 cycles (0.031 N_f), ceased to grow after 83000 cycles and remained dormant up to the final failure of the specimen, see Figure 4.3(b).

It follows that the mechanical effect in corrosion fatigue still plays a very important role for the incubation of major microcrack initiation. In the modelling work (Chapter 5) the critical number of cycles for a major corrosion fatigue crack initiation under various stress levels will be further discussed.

With the assistance of aggressive environmental attack multiple-crack initiation may be operative in corrosion fatigue. The final failure was clearly dominated by the major crack evolution, rather than the average crack evolution process. The same mechanism was reported in [1]. It follows that attention should be focused on the initiation, growth and coalescence behaviour of major cracks that lead to final failure in corrosion fatigue.

Sequence of events in corrosion fatigue

The sequence of events that were recorded by replicas in the crack evolution from experiments, is illustrated schematically in Figure 4.4. The following processes are involved:

- (1) Small isolated corrosion pits initiate and gradually transform from an initially circular shape (Figure 4.4 (b)) to an elongated notch shape. Following stage I short cracks develop (Figure 4.4 (c));
- (2) Stage I short cracks propagate and then transform to stage II cracks (Figure 4.4(d)), which propagate perpendicular to the tensile direction (Figure 4.4(e));
- (3) Several cracks link up along the fracture plane, i.e. the maximum tensile stress plane, eventually leading to specimen fracture (Figure 4.4 (e)).

4.1.2 Pitting

Pits/microcracks started to initiate during the early stages of the corrosion fatigue process and continued to initiate during the rest of fatigue life. But the rate of initiation decreased as existing cracks grew longer.

Experimental observations

Analysis of replicas taken during tests revealed the following features concerning the pitting process:

- (1) Under cyclic stress conditions the inclusion-matrix interfaces dissolved to varying extents, and inclusions gradually isolated from the matrix.
- (2) Generation of each pit was enhanced by the application of cyclic stress, therefore the incipient cracks also initiated at these pits;
- (3) Dissolution occurred at inclusions, inclusion-matrix interfaces and in the adjacent matrix leading to the nucleation and coalescence of micro pits. The linking up of micro pits resulted in the formation of incipient cracks in the plane of maximum shear stress.
- (4) The incipient cracks tended to initiate more rapidly under high stress levels than under low stress levels.
- (5) Pits already formed appeared to prevent further pitting in the surrounding areas having less effective inclusions. This phenomenon has also been reported by Hoar et al [3].
- (6) Initially corrosion products piled up surrounding the pit, see Figure 4.5(a). In this figure the dark point in the centre is the pit and the grey circle is corrosion products. It was observed that cracks initiated from within the area, either from the dark point or from somewhere adjacent this point, see Figure 4.5(a). The size of this corroded area was also observed to be decisive for the final stage I crack length. The crack transition occurred at the boundary of this area, see Figure 4.5(d).

It has also been observed that the size of the isolated pit, and the associated corroded area, was equal to one or two grain sizes. The final stage I crack developed from the isolated pit was found to have a length of one or two grain diameters. However where several micropits linked up, the final stage I crack length was much longer than that generated from an isolated pit.

Pitting mechanisms

A search of the literature does not provide a definitive answer to the question of which defect occurs first, i.e. a pit or a crack. In the present work some short cracks were found not to be associated with pits and some pits did not give rise to crack development. However the majority of cracks were observed to be associated with and develop from pits.

In practice the surface of every piece of metal or alloy has physical and chemical inhomogeneities that are more susceptible to attack in an aggressive environment when compared with the surrounding matrix. It is generally acknowledged that this increasing susceptibility is related to local imperfections of the surface passive film. It can be anticipated that inhomogeneities in the chemical composition of a surface will affect the protective properties of passive films more strongly than will a physical defect, particularly for a mechanically well-prepared (i.e. ground) surface. However conjoint chemical and physical process are also very important.

In an aggressive environment, chloride ions agglomerate at sulphide inclusions, this probably being associated with iron cation permeation of the defective oxide film. The subsequent chloride salt layer which forms at sites on the surface of film undergoes hydrolysis and produces an acidic environment that attacks both the inclusion itself and the surrounding metal. Consequently crevices between inclusion and matrix may form during the initial corrosion stage. The H_2S produced during dissolution of sulphide inclusions accelerates corrosion and prevents repassivation of pits.

Pit development

The following locations are thought mainly to be responsible for inducing the formation of weak spots in the passive film [2]:

- (a) Interfaces between the matrix and non-metallic inclusions where differences in coefficients of thermal expansion exist (e.g. MnS in a martensitic matrix);
- (b) Grain boundaries and triple points which can give rise to micro-stress concentrations;
- (c) Surface machining/polishing marks or notches.

All these effects, separately or in combination can, once the passive film is ruptured, lead to the formation of an electrochemical cell. Under cyclic shear stress conditions and in an 0.6M NaCl solution, as used in the present tests, pits developed quickly at Mn-rich sulphide inclusions.

Although pit nucleation often depends on the distribution of inclusions, in some cases pits are not formed at inclusions emerging on the steel surface. Depending on their geometry and chemical composition, certain inclusions are more efficient in nucleating pits than others [2].

For specimen TC5 at a stress range of 728 MPa, defects development during corrosion fatigue are illustrated in Figure 4.5(a) which clearly shows pit formation after 4320 cycles ($N/N_f=0.025$). The sizes of the pits are 15 μm (pit 1) and 11 μm (pit 2) respectively. It was observed that pits took the shape of a circle.

The role of the applied stress

As the applied shear stress range was increased, the number of pits observed also increased. Consequently the number of cracks which developed increased and multiple crack coalescence occurred extensively in both the stage I and stage II regimes, see Figure 4.6 (a-e). It would appear that the density of pits which nucleate increases with increasing applied shear stress level because the passive film is broken more easily and frequently creating weak spots in the film.

In contrast as the shear stress level decreased the number of cracks decreased, and the average crack-to-crack distance increased due to decreasing crack density. As a result, the frequency of crack coalescence reduced, see Table 4.3.

From Table 4.3 it can be seen that the general trend in the number of cracks contributing to the formation of a dominant crack was also reduced as the applied shear stress decreased. For example when the applied shear stress range was 415 MPa the major crack developed from an individual crack, whilst those dominant cracks developed in other specimens, subjected to high stress ranges, were found to be the result of multiple crack coalescence.

Pit growth rate

Pit growth rates obtained during corrosion fatigue tests have been calculated based on information recorded from replicas taken during experiments. It was found that the diameter of the major pit, which developed to form the major crack, increased in proportion with time (t) to the power of $1/3$. By assuming a hemispherical pit shape and a constant dissolution rate the corrosion pit growth law can be formulated:

$$2r - 2r_0 = B(t - t_0)^{1/3} \quad (4.2)$$

where $2r$ is the pit diameter, $2r_0$ is the initial defect size from which the pit develops e.g. an inclusion, and B is a constant which relates to the dissolution rate and is also a function of stress level (details in Chapter 5, section 5.2), while t_0 is the major pit initiation time and t is the time for the major pit to grow. Figure 4.7 (a), (b) and (c) shows the prediction of pit growth as a function of time using Equation (4.2), in comparison with the observation for specimens TC5, TC18 and TC13 respectively.

4.1.3 Stage I crack initiation

The dominant crack or other major cracks are likely to initiate during the very early stages of corrosion fatigue under a high stress level, however it is fairly difficult to distinguish between a microcrack from the pit perimeter or from an inclusion due to corrosion products covering the site of crack initiation. For the present study, a surface replica technique, optical microscopy and SEM analysis were used for the determination of the initiation and growth of pits and microcracks. Analysis of replicas taken at regular intervals during tests allowed a backtracking from the final fracture through the crack development stage to the initial pitting stage.

Those surface defects, such as non-metallic inclusions, polishing scratches and pits which maintained their originally shape and size up to specimen fracture were not defined as cracks. It should be noted that the defects described above were different from non-propagating cracks growing in the stage I regime.

During experiments localised pitting was observed to develop quickly after the specimen was immersed in the NaCl solution regardless of the surface location. Most microcracks initiated from pit roots; however, some microcracks were found to initiate and grow within the matrix and were not associated with a pitting event.

For example, observation of pitting behaviour showed there were three possible processes operative during cyclic loading:

- (a) conventional hemispherical pit development.
- (b) micro-pits development which then expanded adjacent to the original pit site showing no signs of in depth growth.
- (c) pit growth development and arrest.

It was noted that as stress levels decreased (c) in the above became more common.

Since pit acts as a small surface notch it is much more likely that a microcrack will initiate at the pit/matrix interface. Figure 4.5(b) shows microcracking from a pit after 13000 cycles ($N/N_f=0.075$). In this case, the length of the microcrack, $25\mu\text{m}$, was less than the average prior austenite grain size (i.e. $30\mu\text{m}$). In addition another microcrack adjacent to the one of interest was observed; however this did not initiate from a pit but from within the matrix. These microcracks were observed to coalesce at a later stage (see crack 2 in Figure 4.5(c), $N/N_f=0.17$). Figure 4.5(c) presents a clearer picture of stage I crack propagation along the maximum shear stress plane, which is the main identifying character of stage I short crack growth path. After the coalescence event of these microcracks (at $N = 30000$ cycles ($N/N_f = 0.17$)), the crack lengths at this stage were $2c_1 = 77\mu\text{m}$, $2c_2 = 93\mu\text{m}$ and $2c_3 = 57\mu\text{m}$ respectively.

4.1.4 Stage I crack propagation

During stage I short crack propagation material microstructure plays an important role and crack growth behaviour will be influenced by neighbouring grains with unfavourable orientations (termed as barriers). On approaching these barriers the crack growth rate may decrease or arrest. The length of a decelerating crack when approaching a barrier depends upon the applied stress level, environment, barrier strength and the influence of adjacent cracks which may or may not contribute to crack coalescence.

To understand this behaviour it is helpful to examine the crack growth process in the form of graphs of crack growth rate against crack length. Typical crack growth behaviour at four different stress levels is shown in Figures 4.8 (a-d). In Figures 4.8 (b), (c), and (d), at stress ranges of 728 MPa and below, individual stage I cracks show marked decelerations in growth below $100\mu\text{m}$, in many cases being around $30\mu\text{m}$ and $60\mu\text{m}$, i.e. one and two prior austenite grain diameters.

When several microcracks were aligned on a plane, and the distance between the tips of the microcracks was within one or two prior austenite grain diameters, the microcracks would coalesce into a single large stage I crack. This is an important phase in the crack growth behaviour and will be discussed in more detail in the next section. In Figure 4.5(b), microcrack 2 and the adjacent microcrack coalesced into a longer crack (crack 2 in Figure 4.5 (c)) and consequently resulted in a crack of length 93 μm , which was longer than the average stage I-stage II transition length of 70 μm .

When the stress range (i.e. 926 MPa) was around that of the in-air fatigue limit stress (i.e. 915 MPa [42]), the first deceleration in crack growth was observed at a surface crack length of approximately 300 μm , see Figure 4.8(a).

4.1.5 Stage I crack coalescence

Stage I microcracks were observed to grow independently (see Figure 4.5(c)), and eventually form stage II cracks. However, crack coalescence could occur in one of two ways, i.e. stage I coalescence, see Figure 4.5(b); and stage II coalescence, see Figure 4.5(f). As the crack growth behaviour is quite different in these two stages, it is appropriate to describe the coalescence phenomena for these two categories: (a) stage I or *short crack coalescence*, and (b) stage II, or *long crack coalescence*.

Stage I coalescence occurs during shear crack growth when microstructural features and grain size are important. Coalescence during this stage is almost exclusively coplanar. The following points were observed during the experiments:

1. Corrosion-induced pits developed into microcracks;
2. Microcracks coalesced one by one when the effective distance between two cracks was less than about 1 or 2 grain diameters. The critical coalescence distance depended upon the applied load, i.e. the higher the stress, the higher was the density of microcracks, and thus the higher was the probability of coalescence;

3. Stage I cracks with a tip-to-tip distance greater than 2 to 3 grain diameters proceeded through a stage II transition in preference to stage I coalescence, see Figure 4.5(d). Often such cracks then coalesced during stage II growth, see Figure 4.5(f).

Stage II crack coalescence is discussed in the section 4.1.8.

4.1.6 Stage I-Stage II crack transition

The final stage I crack length, measured at the stage I-stage II crack transition point, is shown in Figure 4.9. From this figure it can be seen that the higher the shear stress range the longer is the average final stage I crack length at the transition. Most of the final stage I crack lengths were found to be within 2 to 3 prior austenite grain diameters, although occasionally some of them were observed to be larger than 4 to 10 grain diameters. Further investigation of the larger stage I cracks revealed that they consisted of 2 or more microcracks, each one of which initiated from an individual pit. Therefore it may be suggested that the average length of final stage I microcrack initiated from a single pit is equal to two average prior austenite grain diameters.

Distinction of two transitions

It should be noted that the stage I to stage II crack transition has different physical meaning from the transition of microstructure-sensitive to microstructure-insensitive crack growth. The former concept is introduced so as to conveniently distinguish the shear-dominated crack growth from the tensile-dominated crack growth, while the later is defined as the instant when the plastic zone size in front of crack tip is equal to or larger than one grain diameter, i.e. prior austenite grain size for the present study, so that the influence of the microstructure diminishes and the crack growth becomes independent of the microstructure.

It has been reported that for most metallic materials in an inert environment the fatigue crack growth will become independent of microstructural features after the crack has propagated a distance of approximately 10 grain diameters [4]. However studies concerning the microstructure-dependent to microstructure-independent transition during corrosion fatigue crack growth has been lacking and to date relevant literature is limited [5].

In regard to the fatigue life N_f , the proportion of cycles needed for the major cracks to transform from stage I to stage II appears to be dependent upon the applied load level. As shown in Figure 4.10, this transition point ranges from 20% to 60% of the total fatigue life time.

Mechanisms for stage I growth

For most loading conditions, the stress attained is a maximum at the surface. Furthermore cyclic stress produces a slip-band groove which deepens with continued cycling eventually forming a crevice or intrusion. Cracks may then form on the slip plane most closely aligned with the maximum shear stress direction. The cracks may extend crystallographically across many grains, with a tilting of the fracture path as the cracks cross a boundary from one grain to its neighbour. This produces a faceted texture with the general fracture plane being coincident with the maximum shear stress plane.

In an aggressive environment this faceted texture may be destroyed by corrosion effects, i.e. dissolution. Stage I crack growth is governed by the local shear stresses and the freedom for movement of dislocations, which in turn depends upon the stress level and the environment. Because the effect of corrosion might be to free dislocation movement process, probably by film removal or by the dissolution of crack-tip material containing dislocation obstacles such as locked dislocation groups.

Stage I crack growth can persist for an appreciable proportion of the fatigue lifetime. Whether this proportion is small or large, depends upon whether crack growth is microstructure-dependent or microstructure-independent. This stage of shear dominant crack growth should be designated as stage I fatigue crack growth because it differs in an essential manner from the stage II fatigue crack growth behaviour. For example [6] under fully reversed torsion fatigue testing in air of the same high strength steel, the fatal crack path was observed to be in the direction parallel to the specimen axis (the maximum shear stress plane) throughout, although the whole process of fatigue crack growth was sequentially divided into microstructure short crack, physical short crack and long crack.

Final stage I crack length

The final stage I crack length depends upon loading mode, applied stress level, microstructural texture, and the environment. For the present case, frequency effects, cathodic polarisation effects, and the effect of applied shear stress range on the final stage I crack length were investigated. Figure 4.9 and Table 4.4 illustrate stage I crack length measured at stage I-stage II transition point under different stress ranges. The results suggest that the higher the applied shear stress range the longer will be the final stage I crack length. The maximum final stage I crack length is $100 \mu\text{m}$, for the stress range of 926 MPa, whilst the minimum is about 15 μm for the stress range of 224 MPa. Surprisingly, the final stage I crack length increases to 58 μm for the lower stress range of 224 MPa, probably due to the prolonged dissolution process in the corrosive environment. Figure 4.11 (a) and (b), and Table 4.5 show the results of the final stage I crack length for various frequencies under two stress ranges, i.e. 400 MPa and 600 MPa. The frequencies ranged from 2Hz to 12.5Hz. Figure 4.11 (a) shows that there is no significant frequency effect on the final stage I crack length at the stress range of approximately 400 MPa, but Figure 4.11(b) illustrates a slightly longer final stage I crack length at a frequency of 12.5Hz and at a stress range of approximately 600 MPa, probably due to the effects of a multiple crack coalescence in stage I.

When specimens were cathodically polarised there appeared to be a significant effect on the final stage I crack length, as illustrated in Figure 4.12 and Table 4.6. Under approximately the same stress range, $\Delta\tau=750$ MPa, there was a big difference in the final stage I crack length for the two specimens, C2 and C4, the former being charged at -1280 mv(SCE) cathodic polarisation and the later under free corrosion potential condition. For specimen C2 the final stage I crack length was found to be over $400\mu\text{m}$, while for specimen C4 the major final stage I crack length was just around $60\mu\text{m}$.

A statistics analysis was employed for the final stage-I crack length using a Weibull distribution function, as given in Equation (4.3):

$$F(x) = \begin{cases} \frac{m}{x_0} (x - v)^{m-1} e^{-(x-v)^m/x_0} & x > v \\ 0 & x \leq v \end{cases} \quad (4.3)$$

where $v=0$ for the present case, m and x_0 are parameters calculated from the present data (final stage I crack length) for various stress levels, different frequencies and different environment conditions. The results are listed in Table 4.7 and illustrated in Figure 4.13(a), (b), (c) and (d). The results demonstrate that the final stage I crack length increases with increasing shear stress range (Figure 4.13(a)), and increases with cathodic polarisation (Figure 4.13 (d)). There is no significant effect of frequency (in ranges from 2Hz to 12.5Hz) on final stage I crack length at a stress range of approximately 400 MPa, see Figure 4.13 (b).

The role of applied stress

At high applied shear stress ranges, i.e. 926 MPa, the tensile stress on the stage I crack plane is large (Figure 4.14(a) illustrates the stress system operative on the surface of the hour-glass specimen), therefore stage II crack growth occurs relatively early in the lifetime i.e. $N_t/N_f < 0.2$. However, at lower applied shear stress ranges, i.e. 415 MPa, the tensile stress on the stage I crack plane is relatively low, and a large number of fatigue cycles is

required for the stage I/II transition to occur i.e. $N_t / N_f > 0.54$. As the crack grows into the matrix an increase in stress concentration arises due to the increasing crack depth, associated with triaxial stress state, and the increase in ratio of tensile to shear stress at the crack root.

Aspect ratio plays an important role in the crack transition stage. For a given stress level a shorter, deeper stage I crack would give way more easily to stage II crack growth. In contrast, a longer and shallower stage I crack experiences greater resistance and as such a crack propagating under a low applied stress will take much longer time to develop sufficient stress concentration to cause the stage I/II transition. For example, for the stress range of 415 MPa, a stage I crack which initiated at an early stage having a surface length of 200 μm , did not transform from stage I growth to stage II growth until the specimen failed. Conversely, in the same specimen, another stage I crack started the stage I/II transition at its length of 58 μm , and eventually propagated in stage II.

The transition from stage I to stage II was not necessarily sudden. Stage I crack growth sometimes decreased in a gradual manner because of the crack experiencing the tensile fatigue resistance and transforming from a two dimension configuration to a three dimension one.

Locations for the transition.

It has been observed that stage II cracking can occur at different positions on stage I crack plane appearing to depend upon the combination of the stress and environment conditions. Most stage II cracking was seen to start from the two tips of the stage I surface crack which was blocked by the grain boundary along the shear stress plane.

For fully reversed torsion the maximum tensile stress plane is at an angle of 45° or 135° to the torsional specimen axis, hence stage I crack plane is subjected to mixed mode

loading, see Figure 4.14 (a). If the grain boundary in front of the crack tip is at 45° or 135° to the specimen axis, i.e. coincident with the maximum tensile stress plane, the stage I crack tip will deviate to the normal stress plane immediately, see Figure 4.14 (b). However in the absence of a favourable 45° or 135° boundary there appears a gradual tilt of the crack path, perpendicular to the maximum tensile stress plane, and crack growth is assisted by corrosion, that is, preferential dissolution at the grain boundary. Eventually, after spanning one or two grain diameters, the stage II crack propagated rapidly along a very straight line at the direction of 45° and 135° to the torsional specimen axis.

Some stage II cracks were found to occur in the root of the crack, see Figure 4.15(a), when the surface crack length was less than one or two grain diameters or at a grain boundary intersecting the stage I surface crack plane at an angle of 45° or 135° rather than at the two ends of stage I crack.

Stage II crack initiation sites exist at the maximum curvature of the stage-I crack plane, or at a grain boundary on the inner surface of the stage I crack plane resulting from the combined effects of stress and chemical and physical inhomogeneities. When stage I in-depth crack growth has propagated to the first or second grain boundary crack growth may be arrested by those microstructural barrier, see Figure 4.14 (c). Locations A and B were found to be favourable sites for stage II cracking for crack growth along the grain boundary AA and BB, see Figure 4.14(c), which lay perpendicular to the maximum tensile stress. From micrographs of failed specimens, see Figures 4.15(a) and (b), it was observed that stage II cracking started immediately from the bottom of the stage I crack plane rather than from the two tips of the stage I crack.

Dissolution around grain boundaries both on the surface and subsurface along the crack plane was found to occur. Such localised attack on the surface crack or at the root of the crack tended to alter the geometry of the stage I crack growth allowing premature transition from the stage I crack to stage II crack.

Summary remarks

1. Stage I crack growth is governed by the local shear stress and the freedom for movement of the dislocations.
2. Tensile stress is the major driving force for stage II crack growth.
3. Final stage I crack length measured at stage I-stage II crack transition point varies from approximately 15 μm to 500 μm under different stress ranges and different environments. The higher the applied shear stress range, the longer is the final stage I crack length, and the fewer is the number of loading cycles for the transition from stage I to stage II cracking.
4. The transition from stage I cracking to stage II cracking can occur at either the two tips of the surface stage I crack, the root of stage I crack, or the inner surface of the stage I crack plane depending upon the microstructure of the material surrounding the crack plane, the environment, the position of the maximum triaxial tension stress and the stress concentration at the crack tip.
5. Dissolution around grain boundary assists the stage I-stage II crack transition. If the dissolution process is inhibited by the cathodic polarisation e.g. $E = -1280 \text{ mV(SCE)}$ for the present test, the stage I crack can grow a distance of as far as ten surface grain diameters before the transition.
6. Frequency in the ranges from 2Hz to 12.5Hz appears to have little effect on the final stage I crack length at a stress range of approximately 400 MPa.

4.1.7 Stage II crack propagation

Conditions for stage II cracking

After the transition from stage I growth to stage II growth, the crack grows rapidly along a very straight line perpendicular to the maximum tensile stress, see Figure 4.15 (a), indicating a decreasing effect of microstructure and increasing importance of tensile stress

which dominates crack growth until final fracture. The conditions for stage II cracking are as following:

1. periodic high stress cycling;
2. notched condition;
3. obstacles at the crack tip blocking the gliding movement of dislocations along the original crack plane;
4. crack growth into the depth of the specimen where triaxiality increases.

The role of tensile stress in the stage I/II transition

When the stage I crack reaches a grain boundary or other microstructural barrier, which blocks the dislocation movement in front of the crack tip region, stage II cracking will occur if the stress state conditions favour a duplex slip for a particular material and environment. The stage II crack growth is along a plane perpendicular to the maximum tensile stress. The criterion for stage II growth is that of the value of the maximum principal tensile stress operating in the specimen in the region of the crack tip, reflecting the fact that the value of the ratio of tensile to shear stress increases with increasing crack depth where conditions of constraint exist and triaxiality increases. The peak tensile stress developed across the crack tip causes a deviation of the crack from its primary slip path which suggests that there is a minimum peak tension stress necessary for stage II growth.

The cleavage component

The important difference of stage II cracking from stage I cracking is the presence of the cleavage component, which alters and governs the crack path, especially for the high strength steels. SEM fractography of the stage II crack path shown in Figure 4.16 indicates clearly the cleavage-like fracture features (low-ductility boundary separation).

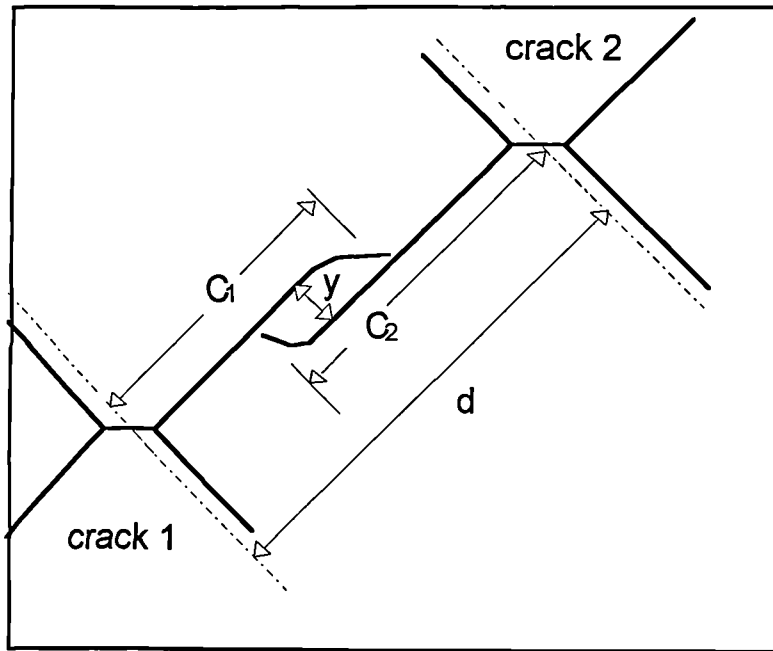
4.1.8 Stage II crack coalescence

Stage II crack coalescence occurs during mode I crack growth. From the present tests, over 80% of specimens failed due to the coalescence of two or more cracks during the final stage of loading, see Figure 4.17 (a) and (b). The distance between two cracks and the relative position of the cracks will dominate the coalescence process where microstructure becomes less important.

Coalescence of parallel cracks

Stage II cracks are observed to grow in a straight line perpendicular to the maximum tensile stress showing little change in their direction during growth. As a result of multiple crack initiation and growth it is inevitable that two coplanar stage II cracks will approach each other with the possibility of coalescence. For off-plane, parallel cracks two possibilities may develop: (i) the two cracks propagate beyond each other, *overlap* to some extent, see Figure 4.17(c), then turn their way to *run into each other*; (ii) in other cases cracks may remain along their original propagation direction and fail to coalesce up to the failure of the specimen. The question which arises from this observation is: what is the critical condition for two parallel cracks to coalesce?

Based on experimental data a straight forward empirical formula was derived to predict crack coalescence.



Schematic view of stage II cracks coalescence, case (i)

Suppose d is the distance between two crack origins, c_1 and c_2 are the crack lengths respectively, y is the vertical distance between two cracks, then $s = c_1 + c_2 - d$ represents the *overlapping* distance. Defining the parameter α as,

$$\tan \alpha = \frac{y}{c_1 + c_2 - d} = \frac{y}{s} \quad (4.4)$$

the following conclusion can be drawn:

$\tan \alpha < 0.4$ or $\alpha < 22^\circ$,	full coalescence
$0.4 < \tan \alpha < 0.6$ or $22^\circ < \alpha < 31^\circ$,	crack move towards each other but do not coalesce
$\tan \alpha > 0.6$ or $\alpha > 31^\circ$,	no coalescence

The physical meaning of α can be understood based on the following:

A single stage II crack will advance along its original direction, this direction being perpendicular to the maximum tensile stress and is associated with the maximum

hydrostatic stress state and volume increase, which is the most favoured site for hydrogen embrittlement and corrosion assisted micro-fracture process. However two closely located cracks tend to attract each other in order to coalesce so that the time for final separation of the specimen is shortened. What appears to happen for two adjacent cracks is a competition between the above two tendencies: *the corrosion process and the crack attraction*. A compromise then turns out to be:

when $\alpha < 22^\circ$, the cracks are close enough and the attraction between them prevails, therefore crack coalescence occurs; when $\alpha > 31^\circ$, corrosion assisted cracking overwhelms the attraction between two cracks, and there is no crack coalescence; when $22^\circ < \alpha < 31^\circ$, the situation lies between the above two cases: cracks move towards each other but do not coalesce.

A detailed study of parallel crack coalescence under the loading condition ($\Delta\tau=728$ MPa) is shown in Table 4.8. Here column 6 indicates the actual coalescence parameter ($\tan\alpha$), measured from experiments, which confirms the proposed coalescence criterion.

Coalescence of perpendicular cracks

Another situation for stage II coalescence is the coalescence of perpendicular cracks. This is shown in Figure 4.17 (d). The condition for the coalescence in this case is simply described by the following expression:

$$\begin{aligned} c_2 \geq d, & \quad \text{crack coalescence;} \\ c_2 < d, & \quad \text{no coalescence;} \end{aligned}$$

In this case, crack c_2 is blocked by crack c_1 .

4.1.9 Crack aspect ratio λ

Cracks propagate both on the surface and in the depth of the specimen. Table 4.9 indicates the crack profile aspect ratio, $\lambda = a / c$, where c is the half crack surface length and a is the

crack depth. The depth of stage I microcracks was measured from the change of focus length of microscope on the surface of the specimen used in test. In addition the depth of cracks at the transition stage was measured from SEM photographs (see Figure 4.18 (b)), and the depth of stage II cracks was obtained by post-examining of *shell marks* on the fracture surface of failure specimen from SEM fractography (Figure 4.18(a)), and optical fractography as well (Figure 4.19(a), (b) and (c)).

General trend

Initially λ , the ratio of crack depth to crack length, is very small during stage I microcrack growth, see Table 4.9, because the depth of the microcrack is very small. Towards the end of the stage I microcrack propagation stage, the crack depth is $a = 20\mu\text{m}$ (for specimen TC5) in this case (see Table 4.9), being less than the average prior austenite grain size ($30\mu\text{m}$). In other words, when the crack depth reaches the boundary of one grain, a crack may transform from stage I to stage II. At this stage the value of λ is greater than 0.6, and the crack profile has developed towards that of a semi-ellipse since surface crack propagation decreases at the expense of in-depth growth. The establishment of a macroscopic stress concentration field at the now wider crack tip assists the development of a stage II crack with the crack plane perpendicular to the maximum tensile stress at an angle of 45° or 135° to the torsional specimen axis. After the transition from stage I to stage II, the crack aspect ratio λ decreases again, indicating that a maximum in λ is reached at the point of the stage I/II transition, see Figure 4.20.

At a low applied load ($\Delta\tau=415\text{ MPa}$), it was found that a stage I crack of length $2c=200\mu\text{m}$ was present which did not change to a stage II crack, while other shorter microcrack ($2c=60\mu\text{m}$) had passed the transition state and propagated in the mode I plane. This phenomenon merits some explanation and may be understood in terms of the crack tip stress concentration. For a given crack depth (a), a longer surface crack ($2c$), which in turn implies a smaller value of aspect ratio λ , will have a larger curvature radius (ρ)

resulting in a lower stress concentration ($K_t \propto \sqrt{a/\rho}$) [7] which is not sufficient to overcome the resistance of the microstructural barrier thereby leading to the transition and stage II crack propagation. In addition the greater the length of the stage I crack, the greater is the crack face area. Under mode III loading such faces are under intimate contact, and the through-mismatch of the two crack faces may induce some closure effect.

The increase in aspect ratio λ will lead to a higher stress concentration and a larger stress gradient ahead of the crack tip and therefore provide a greater driving force for the transport of hydrogen into the region of maximum triaxiality. It can be thought of in terms of an enhanced environmental influence arising from an increase in hydrostatic tension, which becomes more important for stresses below the in-air fatigue limit.

Experimental observations

Specimen TC12, under a reversed shear stress range of 733 MPa in a 0.6M NaCl solution at pH value of 6, was taken out of the fatigue test apparatus after 35000 cycles ($0.2N_f$, before the transition of a crack from stage I to stage II). The configuration of the randomly distributed cracks in stage I was observed and measured directly under the optical microscope. The results are shown in Table 4.9.

The profile of cracks in the final stage was obtained by post-examining the *shell marks* on the fracture surface. The results of specimens FC2, TC13, and FC4 subjected to fully reversed torsion at applied shear stresses of 616, 415, and 400 MPa respectively are presented in Table 4.10.

Shown in Table 4.11 is the depth of cracks at transition from stage I to stage II for different stress ranges. For specimens under the shear stress ranges at 728, 750, 742, 400 and 599 MPa, the crack depth was found to be in the range of 17 to 53 μm . These values are less than two average prior austenite grain diameters. Along the in-depth crack growth

path the transition position from shear mode to tensile mode of crack growth was also at the first or second prior austenite grain boundary for the stress ranges from 400 to 750MPa.

These results may explain the variation of the final stage I crack length on the surface at different applied shear stress ranges. The higher the applied shear stress range, the longer is the average final stage I crack length on the surface, while the stage I crack in depth is approximately the same.

Mechanistic views

A number of mechanisms which are noted below are thought to play a possible role in the aspect ratio development.

1. Under higher applied shear stress ranges, the dislocation movement can overcome the first, second or subsequent grain boundaries along the primary slip system, and the stage I crack propagates a relatively long distance on the surface due to the free-surface effect until the dislocation movement is blocked at the next grain with an unfavourable slip orientation.
2. Under reversed torsion tests, the shear stress reaches its maximum on the surface at the minimum section of the hour-glass specimen, while the minimum shear stress occurs in the centre line of the specimen axis. As the shear stress distribution is a function of the radius of the specimen, $\Delta\tau \propto 1/r^3$, the shear stress will become smaller with a steep gradient when travelling from the surface into the matrix. The incipient crack will therefore grow more rapidly on the surface than in the depth and the crack will therefore not assume a semi-circle shape. The higher the applied shear stress, the longer will be the surface crack length in stage I, whilst the crack length in depth in stage I is not necessarily in proportion to its dimension along the surface.

Crack profile development

For very small stage I cracks, observed on the surface of specimen TC12, a/c is found to be 0.2 to 0.4. It was assumed that initiation of the crack, either by the fracture of stringers of non-metallic inclusions or by pit-induced microcracking, generates relatively long, shallow cracks, with depth and surface dimensions being in the ranges of 4 μm deep/35 μm long, 8 μm /81 μm , and 10 μm /85 μm , see Table 4.9.

It is instructive to note that for crack 14 on specimen TC5 subjected to approximately the same stress range as that for specimen TC12, the maximum value of a/c was measured and found to be 0.828 ($2c = 48 \mu\text{m}$, $a = 20 \mu\text{m}$) at the transition from stage I to stage II. This high value of aspect ratio was understood to play a major role in raising the tensile stress in front of the crack tip which in effect caused the crack to change its propagation direction to that perpendicular to the maximum tensile stress. After the crack had grown through a few more grains in the direction perpendicular to the maximum tensile stress, having a surface length $2c = 237 \mu\text{m}$, the crack profile had developed towards that of a semi-ellipse, with aspect ratio being 0.627.

After the failure of specimens TC13, FC2, and FC4, *shell marks* of the major crack remaining on the fracture surface were measured. The details of these *shell marks* are shown in Table 4.10 and Figure 4.19(a), (b) and (c). From the study of these *shell marks* the final stage II cracks aspect ratio, λ , was obtained and found to be in the range of 0.645 to 0.787 for stress ranges from 400 MPa to 616 MPa.

From Figure 4.19 (b), it can be seen that major crack front lines consisted of a semi-elliptical configuration having an aspect ratio λ in excess of 0.6. The relationship between crack aspect ratio, λ , and crack size, \sqrt{ac} , is shown in Figure 4.20 from experimental measurement. Cox and Morris [8] used a Monte Carlo simulation to model the growth of

small fatigue cracks through stochastic microstructures. Their curve, illustrated in Figure 4.21, shows good agreement with the results from the present study shown in Figure 4.20.

In addition the final surface crack lengths measured before fast fracture, have been tabulated in Table 4.10. At the point of instability of specimen fracture, the major crack depth was between 4.98 to 6.20 mm, while the surface length was between 15.43 to 16.99 mm. Therefore it could be established that when the surface length of the major crack reached 15 mm, the specimen failed. This critical crack length can be used as an alternative failure criterion for the present study.

The critical crack length for a given material is the length the crack attained by the last cycle causing complete failure. It varies considerably with different materials. Generally harder materials, particularly those with high proof stress/tensile stress ratio, have shorter critical crack lengths, whilst those materials with capacity for plastic deformation have longer critical crack lengths.

4.1.10 pH value in the crack tip

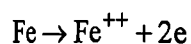
The approximate pH value of the solution within the crack tip at final stage of crack growth for specimen TC11, was measured by freezing the fatigue specimen in liquid nitrogen followed by pressing pH indicator papers onto the fractured surface of the specimen. The bulk solution used for corrosion fatigue was 0.6M NaCl solution with pH=6. The pH value of the liquid at the crack tip was found to be approximately 3 to 4, whilst that along the crack growth path between the tip region and the outer surface was approximately 5, and that near the surface area was approximately 12.

From their experiments Ray *et al* [9] found that after rotating a specimen without stress for 1300000 reversals the pH value of the liquid at the mouth of the crevices or micro pits was approximately 4.5 on the external surface of the specimens of a mild steel, whilst after

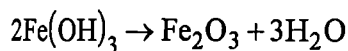
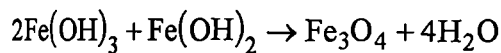
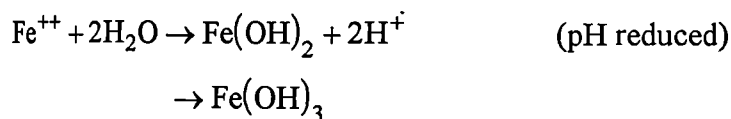
34000 reversals under rotating bending corrosion fatigue at 192 MPa with R=-1, the corresponding pH value was between 3 and 3.5. The application of cyclic stress appeared to enhance the dissolution and hydrolysis of the metal within the crevices and micropits during the early stage of fatigue. Based on the present test result, it can be suggested that the cyclic stress contributes to lower the pH values during the whole process of corrosion fatigue.

Observation of pH values as low as 3 to 4 implies some contribution from the hydrolysis of Fe³⁺ ions which are much more strongly hydrolysed than Fe²⁺ ions. This would be expected near the mouth of crevices or cracks where dissolved oxygen from the bulk solution can oxidise Fe²⁺ to Fe³⁺ ions.

Primary anodic reaction



Secondary anodic reaction



Cathodic reaction



At the root of a pit or at the tip of a crack, the oxygen concentration is expected to be low; hence the production of a low pH condition will be due to the hydrolysis of Fe²⁺ ions, which is likely to produce a pH below 4 [10].

Comparison with other published work

The reduction in pH indicates some contribution of stress-enhanced metal dissolution to create acidic conditions within the crack. Consequently, the hydrogen content at the crack

tip is also increased. The stress gradient ahead of the crack tip then drives absorbed hydrogen atoms into the lattice where they accumulate in the region of highest dilatation, affecting the mobility of dislocations within the immediate surroundings [11].

Acidification of solutions contained within pits and crevices is generally explained by the hydrolysis of salts produced by anodic dissolution of the metal or alloy [12]. In addition to the effect of hydrolysis, Suzuki *et al* [13] considered the formation of hydrochloric-complexes of cations of the dissolved metal to be a process leading to a decrease in pH. Rhodes [14] and Suzuki [13] considered the effect of high Cl^- concentration on the increase of hydrogen ion activity. It is known that hydrogen ion activity in unbuffered solutions such as hydrochloric acid significantly increases when chloride is added.

4.2 Frequency effect

Review of frequency effect

Probably the most widely documented effect in corrosion fatigue studies is the effect of test frequency. This is not surprising as corrosion is a time dependent process. For most steels the general effect of frequency is to increase the crack growth rate as cyclic frequency decreases. For medium-strength steels, a maximum enhancement is observed near 0.01 Hz [15]. For ultra-high strength steels, there appears to be no lower frequency limit where hydrogen effects become increasingly severe. There is general agreement that at frequencies greater than 0.01 Hz, all steels show hydrogen-enhanced cracking tendencies in the stage II crack growth regime. This applies to either gaseous hydrogen or aqueous environments where the hydrogen evolution reaction is controlling [15].

To understand the frequency effect, it is of paramount importance to identify the rate-limiting step in the transport, chemical reaction and fracture sequence for corrosion fatigue

crack growth [16–19]. In addition, the effect of stress intensity factor must be considered. The frequency dependence may be specific to each of the three ΔK regimes.

ΔK_{th} and near-threshold regimes

Two unique kinds of frequency dependence were reported [20] for near-threshold corrosion fatigue crack propagation, notably, da/dN remains constant with increasing frequency, or alternately, da/dN increases with increasing frequency. No data appear to be available which show increasing near-threshold corrosion fatigue crack growth rates with decreasing frequencies.

Moderate ΔK "plateau" regime

For ΔK levels where the power-law dependence of da/dN approaches the plateau behaviour, sub- K_{ISCC} corrosion fatigue growth rates generally increase with decreasing frequency. A saturation crack growth rate is often observed for low frequencies, see Figure 4.22 [43].

Mass transport and reaction rate modelling gives some mechanistic explanation for frequency dependence on corrosion fatigue in aqueous environments [18, 21, 22]. Crack growth per cycle is assumed to be proportional to the amount of hydrogen generated at the crack tip by chemical or electrochemical reactions. The frequency dependence is determined by the slow, rate-limiting transport or reaction process, coupled with other fast steps in the corrosion fatigue sequence. This subject has been extensively investigated by Wei and co-workers [18]. For steels in aqueous chloride, hydrogen is produced by electrochemical reactions at the straining crack tip in amounts proportional to the total charge passed per cycle. Where electrochemical reactions on the clean crack surface is the rate limiting process, lower frequencies result in longer exposure time per cycle and therefore increased charge.

The film rupture model

Based on a sequence of passive film rupture at the crack tip, oxidation and progressive repassivation of exposed metal, and a rupture of the freshly formed film, models of environment fracture have been developed for cyclic loading by Ford and co-workers [23–26]. A brief discussion of different quantitative expressions for the effects of ΔK , frequency, metallurgical variables and environment chemistry is given below.

It has been proposed [23-26] that crack growth may be described in terms of a film rupture event, see Equation (4.5),

$$\left(\frac{da}{dN}\right)_{cf} = \frac{da}{dr} \frac{dr}{dN} = \frac{1}{f} \frac{da}{dt} \quad (4.5)$$

where da/dr is the crack advance per film rupture event plus a dissolution event and dr/dN is the number of rupture events per load cycle (N). Both da/dr and da/dt are related by Faraday's Law to the amount of charge (Q_f) that passes during metal dissolution between rupture events.

The time between rupture events (t_f) is given by the ratio of the film-fracture strain (ε_f) to crack tip strain rate $(d\varepsilon/dt)_c = \dot{\varepsilon}_c$; the crack-tip strain range ($\Delta\varepsilon_{CT}$) is given by the average crack-tip strain rate divided by loading frequency; and dr/dN is given by the crack-tip strain range to ε_f ratio. Combining these terms with Equation (4.5) leads to the following:

$$\left(\frac{da}{dN}\right)_{cf} = \frac{M}{\rho Z F} \left(\frac{\Delta\varepsilon_{CT}}{\varepsilon_f}\right) Q_f = \frac{1}{f} \left(\frac{M}{\rho Z F}\right) Q_f \left(\frac{\dot{\varepsilon}_c}{\varepsilon_f}\right) \quad (4.6)$$

where M and ρ are the atomic weight and density of the dissolving metal, Z is the number of electrons involved in oxidation, and F is Faraday's constant. The charge passed per rupture event is given by

$$Q_f = \int_0^{t_r = \epsilon_f / \dot{\epsilon}_c} i(t) dt \quad (4.7)$$

where $i(t)$ is the transient current associated with dissolution during reformation of the ruptured film. Hudak [27] determined $i(t)$ for a straining electrode in a simulated crack-tip solution; calculation of Q_f for substitution into Equation (4.6) yields the following:

$$\left(\frac{da}{dN} \right)_{cf} = \left(\frac{2Mi_0}{\rho ZF} \right) \frac{1}{f} \left(\frac{t_0}{\epsilon_f} \right)^{1/2} \dot{\epsilon}_c^{1/2} \quad (4.8)$$

where i_0 is the bare-surface current density at the instant of film rupture, and t_0 is the time for the initial decrease in the transient current decreasing according to the reciprocal square root of time between ruptures; more generally, current depends on time to the power of $-\beta$. Hudak determined the ΔK dependence of crack-tip strain rate for type 304 stainless steel; the total environmental crack growth rate was obtained by summing Equation (4.8) with an empirical result for inert environment mechanical fatigue:

$$\left(\frac{da}{dN} \right)_e = C(\Delta K - \Delta K_{th})^n + \left(\frac{2Mi_0}{\rho ZF} \right) \left(\frac{t_0 \epsilon_0}{\epsilon_f} \right)^{1/2} \Delta K \frac{1}{\sqrt{f}} \quad (4.9)$$

where C , and n are material constants from the inert environment fatigue law, and ϵ_0 is a constant from the measured $(d\epsilon / dt)_c - \Delta K$ relationship.

Ford and co-workers previously derived an analogous expression for $(da / dN)_e$:

$$\left(\frac{da}{dN} \right)_e = \left(\frac{da}{dN} \right)_m + \eta g(\beta) \Delta K^\gamma f^{\beta(\beta-1)} \quad (4.10)$$

here $g(\beta)$ is stated generally to describe environment chemistry and metallurgical effects on corrosion fatigue crack growth kinetic, γ and η are empirical parameters defined by the da/dN versus ΔK curve fitting, with γ equal to between 2 and 5.5, and η as a constant, while f is the loading frequency, β is an exponent, $\left(\frac{da}{dN} \right)_e$ is total environment crack growth rate, and $\left(\frac{da}{dN} \right)_m$ is the mechanical crack growth rate.

The film-rupture model predicts a variety of frequency effects on corrosion fatigue.

Hudak [27] recently demonstrated substantial differences in the predicted and measured frequency dependence of corrosion fatigue for type 304 stainless steel in high-temperature water and in NaCl solution. A dramatic underprediction of crack growth rates, by one to two orders of magnitude, is seen for ambient-temperature chloride, when Equation (4.10) was used based on the film rupture modelling. The poor agreement was ascribed to a dominant hydrogen embrittlement contribution to corrosion fatigue.

The Austen-Walker model [28–30]

Several crack growth models were proposed based on the assumption that $(da/dN)_e$ is determined by the extent of hydrogen diffusion (ΔX) within the plastic zone and during the time of a single loading cycle

$$\left(\frac{da}{dN}\right)_e = \frac{\Delta X}{\text{cycle}} = 4\sqrt{D_H t} = 4\sqrt{D_H / f} \quad (4.11)$$

with D_H being the diffusivity of hydrogen in steels, and t the time per load cycle. Physically, $(da/dN)_e$ is equated to the mechanical fatigue rate when the extent of hydrogen diffusion is less than one striation spacing. For diffusion distances that exceed the monotonic plastic-zone size ($r_p = (1/2\pi)(K/\sigma_{ys})^2$ for plain stress) $(da/dN)_e$ equals the maximum fatigue crack-tip opening displacement per cycle

$$\delta_{\max} = \frac{0.5\Delta K^2}{(1-R)^2(2\sigma_{ys})E} \quad (4.12)$$

For intermediate ΔX , corrosion fatigue crack growth rate is governed by the following equation:

$$\left(\frac{da}{dN}\right)_e = \frac{(\Delta X - S)}{(r_p - S)}(\delta_{\max} - S) \quad (4.13)$$

$$S = C\Delta K^m$$

with the striation spacing described by the standard Paris expression and C and m are material constants. The Austen-Walker model predicts ΔK dependent plateau crack growth rates as:

$$\left(\frac{da}{dN}\right)_e = 37.3 \frac{\sigma_{ys}}{E} \sqrt{D_H / f} \quad (4.14)$$

For corrosion fatigue, the effect of frequency on $(da/dN)_{cf}$ depends on alloy repassivation kinetics, particularly the β exponent in Equation (4.10); typically, β equals 1/2 and $(da/dN)_{cf}$ is predicted to increase with decreasing frequency.

Based on both film rupture model and hydrogen diffusion, a more general relationship would be that, $(da/dN)_{cf}$ is a power law function of $1/f$, giving as a first approximation:

$$\left(\frac{da}{dN}\right)_{cf} \propto \left(\frac{1}{f}\right)^n \quad (4.15)$$

Brown-Hobson model for short cracks

For the short crack growth regime, there is little data available on frequency effects on corrosion fatigue crack growth.

The Brown-Hobson model was used to rationalise short crack fatigue test results and to represent crack growth rate in the microstructurally sensitive crack, MSC, regime.

$$\frac{da}{dN} = C(d - a) \quad (a < d) \quad (4.16)$$

where d is the distance between the crack origin and the dominant microstructural barrier, a is the surface crack length and C is a constant dependent upon stress level, frequency and metal/environment system.

The relationship between the frequency and the coefficient C for stage I crack growth at a given stress level is proposed here to have the following form:

$$C = C_1 \left(\frac{1}{f} \right)^m \quad (4.17)$$

The stage I crack growth rate for the frequency dependence would take the form as shown in Equation (4.18),

$$\left(\frac{da}{dN} \right)_{cf} = C_1 \left(\frac{1}{f} \right)^m (d - a) \quad (4.18)$$

Experiments on frequency effect

In order to study the effect of frequency, the calibration of stress responses under varying frequencies, 2, 4.8, 5.2, 7.3, 10, and 12.5 Hz was carried out. For a given loading torque the corresponding stress range at frequency 5Hz was taken as the basic standard for comparison purposes; the deviation of stress ranges from the value obtained at 5Hz was recorded as a standard error due to the variation in frequency. It was found that for stress ranges from 400 MPa to 800 MPa the standard error at frequency 2Hz was approximately -2%, and at frequency 12.5 Hz was approximately 5.72%. The applied stress increased with increasing frequency for the torsion fatigue test machine used. Frequencies lower than 2Hz or higher than 12.5 Hz are difficult to attain due to limitations of the test equipment.

Torsion fatigue testing was conducted at frequencies of 2, 5 and 12.5 Hz respectively under different applied stresses. The experimental results, presented in Table 4.12 and Figure 4.23, show that a decrease in cycles to failure occurs with decreasing frequency.

Figure 4.24 (a), (c) and (b), (d) show the a-N and da/dN-a curves respectively for the dominant failure crack under the two stress ranges (approximately 400 MPa and

600MPa). At the lower stress level the fatigue lifetime is significantly reduced at a frequency of 2Hz (Figure 4.23). The slowing down of crack growth rate is due to the microstructural barriers which play an important role during the early stages of crack growth (Figure 4.24(b)). At higher stress levels, difference between a-N curves for 2Hz and the other two frequencies reduces (Figure 4.24(c)), indicating a slightly decreasing frequency effect on crack growth. However the general trend of lower frequency giving rise to shorter fatigue life remains the same. Figure 4.24(d) also shows that the barrier effect is reduced at higher stress level, especially at lower frequency.

When the Brown-Hobson model is applied to the present test results, the relationship between frequency and the coefficient C, for stage I crack growth at a stress range of approximately 400 MPa, can be obtained, see Figure 4.25. The regression analysis for this data is shown as follows:

$$C = 2.779 \times 10^{-5} \left(\frac{1}{f} \right)^{0.687} \quad (4.19)$$

Substituting C from Equation (4.19) into Equation (4.18), gives the following relationship for short fatigue crack growth behaviour at a stress range of 400 MPa:

$$\left(\frac{da}{dN} \right)_{cf} = 2.779 \times 10^{-5} \left(\frac{1}{f} \right)^{0.687} (90 - a) + 10^{-6} \quad (4.20)$$

here a is in μm and f in Hz. Technically when crack growth rate is lower than $10^{-6} \mu\text{m}/\text{cycle}$, or $10^{-12} \text{m}/\text{cycle}$, the crack can be regarded as being non-propagating.

Figure 4.26 shows the predication of the stage I crack growth rate using Equation (4.20). It appears that the prediction agrees well with that of the experimental data for the given stress range of approximately 400 MPa.

It was also observed that the number of cracks initiated increased as the frequency increased, see Table 4.13 and Figure 4.27 For the stress range of approximately 400 MPa,

the number of crack gradually increased, being 3, 5, and 9 with increasing frequencies of 2, 5, 12.5 Hz respectively. However, for the stress range of approximately 600 MPa, the number of cracks increases massively with frequency, being 214 cracks at a frequency of 12.5Hz as compared with 12 cracks at a frequency of 5Hz. The combined effect of high stress level and high frequency in corrosion fatigue results in extensive oxidation film rupture on the surface of the specimen, and the development of numerous weak spots where cracks could develop. Increasing the strain rate might increase fatigue life, but produce multiple cracks on the surface.

Further comments

Although the general notion is that corrosion fatigue crack growth rates increase with decreasing cyclic loading frequency, because of increasing time per cycle available for increased chemical reaction and mass transport, this trend may be altered for cases in which increased frequency increases the rate of environmental cracking because of (1) enhanced mass transport by connective mixing, (2) enhanced crack-tip strain and surface creation rates, and (3) reduced crack-tip blunting by dissolution. The frequency dependence of cycle-time-dependent corrosion fatigue is accordingly complex.

4.3 Cathodic polarisation effects

Corrosion fatigue can be divided into a two-stage process consisting of initiation and propagation. In service corrosion fatigue cracks are often seen to nucleate at corrosion pits. Corrosion pitting in structural steels can be completely prevented by cathodic protection. However, it is known that excessive cathodic protection can cause increased crack growth rate in steel due to the effects of hydrogen adsorption and embrittlement. Thus cathodic protection can have *opposing* effects on the above two stages.

Experiments

Four specimens (C1, C2, C3 and C4) of BS251A58 steel were prepared and tested to study the effect of cathodic polarisation on crack development. For convenience and consistency, the dominant crack in this study is denoted as crack 1, and the other cracks were named as crack 2, crack 3 etc.

Table 4.14 illustrates the fatigue life time for specimens C1, C2, C3 and C4. Table 4.15 lists the number of cycles required to cause the nucleation of the dominant crack with or without cathodic polarisation, and the number of cycles when crack growth rate decreases. Further investigation has confirmed that the slowing down in crack growth occurs at the crack transition from stage I to stage II, and at the application of cathodic polarisation. The total number of cracks observed from specimens C1, C2, C3 and C4 is given in Table 4.16.

Figure 4.28 (a), (b), and (c) presents details of a versus N and da/dN versus a for specimens C2, C3 and C4 respectively. Figure 4.28 (d) shows the dominant crack growth rate for specimens C2, C3 and C4. Note: data for specimen C1 was not available as no replication was undertaken during the test.

Specimens C1 and C2, cathodically protected in an aerated 0.6M NaCl solution, were stressed at a stress range of 750 MPa, approximately 20% below the fatigue limit in air (915 MPa). Tests were run to failure maintaining the specimen potential by means of potentiostat at a value of -1280 mv (SCE). It was found that the fatigue lifetimes of both specimens (C1 and C2) are longer than that of specimen C4 subjected to the free corrosion potential, see Figure 4.29.

Replication was carried out for specimen C2, but not for C1. The fatigue life of specimen C2 seems to be shorter than that of specimen C1, as specimen C2 was intermediately

stopped for the replication and the surface of specimen C2 could be without cathodic protection at that interval possibly allowing anodic reaction to occur. However there is not much difference in the fatigue life for both specimens, with 437000 cycles for specimen C1 and 375000 cycles for specimen C2. It was also noted that only one crack developed on the surface of specimen C1 whilst there were two cracks on the surface of specimen C2, of which only crack 1 became the dominant failure crack. Crack 2 stopped growing when the crack length arrived at approximately 250 μm .

Two stage test

Specimen C3 was initially subjected to loading at a cyclic stress range of 750 MPa in a 0.6M NaCl solution without cathodic potential. The free corrosion potential of the central section surface of specimen C3 was recorded at -650 mv (SCE) when specimen C3 was in the recirculating solution for a period of 20 minutes. Several cracks was found to transform from stage I crack growth to the stage II crack growth; the crack path changed from along the shear plane to an angle of 45° or 135° to the specimen axis after 45000 cycles. A cathodic potential of -1280 mv (SCE) was then applied to the central section of the specimen and fatigue loading was applied until the specimen failure.

Replicas were taken to detect the crack growth behaviour. The fatigue life of specimen C3 was 180805 cycles, being shorter than specimen C1 and C2, but longer than that of specimen C4 which was tested without an applied potential throughout.

Free corrosion potential condition

Of the four tests, specimen C4, was fatigued in a 0.6M NaCl solution without cathodic polarisation, and was found to have the shortest life time, the total number of cycles to failure being 132100. The extent of corrosion was the highest, especially during the stage I crack growth stage. Again replicas were taken to detect crack growth.

Experimental observations

Figure 4.28 (a), (b) and (c) shows the three sets of crack growth rate data, for specimens C2, C3 and C4 respectively. From the a-N curves it is found that the cracks grew faster for specimen C4 than for specimens C3 and C2. From Figure 4.28 (c), a decrease in crack growth rate corresponded to the crack transition from stage I to stage II for specimen C4. For specimens C2 and C3, however, decreases in crack growth rate were related to both the stage I-to-stage II crack transition and cathodic polarisation effect.

For specimen C2, the marker (T) in Figure 4.28 (a), refers to the crack transition from stage I to stage II. The major crack, crack 1, consists of three stage I cracks joining together.

For specimen C3, the marker (T) in Figure 4.28 (b), refers to the crack transition from stage I to stage II; and the marker (CP) indicates the point when cathodic potential -1280 mv(SCE) was applied on the specimen. The decrease of crack growth rate is observed at the crack growth transition from stage I to stage II, and also observed after cathodic polarisation was applied for a period of 10000 cycles.

For specimen C4, the marker (T) in Figure 4.28 (c), refers to the crack transition from stage I to stage II growth.

Figure 4.28 (d) compares major crack growth behaviour for the three specimens C2, C3 and C4.

Proportion of cycles in each stage

For specimen C2 (100% CP) the stage I crack growth rate decreased with cathodic polarisation, and the majority of the fatigue life ($0.76 N_f$) was spent in the propagating of

a stage I crack and its transition from stage I to stage II. After the transition, the stage II crack propagated rapidly for the rest of fatigue life. The fracture surfaces of the stage I crack growth regime and stage II crack growth regime are shown in Figure 4.30 (a) and (b). An elliptical crack shape can be observed at the end of stage I crack growth and the crack surface is relatively smooth due to crack face rubbing during this period. However, compared to free corrosion tests in the stage II crack growth regime, there was less corrosion on the fracture surface of specimen C2.

In contrast, for specimen C4 (0% CP), which was exposed to a 0.6M NaCl solution without cathodic polarisation, only a small portion of fatigue life was spent during the growth of a stage I crack and its transition to a stage II crack ($0.15 N_f$ to $0.28 N_f$). Stage II crack growth occupied most of the lifetime in corrosion fatigue. Figure 4.31(a) shows the fracture surface of specimen C4, and Figure 4.31(b) presents a close-up view of the crack initiation site and stage I crack regime. Rather different features on the fracture surface for the stage I crack growth regime and stage II crack growth regime can be observed. The stage I crack growth was associated with metal dissolution, and the crack surface was corroded and covered with corrosion product. The dissolution process resulted in a broad crack, and a shorter final stage I crack length on the surface, compared with that for specimen C2. Figure 4.31(a) also illustrates the stage II crack growth path, showing corrosion product still left on the fracture surface.

For specimen C3 (75% CP), the number of cycles spent during the development of a stage I crack was the same as that for specimen C4, however the time spent during stage II crack growth was longer after a cathodic potential was applied to the specimen. It was found the crack growth rate decreased when a cathodic potential -1280 mv (SCE) was applied for a period of 10000 cycles; this suggests that cathodic polarisation still has a protective effect on initial stage II crack growth. However, after a further 85400 cycles, the crack propagated very fast until the specimen failure. Probably when the cathodic potential i.e. -1280 mv (SCE) was applied on the surface of the specimen for a longer

period, the hydrogen would be adsorbed and diffused in the crack tip, inducing material decohesion in front of the crack tip and resulting in hydrogen embrittlement; as a result crack would grow faster in the later stage II crack growth regime. Figure 4.32 (a) demonstrates a crack propagation in stage I in 0.6M NaCl solution without cathodic polarisation (note: extensive corrosion product), and the crack propagation in stage II with cathodic polarisation (little corrosion product). Figure 4.32 (b) shows a close-up view of Figure 4.32(a), in which dissolution processes occurred and corrosion product was deposited and cracked during stage I crack growth and the stage I /II transition.

The results above suggest that for the present material the cathodic polarisation, -1280 mv(SCE), has an inhibiting effect on stage I crack initiation, stage I crack growth, the transition from a stage I crack to a stage II crack and the early stage II crack growth stages. However, after a certain period of cathodic polarisation, the stage II crack growth rate would be accelerated by hydrogen embrittlement.

Final stage I crack length

The final stage I crack lengths observed from specimens C2, C3 and C4 were presented earlier in Figure 4.12 (a), (b) and (c) respectively. The final stage I major crack length observed from specimen C2, with cathodic polarisation, is longer (i.e. 494 μm) than that from specimen C4 (i.e. 67 μm) which was tested without cathodic polarisation. From specimen C3 it was found the major final stage I crack length is 173 μm .

These observations can be explained by considering the stage I crack shape development under different electrochemical condition. For specimens C3 and C4, as the stage I crack propagated in the bulk 0.6M NaCl solution, the metal in the crack tip and the crack flank was dissolved continuously producing a broad crack shape, leading to a favourable state for duplex slip operation, consequently the stage I crack growth would give way to stage

II crack growth after it propagated a distance of two or three prior austenite grain diameters.

However, for specimen C2 and specimen C1 the stage I major crack was growing under cathodic potential charge, and the metal in the crack tip and the crack flank was prevented from dissolving by cathodic potential, resulting in the crack growing with a narrow and elongated shape along the shear stress plane. With a low value of aspect ratio and a long and shallow shape the stress concentration in the crack front was low, and the crack grew in such a fashion that expanded its surface length to as far as ten grain diameters before it eventually changed from stage I crack growth to stage II crack growth.

Suppression of pitting

With cathodic polarisation of -1280 mv (SCE), the number of pits was dramatically reduced, consequently the number of cracks was also reduced, see Figure 4.33.

Under cathodic polarisation, the crack found in specimen C2 was associated with the non-metallic inclusion along the prior austenite grain boundary. The stage I crack initiated from this site and propagated along the shear stress plane on the surface due to the free surface effect and the deformation incompatibility between the inclusion and the matrix. No sign of pitting was noted on the rest of the specimen surface. The stage I crack propagated slowly and consumed a large proportion of fatigue lifetime until it gave way to stage II crack growth perpendicular to the tensile stress. The final stage I crack length was about 500 μ m, being the total length of three co-planar cracks coalescing together.

Another crack, crack 2, also initiated from an inclusion and propagated along the shear stress plane for a distance of 200 μ m. After transferring from stage I crack growth to stage II crack growth, the crack stopped growing when it extended a further distance of 50 μ m in stage II. Probably the stage I/II crack transition just occurred on the surface, not

in the depth yet. It appears that cathodic polarisation plays an important role for the early stage II crack growth.

It is considered therefore that cathodic polarisation prevents pits from initiating and consequently inhibits the development of cracks.

Current-time and corrosion potential-time

The corrosion current recorded from the specimen throughout the test, as a function of time, for specimens C1 and C3, is given in Figure 4.34(a) and Figure 4.35(a) respectively. In addition, the rest corrosion potential as a function of time was measured during the fatigue test for specimens TC7 and TC10, which were immersed in the bulk 0.6M NaCl solution under two stress levels of 504 MPa and 609 MPa respectively, see Figure 4.36 and Figure 4.37.

It was found that the rest corrosion potential decreased with increase in test time eventually tending towards a constant, being about -650 mv for both specimens TC7 and TC10. A sudden rise was noted which corresponded to the occasion when the surface of the specimen was cleaned by acetone after 100000 cycles and then immersed in the bulk solution again. Soon after being immersed into the solution, the surface film was attacked by the chloride ions leading to the decrease of the rest corrosion potential. When the rest corrosion potential reached a relatively stabilised value of -650 mv(SCE), which is the stabilised rest corrosion potential for the particular metal/environment solution, the surface oxidation film was no longer, or less, attacked by the aggressive solution.

Effect of solution purity

The chemical composition of solution is also very important for corrosion fatigue under different electrochemical conditions. Two more specimens C5 and C6, were tested with

cathodic polarisation, -1280 mv (SCE) at two shear stress ranges of 613 and 616 MPa, in an environment of 0.6M NaCl solution made of the vacuum salt which was is much purer than the laboratory salt; see Table 4.17 (a) and (b).

The test results illustrated that the fatigue lifetime in vacuum salt solution with cathodic polarisation was longer ($N_f > 1000000$) than that in the solution made from laboratory salt with cathodic polarisation. Another reason can be the applied stress level is so low that crack initiation is very difficult with a cathodic polarisation (i.e. -1280 mv (SCE)).

When the applied stress level drops below some critical value, it is suggests that failure will not occur with cathodic potentials around -1000 mv (SHE i.e. Standard Hydrogen Electrode) [31]. This is due to the mechanical effect being too small to initiate a crack and the absence of the dissolution process due to cathodic polarisation effect which aid the nucleation of pits and subsequently cause crack initiation.

Comparison of results with published work

Lee and Uhlig [31] conducted fatigue tests under conditions of cathodic polarisation on 4140 steel heat-treated to various hardness levels. It was found that cathodic protection was effective in an aerated 3% NaCl solution for steels having hardness values from Rc20 to Rc40. For optimum protection, steels must be polarised below -0.49 V (SHE). Steel of Rc52 at this potential exhibited longer fatigue lifetime than normal, but suffered increasing hydrogen damage below -1 V (SHE), see Figure 3.26.

For the present study, the hardness values of the steel tested were approximately Rc48 to Rc52. When specimens C1 and C2 were cathodic polarised at -1280 mv (SCE) and subjected to corrosion fatigue, they failed after around 400000 cycles. Compared with a free corrosion potential condition, increased time was observed for fatigue crack nucleation under cathodic polarisation, and fewer cracks were formed. The growth of

stage I crack was extended to a distance about 500 μm , and the transition from stage I crack growth to stage II crack growth and early growth of stage II were inhibited by cathodic protection. However, the growth of stage II crack was enhanced by cathodic polarisation due to hydrogen damage after the crack length approached 500 μm .

A similar beneficial effect of cathodic polarisation was reported by Rajpathak and Hartt [32] based on measurements of corrosion fatigue crack initiation and early growth to a crack depth of 1 mm at the root of a notch.

Discussion

The effects of cathodic polarisation on crack initiation of smooth specimens and crack propagation can be understood from the present experiments. Presumably, anodic dissolution leading to either enhanced plastic deformation or localised pitting is beneficial for crack initiation [33–36]. Here, hydrogen plays a secondary role, particularly for moderate potentials, fast-loading frequencies and near-threshold stress intensities typical of the smooth specimen studies. On the other hand cathodic polarisation enhances moderate ΔK rates of corrosion fatigue crack propagation by a hydrogen embrittlement (HE) mechanism. Slow-loading frequencies, significant plastic straining and concentrated hydrogen production within the occluded crack provide the basis for HE as the alternative process, and dissolution becomes less important. Cathodic polarisation can be either beneficial or deleterious to the corrosion fatigue resistance of a component [21, 37, 38]; the effect depends upon the level of applied cathodic current, and the crack growth i.e. initiation or propagation.

There is a wealth of experimental evidence indicating that the environment plays an important role in dictating the extend of slip irreversibility and fatigue life [39, 40]. It has been demonstrated by numerous workers that fatigue life is markedly improved in vacuum or in dry, oxygen-free media as compared to moist laboratory air. Considering the case of

fatigue of pure metals in a vacuum or in an inert environment; here single slip during the tensile loading cycle produces a slip step at the surface of the specimen. The extent of surface slip offset can be dramatically diminished by reverse slip during unloading or subsequent compression loading in fully reversed fatigue. In an inert environment, surface roughening during fatigue occurs primarily by a random process. On the other hand, when slip steps form during the tensile portion of a fatigue cycle in laboratory air or in a chemically aggressive medium, the chemisorption of the embrittling species (such as oxygen or hydrogen) or the formation of an oxide layer on the freshly formed slip step makes reverse slip on the same slip plane upon load reversal difficult. In an embrittling medium this process can provide a mechanism of enhanced surface roughening as well as easy transport of the embrittling species to the bulk of the material preferentially along the persistent slip bands, thereby facilitating crack nucleation.

However, with cathodic polarisation surface dissolution can be prevented although once a crack initiates, and propagates along the maximum shear stress plane, it can be easy for the crack to grow on the primary slip plane because there are no corrosion products depositing on the specimen surface, which act to block slip. As a result a relative long surface stage I crack length can be observed. Without the effects of cathodic polarisation a crack can initiate, and corrosion products can deposit close to the original crack site which make it difficult for reverse slip to glide along the primary slip plane on the surface upon load reversal. The crack therefore extends more easily in depth rather than on the surface, resulting in a favourable condition for duplex slip operating, consequently the transition of stage I crack growth to stage II crack growth will occur at a relatively short length of surface stage I crack.

4.4 Electrolyte composition effect

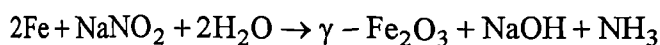
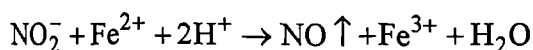
In an aggressive environment, initial defects, such as pits, play an important role for crack nucleation. The early stages of crack development which can often dominate fatigue lifetime can be eliminated by pitting and the creation of local stress concentrations.

Where chloride is the aggressive species in pit development it is possible to introduce chemical which inhibit the development of pits; in these cases corrosion fatigue lifetime may be improved.

NaNO₂ as an inhibitor

Specimen CN1 was subjected to corrosion fatigue at shear stress range of 912 MPa, in 0.01M NaNO₂+0.6M NaCl solution; it failed after 105000 cycles. Specimen CN2 was fatigued in a 0.1M NaNO₂ + 0.6M NaCl solution at shear stress range of 637 MPa. After 3613717 cycles, it failed at the 'O' rings which sealed the specimen/chamber rather than at the central section of the test specimen where stress was at its highest. This could be accounted for by stress-assisted crevice corrosion of the specimen. Further investigation found that there was a thick yellow oxidation film covering the surface of the specimen. After removing the film, there was surprisingly no sign of pitting on the surface of the specimen, and its surface was still as-polished. It is assumed that if specimen had not failed at the 'O' ring, it would have had a longer fatigue life due to the absence of pitting.

The possible reaction could occur as following:



in the reaction, H⁺ is consumed, so that NO₂⁻ inhibits the tendency for a decrease in solution pH. In addition a γ - Fe₂O₃ oxidation film is produced .

This fatigue test result is supported by results from a corrosion test carried out on a metallographic sample in a solution of the same composition. Here no pits were found on the surface of the sample after exposed in 0.6M NaCl + 0.5M NaNO₂ solution for more than 6 days. This suggests that the effectiveness of the inhibitor increases with increase in concentration within the solution.

Specimen CN3 was fatigue tested at stress range of 613 MPa, in 0.6M NaCl + 0.001M NaNO₂ solution. The fatigue life was slightly longer than that of specimen TC18 in 0.6M NaCl solution at the same stress level suggesting a minor effect of nitrite at this low concentration.

The role of Na₂SO₄

Although SO₄²⁻ is always regarded as an aggressive ion for metallic materials, it is recognised as a non-aggressive ion when present in 0.6M NaCl solution (pitting solution). It should be noted that its inhibition effect depends upon its concentration ratio in the solution and can act as an aggressive ion should its concentration drop below a critical value.

Specimens S1 and S2 were tested subjected to fully reversed torsional load cycling at stress ranges of 629 MPa in 0.6M NaCl + 0.02M Na₂SO₄ solution and 650 MPa in 0.6M NaCl + 0.1M Na₂SO₄ solution respectively. The corrosion fatigue life was slightly increased, as compared with that in a 0.6M NaCl solution, see Figure 4.38.

High concentration of NaCl

For comparison purpose, specimen S3 was subjected to corrosion fatigue in a 2M NaCl solution at a stress range of 626 MPa in an aim to study the effect of the chloride

concentration on corrosion fatigue lifetime. There appeared to be no significant effect on the fatigue life, see Figure 4.38, although the number of cracks was increased, being 48, compared with 12 cracks from specimen TC18 at a stress range of 613 MPa in a 0.6M NaCl solution.

Crack growth rate as a function of crack length is shown in Figure 4.39, for specimen S3, and is compared with test data for specimen TC18 in a 0.6M NaCl solution under shear stress range of 613 MPa. From these figures crack growth behaviour appears to be similar for both environments.

Comparisons

The fatigue lives of specimens CN1, CN2, CN3, S1, S2, and S3 were tabulated in Table 4.18 and presented in Figure 4.38. The S-N curve obtained in a 0.6M NaCl solution is also plotted in this figure. It was found that fatigue life of specimens CN1, CN2, S1, S2 and S3 were located to the right of S-N curve obtained in the 0.6M NaCl solution or near to it, indicating an increase in corrosion fatigue life attributed to the presence of NO_2^- and SO_4^{2-} in the 0.6M NaCl solution. However a high concentration of chloride or very low concentration of nitrite in solution did not have a significant effect on fatigue life.

Inhibition mechanisms

The inhibition of pitting mechanisms might be different for different inhibitors and metals. In general two mechanisms have been recognised [2]:

- (1) competitive adsorption;
- (2) repair of a protective film on the metal surface.

The inhibitor ion, NO_2^- , reacting with other ions, can produce a relatively thick oxide film on the specimen surface which prevents the surface from being attacked, and in turn prevents the surface from pitting. The crack initiation process could be inhibited when sufficient concentration of inhibitor is present in a 0.6M NaCl solution; the time for crack initiation would accordingly be increased.

Boukersons and Cottis also observed similar results for a $\text{Cl}^- / \text{NO}_2^-$ pitting solution in corrosion fatigue [41]. In their study, fatigue life was increased in a pitting solution of 0.01M NaNO_2 + 0.6M NaCl solution.

The addition of small concentrations of sodium nitrite to sodium chloride solution increases the corrosion fatigue lifetimes of a structural steel. The extended life is attributed to the inhibition of pitting, the creation of oxide-induced crack closure, together with the reduction in crack coalescence as a result of the lower crack density.

4.5 Torsion fatigue tests in air

Seven hour-glass specimens were tested under fully reversed torsion fatigue using the same torsion test machine, under stress ranges from 980 MPa to 1285 MPa.

The results of these fatigue tests are listed in Table 4.19 and plotted in Figure 4.40. Here symbol ∇ indicating the present study and symbol O indicating the data obtained by Rehman [6] and Murtaza [42] testing the same material. All results are seen to lie close to a best-fit line and are within experimental scatter typical for a fatigue test.

The relationship between fatigue life and applied shear stress amplitude in air for BS251A58 steel is obtained as:

$$\tau = 913.85 (N_f)^{-0.0445}$$

in air

(4.21)

where τ is in MPa.

References

- [1] C. M. Suh, R. Yuuk and H. Kitagawa (1985) Fatigue microcracks in a low carbon steel, *Fatigue Frac. Engng. Mater. Struct.* Vol. 8, No.2, pp.193-203.
- [2] Z. Szklarska-Smialowska (1986), *Pitting Corrosion of Metals*.
- [3] T. P. Hoar, D. C. Mears and G. P. Rothwell (1965) *Corros. Sci.*, vol.5, p.297.
- [4] D. Taylor (1982) Euromech colloquium on short fatigue cracks, *Fatigue Frac. Engng. Mater. Struct.* 5, p.305.
- [5] R. Akid (1994), Modelling environment-assisted short fatigue crack growth, *Advances in Fracture and Structural integrity*, Eds. V. V. Panasyuk, D. M. R. Taplin, M.C. Pandey, O.ye. Andreykiv, R. O. Ritchie, J. F. Knott and P. RamaRao.
- [6] Hafeez Ur Rehman (1991) The Influence of microstructural variables on the growth of short fatigue cracks in a high strength steel. *Ph.D thesis*, University of Sheffield, September 1991.
- [7] J. F. Knott (1973), *Fundamentals of Fracture Mechanics*, London Butterworths, Ch. 3, pp.46-90.
- [8] B. N. Cox and W. L. Morris (1987) The statistics of the shape of small fatigue cracks, *Fatigue* 87, pp.241-250.
- [9] G. P. Ray, R. A. Jarman and J. G. N. Thomas (1985) The Influence of non-metallic inclusions on the corrosion fatigue of mild steel. *Corrosion Science*, 25, No.3 pp.171-184.

- [10] A. Turnbull (1983), The solution composition and electrode potential in pits, crevices and cracks. *Corrosion Science*, **23**. No.8, pp.833-870.
- [11] R. A. Oriani, J. P. Hirth and M. Smialowska (1985), *Hydrogen Degradation of Ferrous Alloys*.
- [12] B. F. Brown (1970), *Corrosion*, Vol. **26**, No.8, P 249.
- [13] T. Suzuki, M. Yamabe and Y. Kitamura (1973), *Corrosion*, Vol.**29**, No.1, P 18.
- [14] P. R. Rhodes (1969), Mechanism of chloride stress corrosion cracking of austenite stainless, *Corrosion*, Vol.**25**, No.11, pp. 462-472.
- [15] W. W. Gerberich (1985), Fatigue, *Hydrogen Degradation of ferrous alloys* (Edited by R.A.Oriani, J.P.Hirth and M.Smialowska). pp.366-413.
- [16] R. P. Wei (1979) Fatigue Mechanisms, *ASTM STP 675*, Edited by J. T. Fong (Philadelphia, PA: ASTM) pp.816-840.
- [17] R. P. Wei and G. Shim (1983) Corrosion Fatigue Mechanics, Metallurgy, Electrochemistry and Engineering, *ASTM STP 801*, pp.5-25.
- [18] R. P. Wei and R. P. Gangloff (1989) Fracture mechanics: Perspectives and Directions, *ASTM STP 1020*, pp.233-264.
- [19] R. P. Wei and G. W. Simmons (1981), Recent progress in understanding environment assisted fatigue crack growth, *Int. J. Fract.* **17**, No.2, pp.235-247.

- [20] R. P. Gangloff (1988), Corrosion fatigue crack propagation in metals, *Proceedings of the First International Conference on Environment-Induced Cracking of Metals*, Eds. R.P.Gangloff and M. B. Ives, October 2-7, 1988, The American Club, Koler, Wisconsin, USA, NACE, pp.55-109.
- [21] P. L. Andresen, R. P. Gangloff, L. F. Coffin, and F. P. Ford (1987), Applications of fatigue analyses: energy systems, *Fatigue 87*, pp. 1723-1751.
- [22] R. Nakai, A. Alavi and R. P. Wei (1988), Effects of frequency and temperature on short fatigue-growth in aqueous environments, *Metall. Trans. A. 19A*, pp.543-548.
- [23] F. P. Ford (1988) Status of research on environmental-assisted cracking in LWR pressure vessel steel, *J. ASTM*, Vol. 110, No.2, pp.113-128.
- [24] F. P. Ford (1983) Embrittlement by the Localised Crack Environment, pp.117-147.
- [25] F. P. Ford and P. L. Andresen (1988) Advances in fracture research (Edited by K. Selama, K. Ravi-Chandor, D. M. R. Taplin and P. Ramo Ra, Oxford , UK: Pergamon Press, pp.1571-1584.
- [26] F. P. Ford (1988), Crack-Tip Chemistry, *Proceedings of the First International Conference on Environment-Induced Cracking of Metals*, Eds. R.P.Gangloff and M. B. Ives, October 2-7, 1988, The American Club, Koler, Wisconsin, USA, NACE.
- [27] S. J. Hudak (1988), Corrosion fatigue crack growth: The role of crack-tip deformation and film formation kinetics, *Ph.D Thesis.*, Lehigh University.
- [28] I. M. Austen and E. F. Walker (1984), Corrosion fatigue crack propagation in steels under simulated offshore conditions, *Fatigue 84*, pp.1457-1469.

[29] I. M. Austen, W. J. Rudd and E. F. Walker (1988) Proceedings of the International Conference on Steel in Marine Structure. Paper ST 5.4.

[30] I. M. Austen (1987) Quantitative assessment of corrosion fatigue crack growth under variable amplitude loading, British Steel Company Report BSC FR S132-8/862 (Rotherham, England: Swiden Laboratories).

[31] H. H. Lee and H. H. Uhlig (1972) Corrosion fatigue of type 4140 high strength steel, *Met. Trans.*, **3**, pp.2949-2959.

[32] S. S. Rajpathak and W. H. Hartt (1987), Formation of calcareous deposits with simulated fatigue cracks in seawater, *Corrosion*, Vol **43**, No.6, pp.339-347.

[33] D. J. Duquette (1988), Corrosion fatigue crack initiation processes, *Proceedings of the First International Conference on Environment-Induced Cracking of Metals*, Eds. R.P.Gangloff and M. B. Ives, Octoble 2-7, 1988, The American Club, Koler, Wisconsin, USA, NACE.

[34] D. J. Duquette, Environment Sensitive Fracture of Engineering Materials, pp.521-537.

[35] R. P. Gangloff and D. J. Duquette (1987), Chemistry and physics of fracture , (Edited by R. M. Latanision and R. H. Jones (The Netherlands: Martinus Nijhoff Publishers BV, 1987), pp.612-645.

[36] D. A. Jones (1988), Contribution of anodically attenuated strain hardening to the mechanism of environmentally induced cracking, *Proceedings of the First International*

Conference on Environment-Induced Cracking of Metals, Eds. R.P.Gangloff and M. B. Lves, Octoble 2-7, 1988, The American Club, Koler, Wisconsin, USA, NACE.

[37] B. Tomkins and P. M. Scott (1982), Environment-sensitive fracture -design considerations, *Metals Tech.* **9**, pp.240-248.

[38] W. D. Dover and S. Dharmavasan (1984), Fatigue of offshore structure - A review, *Fatigue 84*, pp.1417-1434.

[39] N.Thompson, N. J. Wadsworth and N. Louat (1956), The origin of fatigue fracture in copper, *Philosophical Magazine* **1**, pp.113-26.

[40] P. Neumann (1983) Fatigue, In *Physical Metallurgy* (eds. R. W. Cahn and P. Haasen), pp. 1554-93, Amsterdam: Elsevier Science.

[41] A. Boukerrous and R. A. Cottis (1990) The Influence of corrosion on the growth of short fatigue cracks in structural steels, *Short Fatigue Cracks*, ESIS 13 (Edited by K. J. Miller and E. R. de los Rios), Mechanical Engineering Publication, London, pp.209-216.

[42] Ghulam Murtaza (1992) Corrosion fatigue short crack growth behaviour in a high strength steel, *Ph.D thesis*, University of Sheffield.

[43] N. J. H. Holroyd and D. Hardie (1983), Factors controlling crack velocity in 7000 series aluminium-alloys during fatigue in aggressive environment, *Corro Sci*, **23**, pp.527-540.

Table 4.1 Corrosion fatigue test in a 0.6 M NaCl solution, at pH=6, frequency of 5Hz

Specimen	$\Delta\tau$ (MPa)	N_f
TC6	926	73800
TC5	728	174320
TC18	613	205000
TC2	612	192000
TC10	609	310500
TC3	547	259500
TC7	504	553000
TC11	433	795000
TC13	415	870500
B10	224	6500000

Table 4.2 Number of cycles to pit initiation N_p , stage I crack initiation N_i , stage I/II transition N_t , and failure N_f for different stress levels

Specimen	$\Delta\tau$ (MPa)	N_p	pit length (μm)	N_i	Initial stage I crack length (μm)	N_t	N_p / N_f	N_t / N_f
TC6	926	5000	15	10000	138	15000~ 221400	0.067	0.20~ 0.30
TC5	728	4320	8	10000	26	40000~ 59268	0.024	0.23~ 0.34
TC18	613	5000	45	10000	55	59500~ 88150	0.024	0.29~ 0.43
TC13	415	271300	16	319000	37	470000~ 600645	0.36	0.54~ 0.69

Table 4.3 Number of cracks contributing to the final failure crack

Specimen	$\Delta\tau$ (MPa)	Total number of cracks observed	Number of cracks forming the dominant crack	N_f
C4	737	136	12	132100
TC5	723	31	18	174300
TC18	595	12	6	20500
TC13	405	5	1	870500

Table 4.4 Final stage I crack length, μm , at different shear stress ranges

Crack	Specimen				
	TC6 (926 MPa)	TC5 (728 MPa)	TC18 (613 MPa)	TC13 (415 MPa)	B10 (224 MPa)
1	335	54	58	63	58
2	270	60	55	35	39
3	256	45	159	36	30
4	83	77	48	37	40
5	86	93	35	64	29
6	68	50	36		25
7	56	57	58		13
8	112	43	66		60
9	44	78	23		33
10	81	53	24		66
11	37	30	29		60
12	86	82	51		15
13	53	104			52
14	185	60			
15	57	48			
16	213	31			
17	131	30			
18	155	32			
19	92	204			
20	121	43			
21	201	64			
22	176	214			
23	29	54			
24	60	71			
25	75	81			
26	191	46			
27	145	44			
28	114	47			
29	34	80			
30	61	47			
31	73	50			
32	64				
33	39				
34	85				
35	41				
36	57				
37	77				
38	26				
39	24				
40	359				
41	40				

continue...

42	30				
43	34				
44	36				
45	40				
46	128				
47	53				
48	44				
49	175				
50	237				

Table 4.5 Final stage I crack length, μm , at different frequencies for specimens FC5, TC13, FC4, FC2, TC18 and FC3

Crack	Specimen					
	FC5 (2Hz)	TC13 (5Hz)	FC4 (12.5Hz)	FC2 (2Hz)	TC18 (5Hz)	FC3 (12.5Hz)
1	70	63	13	56	58	124
2	44	35	51	149	55	42
3	30	36	47	54	159	53
4		37	22	93	48	100
5		64	23	44	35	125
6			48	31	36	51
7			62	124	58	59
8			69	26	66	222
9			52	19	23	38
10			32	102	24	26
11				51	29	41
12				43	51	47
13						35
14						30
15						127
16						108
17						99
18						41
19						305
20						56

Table 4.6 Final stage I crack length, μm , for specimens C2, C3 and C4.

Crack	Specimen		
	C2	C3	C4
1	494	173	67
2	200	90	110
3		91	130
4		122	19
5		32	47
6		94	39
7		36	25
8		404	50
9		80	32
10		194	17
11		54	95
12		91	170
13		147	22
14		304	170
15			31

Table 4.7 Parameters for Weibull distribution function of final stage-I crack length, μm , in corrosion fatigue, and in comparison with the corresponding mean value and standard deviation of the test data

Specimen	$\Delta\tau$ (MPa)	x_0	m	$E(\xi)$ (μm)	Test data (mean) (μm)	$D(\xi)$ (μm)	Test data (deviation) (μm)
TC6	926	0.12694E+30	14.2755	105.4	105.4	81.79	81.71
TC5	728	0.11230E+24	12.5078	66.84	66.84	42.24	42.26
TC18	613	0.64791E+19	10.7585	53.48	53.48	36.01	36.02
TC13	415	0.88197E+25	14.7820	47.01	47.01	15.19	15.18
B10	224	0.33715E+18	10.2617	48.63	48.63	32.58	32.58
FC2	616	0.35495E+25	13.0719	72.6	72.6	45.71	45.38
FC3	621	0.12000E+27	13.0719	95.04	95.04	78.35	77.71
FC4	400	0.40806E+25	14.3885	49.51	49.51	17.77	17.99
FC5	399	0.16465E+23	13.0719	48.13	48.13	20.09	20.12
C2	750	0.11732E+77	29.8507	347	347	208.79	207.89
C3	750	0.33767E+36	16.5289	136.6	136.6	103.73	105.17
C4	742	0.76690E+21	11.2676	68.23	68.23	53.73	53.70

Table 4.8 Coalescence of parallel cracks. Specimen TC5, $\Delta\tau = 728\text{MPa}$,
0.6M NaCl solution at pH 6

crack pair No.	c_1 (μm)	c_2 (μm)	d (μm)	y (μm)	$\tan\alpha=y/[c_1+c_2-d]$	Coalescence
20,21	928	1104	1585	109	0.245	yes
15,16	1560	1674	2631	232	0.380	yes
12,13	1169	789	1914	126	0.35	yes
17,19	2300	1620	3225	361	0.52	move towards each other but do not coalesce
15,17	2502	2306	2502	896	0.38	yes
18,19	1351	1264	1544	638	0.59	move towards each other but do not coalesce

Table 4.9 Crack aspect ratio λ at different stages of crack propagation,
0.6 M NaCl solution at pH 6

Specimen	Crack No.	$2c$ (μm)	a (μm)	$\lambda=a/c$	N/N_f	Stage
TC12 $\Delta\tau = 733\text{MPa}$	1	31.6	4.0	0.253	0.2	I
	2	33.5	6.0	0.358	0.2	I
	3	31.2	3.5	0.224	0.2	I
	4	84.8	10.1	0.238	0.2	I
	5	34.6	4.0	0.231	0.2	I
	6	81.0	7.5	0.185	0.2	I
	7	57.4	10.5	0.366	0.2	I
TC5 $\Delta\tau = 728\text{MPa}$	14	48.3	20.0	0.828	0.28	I/II transition
	15	54.0	16.92	0.627	0.28	I/II transition
	14	236.7	83.33	0.704	0.46	II

Table 4.10 The front line length and depth of *Shell Mark* on the fracture surface of failure specimens

Specimen	$\Delta\tau$ (MPa)	$2c$ (mm)	a (mm)	$\lambda=a/c$	Crack
FC4	400	15.75	6.197	0.787	crack 1
	400	7.15	2.22	0.621	crack 2
TC13	415	15.43	4.976	0.645	crack 1
FC2	616	16.99	5.496	0.647	several cracks joining up

Table 4.11 Crack depth for crack propagation at stage I/II transition, measured from SEM

Specimen	$\Delta\tau$ (MPa)	Crack	a (μm)	2c (μm)	$\lambda=a/c$
TC5	728	14	20	48	0.828
		15	17	54	0.704
C3	750		40	70	1.142
C4	742	1	45	60	1.5
FC4	400	1	41	108	0.762
		2	53	90	1.177
TC2	612	1	42	102	0.826

Table 4.12 Corrosion fatigue tests in a 0.6 M NaCl solution, at various frequencies

Specimen	$\Delta\tau$ (MPa)	N_f	Frequency (Hz)
FC2	616	160000	2
TC18	613	205000	5
FC3	621	230000	12.5
FC5	399	801500	2
TC13	415	870500	5
FC4	400	1202154	12.5

Table 4.13 Number of cracks contributing to the final failure crack

Specimen	$\Delta\tau$ (MPa)	Total number of cracks observed	Number of cracks forming the dominant crack	Frequency (Hz)	N_f
FC2	616	12	3	2	160000
TC18	613	12	6	5	205000
FC3	621	214	4	12.5	230000
FC5	399	3	1	2	801500
TC13	415	5	1	5	870500
FC4	400	9	2	12.5	1202154

Table 4.14 Corrosion fatigue test in a 0.6 M NaCl solution, with or without cathodic polarisation, frequency of 5Hz

Specimen	$\Delta\tau$ (MPa)	N_f	Cathodic polarisation
C1	750	437000	E=-1280 mv (SCE)
C2	750	375000	E=-1280 mv (SCE)
C3	750	180805	initially at free corrosion potential, followed by cathodic potential charge after 45000 cycles, E=-1280mv
C4	742	132100	free corrosion potential

Table 4.15 Effect of cathodic polarisation on fatigue life and fatigue crack propagation of specimens C2 and C3, compared with specimen C4 without cathodic polarisation

Specimen	Initial cycles, without cathodic polarisation	Additional cycles with cathodic polarisation	Total cycles to failure	Cycles for the major crack nucleation	Cycles for the first slowing-down of crack growth	Cycles for the second slowing-down of crack growth
C1	none	437000	437000			
C2	none	375000	375000	30000	62300	285000
C3	45000	135805	180805	20500	33400	55000
C4	132100	none	132100	20000	30000	

Table 4.16 Number of cracks contributing to the final failure crack

Specimen	$\Delta\tau$ (MPa)	Total number of cracks observed	Num. of cracks forming the dominant crack	Cathodic polarisation (CP) or free potential (CF)	N_f
C1	750	1	1	CP	437000
C2	750	2	1	CP	375000
C3	750	15	5	CP+CF	180805
C4	742	136	12	CF	132100

Table 4.17 (a) Maximum limits of impurities of vacuum salt (BDH Laboratory Supplier)
(minimum assay ignition 99.9%)

water-insoluble matter	0.003%	Barium (Ba)	0.001%
Bromide (Br)	0.005%	Calcium (Ca)	0.002%
Ferrocyanide ($\text{Fe}(\text{CN})_6$)	0.0001%	Copper (Cu)	0.0002%
Iodide (I)	0.001%	Iron (Fe)	0.0001%
Nitrogen compounds (N)	0.0005%	Lead (Pb)	0.0002%
Phosphate (PO_4)	0.001%	Magnesium (Mg)	0.001%
Sulphate (SO_4)	0.00004%	Potassium (K)	0.005%

Table 4.17 (b) Maximum limits of impurities of laboratory salt
(assay 99.5%)

Sulphate (SO_4)	0.05%	Heavy metals (as Pb)	0.001%
Bromide (Br)	0.01%	Ammonium (NH_4)	0.002%
Iron (Fe)	0.001%	Loss on drying (300°C)	1% (max)

Table 4.18 Corrosion fatigue test in different solutions, at frequency of 5Hz

Specimen	$\Delta\tau$ (MPa)	N_f	Environment
CN1	912	105000	0.6M NaCl + 0.01M NaNO_2
CN2	637	>3613717	0.6M NaCl + 0.1M NaNO_2
CN3	613	230000	0.6M NaCl + 0.001M NaNO_2
S1	630	278500	0.6M NaCl + 0.02M Na_2SO_4
S2	649	339000	0.6M NaCl + 0.1M Na_2SO_4
S3	626	254000	2M NaCl

Table 4.19 Fatigue test in air

Specimen	$\Delta\tau$ (MPa)	N_f
A4	1285	3000
A6	1176	14000
A1	1020	225000
A2	1020	233000
B5	1012	180500
B16	1006	>1000000
B14	980	>2000000

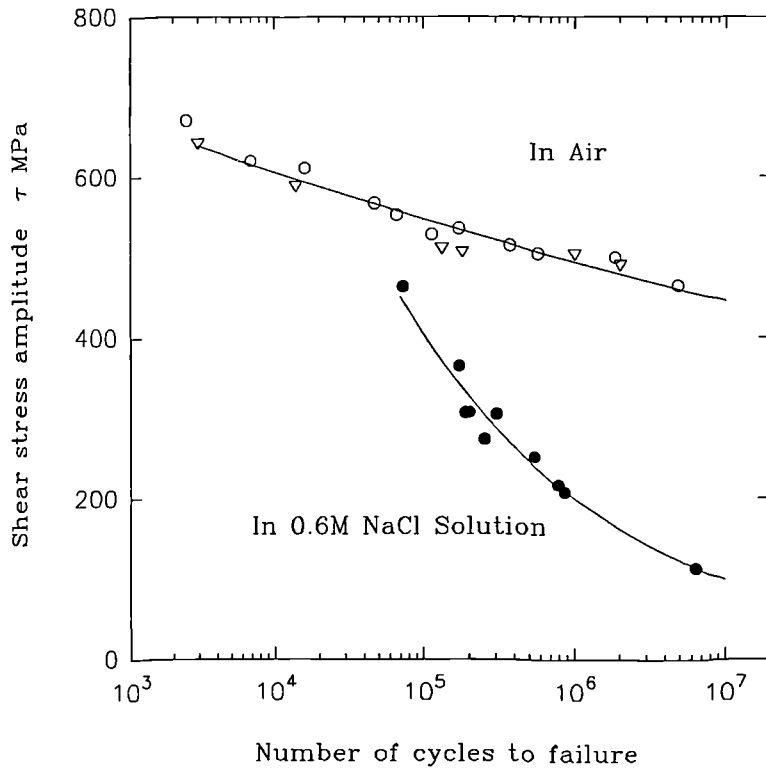


Figure 4.1 Fatigue endurance in air and in a 0.6M NaCl solution.

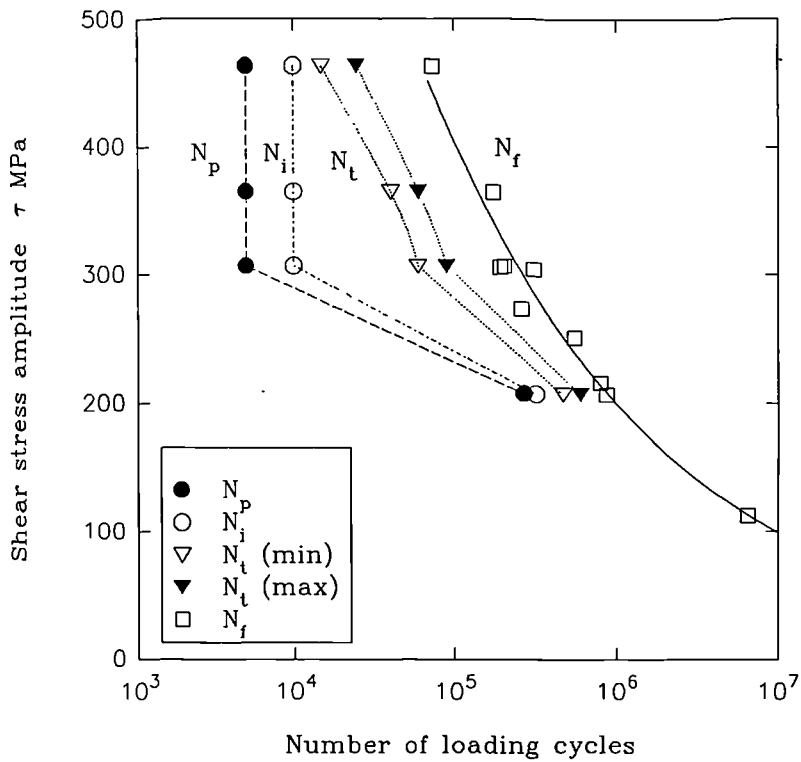


Figure 4.2 The number of loading cycles to pit formation N_p , stage I crack nucleation N_i , stage I/II transition of crack growth N_t , and final failure N_f in a 0.6M NaCl solution.

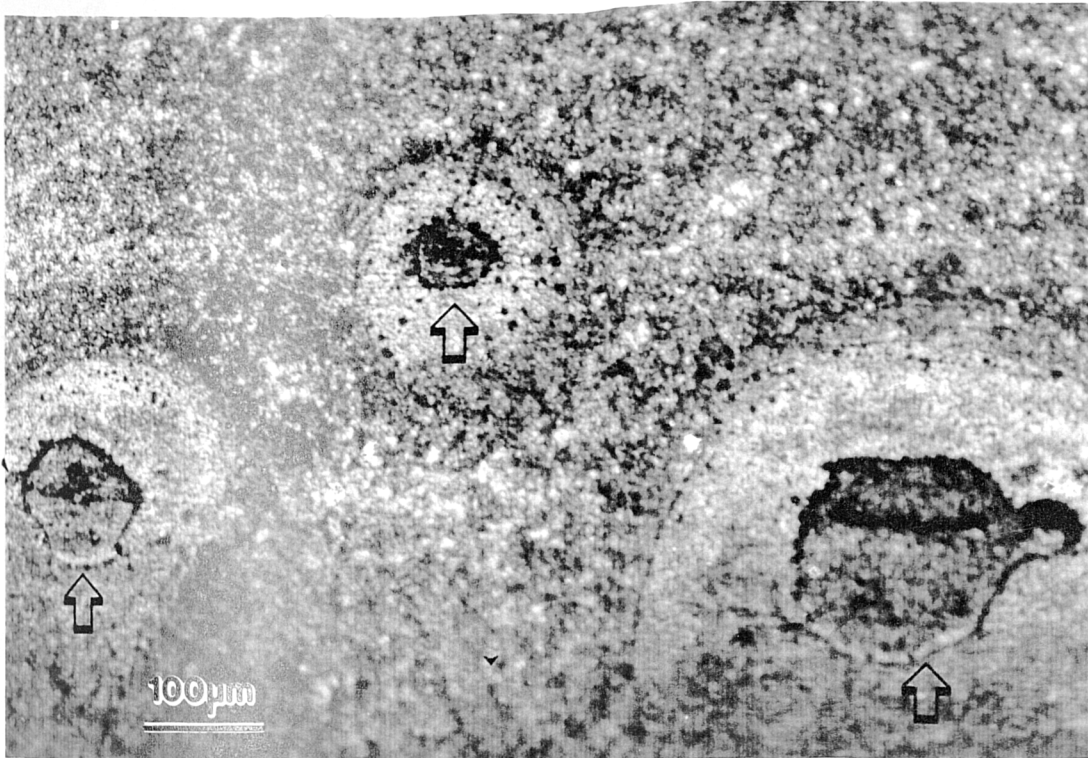


Figure 4.3(a) P formation on the surface of the specimen after 5000 cycles in a 0.6M NaCl solution, $\Delta\tau=733$ MPa, specimen TC12.

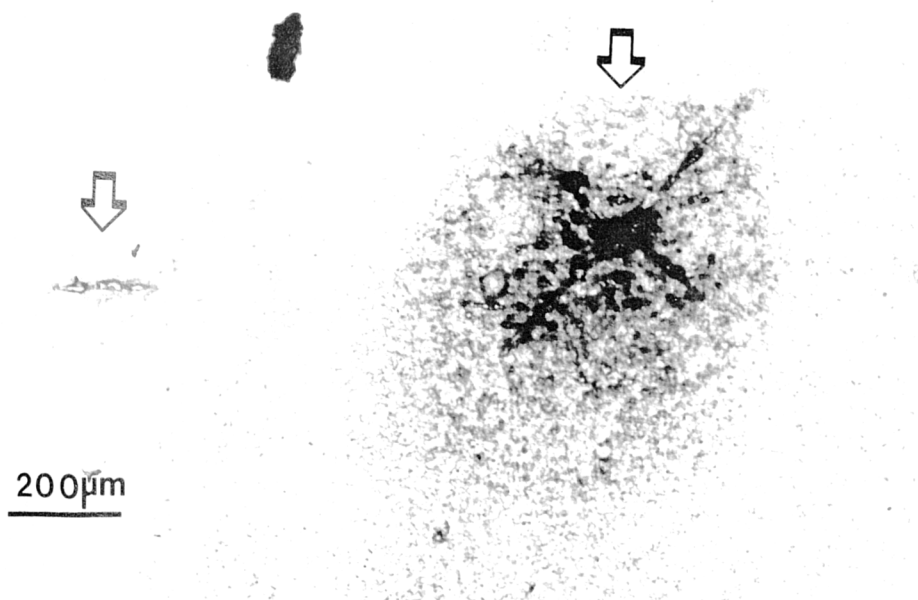


Figure 4.3(b) A crack propagating in stage II. Another crack stops growing at stage I on the surface of specimen TC13 after 601000 cycles in a 0.6M NaCl solution, $\Delta\tau=415$ MPa.

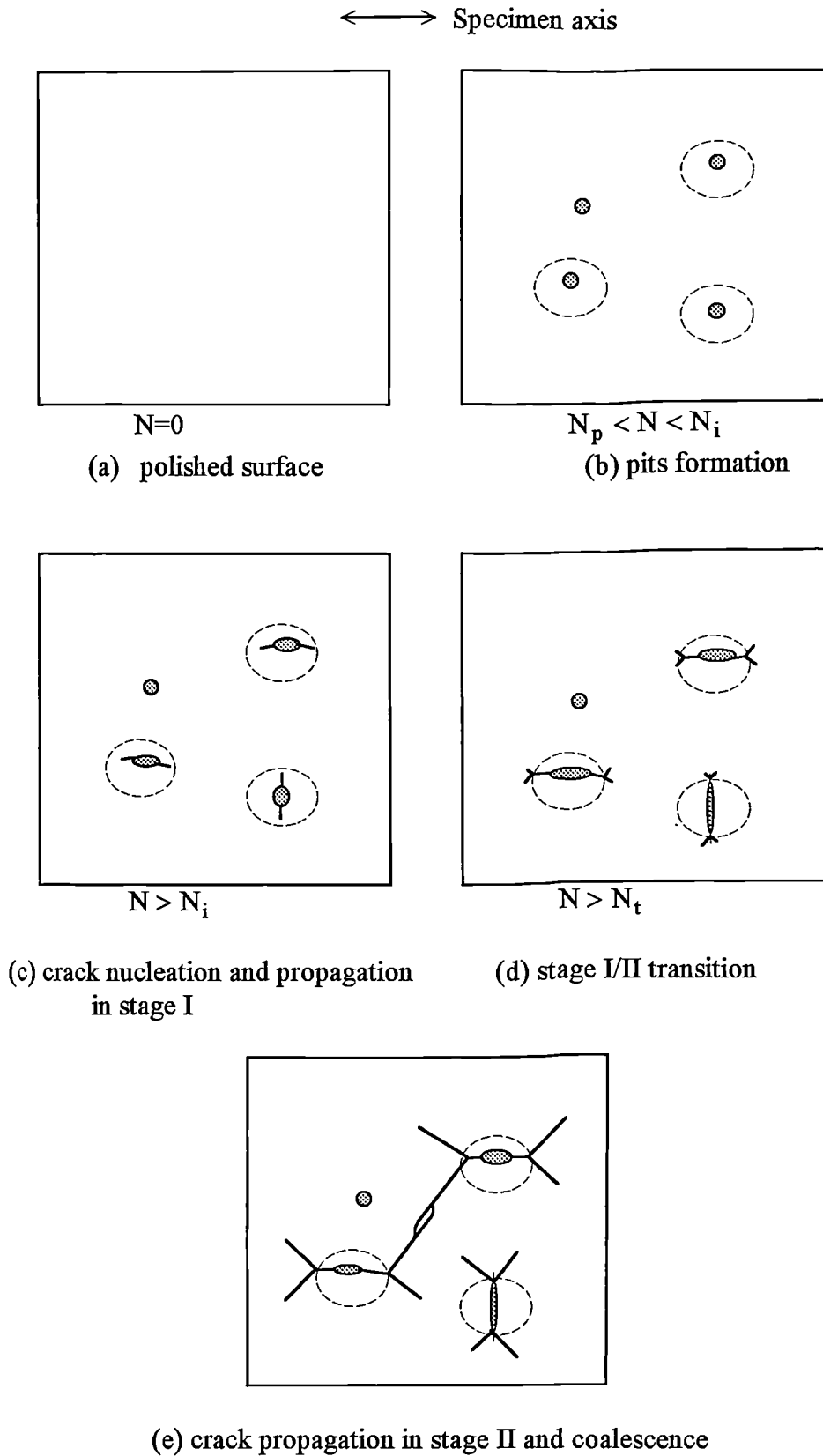


Figure 4.4 Schematic illustration of the sequence of events involving corrosion fatigue crack initiation, propagation and coalescence of BS251A58 steel under fully reversed shear loading conditions.

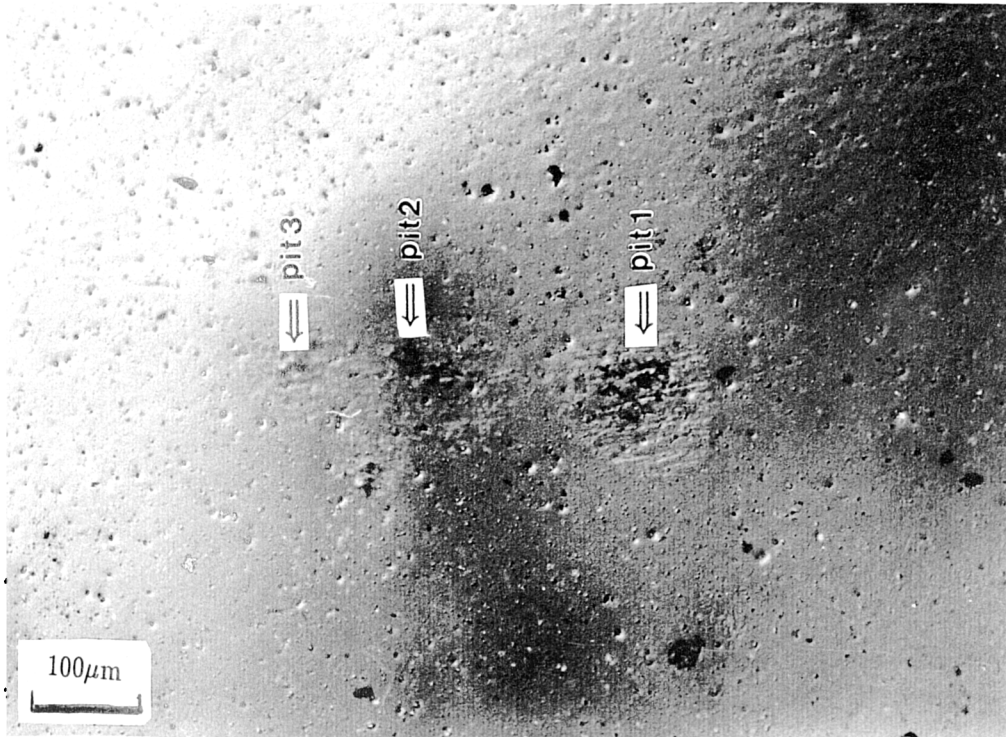


Figure 4 a) Pit formation after 4320 cycles at crack initiation sites 1, 2 and 3

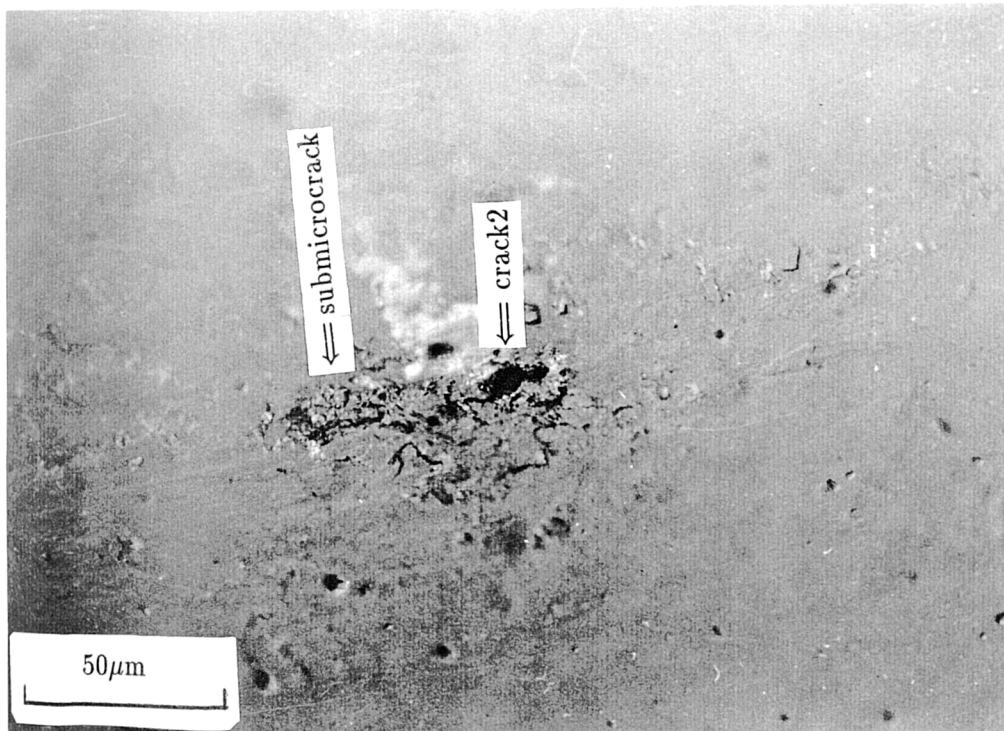


Figure 4.5(b) Microcrack initiation from pits and matrix after 13000 cycles.

Figure 4.5 The evolution of cracks in specimen TC5. The specimen axis is horizontal, $\Delta\tau=728$ MPa, $N_f=174320$, in a 0.6M NaCl solution.

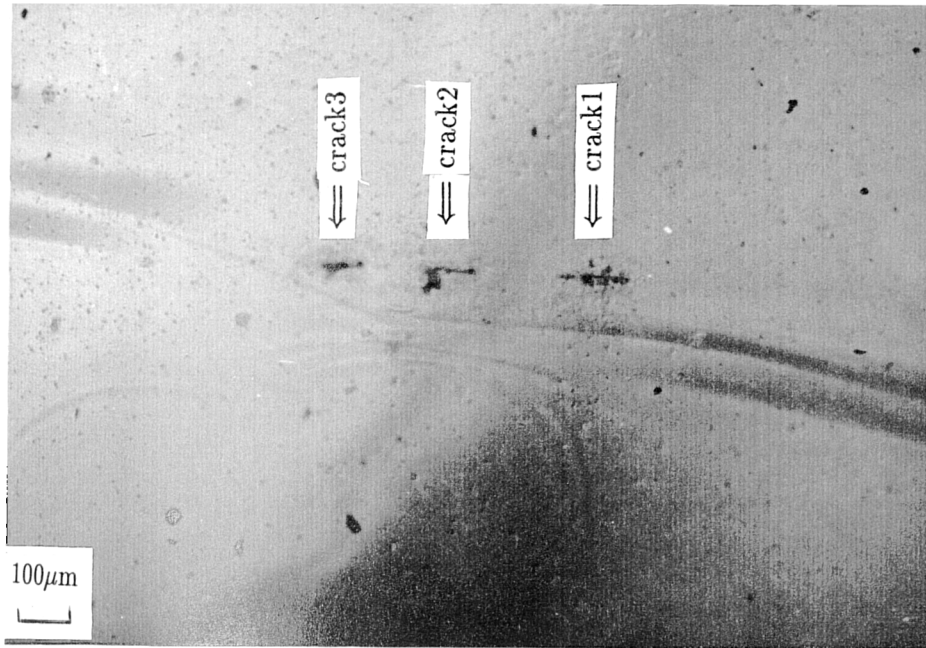


Figure 4 5) Stage I crack propagation after 30000 cycles.

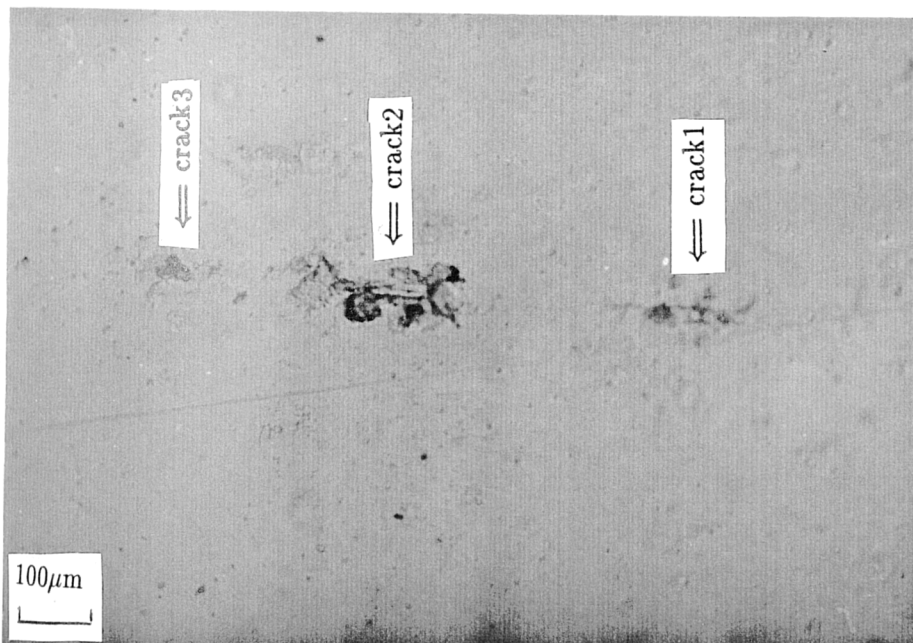


Figure 4.5(d) Crack propagation during stage I to stage II transition after 50000 cycles.

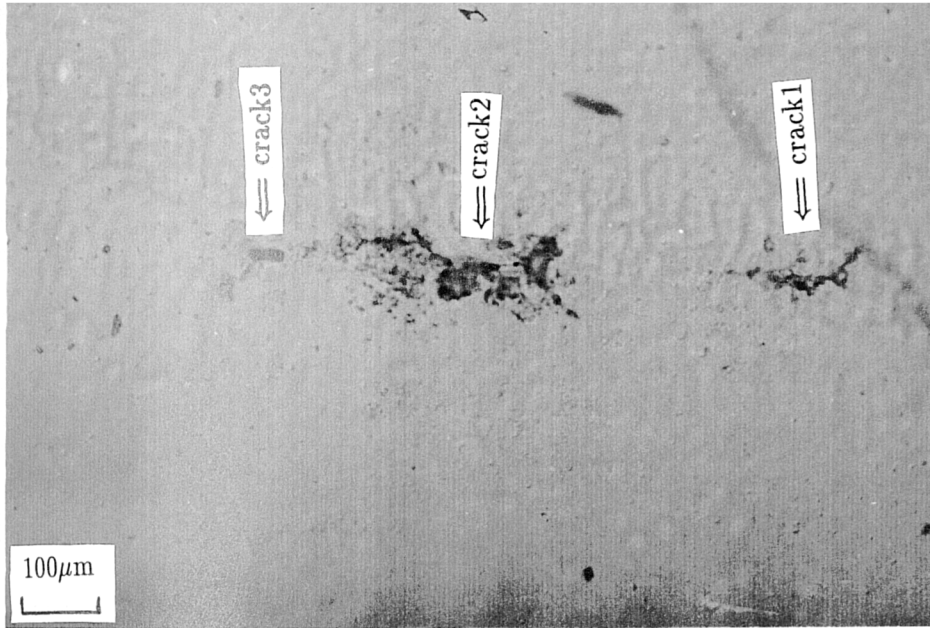


Figure 4.5(e), Stage II crack propagation after 60000 cycles.

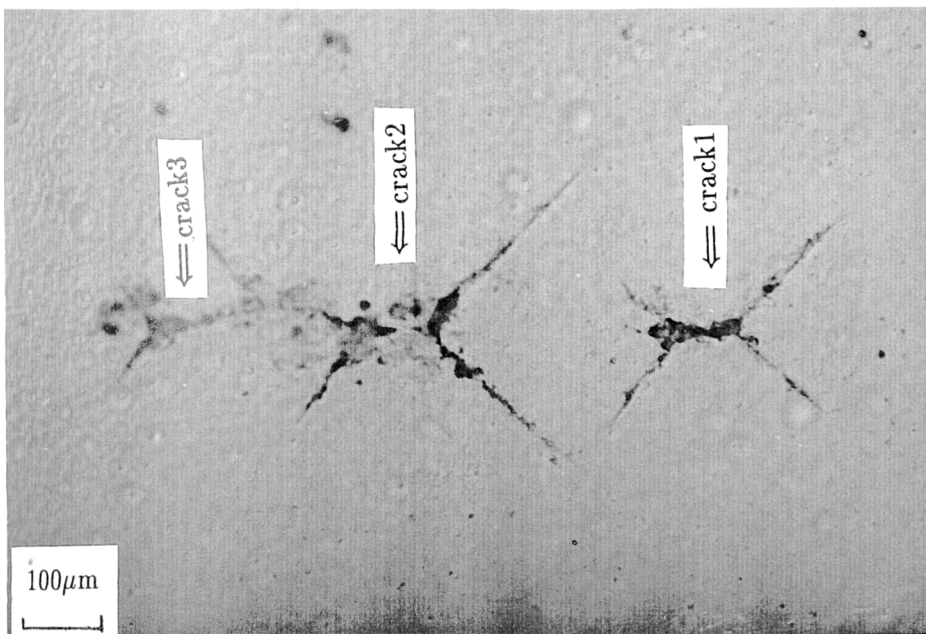


Figure 4.5(f) Crack coalescence after 90000 cycles.

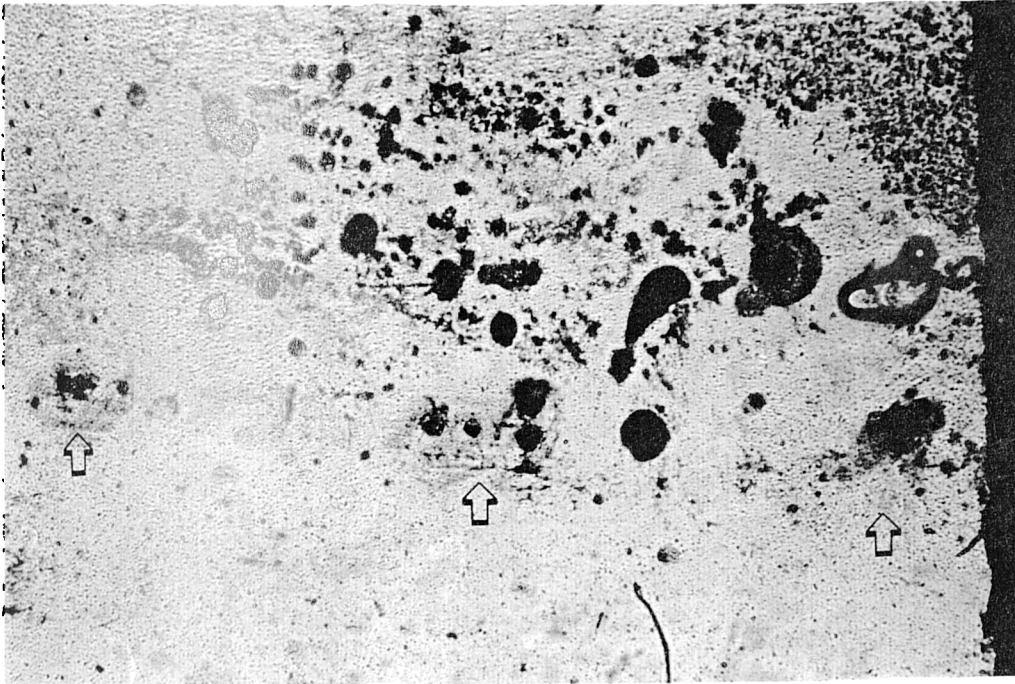


Figure 4.6 (a) Pit formation after 5000 cycles at crack initiation sites.
 $N/N_f = 0.067$.



Figure 4.6(b) Stage I crack initiation from pits after 10000 cycles.
 $N/N_f = 0.13$.

Figure 4.6 The evolution of cracks in specimen TC6. The specimen axis is horizontal, $\Delta\tau = 926$ MPa, $N_f = 73800$, in a 0.6M NaCl solution.
500 μm (the same magnification for (a) to (f)).

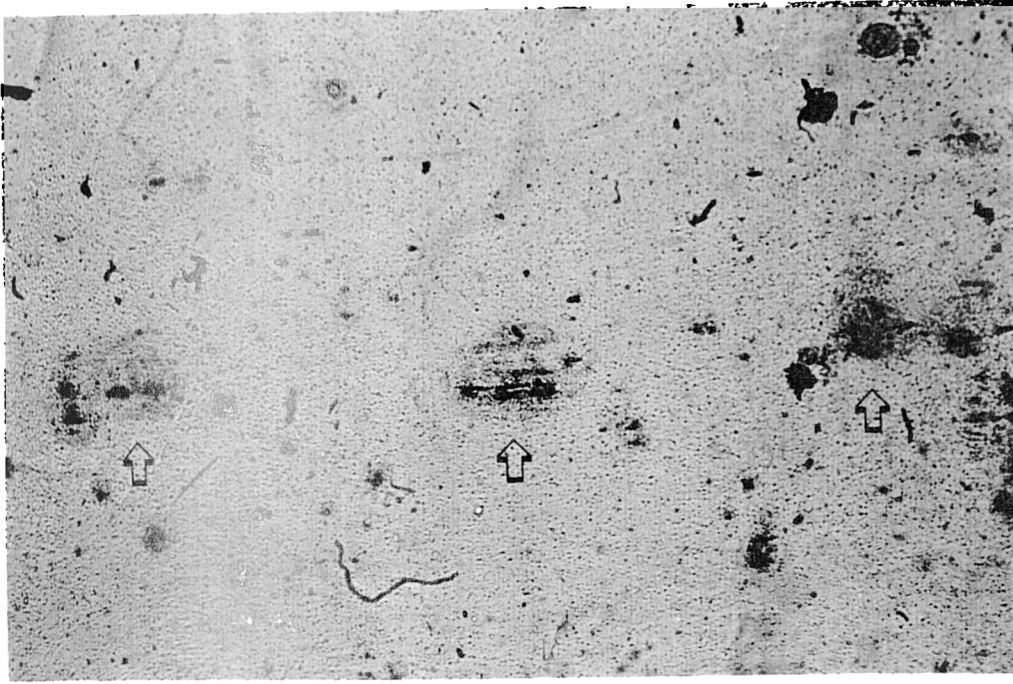


Figure 4.6(c) Stage I crack propagation and transition from stage I to stage II after 15000 cycles. $N/N_f = 0.20$.

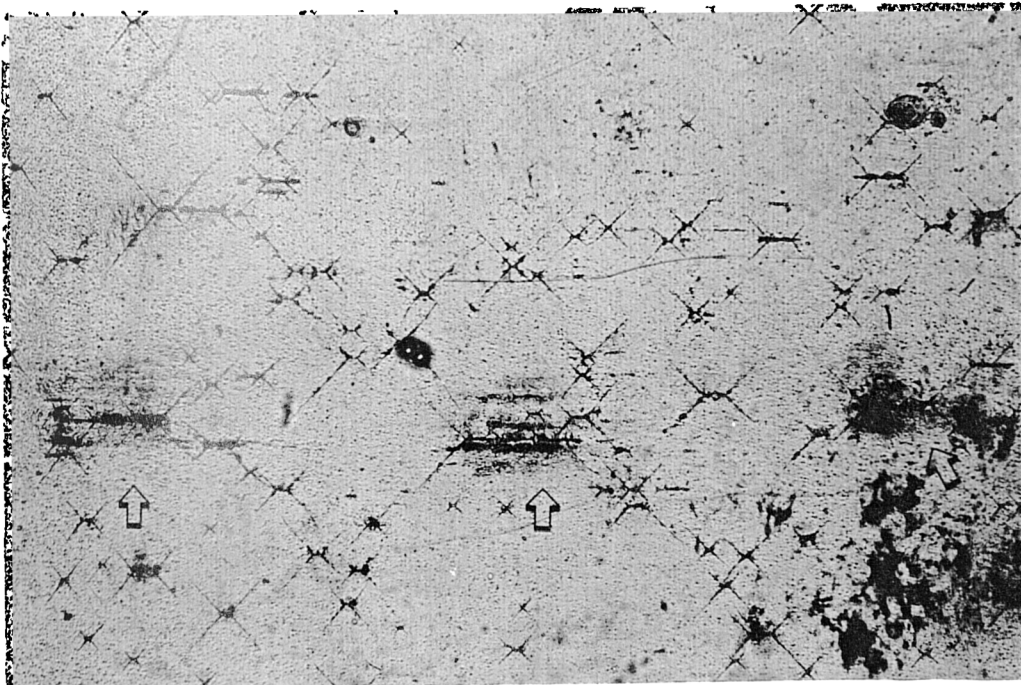


Figure 4.6(d) Stage II crack propagation after 57000 cycles. $N/N_f = 0.77$.

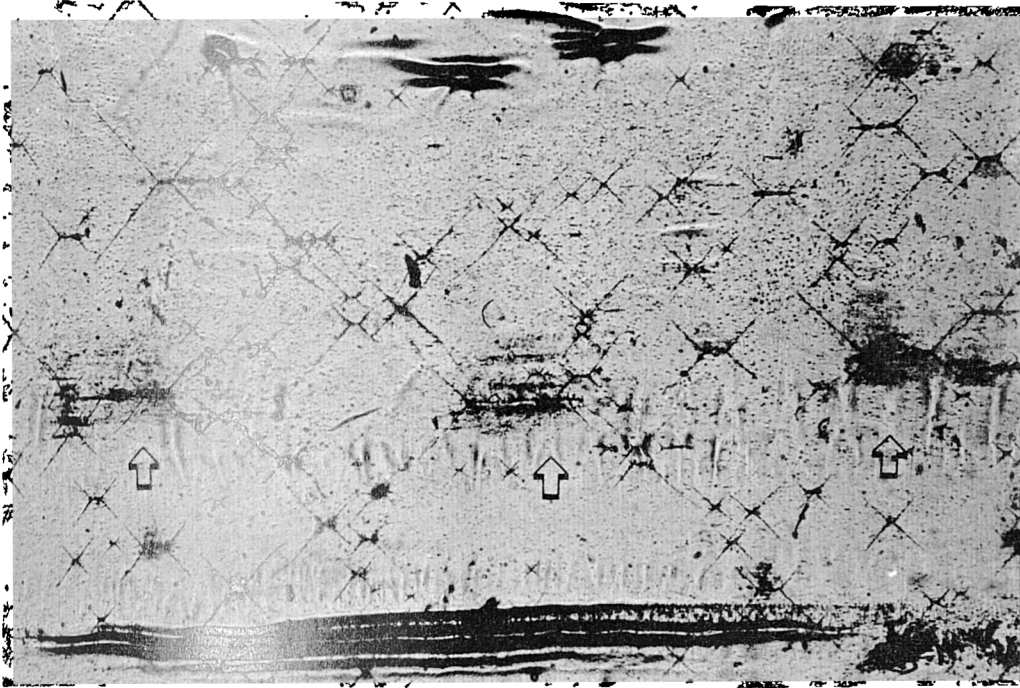


Figure 4 Multiple crack coalescence after 61000 cycles.
 $N/N_f = 0.$

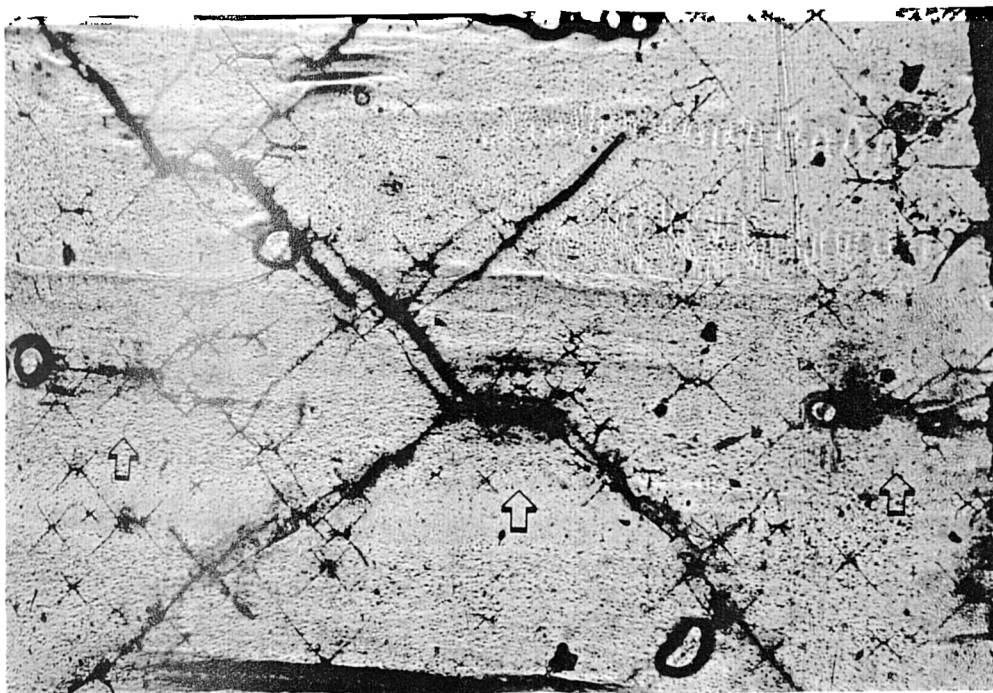


Figure 4.6(f) Fatal crack formation after 72800 cycles. $N/N_f = 0.98.$

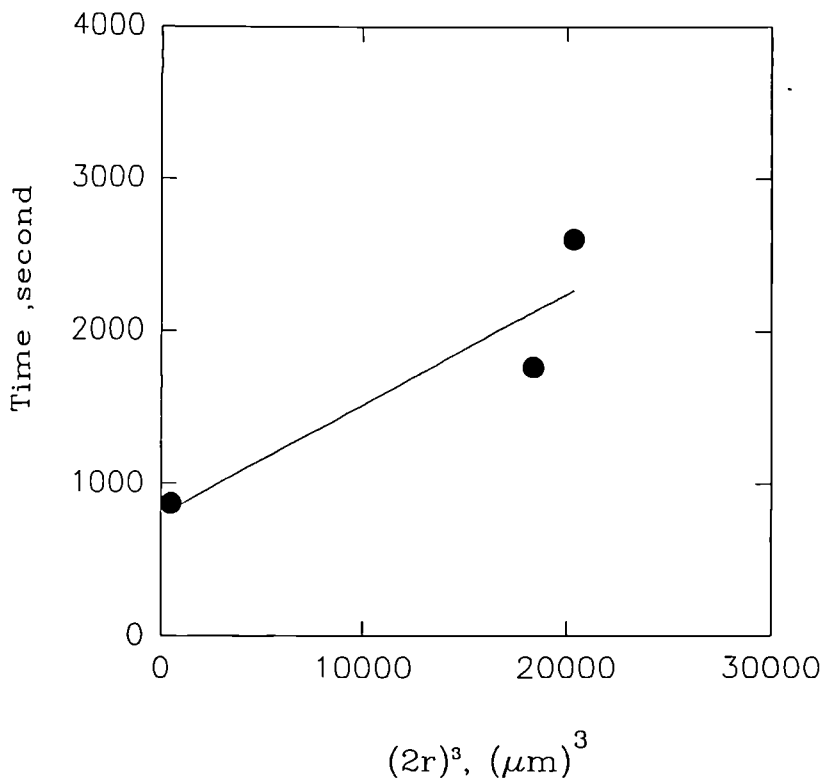
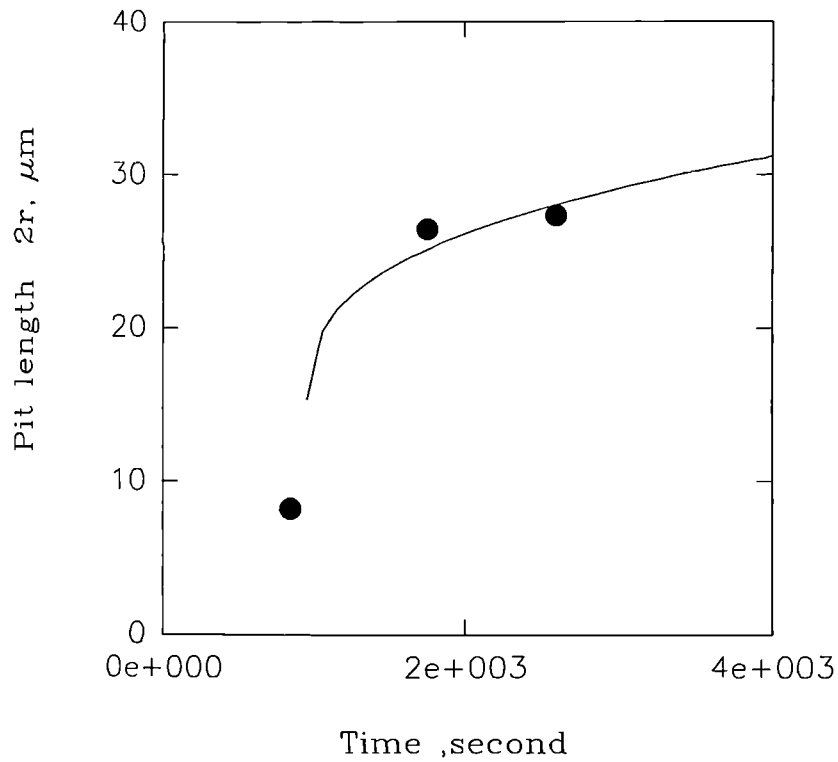


Figure 4.7(a) TC5, $\Delta\tau=728$ MPa.

Figure 4.7 Comparison of pit growth rates at various stress levels. Solid line represents a regression analysis (Equation (4.2)) through the experiment data points

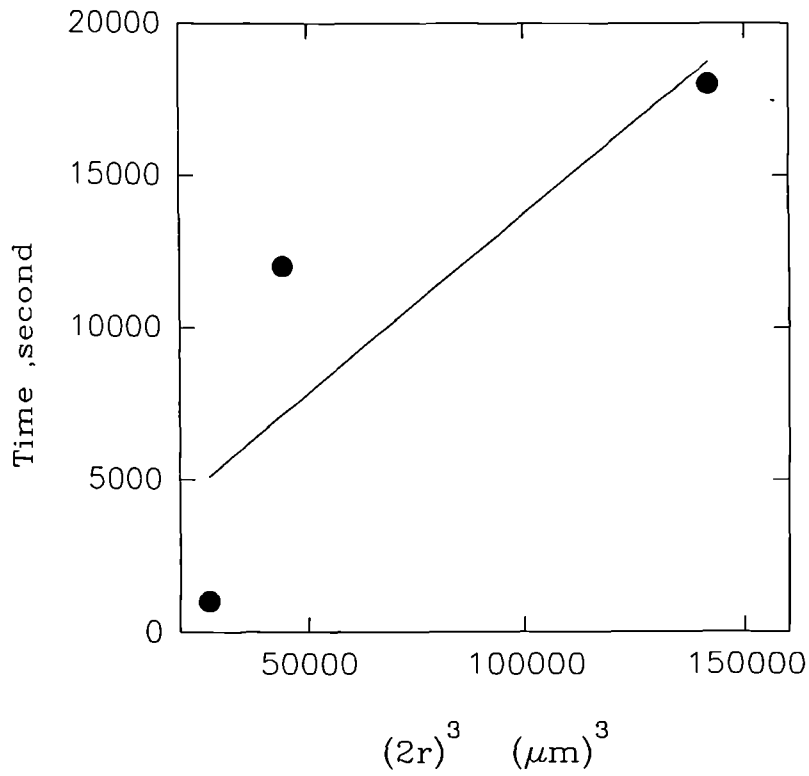
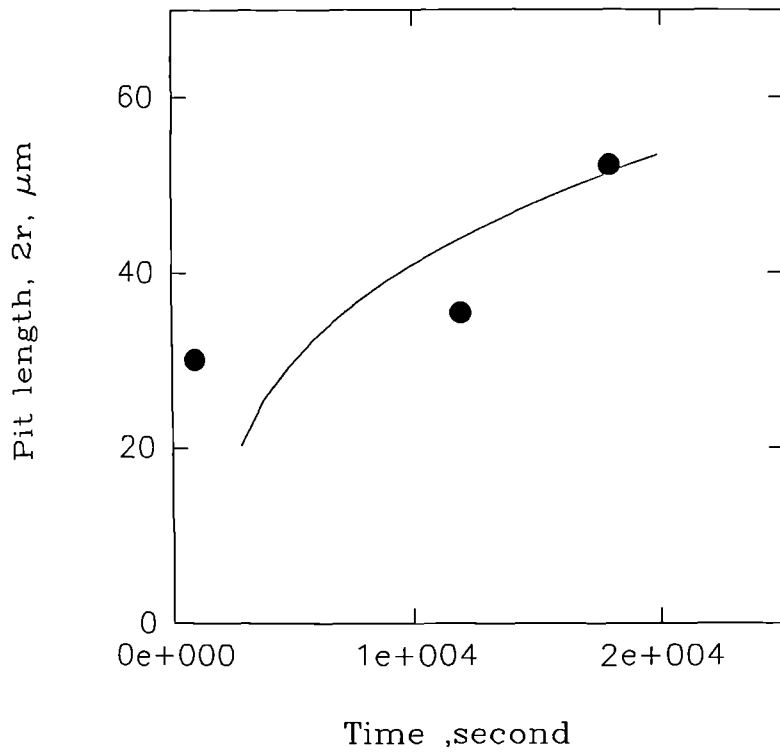


Figure 4.7(b) TC18, $\Delta\tau=613$ MPa.

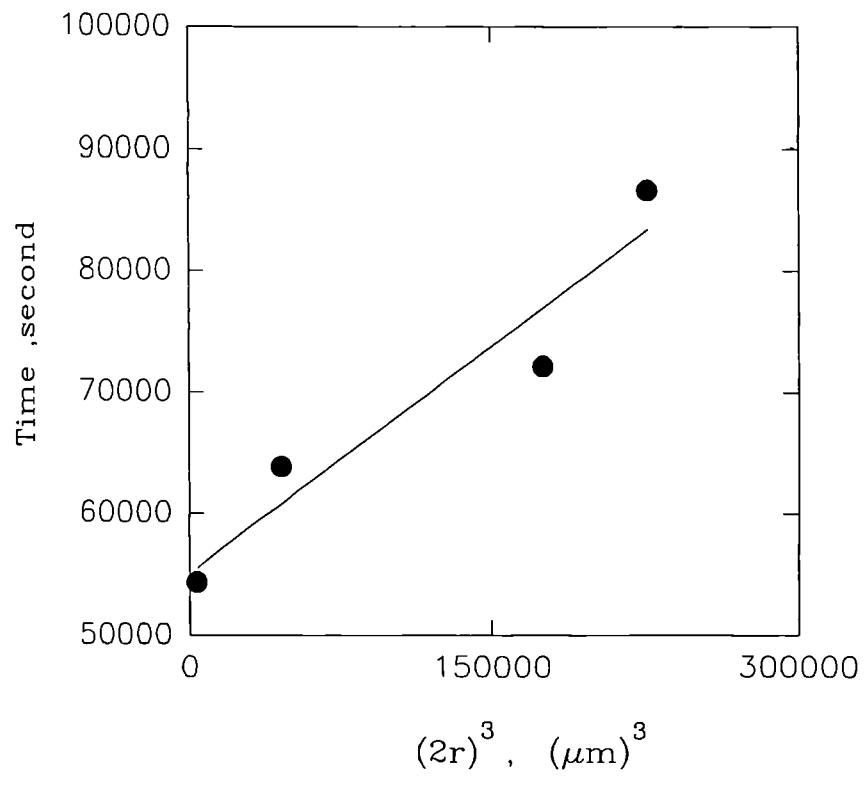
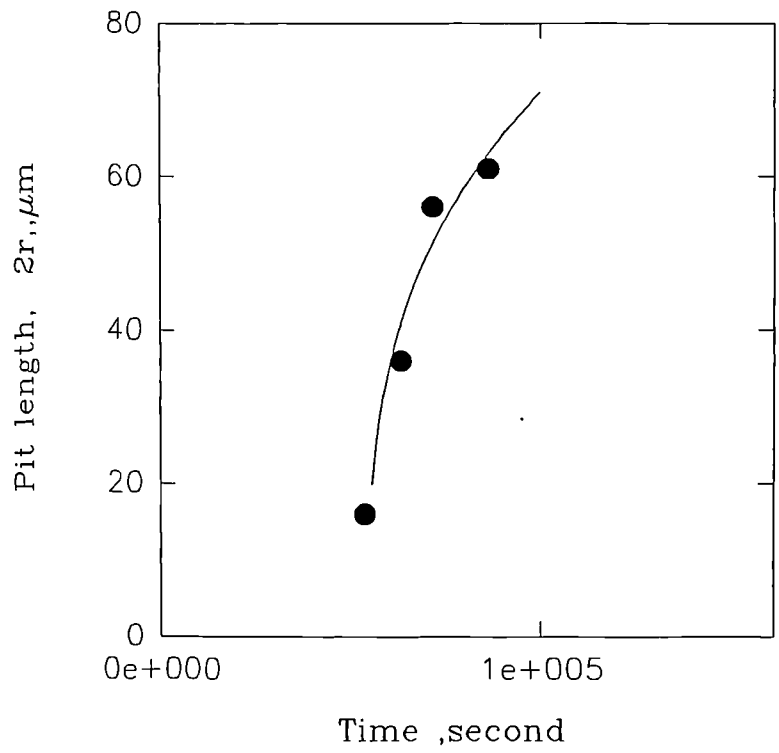


Figure 4.7(c) TC13, $\Delta\tau=415$ MPa.

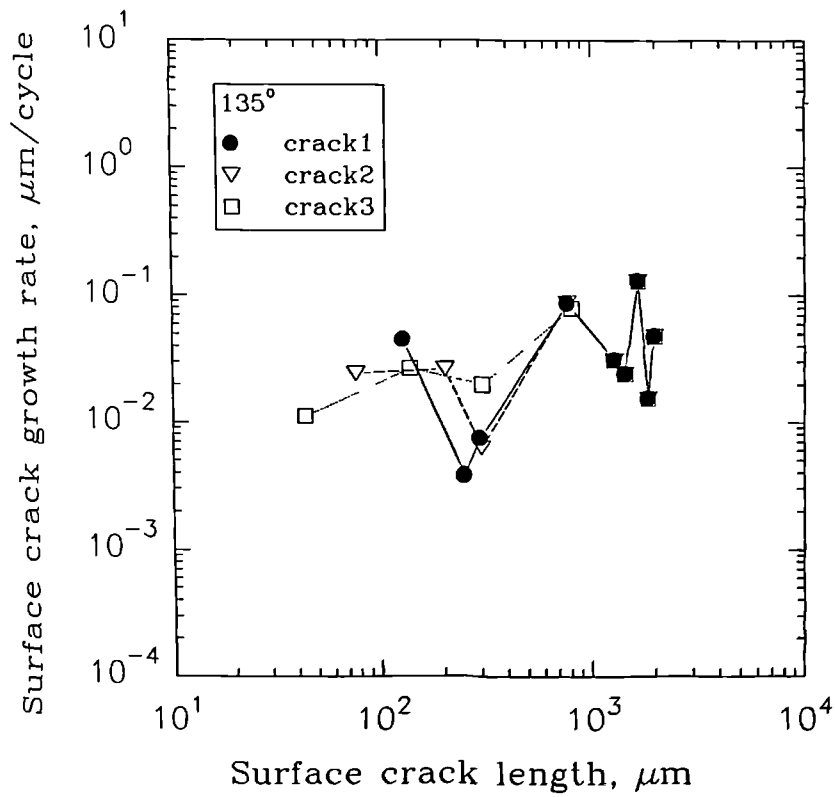
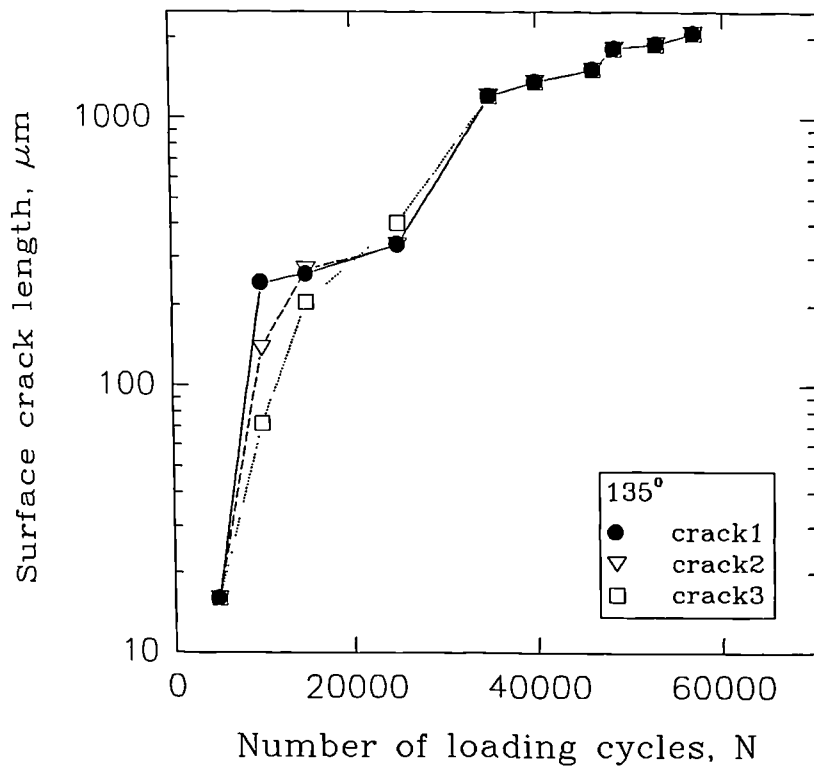


Figure 4.8(a) Major fatigue crack growth rates for three cracks in specimen TC6, $\Delta\tau=926$ MPa, in a 0.6M NaCl solution.

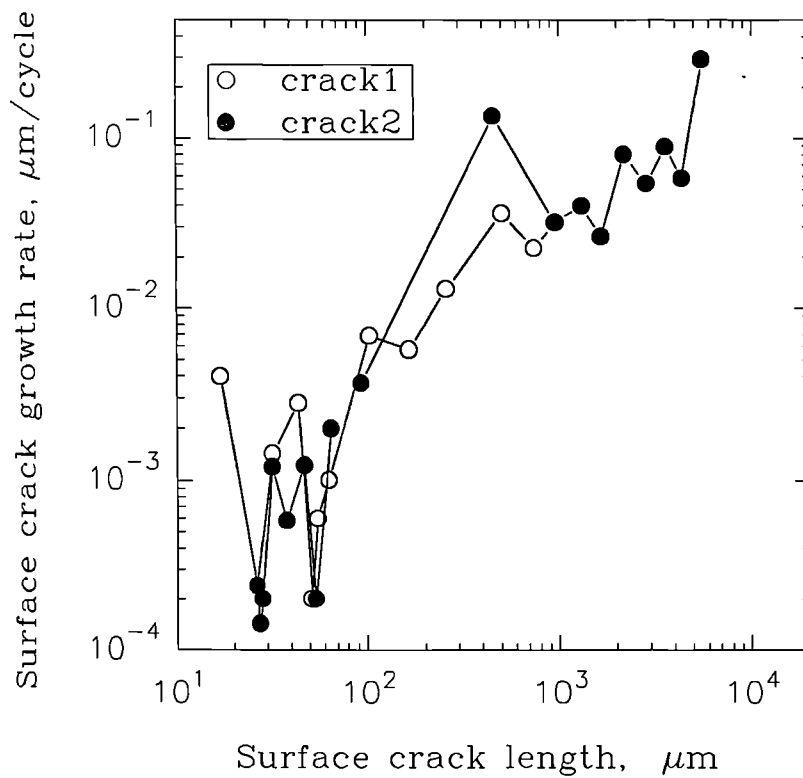
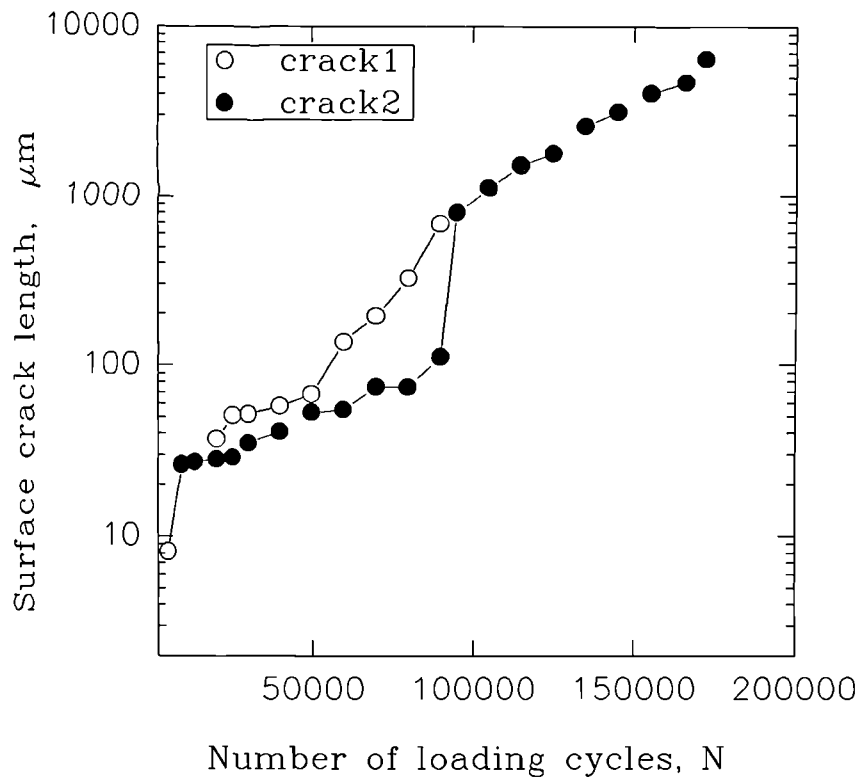


Figure 4.8(b) Major fatigue crack growth rates for two cracks in specimen TC5, $\Delta\tau=728$ MPa, in a 0.6M NaCl solution.

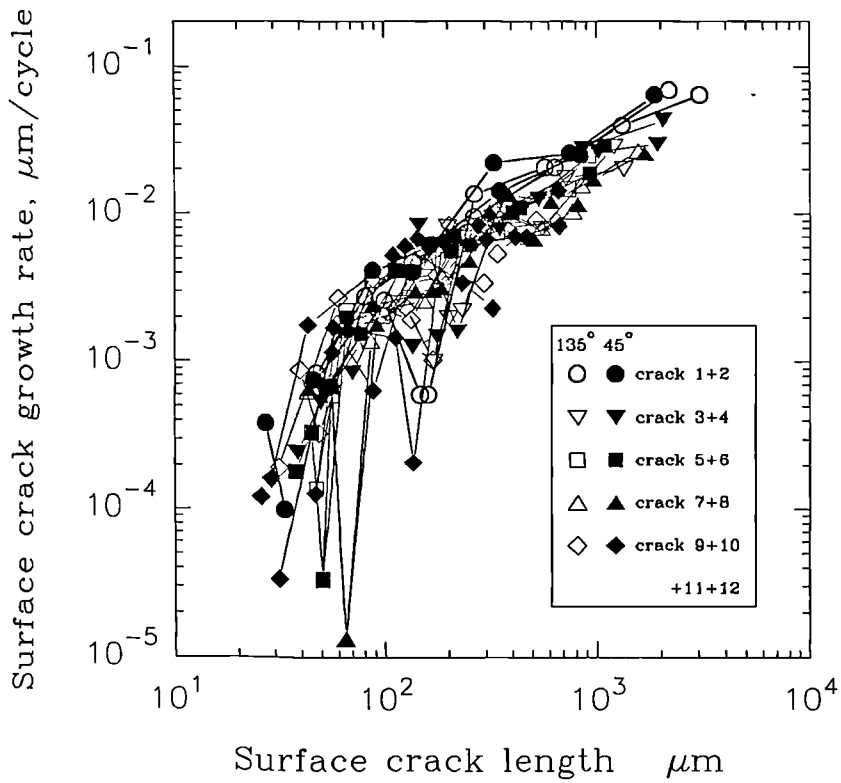
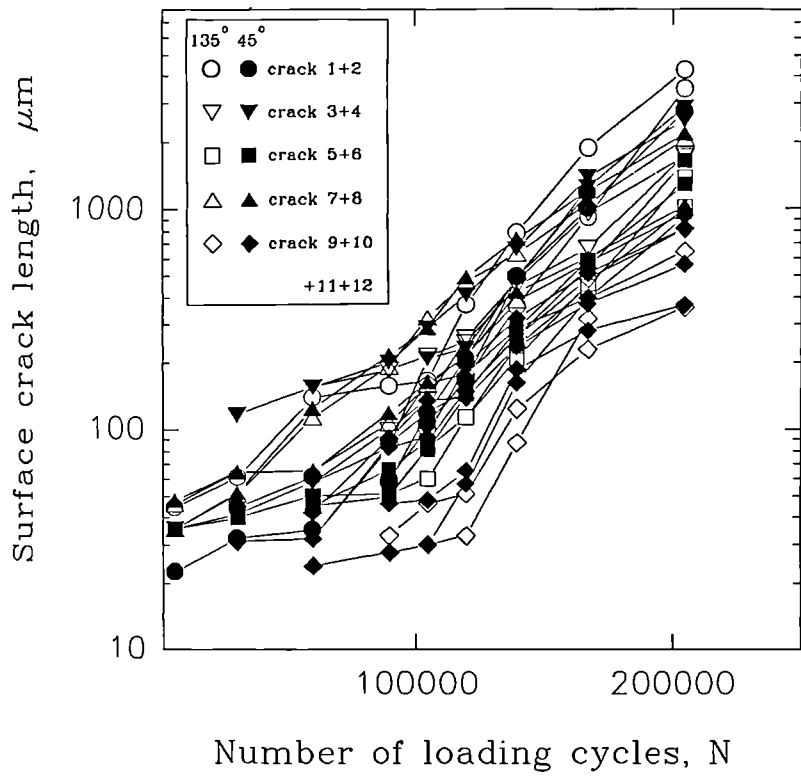


Figure 4.8(c) Fatigue crack growth rates for twelve cracks in specimen TC18, $\Delta\tau=613$ MPa, in a 0.6M NaCl solution. Note that the stage II crack growth direction is at either 45° or 135° to the specimen axis.

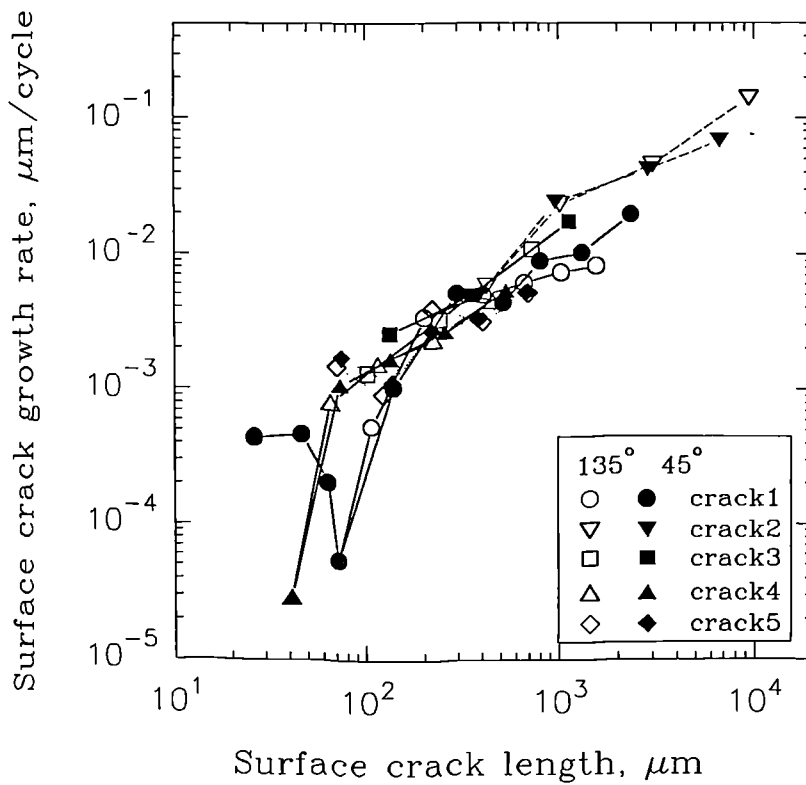
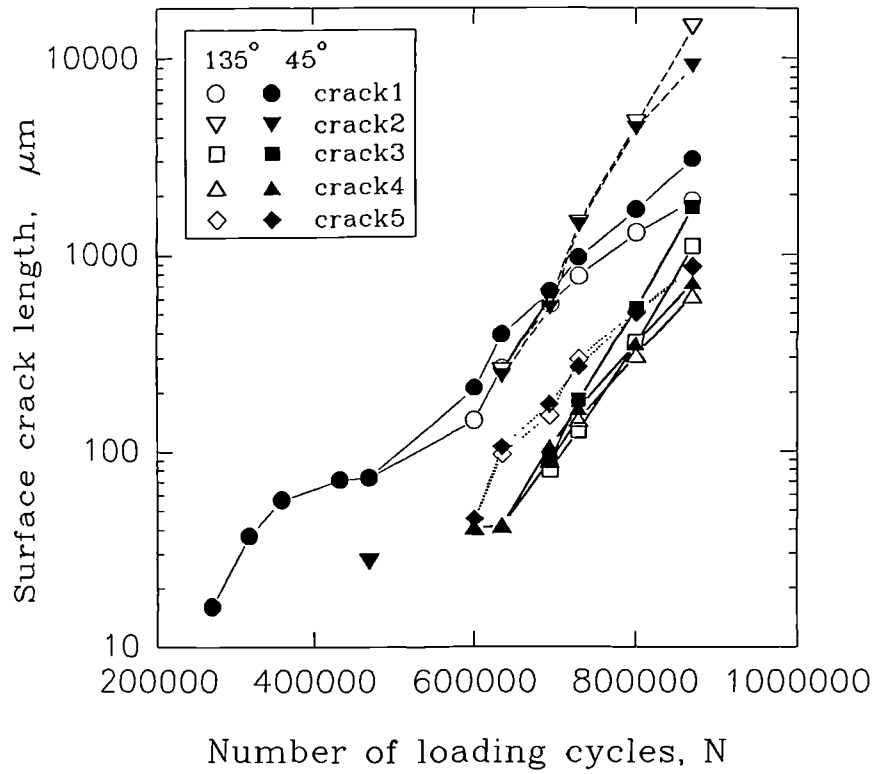


Figure 4.8(d) Fatigue crack growth rates for five cracks in specimen TC13, $\Delta\tau=415$ MPa, in a 0.6M NaCl solution.

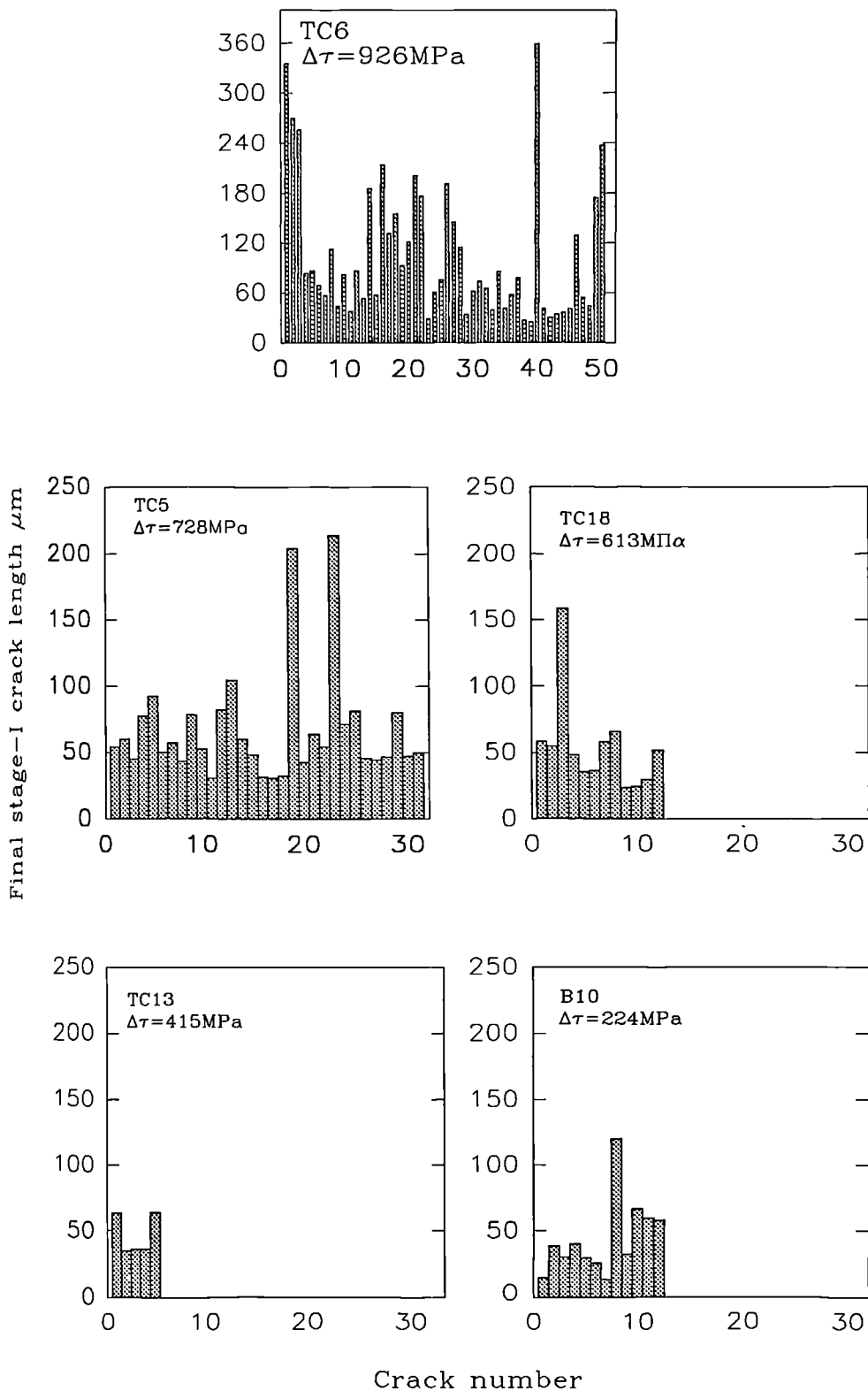


Figure 4.9 Stage I crack length measured at stage I-stage II crack transition point under different stress ranges for specimen TC6, $\Delta\tau=926$ MPa; specimen TC5, $\Delta\tau=728$ MPa; specimen TC18, $\Delta\tau=613$ MPa; specimen TC13, $\Delta\tau=415$ MPa; and specimen B10, $\Delta\tau=224$ MPa.

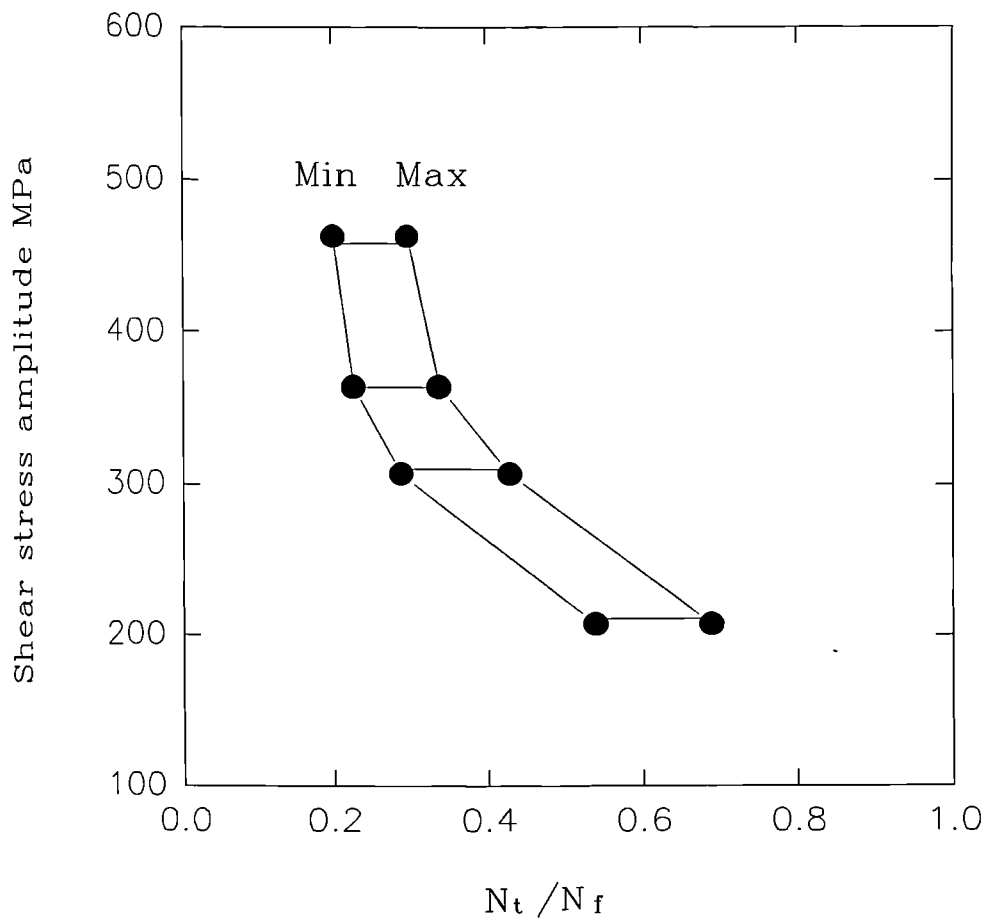


Figure 4.10 Minimum and maximum proportion of cycles required for the transition from stage I to stage II crack propagation. N_t =number of cycles to stage I-stage II transition, N_f = total number of cycles to failure.

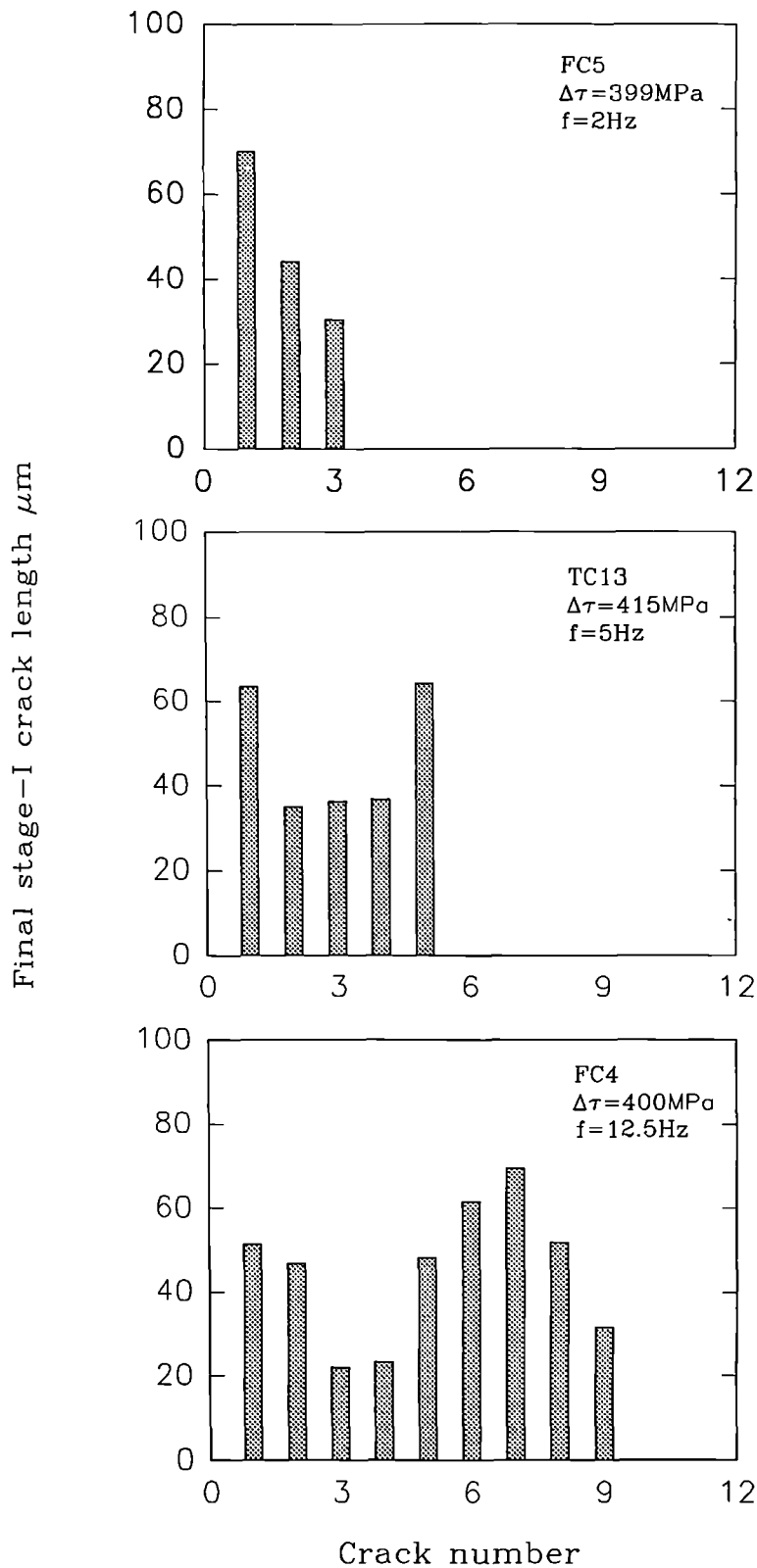


Figure 4.11(a) Final stage I crack length at frequencies of 2Hz, 5Hz and 12.5 Hz, $\Delta\tau \approx 400\text{MPa}$.

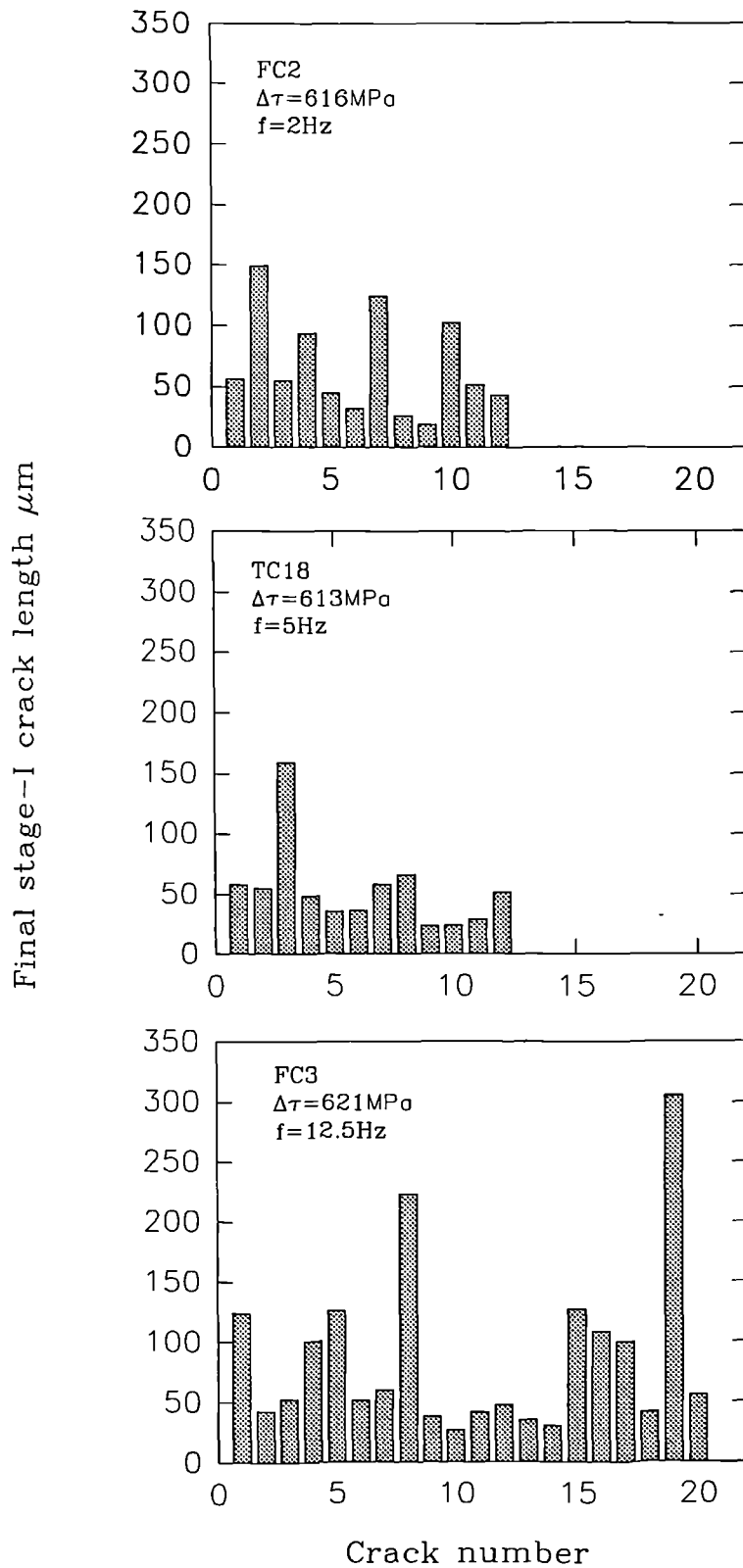


Figure 4.11(b) Final stage I crack length at frequencies of 2Hz, 5Hz and 12.5 Hz, $\Delta\tau \approx 600\text{MPa}$.

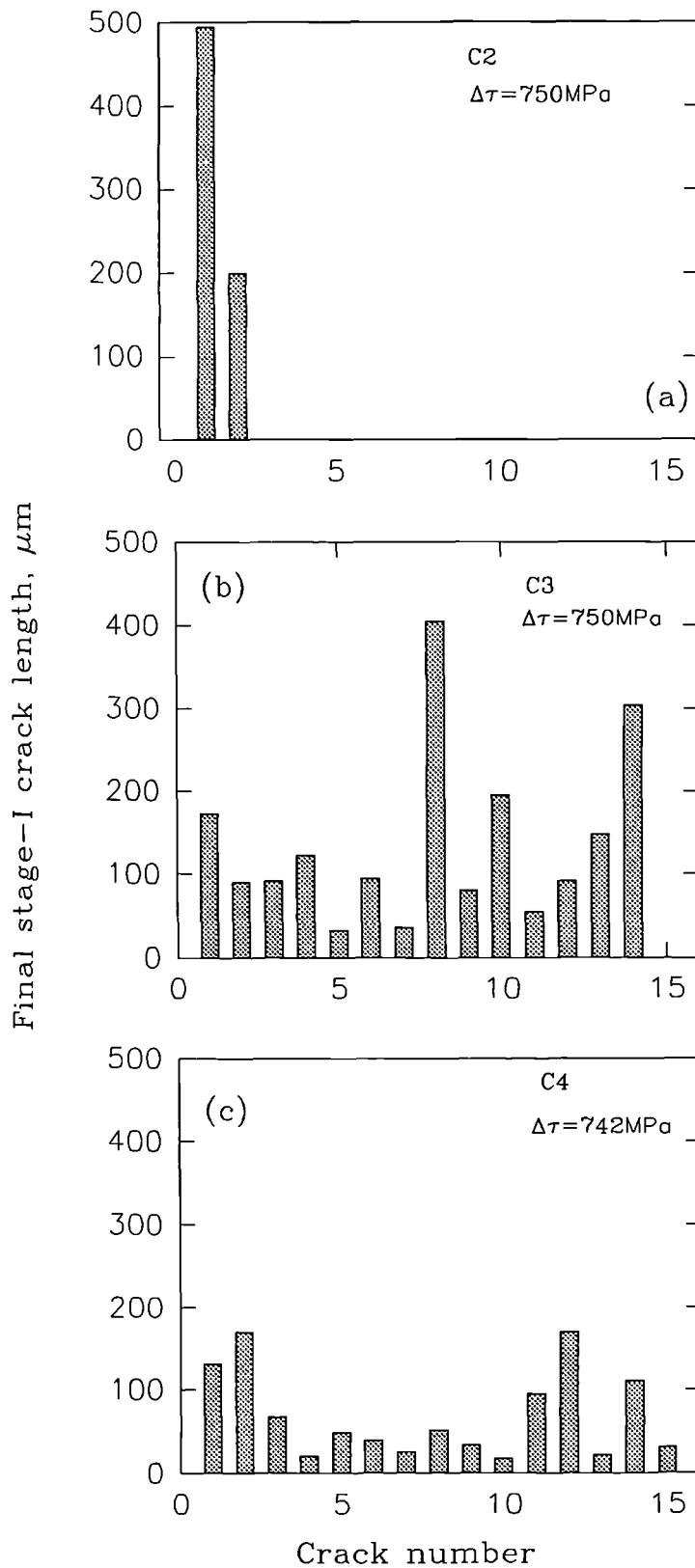


Figure 4.12 Final stage I crack length in different environments: (a) Specimen C2 with cathodic polarisation, $E=-1280$ mv (SCE); (b) Specimen C3, initially under free corrosion potential condition, then followed by cathodic polarisation after 45000 cycles ($N/N_f = 0.25$); (c) Specimen C4 under free corrosion potential.

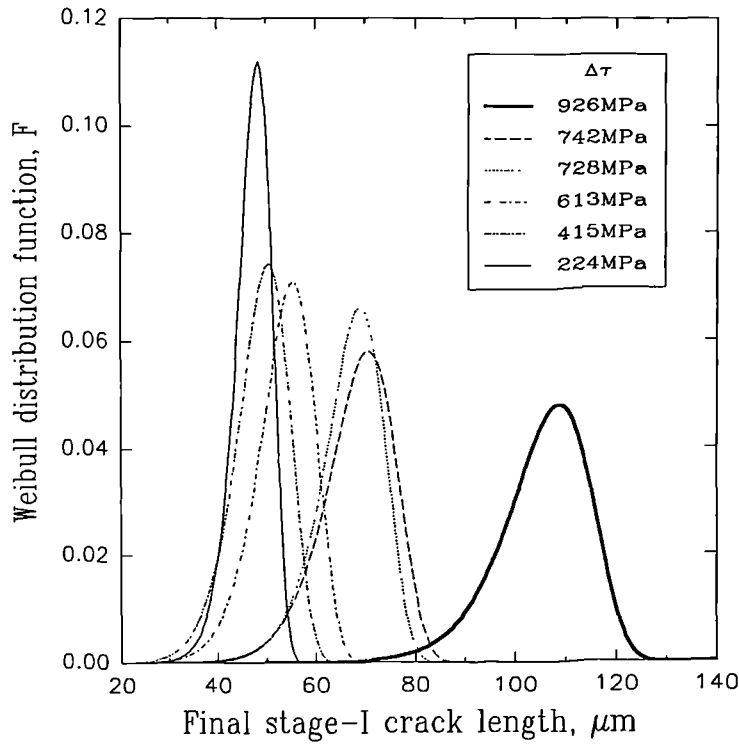


Figure 4.13(a) Weibull distribution function for final stage I crack length under different stress levels for specimen TC6, $\Delta\tau=926$ MPa; specimen TC5, $\Delta\tau=728$ MPa; specimen TC18, $\Delta\tau=613$ MPa; specimen TC13, $\Delta\tau=415$ MPa; and specimen B10, $\Delta\tau=224$ MPa.

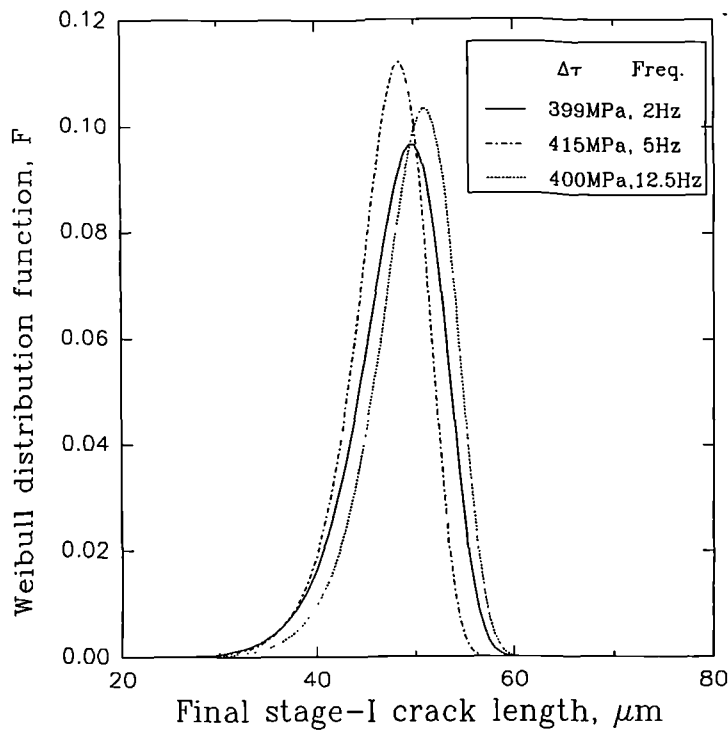


Figure 4.13(b) Weibull distribution function for final stage I crack length at different frequencies for the stress range of approximately 400 MPa.

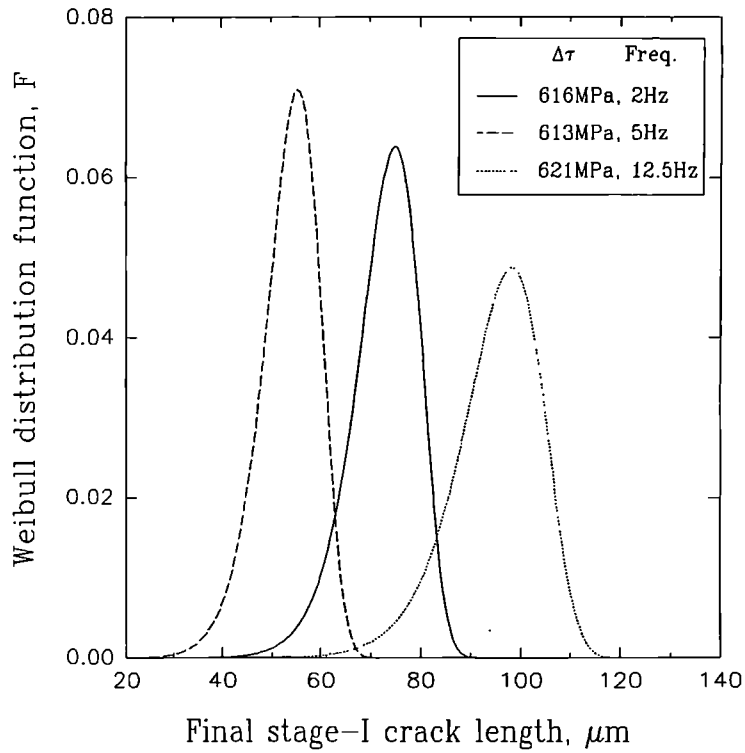


Figure 4.13(c) Weibull distribution function for final stage I crack length at different frequencies for the stress range of approximately 600 MPa.

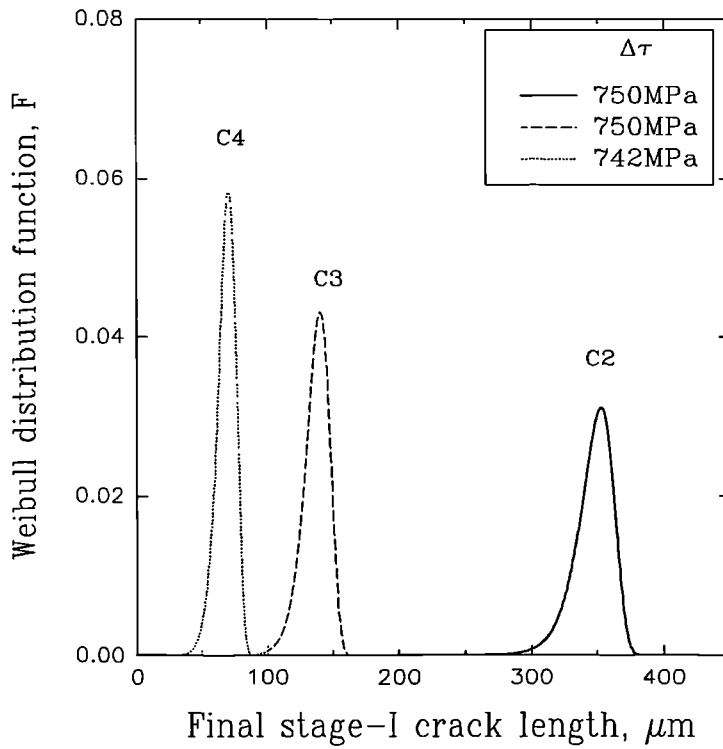


Figure 4.13(d) Weibull distribution function for final stage I crack length in different environments for specimens C2, C3 and C4.

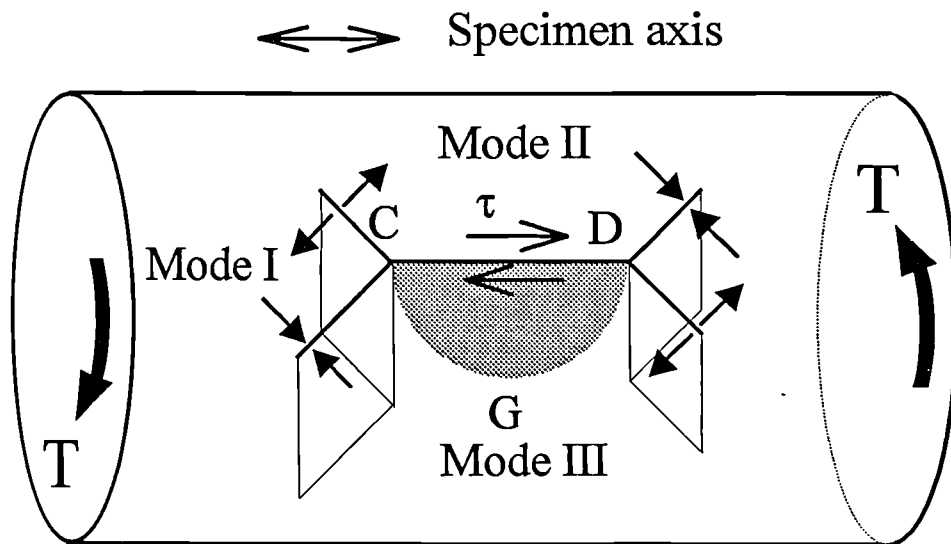


Figure 4.14 (a) Schematic view of stress state for a stage I crack on the surface of a specimen subjected to torsion.

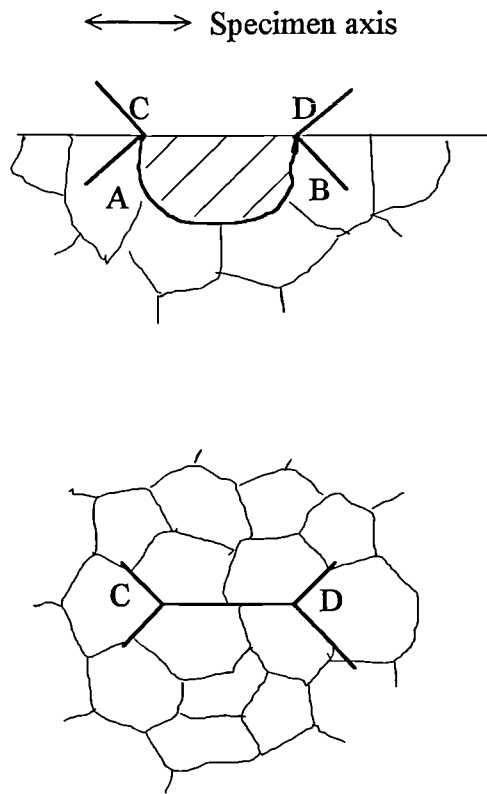


Figure 4.14 (b) Schematic view of surface stage I/II crack transition occurring at two ends of stage I crack, C-D.

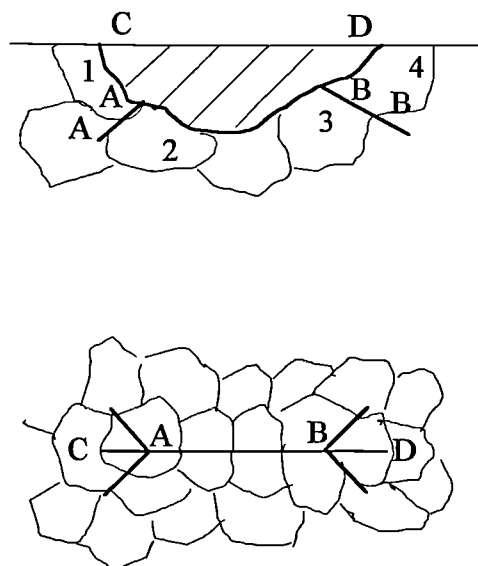


Figure 4.14 (c) Schematic view of sub-surface stage I/II crack transition occurring at the bottom of stage I crack, A-B.

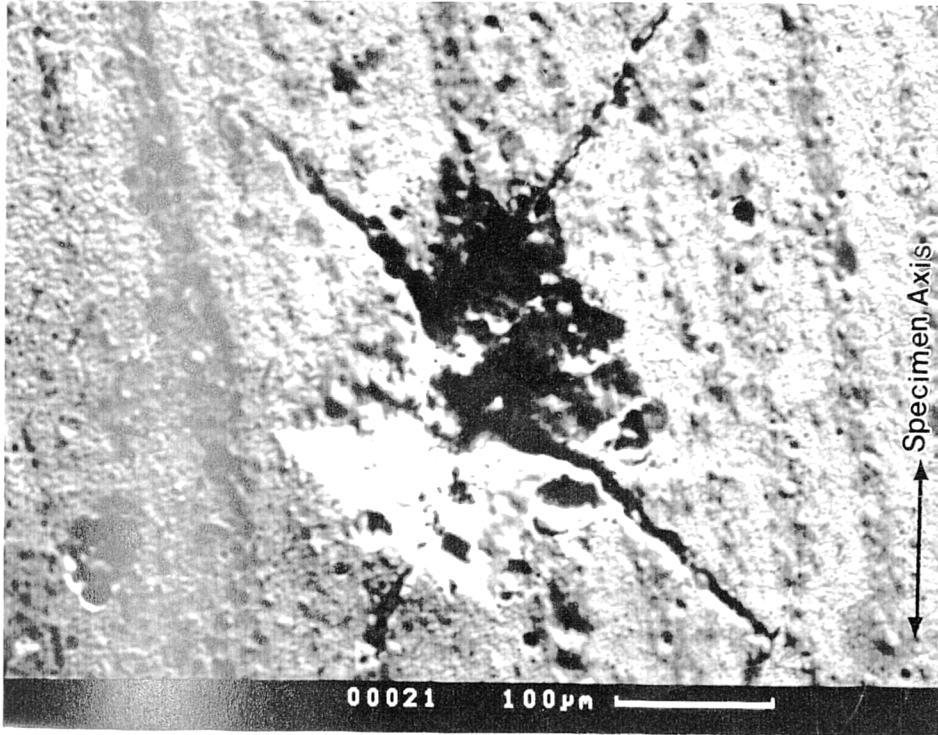


Figure 4.15 (a) SEM morphology showing stage II cracking from the bottom of the stage I crack.

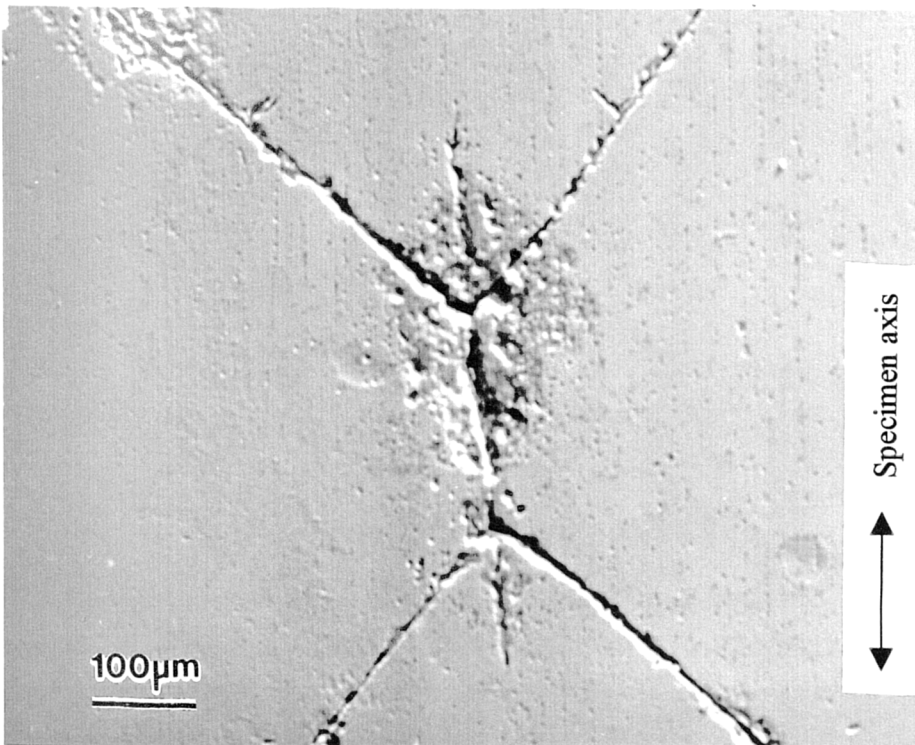


Figure 4.15 (b) SEM morphology showing stage II cracking from the bottom of the stage I crack.

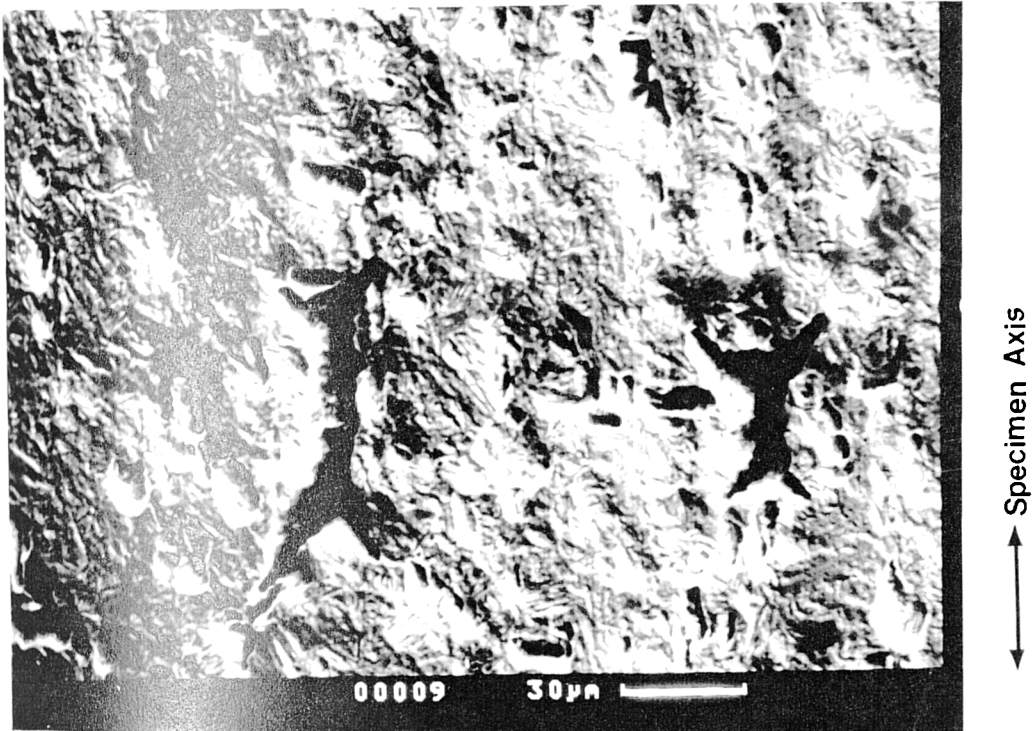


Figure 4 15(c) SEM morphology showing crack transition from stage I to stage II.

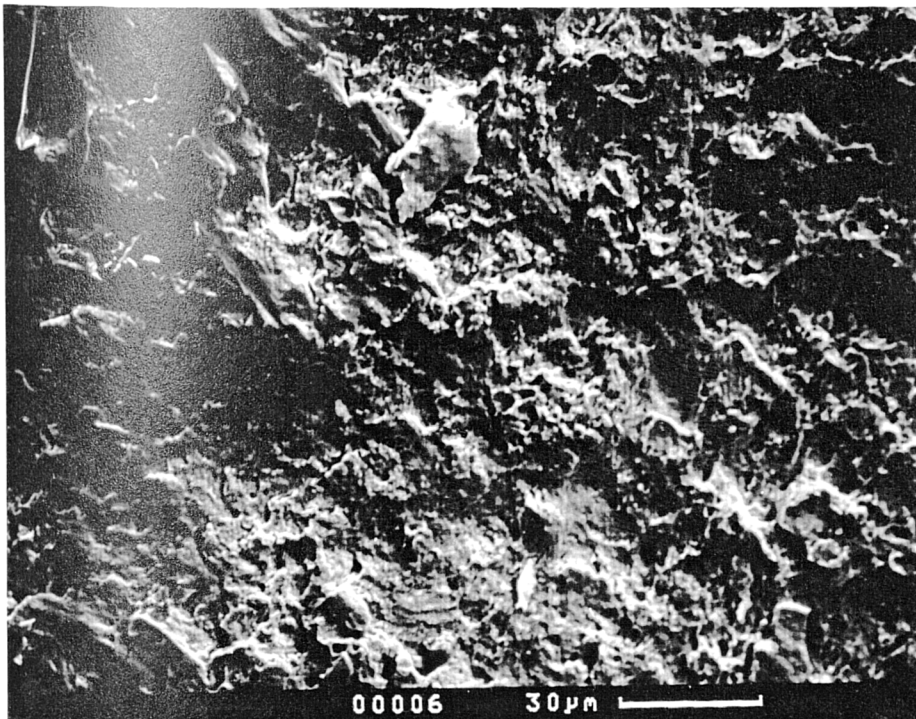
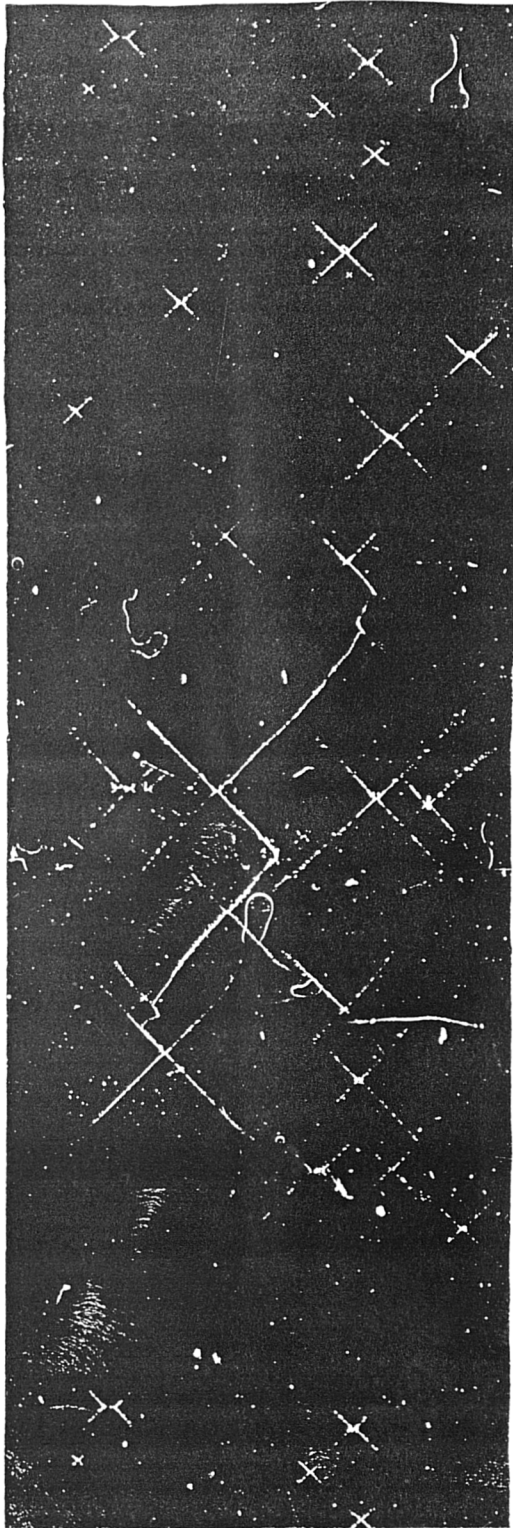


Figure 4.16 SEM fractography of stage II crack propagation path, indicating the cleavage-like fracture and low ductility boundary separation.



— 1 mm, \leftarrow — \rightarrow Specimen Axis

Figure 4.17(a) Multiple crack coalescence on the surface of the specimen in the final stages of corrosion fatigue for specimen TC5, $\Delta\tau=728$ MPa.



— 2 mm, ◀ — ▶ Specimen Axis

Figure 4.17(b) Crack coalescence on the surface of the specimen in the final stages of corrosion fatigue for specimen TC18, $\Delta\tau=613$ MPa.

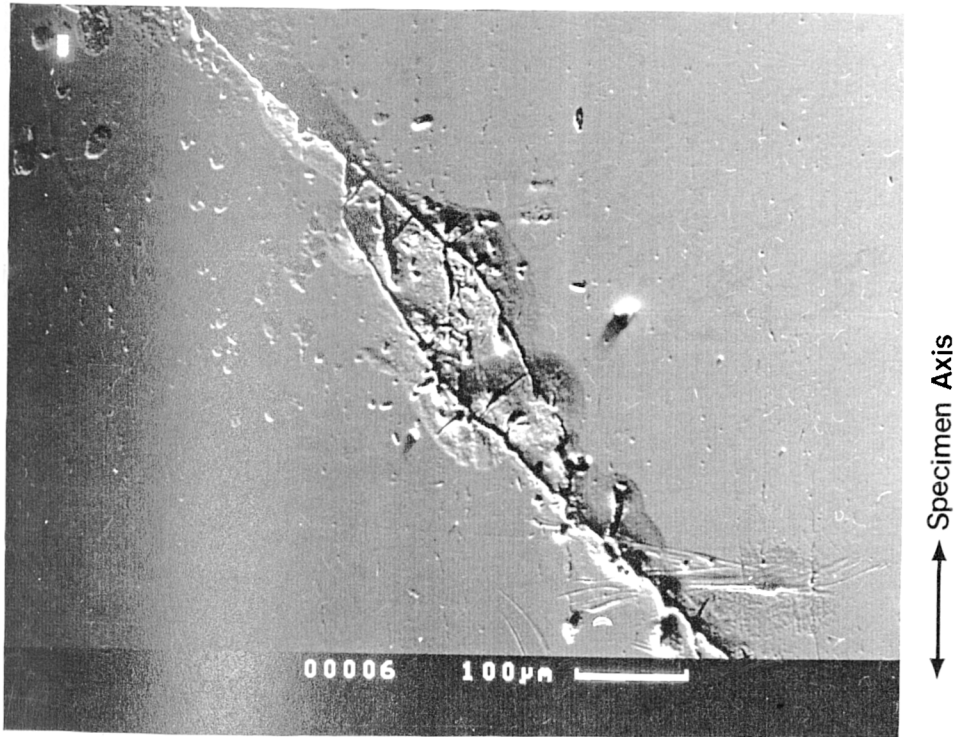


Figure 4.17(c) Coalescence of two parallel off-plane cracks.

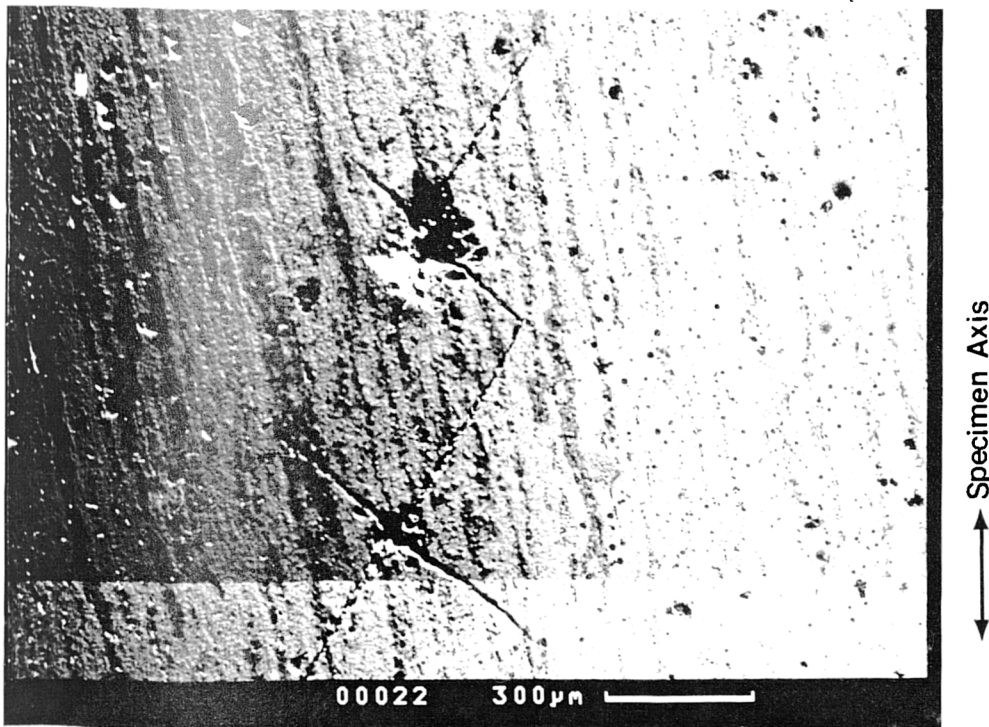


Figure 4.17(d) Coalescence of two perpendicular cracks.

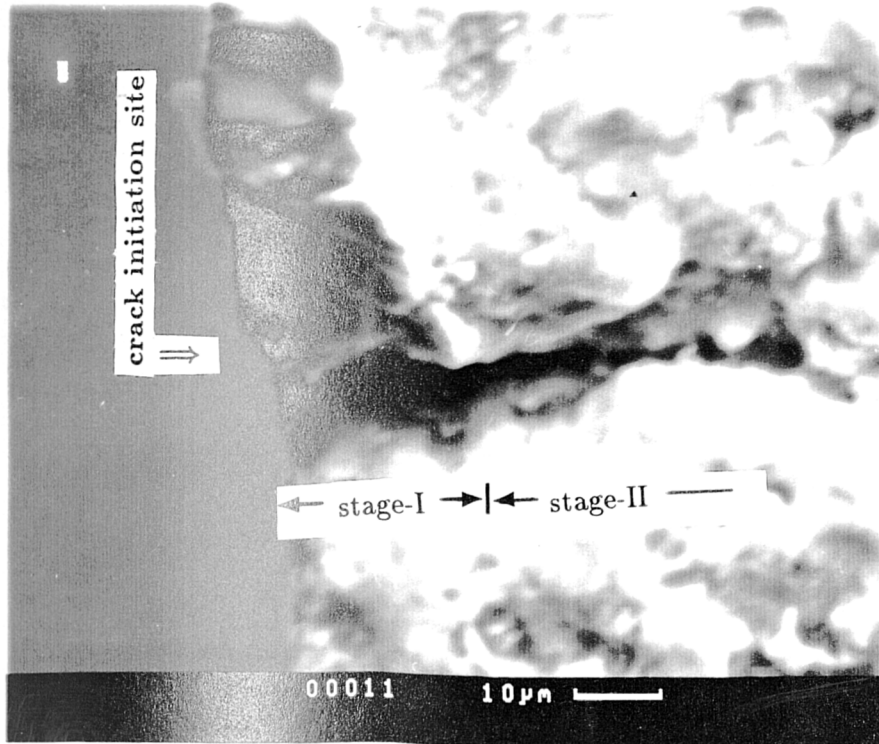
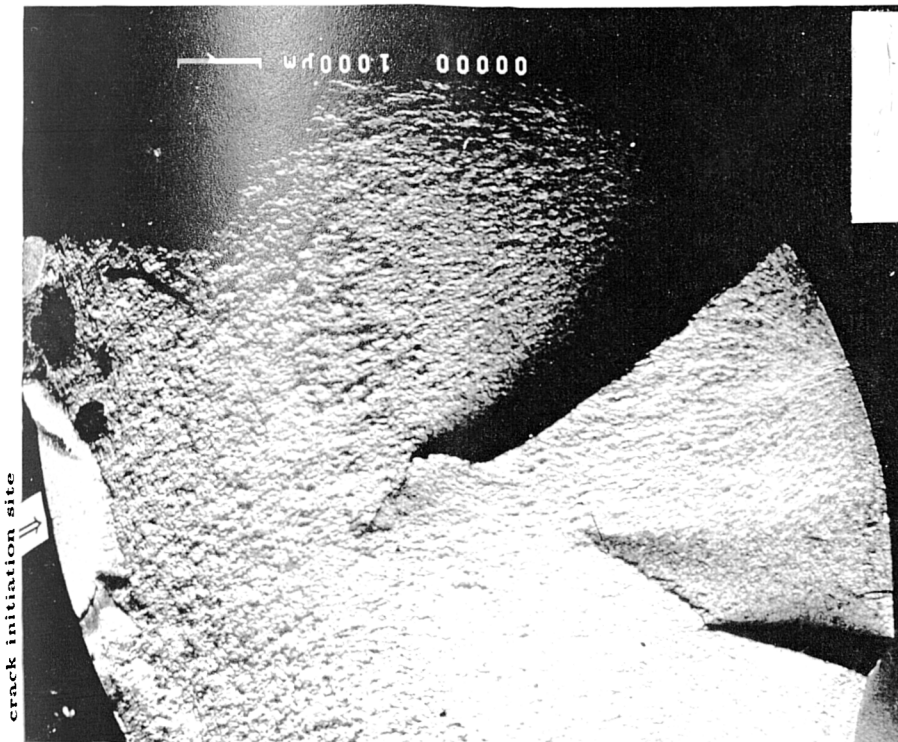


Figure 4.18 (a) Overview of fracture surface of specimen TC5 (b) Close view of crack initiation site, and crack propagation in stage I and stage II, $\Delta\tau = 728$ MPa.

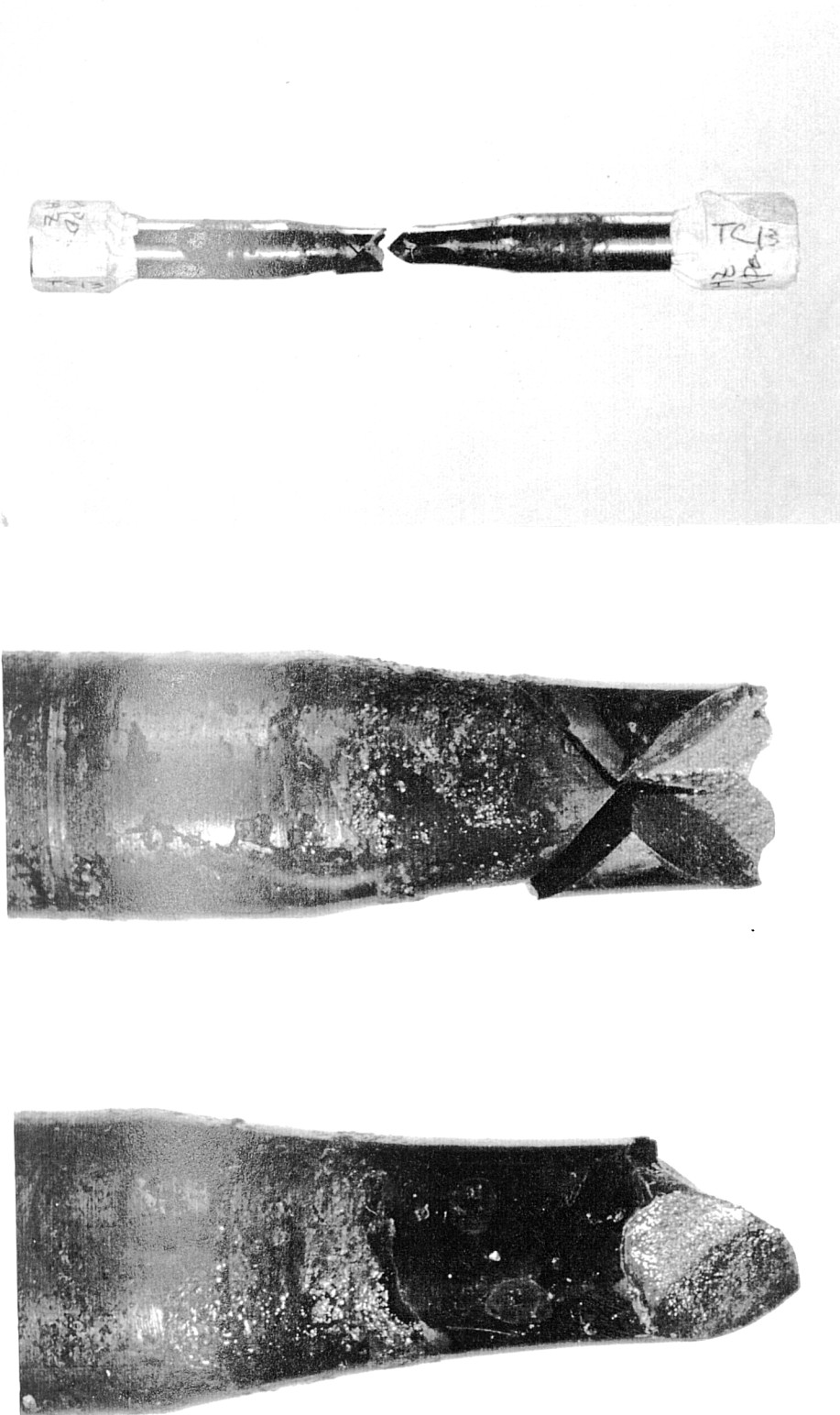


Figure 4.19(a) 'Shell marks' on the fracture surface of specimen TC13, $\Delta\tau=415$ MPa, $f= 5$ Hz, 0.6M NaCl solution.

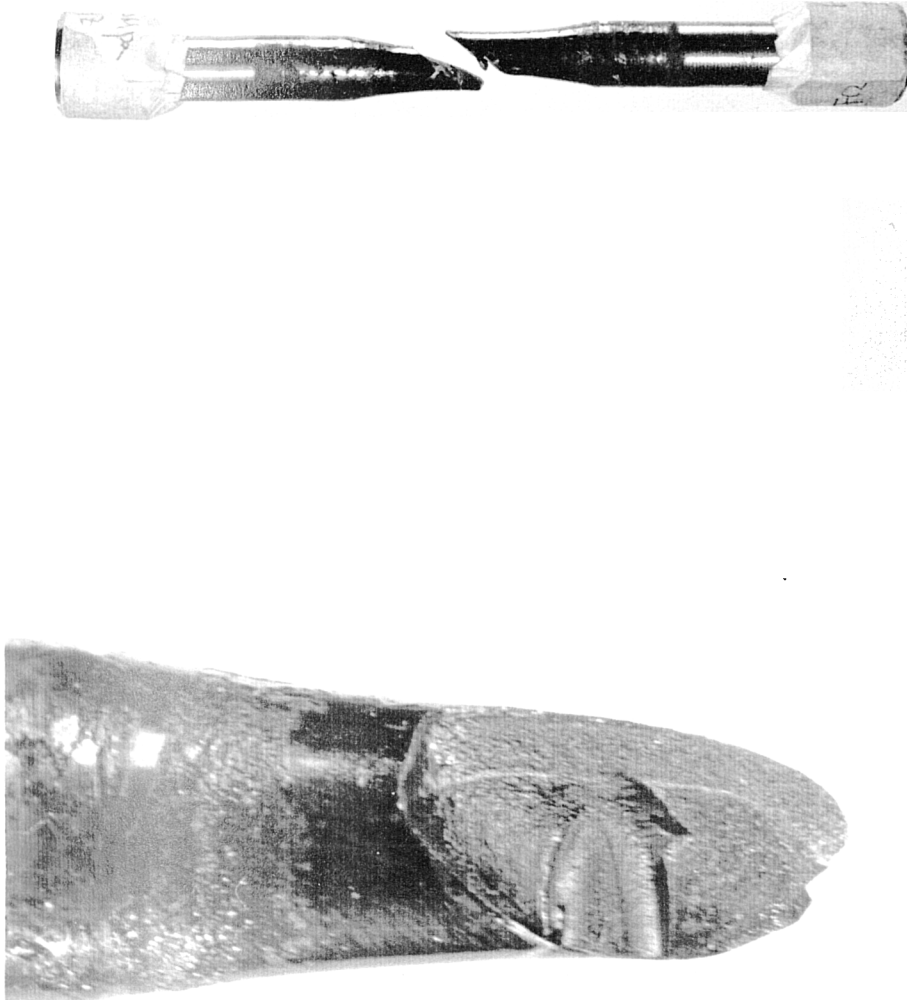


Figure 4.19(b) 'Shell marks' on the fracture surface of specimen FC2, $\Delta\tau=616$ MPa, $f=2$ Hz, 0.6M NaCl solution.

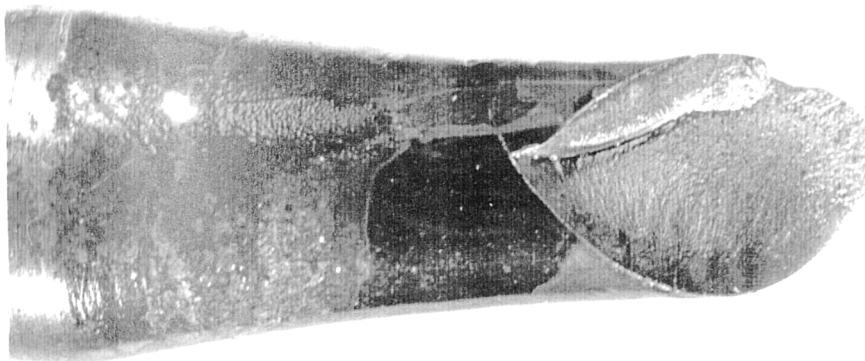
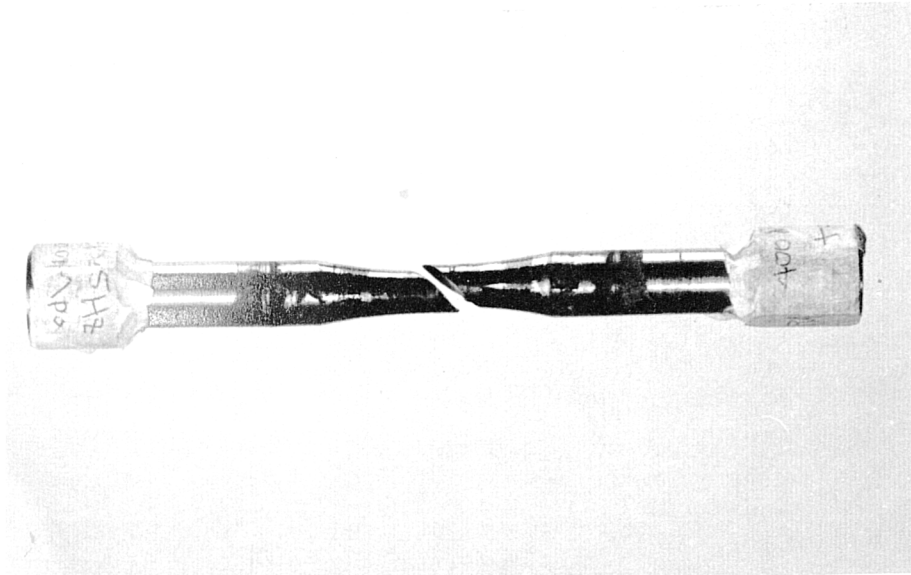


Figure 4.19(c) 'Shell marks' on the fracture surface of specimen FC4, $\Delta\tau=400$ MPa, $f=12.5$ Hz, 0.6M NaCl solution.

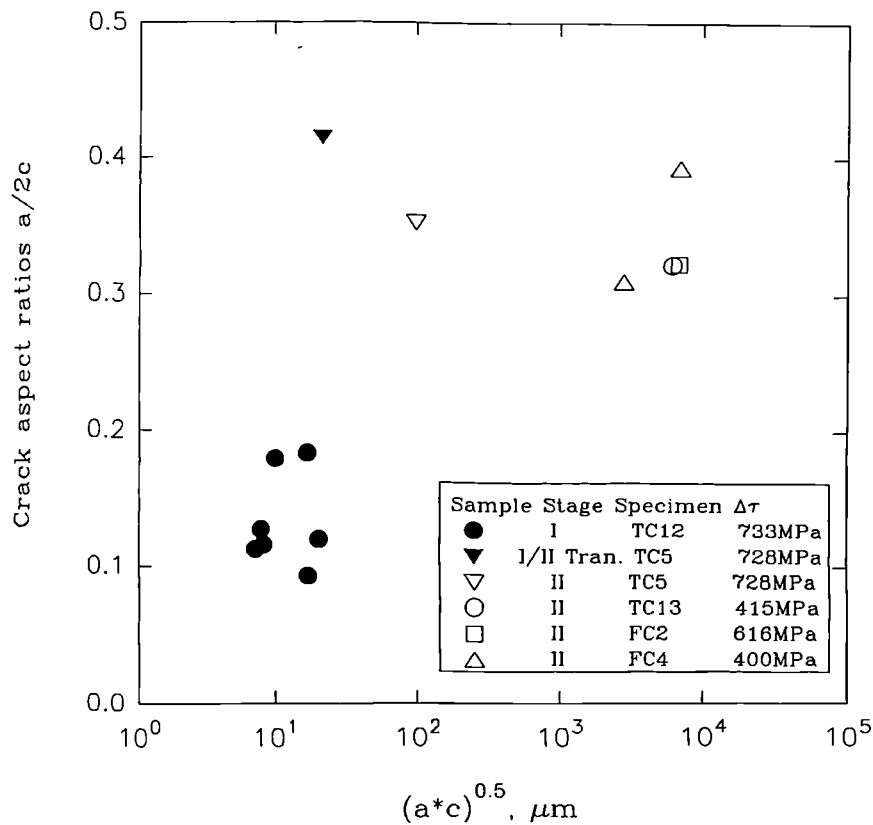


Figure 4.20 Crack aspect ratio in BS251A58 steel as a function of the crack size \sqrt{ac} in corrosion fatigue in a 0.6M NaCl solution.

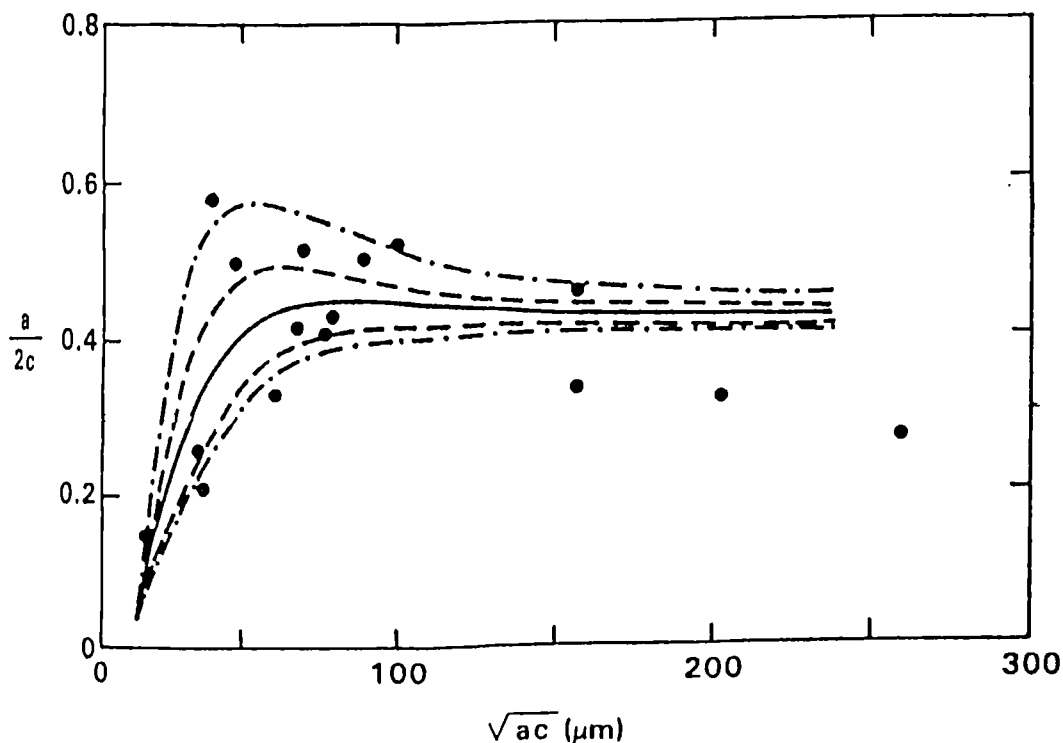


Figure 4.21 Aspect ratios of small cracks in Al 7075-T6 as a function of the crack size \sqrt{ac} from [8]. The data (circles) were taken at stress amplitude of 408 MPa. The curve shows the distribution of $a/2c$ found in simulations of 100 cracks. The solid curve shows the average of $a/2c$ in the simulation, and the chain-dot curves 95% confidence of the data.

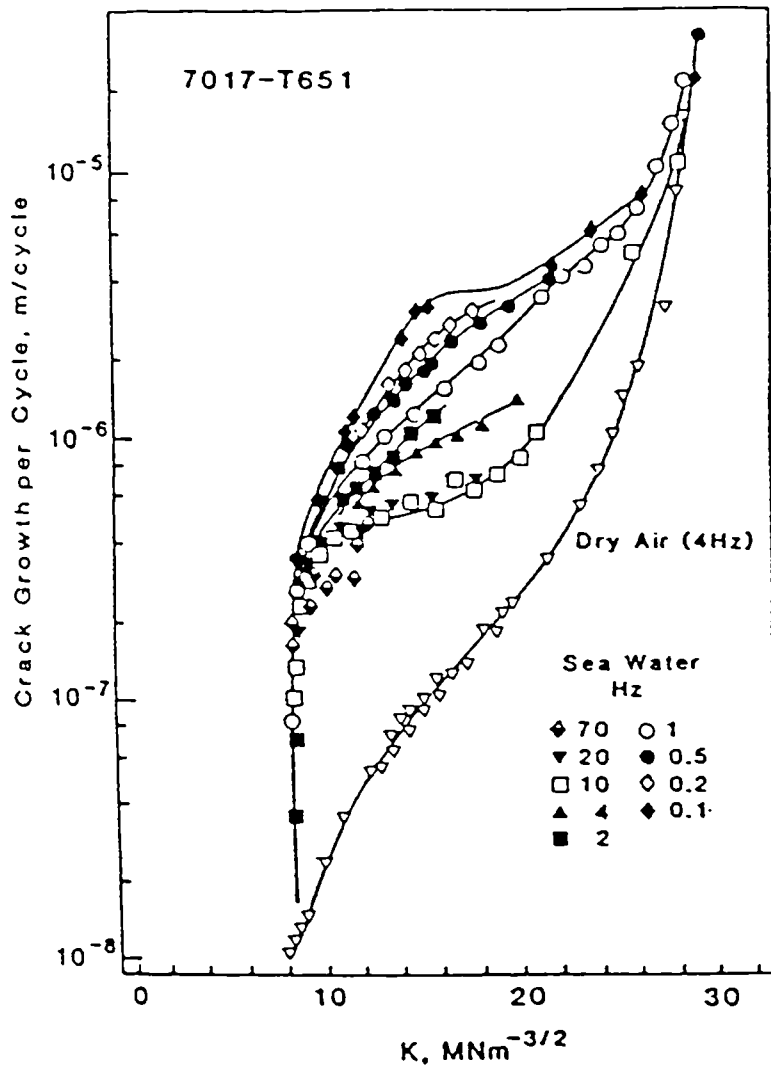


Figure 4.22 The effect of frequency on corrosion fatigue crack growth rate for 7071-T651 aluminium alloy in seawater [43].

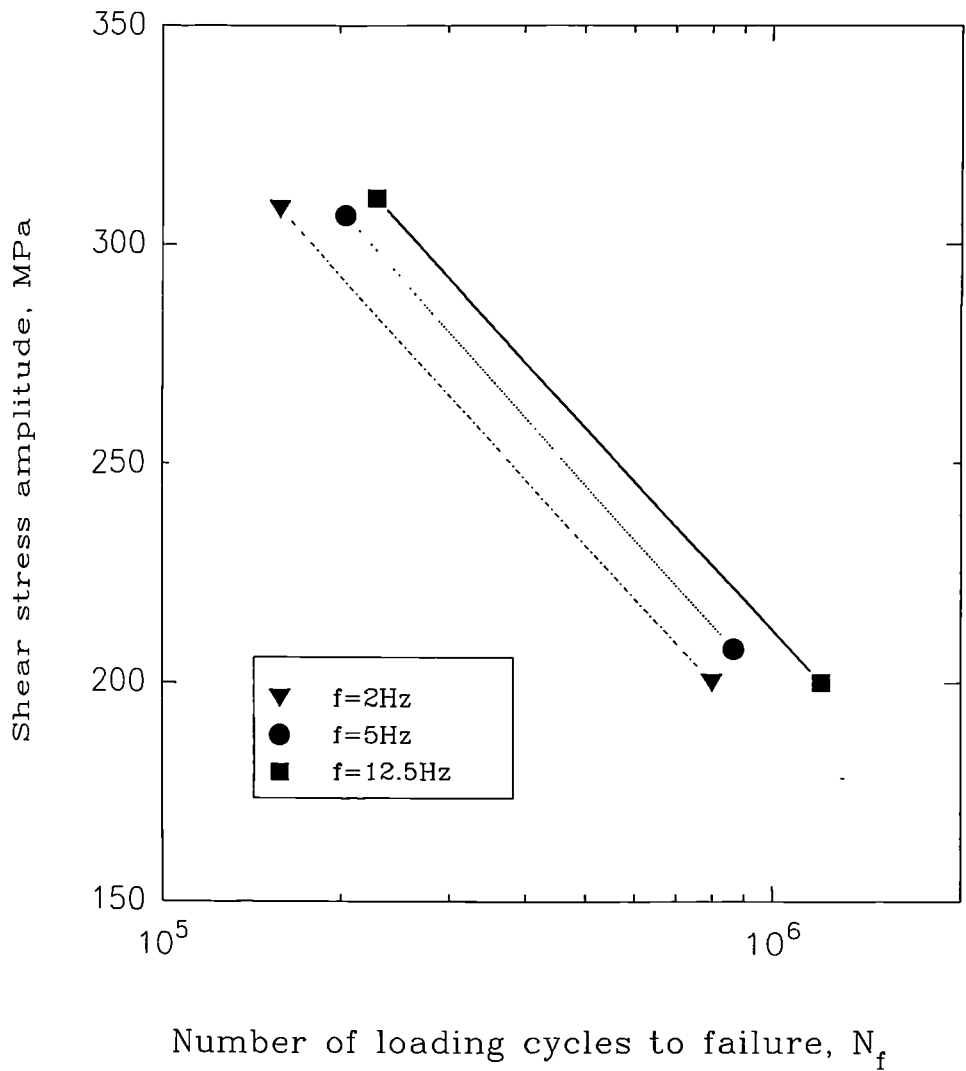


Figure 4.23 Fatigue lifetime in a 0.6M NaCl solution at different frequencies, 2, 5, and 12.5Hz.

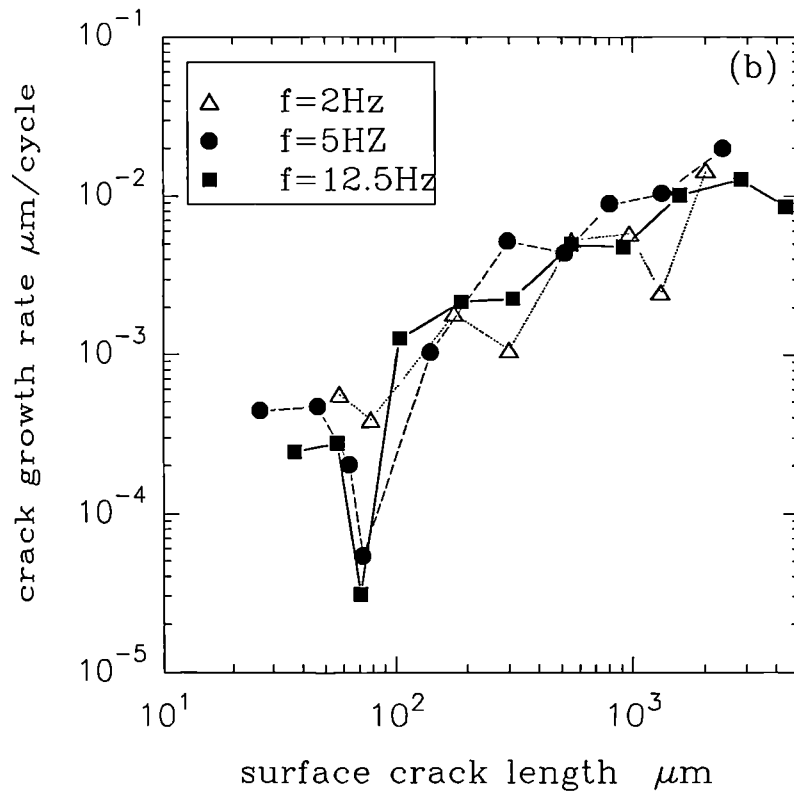
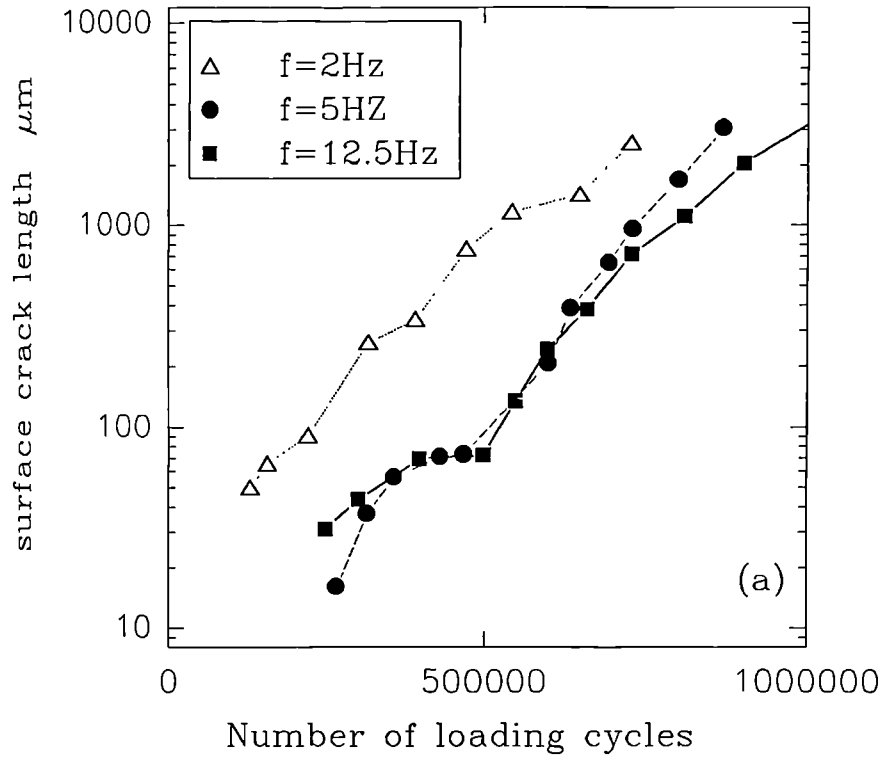


Figure 4.24 The effect of frequency on crack growth at $\Delta\tau \approx 400 \text{ MPa}$. (a) a versus N and (b) da/dN versus a .

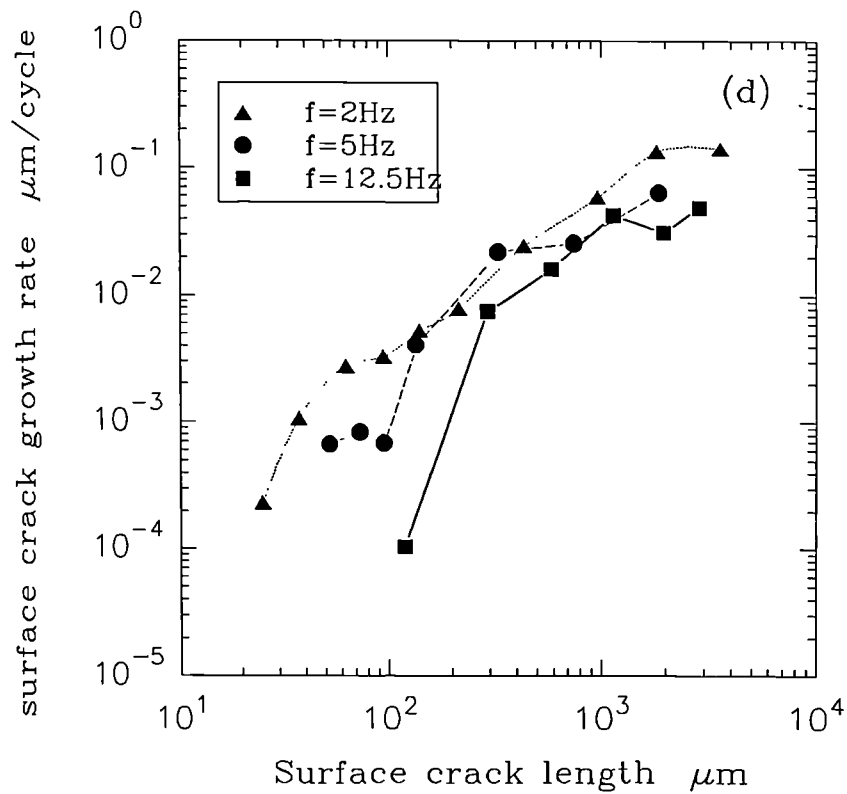
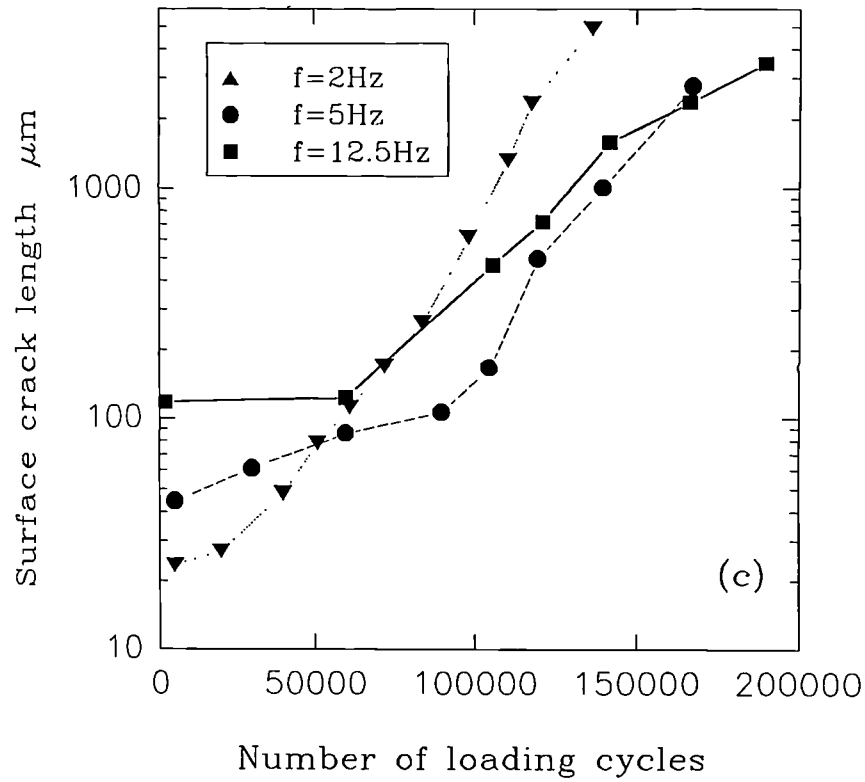


Figure 4.24 The effect of frequency on crack growth at $\Delta\tau \approx 600$ MPa. (c) a versus N and (d) da/dN versus a.

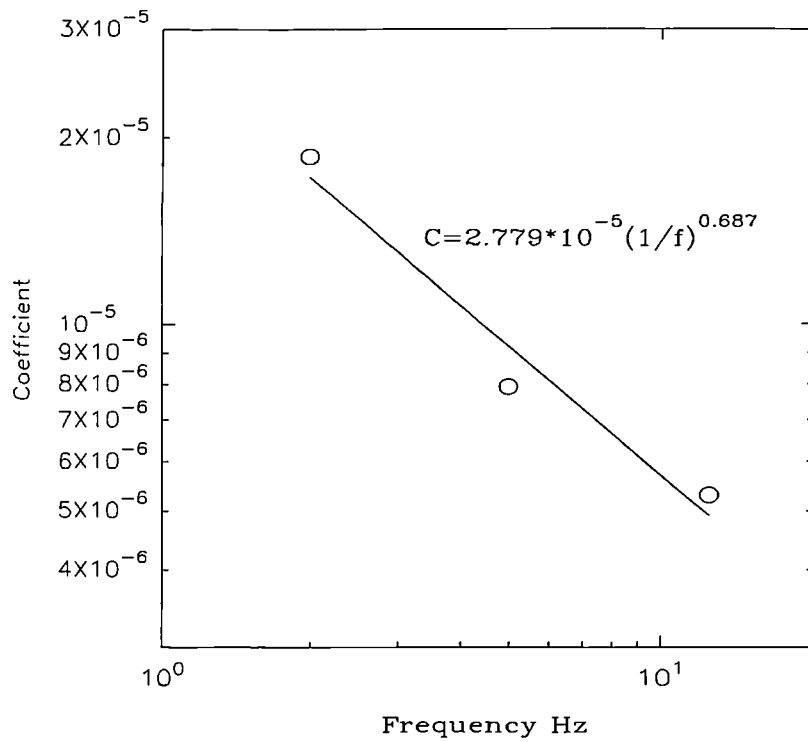


Figure 4.25 Coefficient C as a function of cyclic frequency for the short fatigue crack regime, $\Delta\tau = 400\text{MPa}$, $R = -1$, 0.6M NaCl solution.

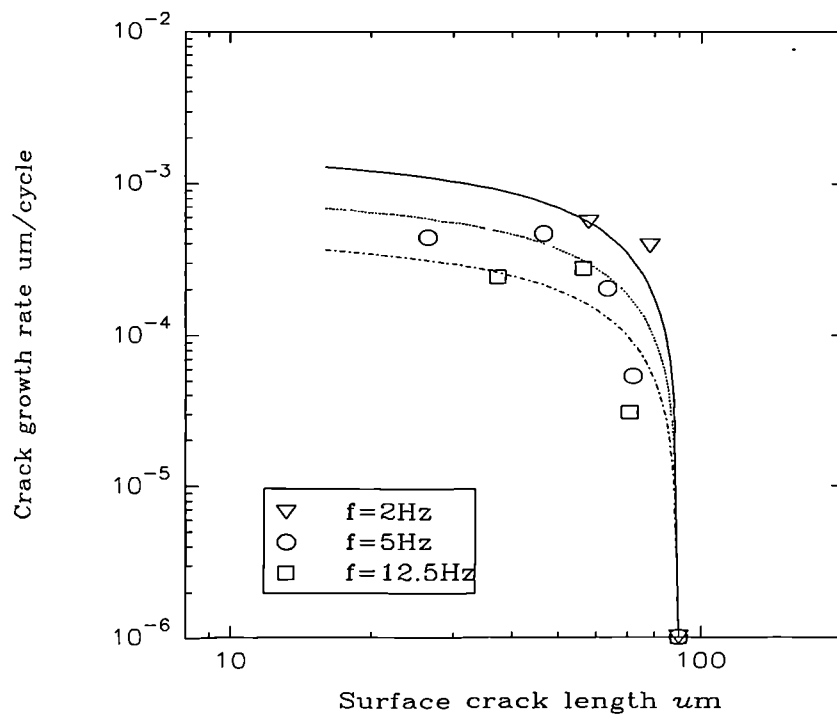


Figure 4.26 Comparison of short fatigue crack growth rate at different frequencies with theoretical prediction of crack growth rate from Brown-Hobson model.

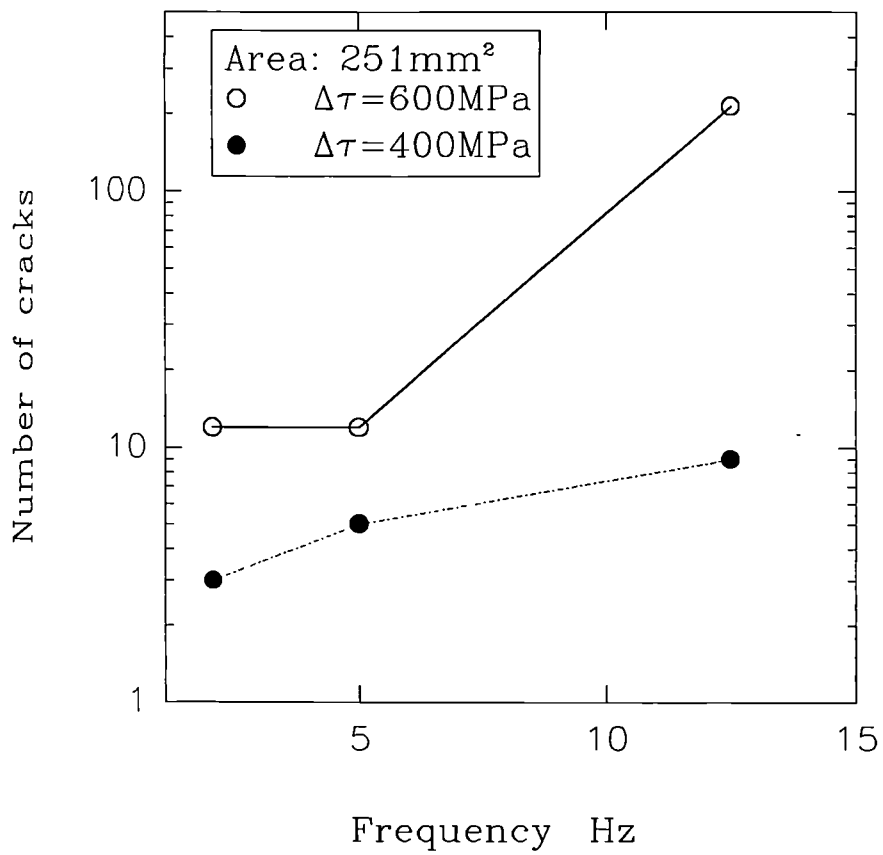


Figure 4.27 Number of cracks increasing with increasing frequency.

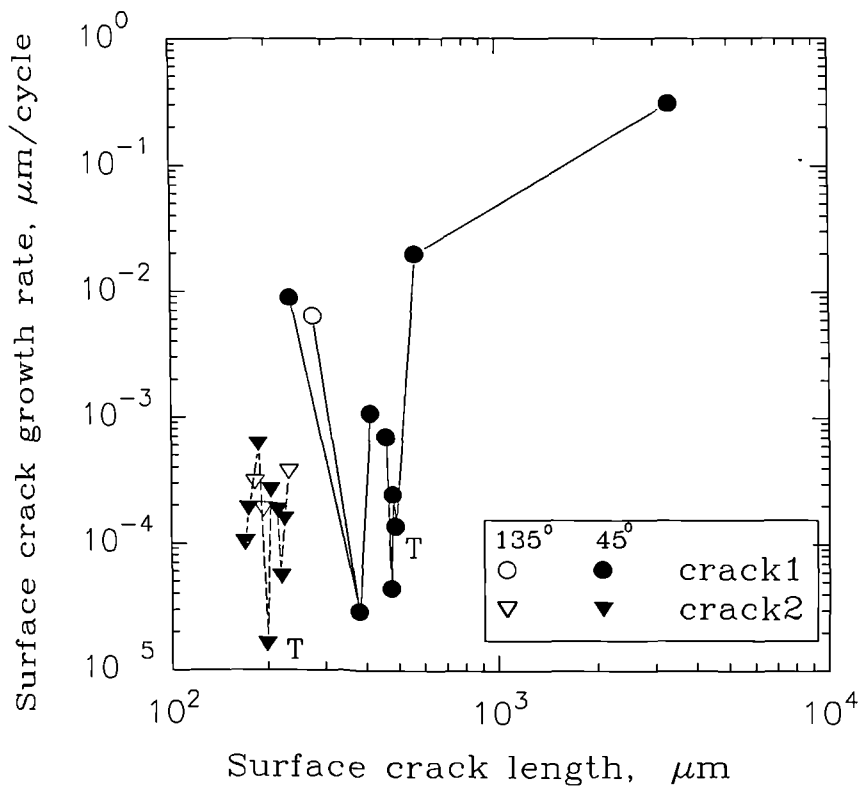
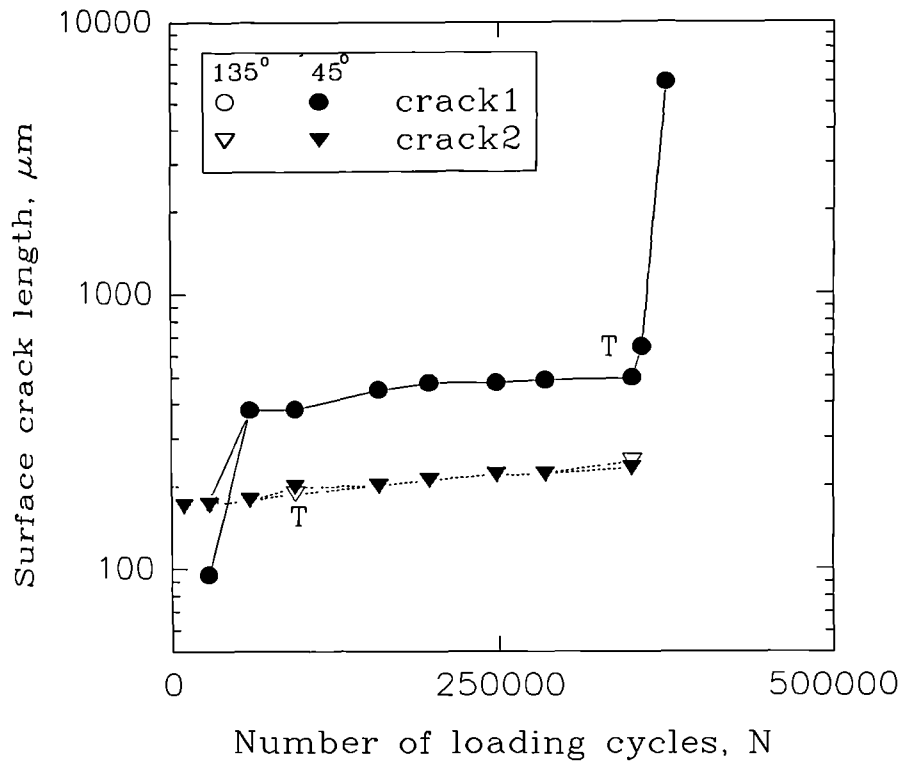


Figure 4.28 (a) Crack growth rate for specimen C2 at a cathodic polarisation potential of -1280 mv (SCE), 'T' corresponds to the stage I/II crack transition. Crack 1 consists of three stage I cracks joining together. $\Delta\tau = 750$ MPa

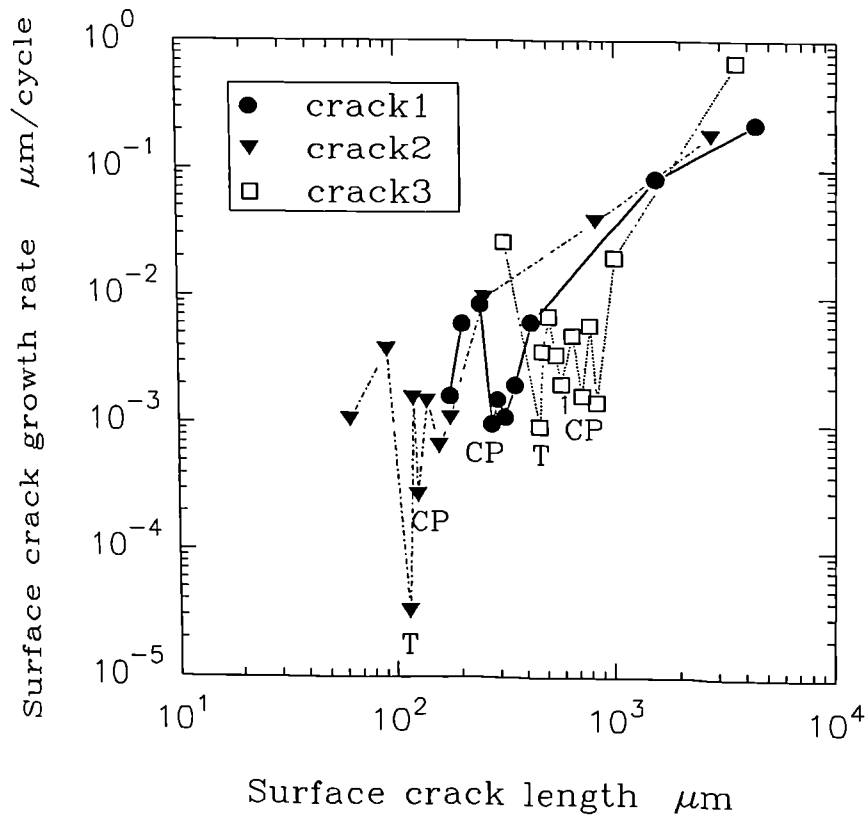
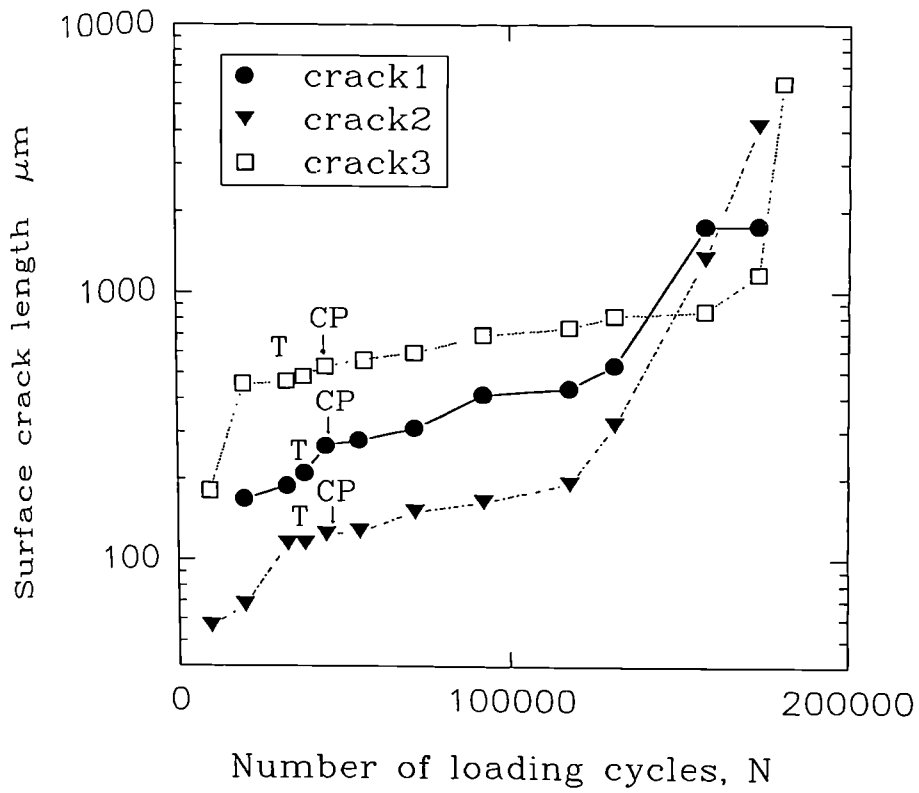


Figure 4.28(b) Crack growth rate for specimen C3. 'T' refers to the stage I/II crack transition, and 'CP' corresponds to the point when a cathodic potential of -1280 mv (SCE) was applied. $\Delta\tau = 750$ MPa

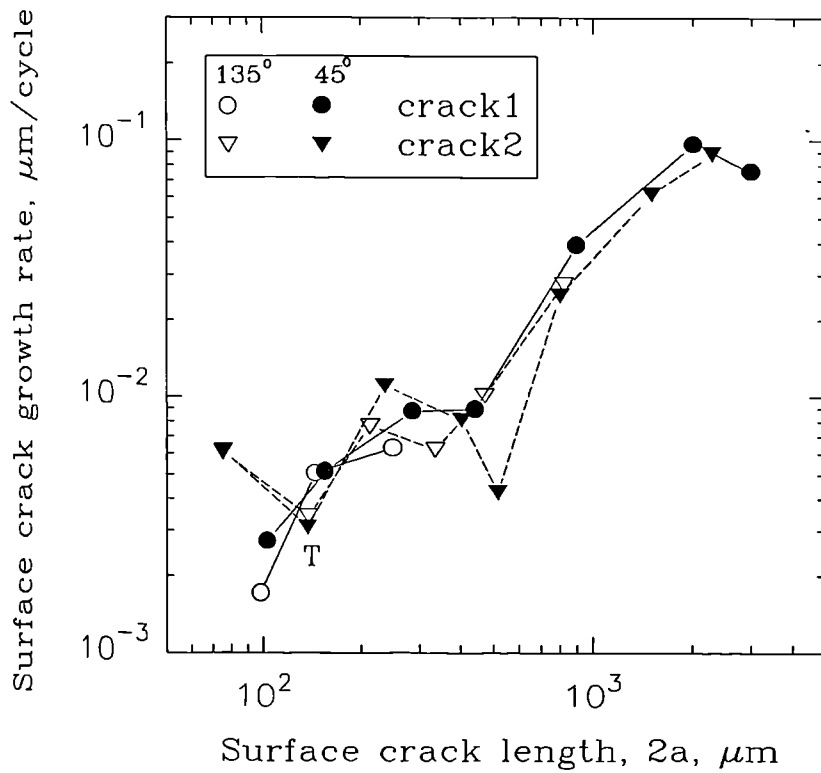
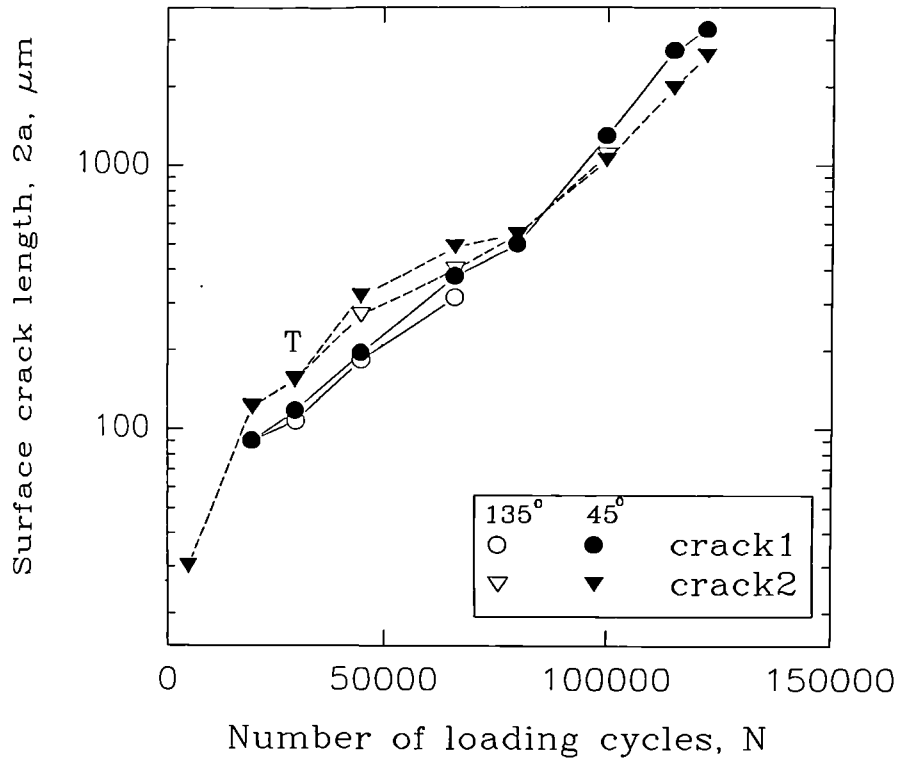


Figure 4.28(c) Crack growth rate for specimen C4. 'T' corresponds to the stage I/II crack transition. $\Delta\tau = 742 \text{ MPa}$

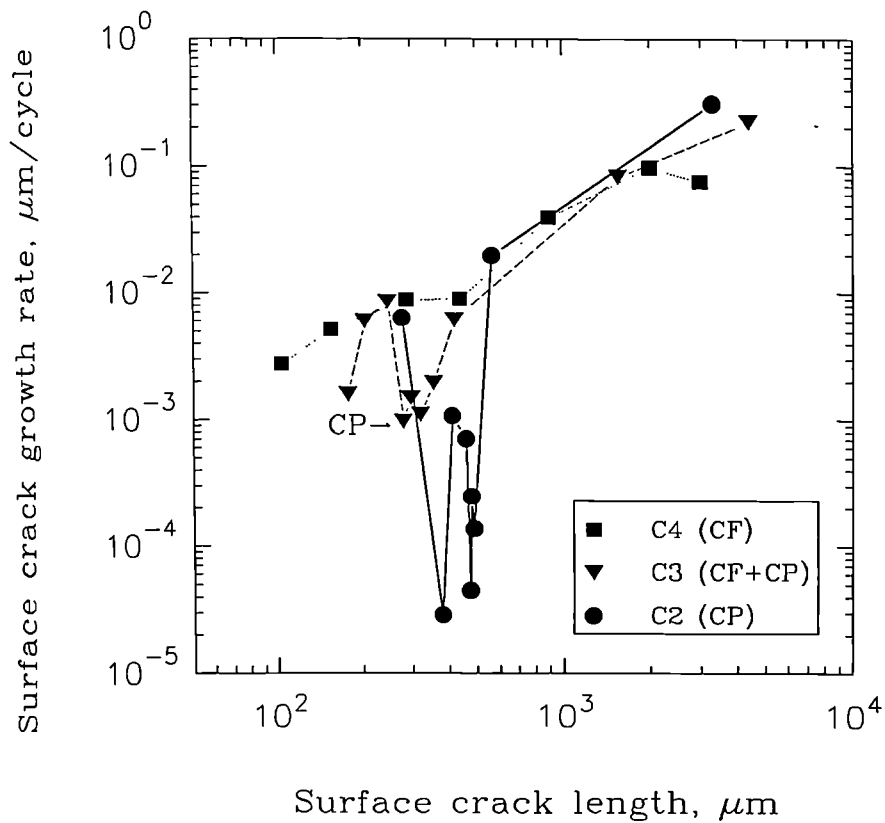
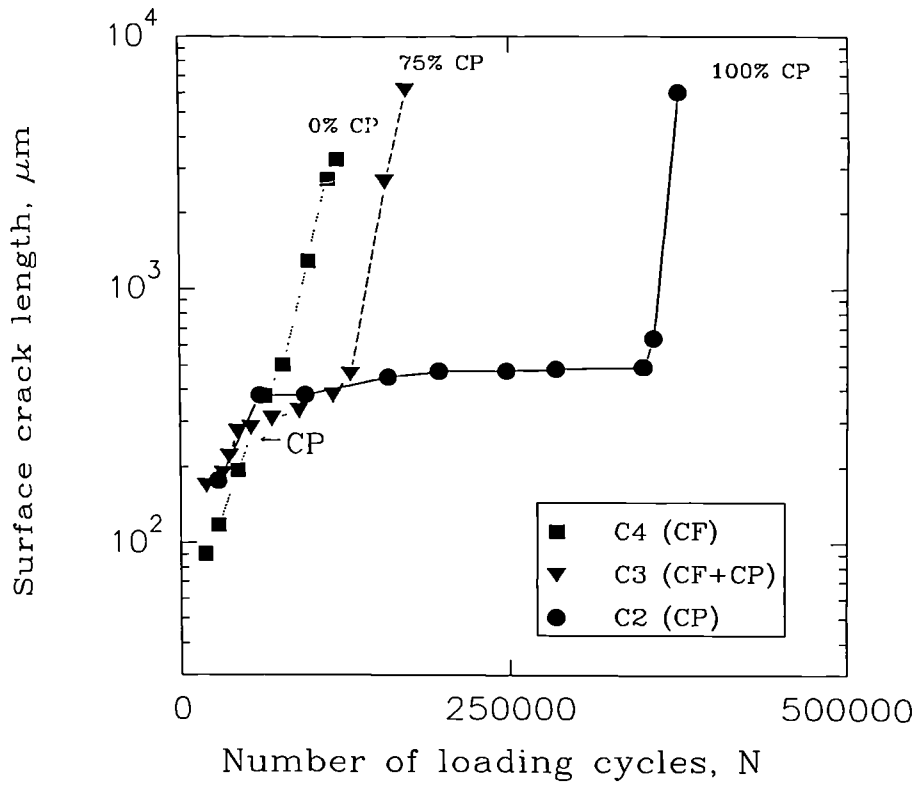


Figure 4.28(d) Dominant crack growth rates for specimens C2, C3 and C4. 'CP' corresponds to the point when a cathodic potential of -1280 mv (SCE) was applied on specimen C3.

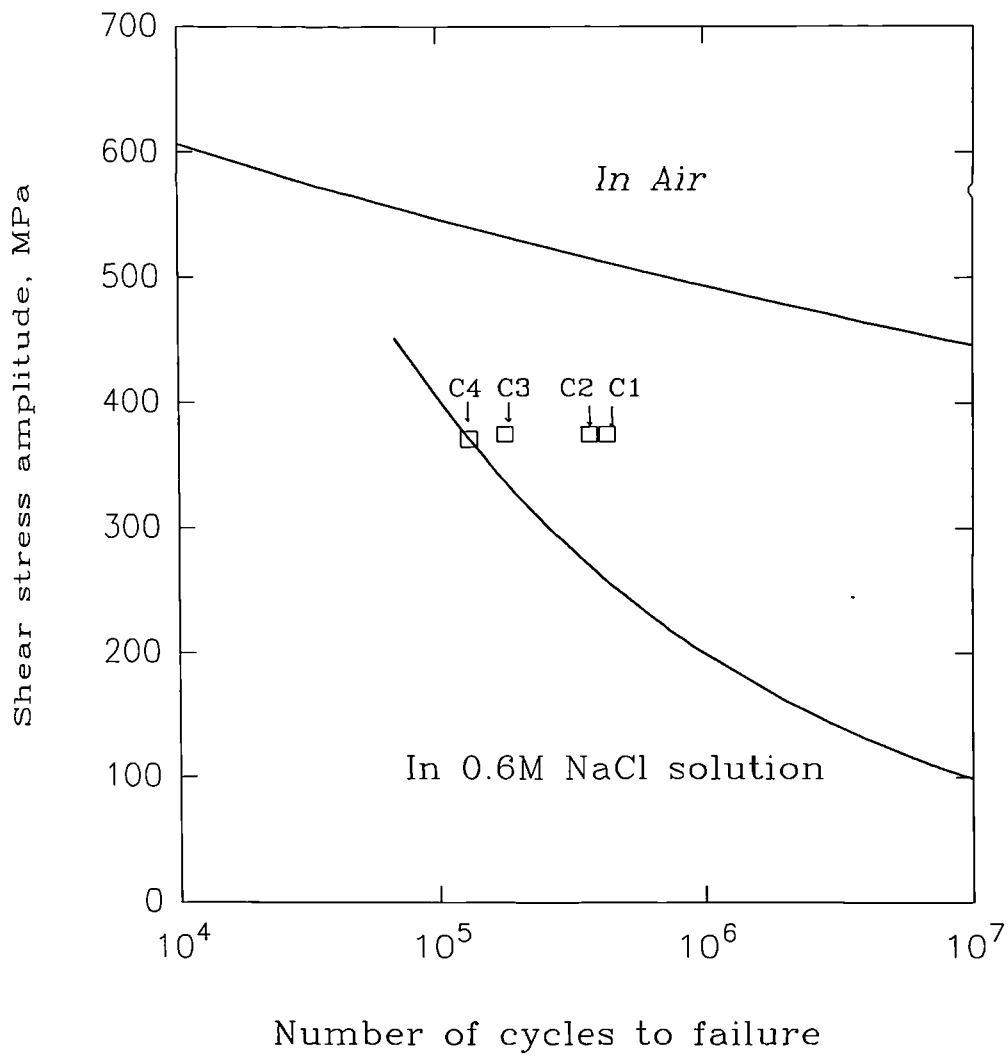


Figure 4.29 Fatigue lifetime for specimens C1, C2, C3 and C4.

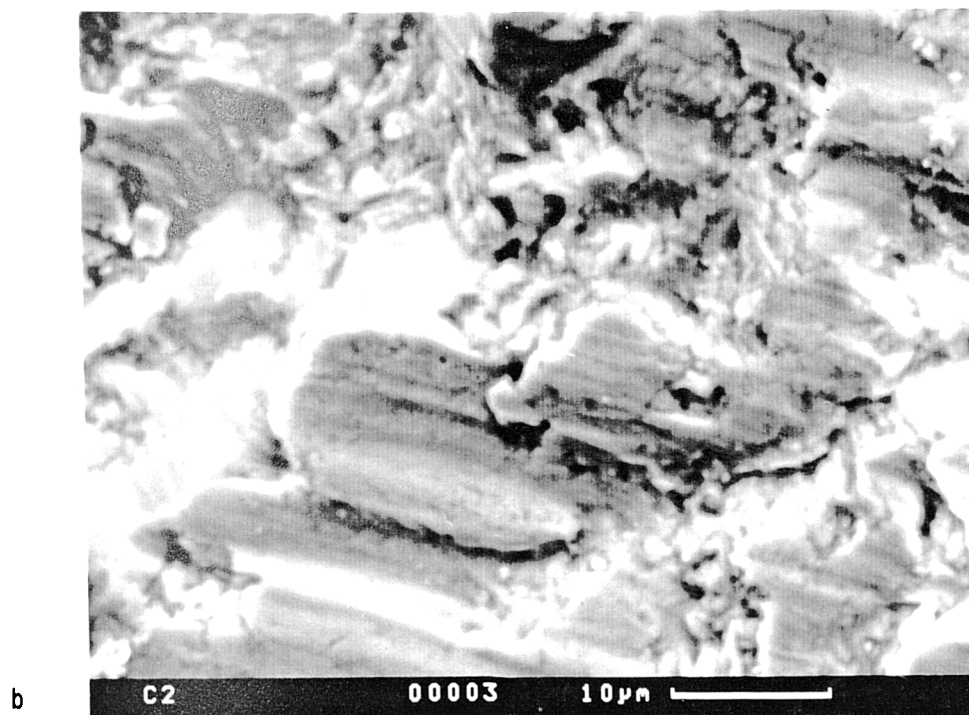
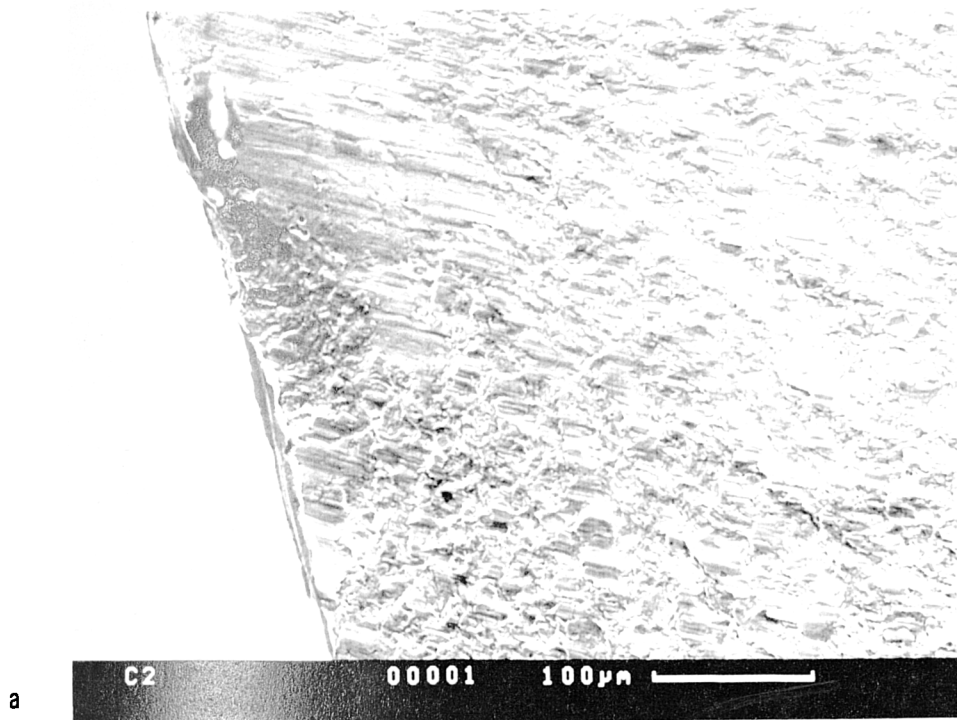


Figure 4.30 SEM fractography (a) fracture surface of specimen C2, (b) magnified view of the crack nucleation site.

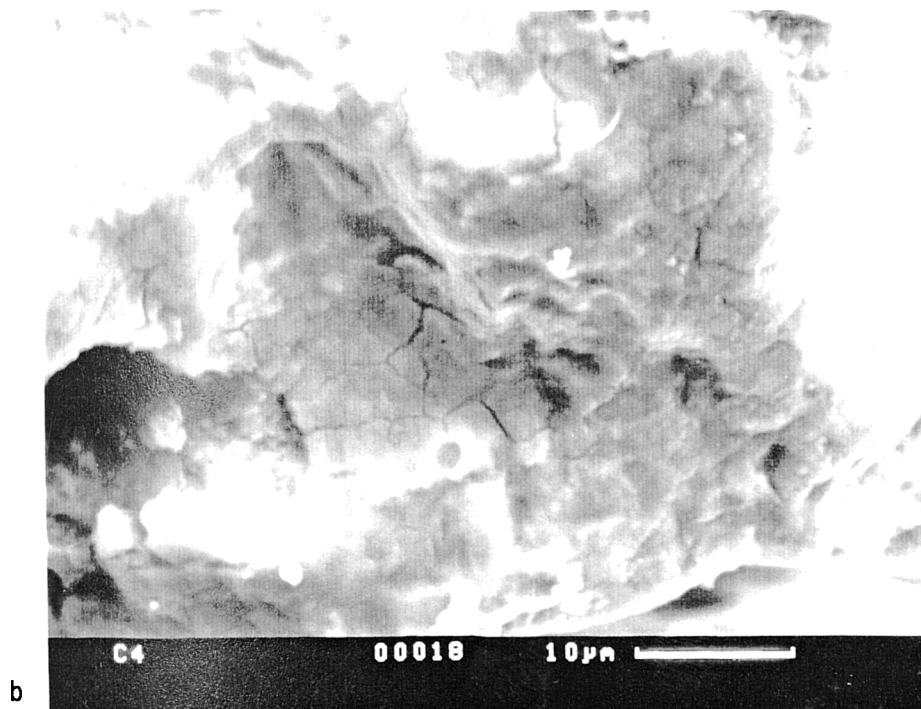
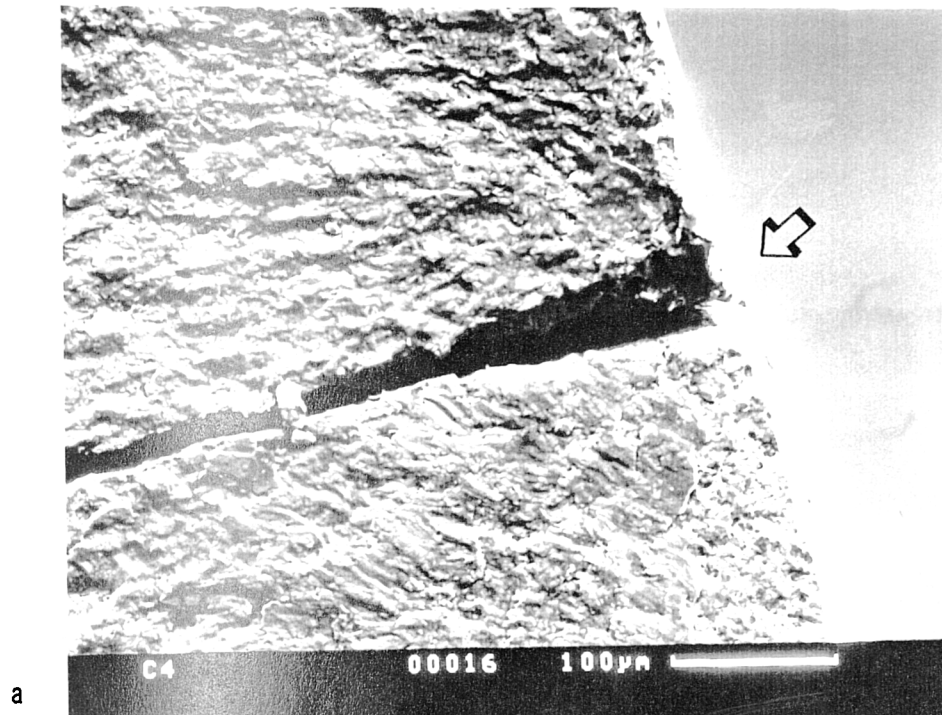


Figure 4.31 SEM fractography (a) fracture surface of specimen C4, (b) magnified view of the crack nucleation site with corrosion products.

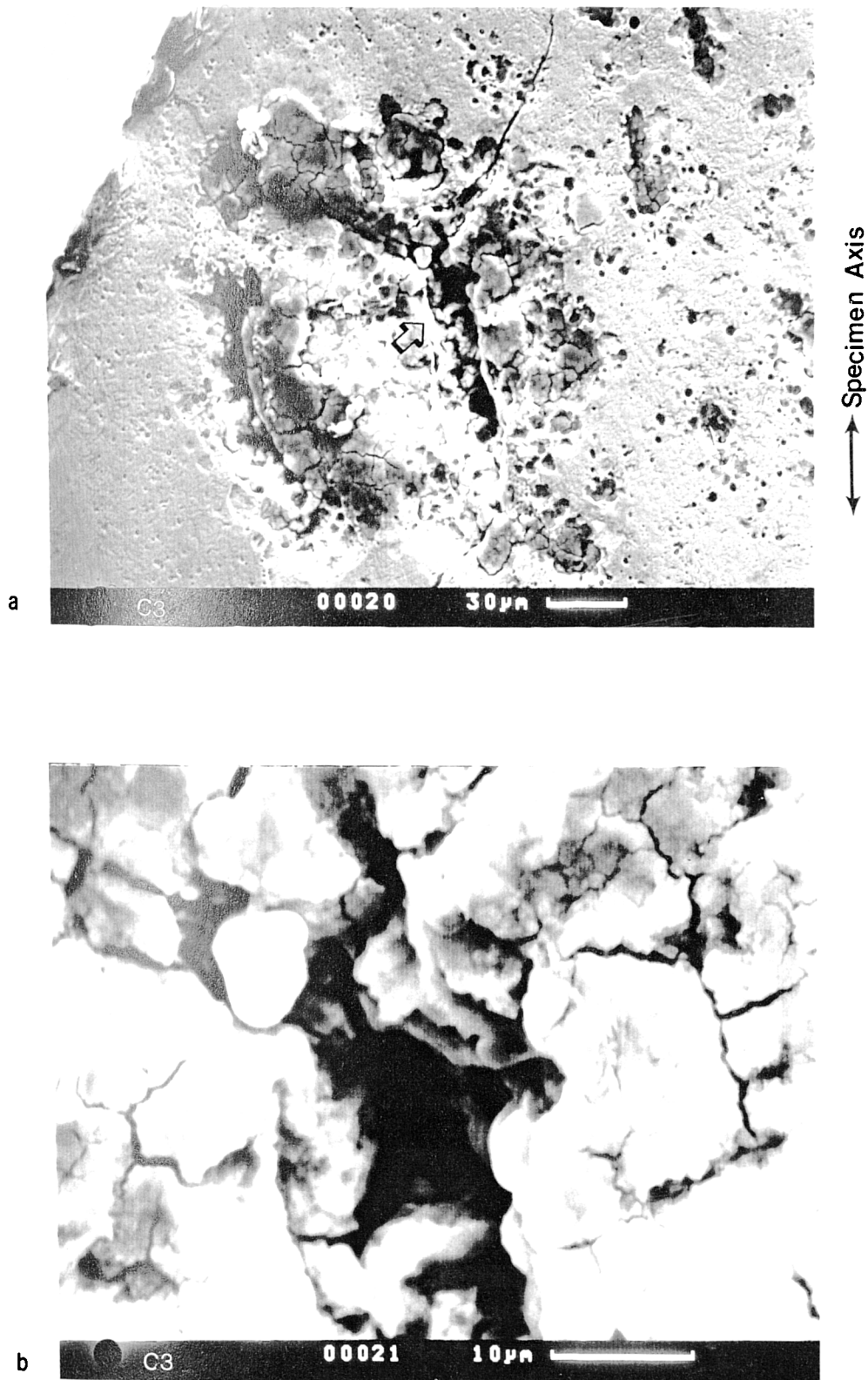


Figure 4.32 SEM morphology of specimen C3 (a) crack growth in stage I under free corrosion potential and crack propagation in stage II with cathodic polarisation, $E = -1280$ mv (SCE); (b) close-up view of the arrow mark showing corrosion product deposit and cracking on the stage I crack path and crack growth transition stage.

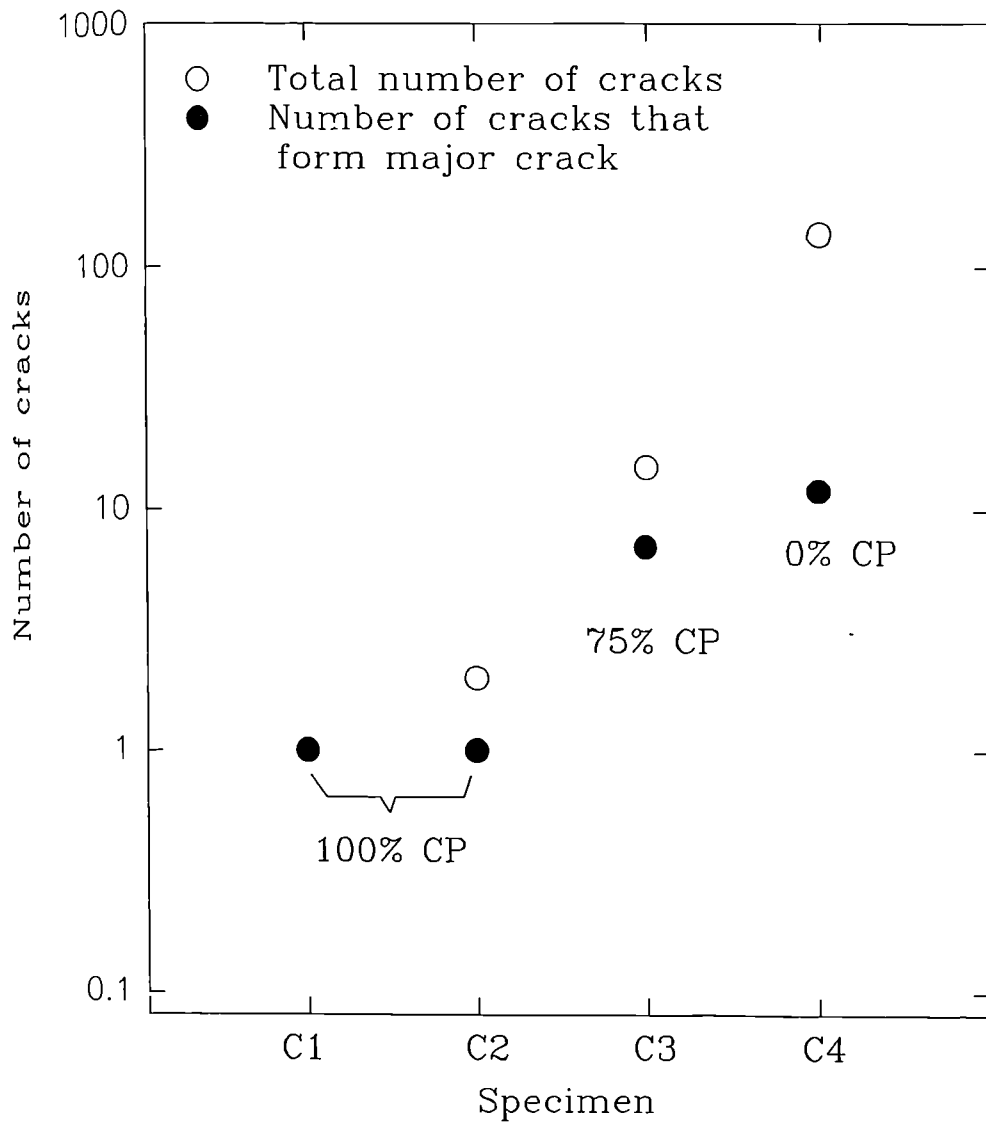


Figure 4.33 Number of cracks on the surface of specimens C2, C3 and C4.

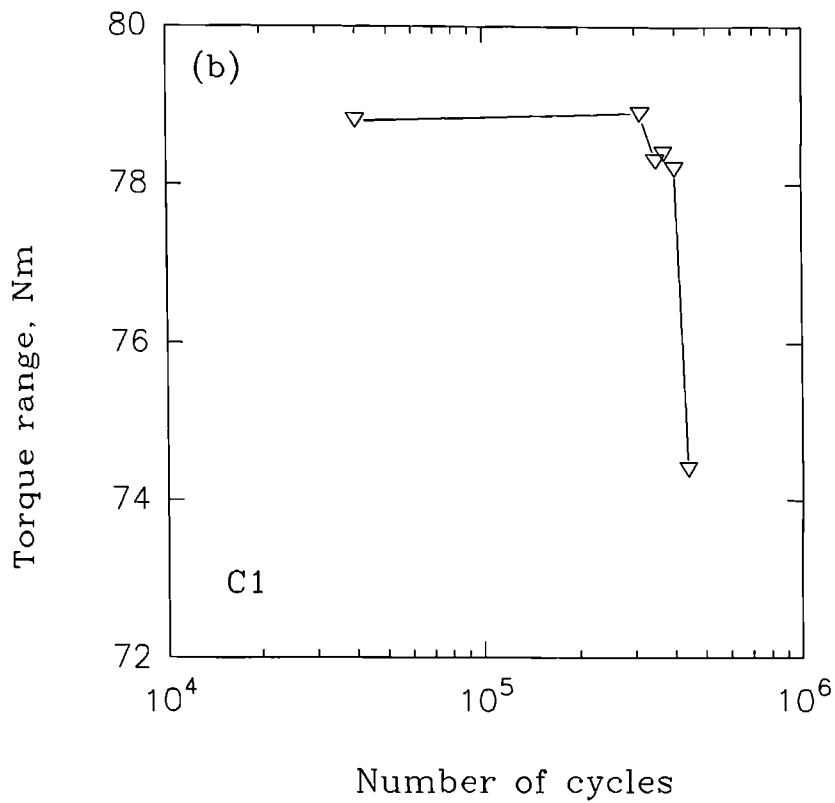
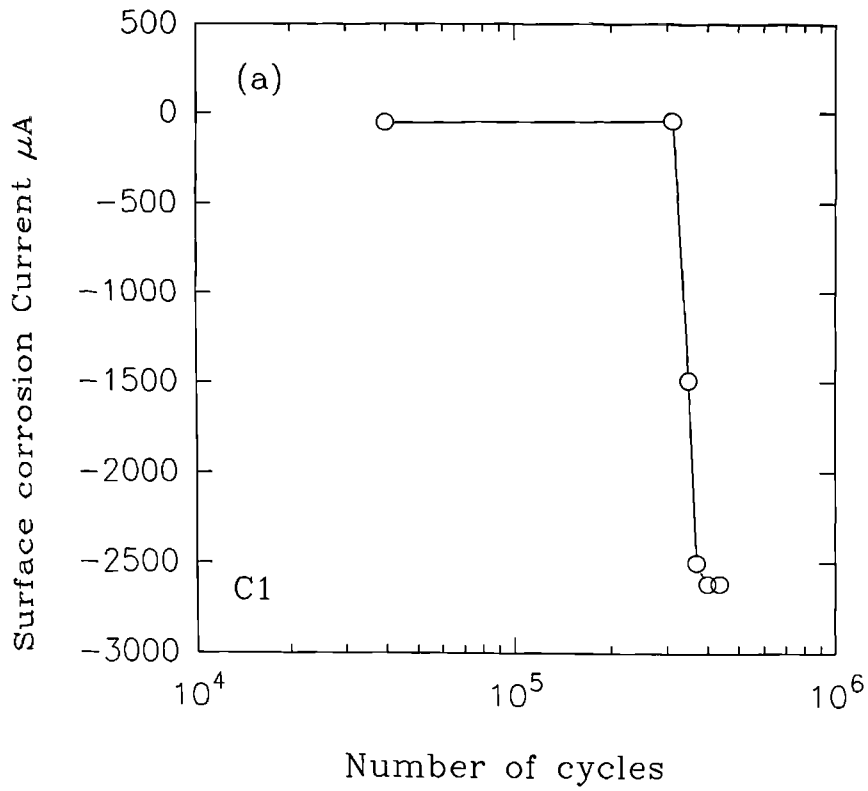


Figure 4.34 (a) Surface corrosion current as a function of loading cycles for specimen C1 and (b) Torque range as a function of loading cycles.

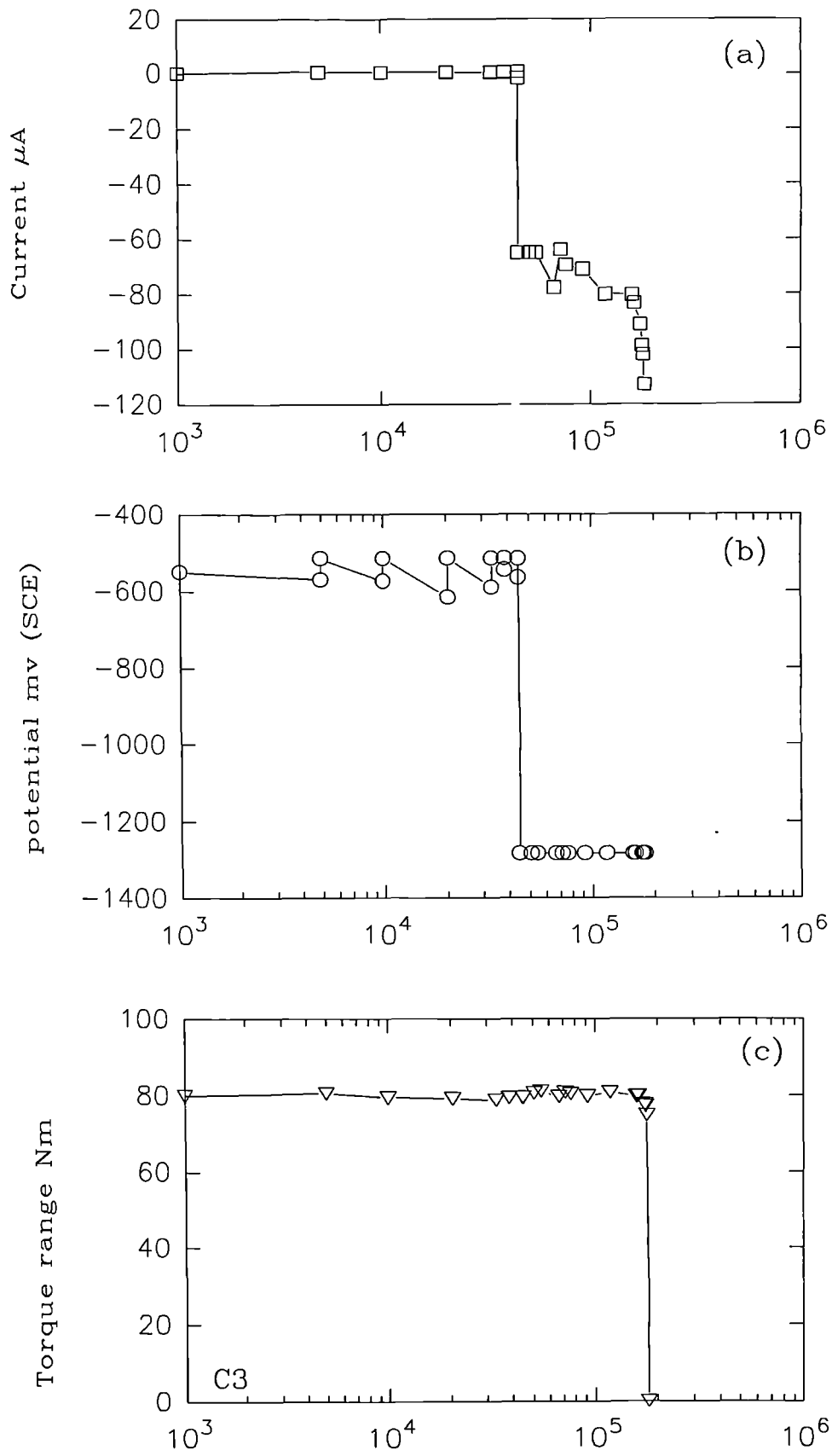


Figure 4.35 (a) Surface corrosion current, (b) surface corrosion potential and (c) torque range as a function of loading cycles for specimen C3.

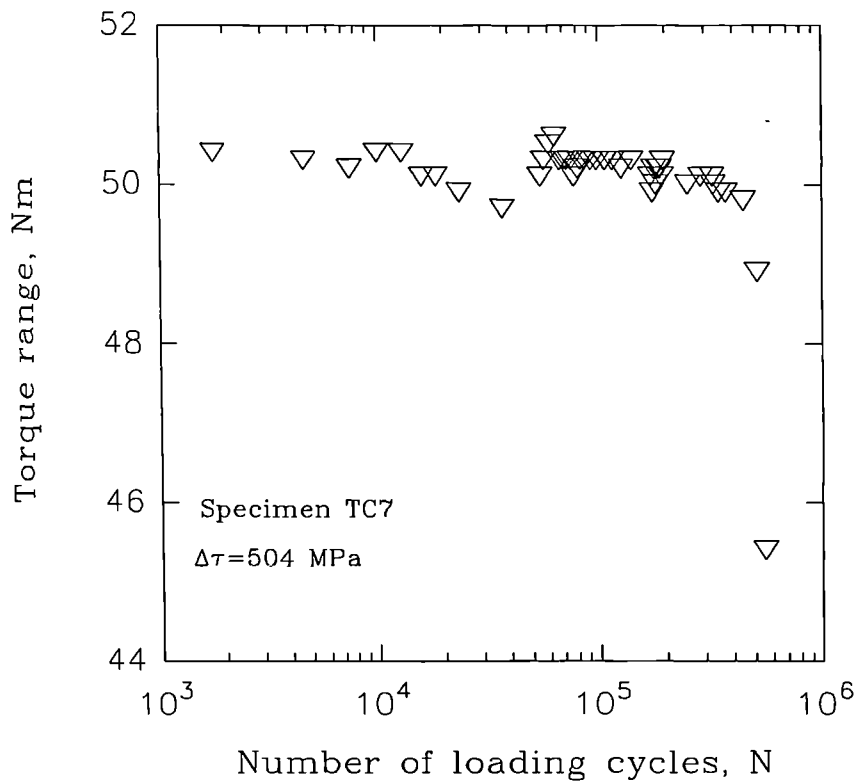
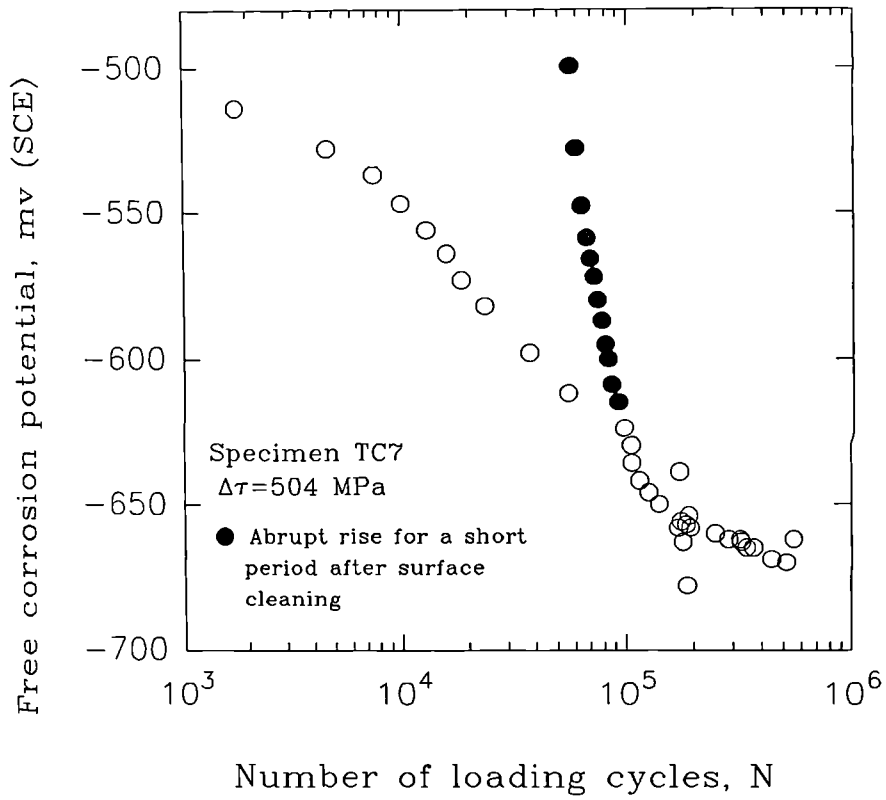


Figure 4.36 Surface corrosion potential and torque as a function of loading cycles for specimen TC7, $\Delta\tau=504$ MPa.

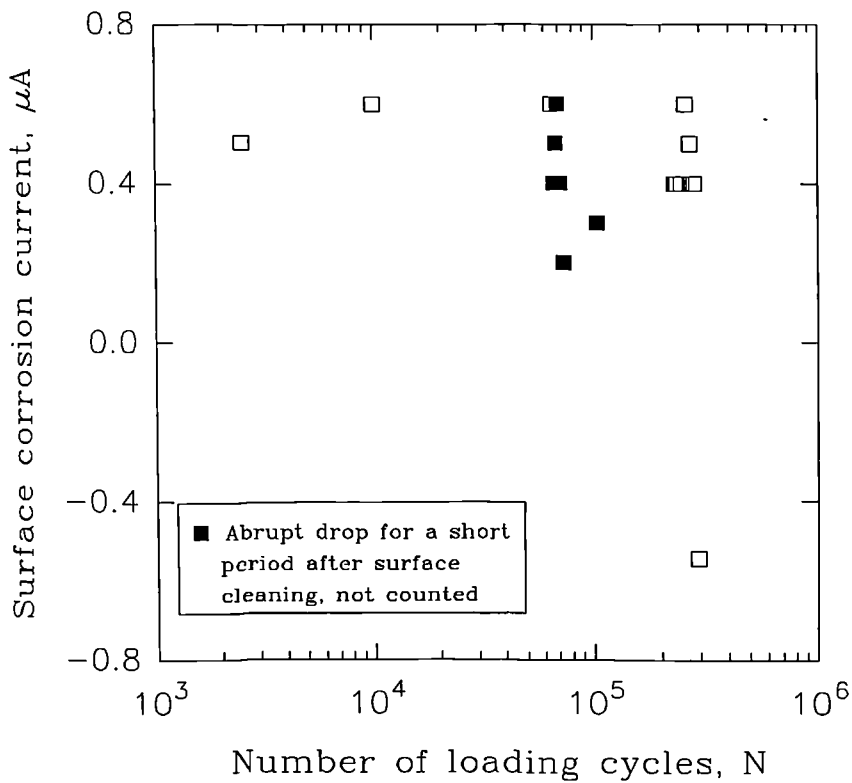
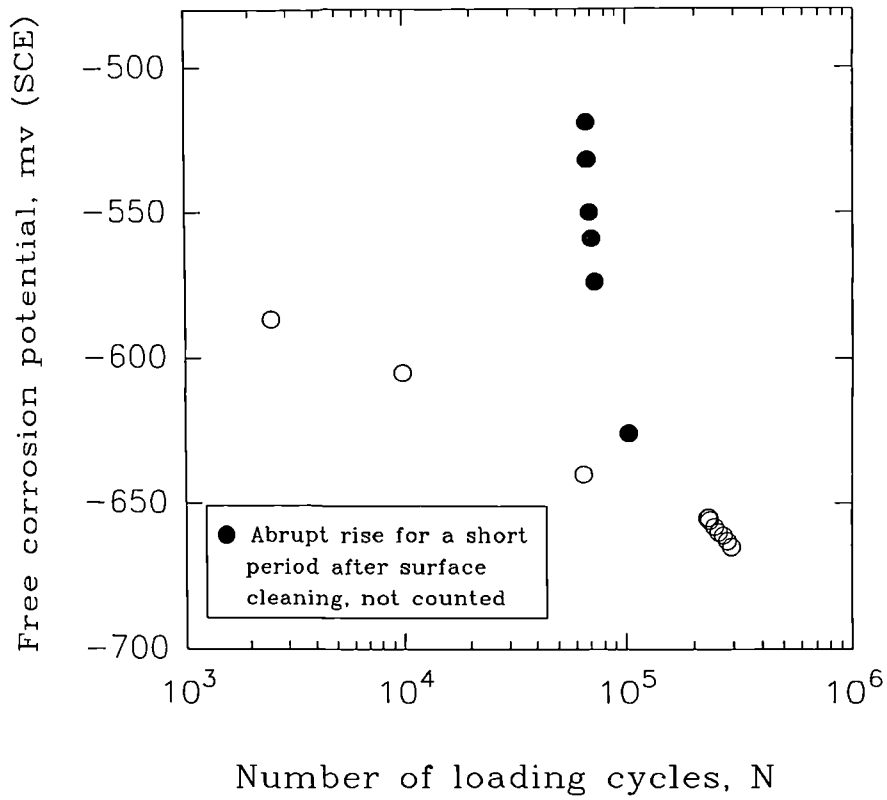


Figure 4.37 Surface corrosion potential and corrosion current as a function of loading cycles for specimen TC10, $\Delta\tau = 609$ MPa.

Specimen	$\Delta\tau$ (MPa)	N_f	Environment
CN1	912	105000	0.6M NaCl + 0.01M NaNO ₂
CN2	637	>3613717	0.6M NaCl + 0.1M NaNO ₂
CN3	613	230000	0.6M NaCl + 0.001M NaNO ₂
S1	630	278500	0.6M NaCl + 0.02M Na ₂ SO ₄
S2	649	339000	0.6M NaCl + 0.1M Na ₂ SO ₄
S3	626	254000	2M NaCl

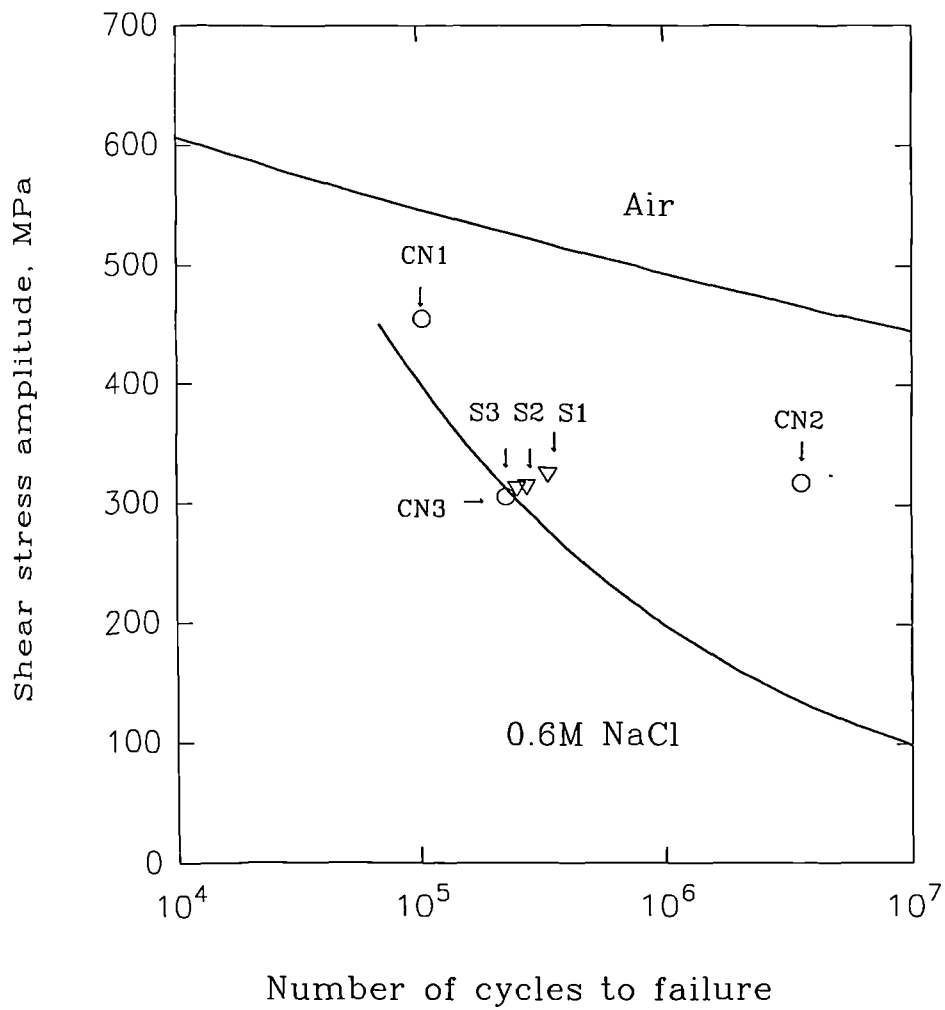


Figure 4.38 Corrosion fatigue lifetime of the test specimens in different solutions.

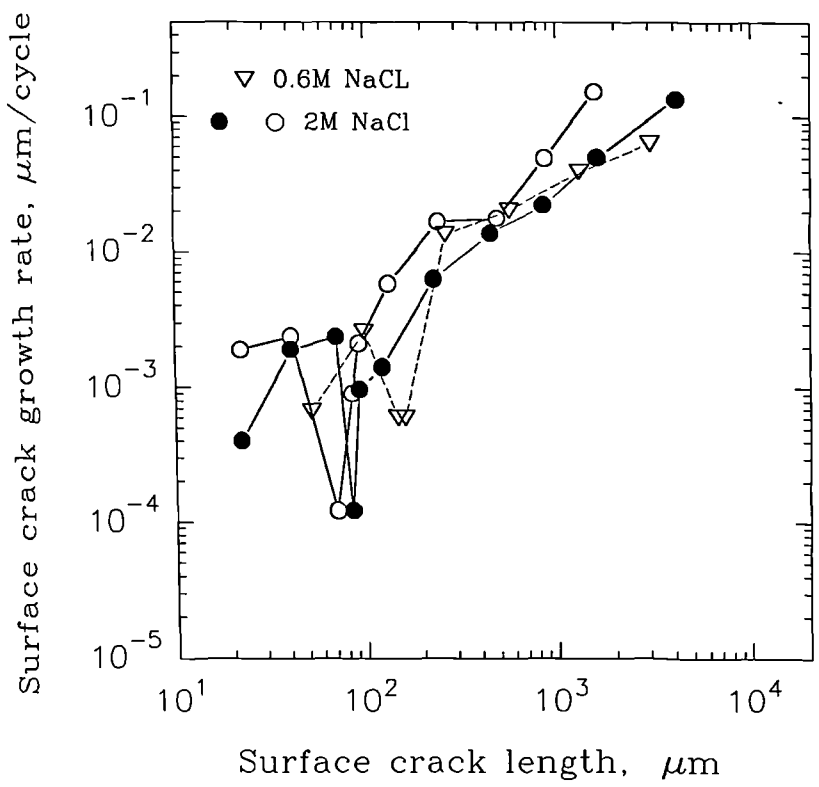
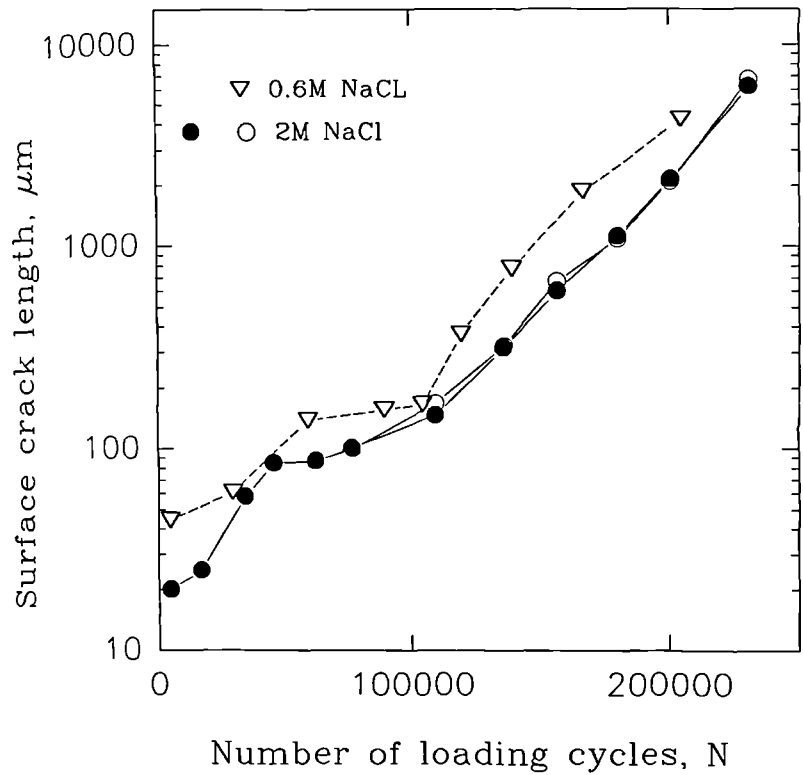


Figure 4.39 Crack growth rate for specimen S3 in a 2M NaCl solution, $\Delta\tau=626$ MPa, compared with the data of specimen TC18, $\Delta\tau=613$ MPa.

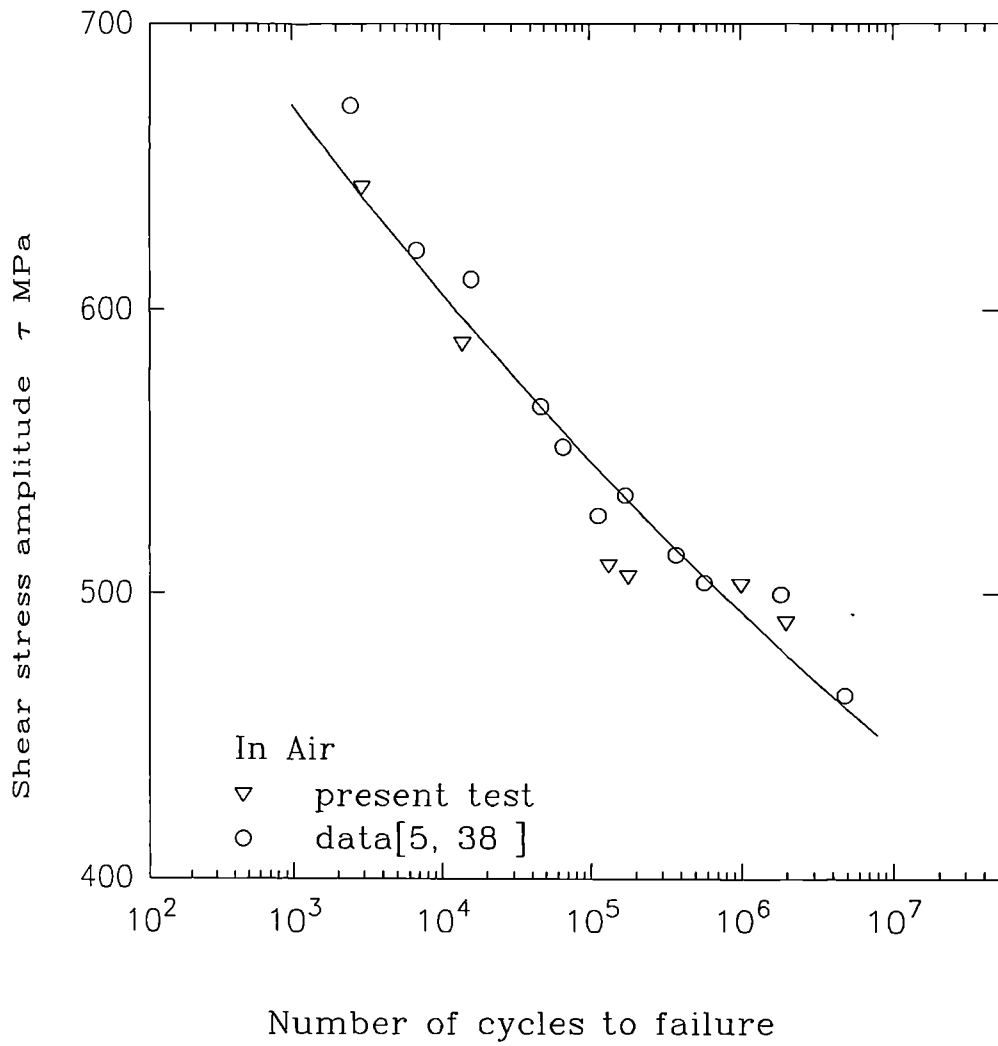


Figure 4.40 S-N curve in air for BS251A58 high strength steel.

Chapter 5 Modelling

In this chapter, a microstructurally-sensitive crack propagation model based on the dislocation representation of a crack is used to provide the theoretical basis to understand the underlying principles of the supposed 'anomalous' short fatigue crack behaviour, to analyse the experimental data, and to predict the fatigue lifetime. Modifications to the model are made to incorporate the corrosive effect on the early stage of crack initiation, stage I to stage II transition, and strain hardening of a parabolic form in order to achieve a more accurate prediction.

5.1 The microstructurally-sensitive crack growth model

The dislocation representation of a crack was first used by Bilby et al in 1963 [1] and the corresponding solution constitutes the so-called Bilby, Cottrell and Swinden (BCS) crack model. Originally the slip planes of the dislocations were considered to be analogous to the lines defined in the macroscopic theory of plasticity, rather than crystallographic ones, and the friction stress or resistance to plastic deformation in the plastic zone was equated to the lower yield stress. An alternative interpretation of this friction stress has recently been given in [2].

Based on the BCS theory, Navarro and de los Rios [2-5] developed a microstructurally-sensitive crack growth model, hereafter referred to as the N-R model to characterise short crack growth behaviour.

In the N-R model [2-5] the crack is assumed to form in the largest and the best orientated grain on the surface in relation to the applied stress. The plastic zone associated with the

crack extends to the grain boundary, where it is blocked. As the crack grows, with the slip band still blocked at the grain boundary, the stress, at a dislocation source in the barrier zone, increases until it reaches a value sufficiently high to activate the source. The next grain yields and, therefore, the plastic-elastic interface moves to the next grain boundary. The above process repeats itself, resulting in stable crack growth in an intermittent fashion, until the final instability is reached. As the crack growth is a direct result of the accumulation of unrecoverable plastic slip at the crack tip, an oscillating growth pattern can be expected due to the intermittent change of plastic zone size ahead of the crack tip. In general the model characterizes most of the observed experimental evidence of short fatigue crack growth and affords a reasonable quantification of experimental data.

Akid and Miller [6, 7], using both the Hobson-Brown (H-B) model and the N-R model, proposed that the crack extension rate was accelerated by the metal dissolution rate in an aggressive environment. The crack growth rate in corrosion fatigue was calculated by the simple addition of the metal dissolution rate and the fatigue crack growth rate in air. The modified model agreed with their experimental results for low carbon steel.

Superposition, however, implies that the dominant barrier to corrosion fatigue crack growth remains the same as that in air, which is often not the case observed in experiments. Within the framework model, it is also difficult to give full account of pit initiation and growth, an important phase in corrosion fatigue, and to characterize the effect of an aggressive environment on the stage I to stage II transition.

In the present study, consideration is given to pit initiation and growth, to the transition from stage I to stage II, to the modification of the strain hardening law to conform to a parabolic form. These new developments, when incorporated into the N-R model, improve the understanding of short fatigue crack growth behaviour and can achieve a more satisfactory prediction of crack growth and fatigue life.

5.2 Pit initiation and propagation

For high cycle fatigue, especially for in-air fatigue, early crack initiation and growth within the first few grains occupy a relatively large proportion of total life when compared with the later stages of growth. A number of factors contribute to this: e.g. for a smooth specimen there is no significant stress concentrator to accelerate early crack initiation and the presence of microstructural inhomogeneities acting as barriers can severely impede crack growth. Although short cracks can grow faster than may be predicted from LEFM theory, in general the average growth rate in the early stage is still less than the growth rate of microstructure-insensitive growth under the same loading conditions. As a result, a key technique to produce tougher fatigue resistance material is to introduce more and stronger barriers in the early stage of crack initiation and growth [8, 9].

However in corrosion fatigue, the contribution of the early crack growth phase becomes much less important in prolonging the total fatigue life because the presence of the aggressive environment greatly reduces the in-air fatigue barrier strength and significantly accelerates early crack initiation and growth in the form of a pitting-crack sequence. The reduction in the number of cycles for crack initiation and early stage growth also accounts for the large difference between the in-air fatigue life and corrosion fatigue life.

In corrosive environments pits are usually found at the origin of fracture surfaces of industrial machinery parts as well as on test specimens. This implies that pit initiation triggers fatigue crack initiation. Therefore, the quantitative evaluation of pitting is very important in the prediction of corrosion fatigue life.

From experimental evidence it was observed, in this work (see Chapter 4, section 4.1.2 *pit growth rate*), that the diameter of the major pit, which formed the dominant crack, increased in proportion with time (t) as the power of $1/3$, i.e. $t^{1/3}$.

A simple dissolution law also gives this 1/3 power law form. For example, assuming a hemispherical pit of radius (r) and a constant dissolution rate (A), the pit volume increases proportionally with time (t) as:

$$\frac{2}{3}\pi r^3 = At$$

$$\text{or } 2r = Bt^{1/3} \quad (5.1)$$

However, the incubation time for major pit initiation, t_o , and the original size of the pit (such as that developed from an inclusion of size r_o), should be taken into account.

Accordingly the corrosion pit growth law can be formulated as following:

$$2r - 2r_o = B(t - t_o)^{1/3} \quad (5.2)$$

where $2r$ is the pit diameter, $2r_o$ is the initial pit size corresponding to the pit developing from an inclusion or other defect, while t_o is the incubation period or major pit initiation time and t is the time for the major pit to grow.

The incubation time for the formation of the major pit, t_o , and constant B (both functions of applied stress amplitude) are presented in Equations (5.3) and (5.4), using natural logarithms and linear regression respectively:

$$\ln t_o = 16.707 - 0.02926\tau \quad (5.3)$$

$$(1/B)^3 = 0.0807 - 0.000190\tau \quad (5.4)$$

Experimental observations showed that the critical pit size, denoted as H_c , at the transition from pit to incipient crack, depends on the cyclic stress amplitude. At higher stress levels, transition occurred at relatively smaller pit sizes. Table 5.2 shows the variation of critical pit size, H_c , in relation to the applied shear stress amplitude. The critical pit size as a function of applied stress amplitude, is calculated with the following equation:

$$\lg H_c = 1.921 - 0.00147\tau \quad (5.5)$$

For all stress levels used in the present study, the relationship (5.2) agrees well with the experimental tendency, as shown in Chapter 4, Figure 4.7 (a), (b) and (c). The parameters, t_o , H_c , H_o (initial pit size), and $(1/B)^3$ for each stress level are listed in Table 5.1.

Substituting Equations (5.3), (5.4) and (5.5) into Equation (5.2), the major corrosion pit size as a function of applied stress amplitude is obtained, as also is the pit growth rate. The prediction of crack initiation from the pit then follows. When the major pit growth reaches the critical pit size, H_c , the incipient crack develops from the pit; the time t for the pit to achieve the critical pit size, is taken as the *crack initiation time*. Because the number of loading cycles is proportional to time in the following form:

$$t = N / f$$

where f is the frequency, it follows from Equation (5.2) that

$$2r - 2r_0 = B[(N - N_0) / f]^{1/3} \quad (5.6)$$

replacing $2r$ by H , and $2r_0$ by H_0 , the pit growth rate is obtained as:

$$\begin{aligned} H - H_0 &= B[(N - N_0) / f]^{1/3} \\ \frac{dH}{dN} &= \frac{B^3}{3f} \left(\frac{1}{H - H_0} \right)^2 \end{aligned} \quad (5.7)$$

If the average pit growth rate is used to describe the pit propagation behaviour, as was actually measured in experiments, the following expression will hold:

$$\begin{aligned} \left(\frac{dH}{dN} \right) &= \frac{1}{(t_2 - t_1)} \int_{t_1}^{t_2} \frac{dH}{dN} dt = \frac{1}{(t_2 - t_1)} \int_{t_1}^{t_2} \frac{dH}{dN} \frac{dN}{f} \\ &= \frac{1}{f(t_2 - t_1)} \int_{t_1}^{t_2} dH = \frac{H_2 - H_1}{N_2 - N_1} \\ &= \frac{B^3}{f} \left[\frac{1}{(H_2 - H_0)^2 + (H_2 - H_0)(H_1 - H_0) + (H_1 - H_0)^2} \right] \end{aligned} \quad (5.8)$$

where t_1 is the time for the pit to grow from H_0 to H_1 , t_2 is the time for the pit to grow to H_2 , and $H_2 > H_1$.

From Equation (5.7) the number of cycles for pit growth can be calculated as:

$$N_{\text{pit}} = f \left(t_0 + (H_c - H_0)^3 \left(\frac{1}{B} \right)^3 \right) \quad (5.9)$$

5.3 Stress concentration around an inclusion or a pit

Analytical solutions for the stress concentration around internal inclusions, which are characterized by elastic moduli that are different from the surrounding matrix (a hole is regarded as having zero modulus) have been given by Goodier [10]. For a surface inclusion or a hole, no analytical results have yet been obtained. However, FEM calculations carried out by Melander [11] showed that the state of stresses around a surface hole is quite similar to that around an internal pore and the maximum deviation between the two cases is within 5%. This means that for most practical applications the stress concentration at a surface pore (such as a MnS inclusion, or pit due to attack in an aggressive environment) can be estimated from the analytical expressions for an internal pore given by Goodier.

Values of stress concentration factors for different cases where a cavity contains material (having modulus E') perfectly bonded to the matrix material (having modulus E), as derived by Goodier [10], are tabulated in Table 5.3. These values are used to evaluate the stress concentration at pits in the present study.

Using a simplified approach based on experimental observations, the inclusion inside a pit has an effective elastic modulus one-third that of the matrix for stress ranges higher than 728 MPa. This drops to one quarter at between 600 and 700 MPa, while it drops to zero for stress ranges less than 600 MPa. Results in Table 5.4 show that the stress concentration varies from 1.5, 1.75, to 2.05 for cases where the stress range is higher than 728 MPa, between 700 MPa and 600 MPa, and less than 600 MPa, respectively.

According to Weiss, Stickler and Blom [12], the field of stress concentration around an isolated micropit was found to extend to approximately twice the radius of the micropit or less. A similar analysis is used to estimate the effective ranges of stress concentration for a pit on the surface of a specimen of BS251A58 steel under reversal torsional test in 0.6M

account by combining the effective ranges of stress concentration. Considering that local pit stresses tail-off in a power of r^{-2} form for a semi-infinite body, Equation (5.10) is proposed to evaluate the stress concentration as a function of distance from the pit.

$$K_t = (K_{t0} - 1) \left(\frac{H_c}{2r} \right)^2 + 1 \quad (r \geq H_c / 2) \quad (5.10)$$

where K_{t0} is the maximum stress concentration at the surface of the pit, H_c is the final size of the pit, which varied with the applied stress level as described by Equation (5.5), r is the distance from the original pit centre and K_t is the local stress concentration as a function of distance from the pit centre.

Consequently, the local stress surrounding the pit, τ_{lc} or σ_{lc} , as a function of the distance from the original pit centre will take the following form:

$$\begin{aligned} \tau_{lc} &= \tau \left[(K_{t0} - 1) \left(\frac{H_c}{2r} \right)^2 + 1 \right], \quad r > H_c / 2 \quad \text{for stage-I growth} \\ \sigma_{lc} &= \sigma \left[(K_{t0} - 1) \left(\frac{H_c}{2r} \right)^2 + 1 \right], \quad r > H_c / 2 \quad \text{for stage-II growth} \end{aligned} \quad (5.11)$$

5.4 Continuous distribution function of dislocation pile-up

Once a crack forms (either solely due to external loading, or due to the combined effect of mechanical load and chemical attack in corrosion), it can be represented as a dislocation pile-up balanced by the internal friction, the barrier blocking force at the ends of the pile-up and the external force. Following Head and Louat's work [13], the balance of an array of discrete dislocations can be conveniently described by a 'smeared-out', continuous distribution of dislocations, as was used in the BCS model [1].

For mathematical simplicity, it is supposed that the polycrystal alloy is composed of equal size grains with grain diameter D . Consider a crack of length $2a$, which may have penetrated a number of grains. Let i be the number of the slipped half grains, then if the crack initiates from the centre of a grain then $c = c_i = iD/2$, $i=1, 3, 5, \dots$ (see Figure 5.1 for

crack initiates from the centre of a grain then $c = c_i = iD/2$, $i=1, 3, 5, \dots$ (see Figure 5.1 for schematic representation); if the crack initiates from the grain boundary, then the value of i should take 2, 4, 6, ... instead. The solution to the equilibrium equation gives the dislocation distribution function which is found to be [4]:

$$f(\zeta_i) = \frac{\tau_o}{\pi^2 A} \left[\cosh^{-1} \left(\left| \frac{1 - n_i \zeta_i}{n_i - \zeta_i} \right| \right) - \cosh^{-1} \left(\left| \frac{1 + n_i \zeta_i}{n_i + \zeta_i} \right| \right) \right] + \frac{\tau_o \zeta_i}{\pi^2 A (1 - \zeta_i)^{1/2}} \left[2 \sin^{-1} n_i + \pi \left(\frac{\tau}{\tau_o} - 1 \right) \right] \quad (5.12)$$

where τ is the applied stress, τ_o is the friction stress, $n_i = a_i / c_i$, $A = Gb / 2\pi$ for screw dislocations, or $A = Gb / 2\pi(1 - \nu)$ for edge dislocations, G is the shear modulus, b the Burgers vector and ν the Poisson's ratio. Grain boundaries are located at $x = iD / 2$ and crack tips at $a = a_i = in_i D / 2$. The variable $\zeta_i = 2x / iD$ describes the position throughout, so that the grain boundary is always at $\zeta_i = 1$ and the crack tip at $\zeta_i = n_i$.

A dislocation lock is included in the analysis to represent the grain boundary which constrains the plastic zone, so that the crack tip plastic displacement ϕ decreases to zero as the crack approaches the grain boundary. The crack extension per cycle is made to be proportional to ϕ and therefore the propagation law of the fatigue crack growth is obtained, as will be discussed at a later stage.

5.5 Critical equilibrium condition

The critical condition by which the plastic zone extends to the next grain determines the value of n_i^c . During the development of the model, there are two approaches to accomplish this calculation. In the earlier version of the model, where the grain boundary is idealised as a thin layer with zero width, represented by a δ function, the critical condition is established such that at a finite distance r_o ahead of the boundary, the stress concentration S reaches a critical value; in the latest version of the model where the grain boundary itself is considered as an extra zone of length r_o which sustains a (finite) friction

stress σ_3^i , the critical condition is attained when the stress at the barrier zone σ_3^i , reaches a critical value $m^* \tau_c$ [5].

For the former case where the barrier is represented by a infinitesimal thin layer, the stress S at a point $\zeta_i > 1$ on the glide plane ahead of the plastic zone is calculated by the expression:

$$S(\zeta_i, n_i, \tau) = \tau + A \int_{-1}^1 \frac{f(\zeta)}{\zeta_i - \zeta} d\zeta \quad (5.13)$$

Solving the integral gives:

$$\frac{S}{\beta_i \tau_o} = \frac{\tau}{\tau_o} + \frac{1}{\beta_i} \left[1 - \frac{2}{\pi} \tan^{-1} \left(\frac{n_i}{\beta_i (1 - n_i^2)^{1/2}} \right) \right] - \frac{2}{\pi} \cos^{-1} n_i \quad (5.14)$$

$$\text{where } \beta_i = \frac{\zeta_i}{(\zeta_i^2 - 1)^{1/2}} = \frac{i\lambda + 1}{(2i\lambda + 1)^{1/2}}, \quad \lambda = D / (2r_o) \quad (5.15)$$

The critical condition is established when:

$$S \geq m^* \tau_c = R \quad (5.16)$$

where R denotes the barrier strength.

From (5.16) the governing equation which determines slip transmission for crack advance and consequently the critical value of n_i^c can be derived as [14]:

$$F(n_i^c, \tau, i) = \frac{\tau}{\tau_o} \left(1 - \frac{\beta_1 m_i \tau_{FL}}{\beta_i m_1 \tau} \right) + \frac{1}{\beta_i} \left(1 - \frac{2}{\pi} \tan^{-1} \frac{n_i^c}{\beta_i \sqrt{1 - (n_i^c)^2}} \right) \quad (5.17)$$

$$-\frac{2}{\pi} \cos^{-1} n_i^c \geq 0$$

where τ_{FL} is the threshold stress for crack propagation unaffected by crack length. For many materials, this stress is the fatigue limit. m_i is the orientation factor of the corresponding grain. For a strain hardened material, τ_o should be replaced by a strain hardening dependent friction stress τ_f , as indicated later in Section 5.8.

For the later case where the barrier zone sustaining a finite friction, the value of n_i^c is found to be expressed by [5]:

$$n_i^c \geq \cos\left(\frac{\pi}{2} \frac{\tau - \tau_{Li}}{\tau_f}\right) \quad (5.18)$$

where $\tau_{Li} = \tau_{FL}/\sqrt{i}$, $i=1, 3, 5, \dots$ for transgranular initiation, and $i=2, 4, 6, \dots$ for intergranular initiation, τ_f is a friction stress in the plastic zone and is strain hardening dependent. Variation in m^* , τ_c and r_0 in relation to the values attained by the same variables at the fatigue limit situation ($n_i \approx 1$), are not taken into account.

When the grain orientation effect is considered Equation (5.18) can be modified to :

$$n_i^c \geq \cos\left(\frac{\pi}{2} \frac{\tau - \frac{\tau_{FL}}{\sqrt{i}} \frac{m_i}{m_1}}{\tau_f}\right) \quad (5.19)$$

It should be noted that for most common materials, the following conditions hold:

$$\lambda = D/(2r_0), \quad \frac{\beta_i}{\beta_1} \approx \sqrt{\frac{i\lambda}{2}} / \sqrt{\frac{\lambda}{2}} = \sqrt{i},$$

$$n_i^c \approx 1, \quad \tan^{-1} \frac{n_i^c}{\beta_i \sqrt{1 - (n_i^c)^2}} \approx \frac{\pi}{2} \quad (5.20)$$

As a result the second term in Equation (5.17) is negligible. Therefore, with τ_0 replaced by a strain hardening dependent τ_f , Equation (5.17) can be rewritten as

$$\cos^{-1} n_i^c \leq \frac{\pi}{2} \frac{\tau}{\tau_f} \left(1 - \frac{\beta_1}{\beta_i} \frac{m_i}{m_1} \frac{\tau_{FL}}{\tau}\right) = \frac{\pi}{2} \frac{\tau - \frac{\tau_{FL}}{\sqrt{i}} \frac{m_i}{m_1}}{\tau_f} \quad (5.21)$$

which actually confirms Equation (5.19).

As will be discussed later, the applicability of Equation (5.17), (5.18), and (5.19) are all examined in comparison with experimental results. Equation (5.19) is found to give slightly better predictions than the other two although the difference is small.

Two limiting conditions, from which some useful conclusions may be obtained, can now be considered:

1) The first case corresponds to the fatigue limit situation, with the crack contained within the first grain unable to penetrate the dominant barrier. In this case $n \rightarrow 1$ and $\tau = \tau_{FL}$ so that from (5.17)

$$F(n \rightarrow 1, i = 1) = 0 \quad (5.22)$$

which means that the crack is blocked at the barrier and the stress concentration is not sufficiently high to activate a new slip band in the next grain. The substitution of the corresponding n and τ values into (5.17) leads to an identity. Resorting to Equations (5.16) and (5.14) the fatigue limit can be expressed as:

$$\tau_{FL} = \frac{m_1 \tau_c}{\beta_1} = 2m_1 \sqrt{r_o} \tau_c D^{-1/2} \quad (5.23)$$

2) The other limit case corresponds to the bulk yielding of the material. The situation now is that when the stress level is of such a magnitude that the first grain yields ($i=1$) and, before a fatigue crack forms, the stress concentration is sufficiently high to activate a new slip band in the next grain; therefore if (5.17) is made to confirm to

$$F(n \rightarrow 0, i = 1) = 0 \quad (5.24)$$

then the applied stress should correspond to the general yield stress. The above relationship can be expressed as:

$$\begin{aligned} \tau_y &= \left(1 - \frac{1}{\beta_1}\right) \tau_o + 2\sqrt{r_o} m_1 \tau_c D^{-1/2} \\ &\approx \left(1 - \frac{1}{\beta_1}\right) \tau_o + \tau_{FL} \end{aligned} \quad (5.25)$$

The expression is widely known as the Hall-Petch relation.

Equation (5.25) indicates that the yield strength of the material has contributions from two parts. One is the internal friction stress which opposes the movement of the slipping dislocations, and the other is the grain boundary strength which blocks the heading dislocation from moving into the next grain. A larger misorientation and a smaller grain size D will both increase the yield strength.

For the case where the crack length is within the first grain, $i=1$, the internal friction could be expressed as:

$$\tau_o = \frac{(\tau_y - \tau_{FL})}{1 - 1/\beta_1} \quad (5.26)$$

For the present material, BS251A58 steel, the monotonic torsion yield stress is $\tau_y=757\text{MPa}$, the in-air fatigue limit is $\tau_{FL}=457.5\text{ MPa}$, $r_o = 0.1\mu\text{m}$, $\beta_1 = 8.703$, therefore $\tau_o = 338.4\text{MPa}$.

5.6 Crack transition from stage-I to stage-II

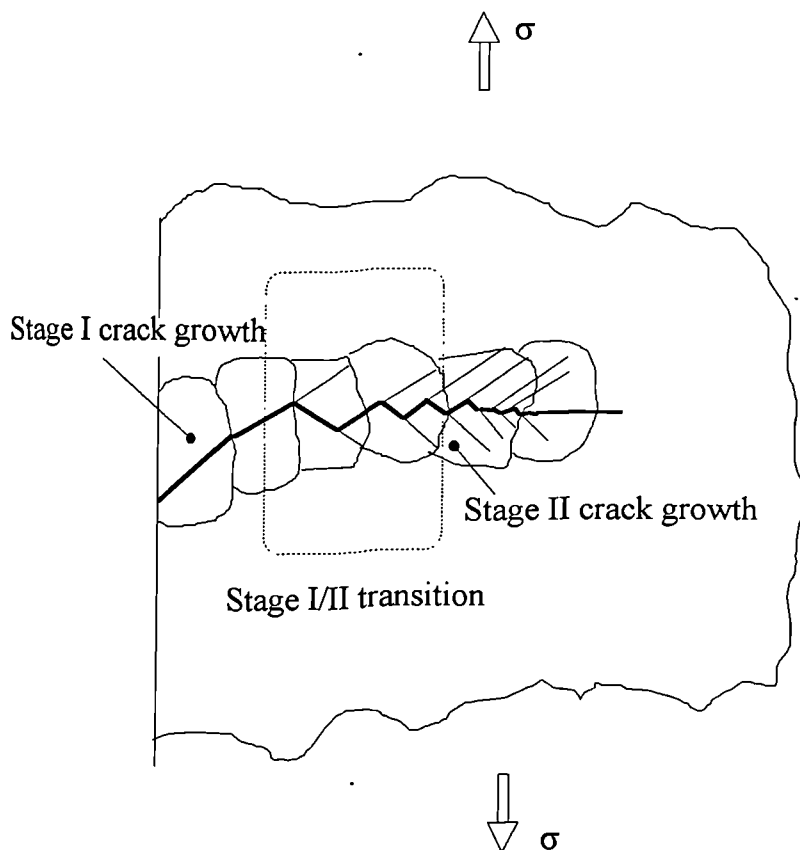
Crack growth transition from stage-I to stage-II was observed in the present tests, see Table 5.6. Forsyth [15] first classified stage-I fatigue crack growth and stage-II fatigue crack growth. The shear stress range controls crack initiation and the early crystallographic short crack growth, i.e. stage-I crack growth. The component of stress range normal to the crack plane controls the initial growth of the stage-II crack. If the material and the conditions of stressing favour duplex slip, the stage-I process gives way to the stage-II process.

The transition from stage-I to stage-II fatigue crack growth in copper single crystals was studied by Cheng and Laird [16], and Wang and Mughrabi [17]. It was observed that transition was accompanied by slip on a secondary slip system. They postulated that transition from the stage-I to stage-II propagation occurs when work hardening at the crack tip in the primary PSB increases so that the resolved local shear stress acting on the secondary slip system is raised sufficiently so as to activate a secondary PSB, i.e. duplex slip is required for stage-II crack propagation. Accompanying the transition there should be a dramatic decrease of stage-I crack propagation on the primary slip system.

In stage I crack propagation there is one slip system that dominates, usually oriented along one of the two maximum shear stress directions. The orientation of the fatigue crack is

also in this 45° direction. On further crack growth other slip system becomes operative and the plastic displacement at the crack tip changes, favouring the opening mode over the shear mode displacement. This is achieved over several grains (usually three to five). At the end of the transition period the opening mode is now the dominant, and the flow stress of the plastic zone has gradually increase its value from τ_o to $\sigma_o = m \tau_o$ where m is the relevant orientation factor.

If a symmetric duplex or multiple slip system sets up in the crack tip, crack propagation can be a result of slip on at least two different planes, and form a zigzag path which can be macroscopically perpendicular to the maximum tensile stress, i.e. stage II cracking.



From another point of view, Miller [18] indicated that an intense fatigue resistance region occurs at the crack transition stage from stage-I to stage-II, when the two dimensional crack becomes a three dimensional one, see Figure 5.2 [18]. It can be expected that the internal friction for stage-II cracking, σ_o , may become the stronger resistance at the crack

transition stage from stage-I to stage-II, because it is higher than the internal friction for shear mode, τ_o .

For the fully-reversed torsional fatigue test, the stress system is illustrated in Figure 5.3. The maximum tensile stress in the direction of 45 or 135 degree to the specimen axis is, in magnitude, equal to the torsional stress in the direction along the specimen axis, i.e. $\sigma = \tau$. The fatigue limit σ_{FL} in air, was obtained from push-pull test using the same material [19]. A similar system equation can be employed to represent the crack growth in stage-II. Parallel to (5.17)-(5.19), the critical equilibrium condition for the case of push-pull test, can be written as:

$$F(n_i, \sigma, i) = \frac{\sigma}{\sigma_o} \left(1 - \frac{\beta_1 m_i \sigma_{FL}}{\beta_i m_1 \sigma} \right) + \frac{1}{\beta_i} \left(1 - \frac{2}{\pi} \tan^{-1} \frac{n_i^c}{\beta_i \sqrt{1 - (n_i^c)^2}} \right) \quad (5.27)$$

$$- \frac{2}{\pi} \cos^{-1} n_i^c \geq 0$$

$$\text{and } n_i^c \geq \cos \left(\frac{\pi}{2} \frac{\sigma - \frac{\sigma_{FL} m_i}{\sqrt{i} m_1}}{\sigma_f} \right) \quad (5.28)$$

A Hall-Petch relation similar to (5.26) can be established by replacing τ_y with σ_y and τ_{FL} with σ_{FL} , which finally gives a value of 617 MPa for σ_o .

For corrosion fatigue in 0.6 M NaCl solution, pH =6, frequency 5Hz, room temperature, the fatigue strength of the material in torsion was found to be 98 MPa for 10^7 cycles to failure, while in the same environment the fatigue strength of the same material under push-pull test was 179.4 MPa. Table 5.5 illustrated the parameters for the present modelling work.

5.7 The effect of grain orientation

The effect of grain orientation is realised by the term m_i / m_1 , where m_1 is the orientation factor related to the first grain and m_i are the factors corresponding to other successive grains.

In the first grain the orientation factor should have a value of approximately one because plastic deformation, and hence crack formation, takes place initially in grains which are most favourably orientated so that the resolved shear stress is at its maximum. Successive m_i values should increase monotonically with i , with the largest increase occurring between the first and the second grains ($i=1$ and 3) and the rate of increase slowing down until m_i attains a value representative of truly polycrystalline behaviour, i.e. the Taylor factor of 3.07 for face centred cubic (FCC) materials, and 2.75 for body centred cubic (BCC) materials [20].

Two empirical formulae obtained in [14, 21] to calculate the progression of orientation factors on FCC materials were:

$$\frac{m_i}{m_1} = 1 + 0.5 \ln(i) \quad \text{for FCC polycrystals (5.29.a)}$$

$$\frac{m_i}{m_1} = 1 + 2.07 \left[\frac{2}{\pi} \tan^{-1} 0.522(i-1) \right]^{1.86} \quad \text{for FCC polycrystals (5.29.b)}$$

For BCC materials, Equation (5.29.b) changes to:

$$\frac{m_i}{m_1} = 1 + 1.75 \left[\frac{2}{\pi} \tan^{-1} 0.522(i-1) \right]^{1.86} \quad \text{for BCC polycrystals (5.30)}$$

Equation (5.29.b) and (5.30) is preferred, because the following points can be realised:

- 1) $m_1=1$,
- 2) the increase of m_i is larger for lower i .
- 3) for sufficiently large i , m_i tends to the value of 3.07 for FCC materials, and 2.75 for BCC materials.

5.8 Strain hardening effect

In terms of the model, it was shown [14] that for slip not to be transmitted to the next grain immediately when the load is applied, the following condition should be satisfied if the effect of grain orientation is included,

$$\frac{\tau}{\tau_0} < \frac{\beta_i - 1}{\beta_i - \beta_1 \cdot m_i / m_1} = 1 + \frac{\beta_i m_i / m_1 - 1}{\beta_i - \beta_1 m_i / m_1} \quad (5.31)$$

which indicates that the ratio τ/τ_0 should be a decreasing function of i , the number of half grains affected by fatigue damage. It means that a constant friction stress τ_0 is not a suitable assumption and that τ_0 should increase with increasing crack length and therefore, a strain hardening law as a function of crack length or position number i , should be determined for the full implementation of Equation (5.17), (5.18) or (5.19). Experimental confirmation of the strain hardening expected within the plastic zone has been obtained by taking dislocation density measurement along the crack path. For example, de los Rios et al [22] studied the type of dislocation pattern formed within the wake of the plastic zone of fatigue cracks. Observation of foils taken next to the fracture surface at increasing distances from the original notch, showed an intensification of strain manifested by higher dislocation density measurements.

The role of work hardening in their model was discussed by de los Rios and Navarro [14]. They used the Bilby's existence condition to calculate a hardening law wherein τ_0 is no longer a constant but varies with crack length and plastic zone size, which enables the model to be employed satisfactorily and predicts a stable growth of fatigue crack. However, the Bilby's relation as a hardening law was found to be too powerful for typical materials: - it describes an ever-stable growth even when the fracture toughness of the material is achieved. Therefore a linear work hardening law was later proposed [21] which reflected more closely the typical FCC material behaviour of the Al-Li 8090 alloy [23]. The model, with the incorporation of the linear hardening law, was able to describe the supposed 'anomalous' short crack growth, the transition from short crack to long crack,

final instability when instant failure occurs and the prediction of fatigue life which agreed reasonably with the experimental results.

For a low-textured, high stacking fault material such as the present tempered martensite BS251A58, strain hardening of a power law form is more likely to occur. Therefore, as a further development to the model, a more general form of power law hardening, particularly a parabolic law, will be introduced in the present study.

Following the method presented in [21], a power law hardening form is employed to describe the strain hardening behaviour of the present material:

$$\tau_f = \tau_0 + k' \bar{\gamma}^q \quad (5.32)$$

where τ_0 is the initial friction stress of the material in the absence of strain hardening, k' is the hardening rate of the corresponding single crystal, $\bar{\gamma}$ is the averaged strain over the whole slip band, and q is the power index between 1 and 0,

For the case $q=1$ Equation (5.32) reassumes the linear hardening law.

The formula to calculate the average strain $\bar{\gamma}$ is [21]:

$$\bar{\gamma} = \frac{bc}{2w} \int_{-1}^1 \zeta f(\zeta) d\zeta \quad (5.33)$$

where b is the Burgers vector, w the width of the slip band, and c the crack length plus the plastic zone size.

With the introduction of Equation (5.32), the equilibrium equation for the dislocation is now:

$$\int_{-1}^1 \frac{f(\zeta)}{\zeta - \zeta'} d\zeta' + \frac{P(\zeta)}{A} = 0 \quad (5.34)$$

$$\text{with } P(\zeta) = \begin{cases} \tau & |\zeta| < n \\ \tau - \tau_0 - k' \left(\frac{bc}{2w} \int_{-1}^1 \zeta f(\zeta) d\zeta \right)^q & |\zeta| \geq n \end{cases} \quad (5.35)$$

In [21], a perturbation method was used to solve the equilibrium equation when linear hardening was introduced into the model. A different method is used here to obtain the solution of Equation (5.34). The necessary steps to solve the equation are given in Appendix A. The final result of the distribution function, with extra subscript i to indicate the crack tip position, is expressed as:

$$f(\zeta_i) = \frac{\tau_f}{\pi^2 A} \left[\cosh^{-1} \left(\left| \frac{1 - n_i \zeta_i}{n_i - \zeta_i} \right| \right) - \cosh^{-1} \left(\left| \frac{1 + n_i \zeta_i}{n_i + \zeta_i} \right| \right) \right] + \frac{\tau_f \zeta_i}{\pi^2 A (1 - \zeta_i)^{1/2}} \left[2 \sin^{-1} n_i + \pi \left(\frac{\tau}{\tau_f} - 1 \right) \right] \quad (5.36)$$

$$\text{with } \tau_f = h(n) \tau_0 \quad (5.37)$$

representing the hardening dependent friction stress, where $h(n)$ is a function describing the effect of power law hardening and satisfies the following relation:

$$h = 1 + [V(\pi R_\tau - 2I_n h)]^q \quad (5.38)$$

$$\text{where } V = \left(\frac{k'}{\tau_0} \right)^{\frac{1}{q}} \frac{c \tau_0 \kappa}{2wG} \quad (5.39)$$

$$I_n = \frac{\pi}{2} - n \sqrt{1 - n^2} - \sin^{-1} n \quad (5.40)$$

$$R_\tau = \frac{\tau}{\tau_0} \quad (5.41)$$

$$\tau_{lc} = K_t \tau = \tau \left[(K_{to} - 1) \left(\frac{a_0}{r} \right)^2 + 1 \right] \quad (5.42)$$

$$R_\tau = \frac{\tau_{lc}}{\tau_0} = \frac{\tau}{\tau_0} \left[(K_{to} - 1) \left(\frac{a_0}{r} \right)^2 + 1 \right] \quad (5.43)$$

$$\kappa = \begin{cases} 1 & \text{for screw dislocation} \\ 1 - \nu & \text{for edge dislocation} \end{cases}$$

For $q=1$, from Equation (5.38) h is found to be:

$$h = \frac{1 + \pi R_\tau p \kappa}{1 + 2I_n p \kappa} \quad \text{with } p = \frac{k' c}{2Gw} \quad (5.44)$$

which is identical to the result of linear hardening obtained in [21].

For a general power law hardening where $0 < q < 1$, a numerical solution of (5.38) will give the hardening factor h as a function of n and R_τ . For a parabolic hardening with

$q=0.5$, an explicit expression for h can be obtained, as detailed in Appendix A, and is expressed as:

$$h = \begin{cases} 1 - I_n V + \sqrt{I_n^2 V^2 + V(\pi R_\tau - 2I_n)} & \text{for } R_\tau \geq 1 \\ 1 + J_n V + \sqrt{J_n^2 V^2 + 2J_n V} & \text{for } R_\tau < 1 \end{cases} \quad (5.45)$$

here $J_n = n\sqrt{1-n^2}$

It is also shown in Appendix A that h always satisfies the following conditions

$$\frac{\partial h}{\partial R_\tau} > 0 \quad (\text{for } R_\tau \geq 1) \quad \text{or} \quad \frac{\partial h}{\partial R_\tau} = 0 \quad (\text{for } R_\tau < 1) \quad (5.46)$$

$$\frac{\partial h}{\partial n} > 0 \quad (5.47)$$

The above relations indicate that extent of hardening increases with increasing n , and/or increasing R_τ . This trend follows the general physical expectation that with the plastic zones blocked by the barrier, the local friction stress to dislocation movement increases with increasing crack length, and also the higher the external load, the greater is the friction stress.

During fatigue crack growth, the generation of plastic deformation will give rise to an intensification of dislocation density which in turn leads to the increase in the friction stress opposing further dislocation movement. This hardening effect, as discussed in [21] and shown in Appendix A, can be considered in terms of the model by replacing the constant τ_0 with a hardening dependent τ_f in the dislocation distribution function (5.12) and, consequently, in the critical balance equations in either (5.17), (5.18) or (5.19). Equation (5.17) is therefore rewritten as:

$$F(n_i^c, \tau, i) = \frac{\tau}{\tau_f} \left(1 - \frac{\beta_1 m_i \tau_{FL}}{\beta_i m_1 \tau} \right) + \frac{1}{\beta_i} \left(1 - \frac{2}{\pi} \tan^{-1} \frac{n_i^c}{\beta_i \sqrt{1-(n_i^c)^2}} \right) \quad (5.48)$$

$$-\frac{2}{\pi} \cos^{-2} n_i^c \geq 0$$

The role of the hardening effect on stable fatigue crack growth was studied in detail in [21] and [24]. The overall result is that cyclic strain hardening helps to reduce the stress concentration ahead of the plastic zone, indicating the higher ability of the hardened

material to resist fatigue crack propagation; it also delays the transition to the long crack regime and extends the region of stable crack growth.

5.9 Crack propagation

Whenever the shear stress, resolved on the slip plane and in the slip direction, is greater than the initial internal friction stress τ_o , dislocation slip is generated -- a microstructural process that usually takes place in the larger and better oriented grains. Due to this localisation of straining, cracks are formed and grow along the slip bands [25, 26]. Slip is arrested on reaching the microstructural barrier which, in the present case, is the grain boundary, and the dislocations pile up against the barrier along the slip band giving rise to a stress concentration ahead of the plastic zone.

The critical condition for the plastic zone to overcome the barrier will be achieved when the crack length is such that n reaches the value of n_i^c , satisfying the critical equilibrium condition either (5.17), (5.18) or (5.19). Once the critical equation is satisfied the plastic zone extends to encompass the whole of the next grain and consequently n_i^c jumps at once to:

$$n_{i+2}^s = n_i^c \frac{i}{i+2} \quad (5.49)$$

Following similar arguments as in [2], the crack growth rate is assumed to be proportional to the displacement between the two crack surfaces ahead of the crack tip, which in turn is equal to the number of dislocations entering the plastic zone, multiplied by the Burgers vector. Performing the integration, the plastic displacement ϕ may be expressed as [2]:

$$\phi_i = \frac{2b}{\pi^2 A} \tau_f c_i \left[n_i \ln \left(\frac{1}{n_i} \right) + \sqrt{1 - n_i^2} \left(\frac{\pi}{2} \frac{\tau}{\tau_f} - \cos^{-1} n_i \right) \right] \quad (5.50)$$

The propagation rate of the crack is therefore:

$$\frac{da_i}{dN} = \alpha (\phi_i)^m \quad (5.51)$$

Tomkins [28]. The constancy in n after the merging point, or transition, reflects the preservation of geometrical similitude in the long crack regime [29, 30].

5.10 The transition and instability of crack growth

One important stage in crack growth is the transition between short and EPFM cracks where the crack growth behaviour changes from structure-sensitive to structure-insensitive. Such a transition should take place, as found by Carlson and Ritchie [31], and Yoder [32], when the plastic zone becomes larger than the grain size. Therefore, in the short crack region, the condition:

$$i \frac{D}{2} < a_{i+2}^c < (i+2) \frac{D}{2}$$

or $\frac{i}{i+2} < n_{i+2}^c < 1$ (5.52)

should be satisfied, where the superscript c in crack length a , refers to the crack length when the plastic slip is transmitted into the following grain.

The next important stage is the point of instability, when crack growth rate accelerates dramatically, followed immediately by total failure. Before instability, the crack extends in a stable and monotonic fashion, therefore,

$$a_{i+2}^c > a_i^c$$

which leads to

$$n_{i+2}^c > \frac{i}{i+2} n_i^c$$
 (5.53)

conversely, when

$$n_i^c \frac{i}{i+2} \geq n_{i+2}^c$$
 (5.54)

instability ensues.

This is referred to as the first type of instability, with $i_{(1)}^{\text{in}}$ denoting the instability value of i .

There is, however, another possibility of instability where the applied load is of such a level that at a given i the inequality in the critical equilibrium condition (5.17), (5.18) or (5.19),

where α and m are material and environmental dependent parameters. The factor α is interpreted as the fraction of dislocations on the slip band which participates in the process of crack extension [25]. The dislocation movement is also expected to be affected by the presence of the aggressive environment, leading to different values of α and m as compared with in-air fatigue.

The above propagation law indicates that fatigue crack growth is an accumulation process of local plasticity. A propagating law of the same kind has been used by other researchers [27]. When $m=1$, it becomes identical to the widely used law $da / dN \propto \Delta CTOD$ in EPFM.

Once a fatigue crack has been initiated, the value of n_i is low, just above zero, and therefore the crack growth rate is high according to (5.50) and (5.51). As the crack grows with the plastic zone blocked by the grain boundary, the value of n_i increases (making in turn ϕ and thus da/dN , decrease) to such an extent that one of two possibilities may occur: if equality in the critical condition (5.17), (5.18) or (5.19) is not satisfied, the crack reaches the grain boundary at which point $n_i=1$, $\phi_i=0$, and the crack will become arrested; alternatively, Equation (5.17), (5.18), or (5.19) is satisfied for a given $n_i=n_i^c$ and consequently the stress concentration ahead of the plastic zone or within the barrier zone will attain the critical value to activate a slip band in the next grain, at which point the value of $c_i=iD/2$ jumps to its new value of $c_{i+2}=(i+2)D/2$, and accordingly the parameter $n_i=n_i^c$ jumps to a new n_{i+2}^s , whose value is evaluated by expression (5.49). Since ϕ_i is a function of n_i and τ , for a given i the growth rate of the crack is thereby determined.

The crack growth mechanism illustrated here explains satisfactorily the oscillation pattern between low and high rates of short crack growth. When the crack becomes longer, the variation in n_i is much reduced (refer to Equation (5.49)), and the growth rate gradually and steadily increases until it tends towards the EPFM regime previously described by

always hold for the whole range of n_i from the previous n_{i-2}^s to 0, which is equivalent to the plastic zone extending from c_{i-2} to infinite. Such a situation corresponds to case when the applied load is so high that slip transmission can not be stopped by any of the microstructural barriers ahead of the crack. At this instance the plastic zone size and the crack growth rate simultaneously attain infinity values. This is referred to as the second type of instability with $i_{(2)}^{in}$ denoting the instability value of i .

A third category of instability occurs when, before the conditions for the first and the second type of instability are attained, the crack reaches the end of the specimen. The corresponding instability value of i is $i_{(3)}^{in} = 2d/D$.

Obviously, the actual instability of crack growth occurs at the earliest of the three possibilities, therefore whenever

$$i \geq i^{in} = \min [i_{(1)}^{in}, i_{(2)}^{in}, i_{(3)}^{in}] \quad (5.55)$$

instant failure takes place.

5.11 Lifetime prediction

From Equation (5.50), since

$$\lim_{n_i^c \rightarrow 1} \phi_i = 0 \quad (5.56)$$

the growth law by Equation (5.51) indicates that the growth rate will tend to zero when the barrier is strong ($n_i^c \rightarrow 1$). This is the case for under fatigue limit loading conditions.

Conversely, for propagating cracks, integration of (5.51) with limits for crack length from initiation size a_0 to final failure size a_f gives crack propagation life as:

$$N = \int_{a_0}^{a_f} \frac{da_i}{\alpha(\phi_i)^m} = \sum_{i=1}^{i^{in}} \int_{a_i^s}^{a_i^c} \frac{da_i}{\alpha(\phi_i)^m} \quad (5.57)$$

where $a_1^s = a_0$, a_i^c is determined by the critical condition Equation (5.48), a_i^s by (5.49), and i^{in} by (5.55).

To perform the integration, bearing in mind that the plastic zone is blocked at a particular value of c_i , and n_i changes from n_i^s to n_i^c , the substitution of $da_i = c_i dn_i$ into (5.57) then

leads to:

$$N = \sum_{i=1}^{i^n} \int_{n_i^s}^{n_i^c} \frac{c_i dn_i}{\left\{ \frac{2b}{\pi^2 A} \tau_f c_i \left[n_i \ln\left(\frac{1}{n_i}\right) + \sqrt{1-n_i^2} \left(\frac{\pi}{2} \frac{\tau}{\tau_f} - \cos^{-1} n_i \right) \right] \right\}^m} \\ = \frac{1}{\alpha} \sum_{i=1}^{i^n} \left(\frac{\pi}{4\kappa} \right)^m \left(\frac{iD}{2} \right)^{1-m} \int_{n_i^s}^{n_i^c} \left\{ \frac{\tau_f}{G} \left[n_i \ln(1/n_i) + \sqrt{1-n_i^2} \left(\frac{2}{\pi} \frac{\tau}{\tau_f} - \cos^{-1} n_i \right) \right] \right\}^{-m} dn_i \quad (5.58)$$

Denoting

$$J_i = \int_{n_i^s}^{n_i^c} \left\{ \frac{\tau_f}{G} \left[n_i \ln(1/n_i) + \sqrt{1-n_i^2} \left(\frac{2}{\pi} \frac{\tau}{\tau_f} - \cos^{-1} n_i \right) \right] \right\}^{-m} dn_i \quad (5.59)$$

$$\Delta_i = \left(\frac{\pi}{4\kappa} \right)^m \left(\frac{iD}{2} \right)^{1-m} J_i \quad (5.60)$$

then

$$N = \frac{1}{\alpha} \sum_{i=1}^{i^n} \left(\frac{\pi}{4\kappa} \right)^m \left(\frac{iD}{2} \right)^{1-m} J_i = \frac{1}{\alpha} \sum_{i=1}^{i^n} \Delta_i \quad (5.61)$$

The theoretical determination of the material, and environment dependent parameters α and m needs a thorough knowledge of dislocation storage, reversibility and annihilation in order to calculate the fraction of dislocations actually involved in crack extension. In the present aggressive environment, the combined action of dissolution and hydrogen embrittlement will affect the dislocation movement, and hence affect α and m . Therefore the theoretical determination of α and m seems to be rather difficult at the present stage. It follows that an empirical determination of these factors by best-fitting to the experimental results is necessary.

Bearing in mind that the early pit development and propagation also contribute to the total failure life time, expression (5.61) gives the crack propagation time, hereafter denoted as N_{crack} . The contribution from the pit has been given in Equation (5.9). Therefore the total corrosion fatigue failure life can be obtained by summing up the two parts as:

$$N_T = N_{\text{pit}} + N_{\text{crack}} = f \left(t_o + (h_c - h_o)^3 \left(\frac{1}{B} \right)^3 \right) + \frac{1}{\alpha} \sum_{i=1}^{i_n} \Delta_i \quad (5.62)$$

When applied to the present high strength BS251A58 spring steel, Table 5.7, Table 5.8 and Figure 5.4 show the result of the S-N curves predicted by the model, together with experimental data. Figure 5.5 illustrates pit growth and crack propagation behaviour from the theoretical prediction in comparison with experimental results.

5.12 Concluding remarks

It is shown that the model affords a convincing explanation of the experimental evidence and observation, and provides a good prediction of the fatigue crack growth and final failure. The good agreement of the model prediction with the experimental results confirms the underlying facts that short fatigue crack suffers from microstructural inhomogeneity and local impedance, and its behaviour cannot be represented as a singly-valued function of the stress intensity factor on which the LEFM approach is based; rather, it is of a crystallographic and microstructure-sensitive nature. Based on the dislocation representation of short cracks, the N-R model proves to be a useful tool to study the behaviour of microstructure-sensitive fatigue cracks.

References

- [1] B. A. Bilby, A. H. Cottrell and K. H. Swinden (1963) The spread of plastic yield from a notch. *Proc. R. Soc. Lond. A* **272**, pp.304-314.
- [2] A. Navarro and E. R. de los Rios (1988) Short and long fatigue crack growth: a unified model. *Phil. Mag.*, **57**, pp.15-36.
- [3] A. Navarro and E. R. de los Rios (1988) An alternative model for the blocking of dislocations at grain boundaries. *Phil. Mag.* **57**, pp.37-42.
- [4] A. Navarro and E. R. de los Rios (1988) Compact solution for multizone BCS crack with bounded or unbounded end conditions. *Phil. Mag.* **57**, pp.43-50.
- [5] A. Navarro and E. R. de los Rios (1992) Fatigue crack growth modelling by successive blocking of dislocation, *Proc. R. Soc. Lon, A* **437**, pp.375-390.
- [6] R Akid and K. J. Miller (1990) The initiation and growth of short fatigue cracks in an aqueous saline environment, *Environmental Assisted Fatigue*, EGF7, ed. P. Scott, *Mechanical Engineering Publication*, London, pp.415-434.
- [7] R. Akid and K. J. Miller (1991) Short fatigue crack growth behaviour of a low carbon steel under corrosion fatigue conditions, *Fatigue Fract. Engng. Mater. Struct.*, **14**, pp.637-649.
- [8] K. J. Miller (1987) The behaviour of short fatigue cracks and their initiation, Part I - A review of two recent books, *Fatigue Fract. Engng. Mater. Struct.*, **10**, pp.75-91.

[9] K. J. Miller (1987) The behaviour of short fatigue cracks and their initiation, Part II - A general summary, *Fatigue Fract. Engng. Mater. Struct.*, **10**, pp.93-113.

[10] J. N. Goodier (1933) Concentration of stress around spherical and cylindrical inclusions and flaws, *J Appl. Mech*, **1**, pp.39-44.

[11] A. Melander (1990) A finite-element study of the notch effect at surface inclusions, *Int.J Fatigue* **12** NO.3 pp.154-164.

[12] B. Weiss, R. Stickler and A. F. Blom (1992) A model for the description of the influence of small three-dimensional defects on the high-cycle fatigue limit, *Short Fatigue Cracks*, ESIS **13**, ed. K. J. Miller and E. R. de los Rios, Mechanical Engineering Publications, London. pp423-438.

[13] A. K. Head and N. Louat (1955) The distribution of dislocations in linear arrays, *Aust. J. Phys.*, **8**, pp.1-7.

[14] E. R de los Rios and A. Navarro (1990) Grain orientation and work hardening considerations on short fatigue crack modelling. *Phil. Mag.* **61**, pp.435-449.

[15] P. J. E. Forsyth (1961), *Proc. Crack propagation Symposium*, College of Aeronautics, Cranfield, UK, **1**, 76.

[16] A. S. Cheng and C. Laird (1983) *Materials Science and Engineering*, **60**, pp.177-183.

[17] R. Wand and H. Mughbrabi (1984) *Materials Science and Engineering*, **65**, pp.235-245.

- [18] K. J. Miller (1993) Two threshold of fatigue behaviour, *Fatigue Frac. Engng. Mater. Struct.* **16**, No. 9, pp.931-393.
- [19] R. Akid, Y. Z. Wang and U. S. Fernando (1993) Influence of loading mode on environment-assisted fatigue crack growth, *Corrosion -Deformation Interaction*, ed. T. Magnin and J-M Gras, Publishers- les edition de physique.
- [20] G. I. Taylor (1938) Plastic strain in metals. *J. Inst. Metals*, **62**, pp.307-324.
- [21] X. J. Xin, E. R. de los Rios and A. Navarro (1992) Modelling strain hardening at short fatigue cracks, *Short Fatigue Cracks*, ESIS **13**, ed. K.J.Miller and E.R.de los Rios, Mechanical Engineering Publications, London, pp.369-389.
- [22] E. R. de los Rios, M. W. Brown, K. J Miller and H. X. Pei (1988) Fatigue damage accumulation during cycles of non-proportional straining. *Basic questions in fatigue* ASTM STP 924, (ed. J. T. Fong and R. J. Fields), Vol. I., pp.194-213. American Society for Testing Materials, Philadelphia.
- [23] X. J. Xin, E. R. de los Rios and A. Navarro (1993) Microstructural sensitive fatigue crack growth in Al-Li 8090, in Durability and Structural Reliability of Airframes, *Proceedings of the 17th Symposium of the International Committee on Aeronautical Fatigue (ICAF93)*, ed. A. F. Blom, Stockholm, Sweden, EMAS, pp.855-882.
- [24] E. R. de los Rios, X. J. Xin and A Navarro (1994) Modelling microstructurally-sensitivity fatigue short crack growth, to appear in *Proc. R. Soc. London*.
- [25] E. R. de los Rios, Z. Tang, and K. J. Miller (1984) Short crack fatigue behaviour in a medium carbon steel. *Fatigue Fract. Engng. Mater. Struct.* **7**, pp.97-108.

- [26] E. R. de los Rios, H. J. Mohamed and K. J. Miller (1985) A micromechanics analysis for short fatigue crack growth. *Fatigue Fract. Engng. Mater. Struct.* **8**, pp.49-63.
- [27] K. Tanaka, M. Kinefuchi, and T. Yokomaku (1992) Modelling of statistical characteristic of propagation of small fatigue Cracks. In *Short Fatigue Cracks*, ESIS **13**, ed. K.J. Miller and E.R. de los Rios, Mechanical Engineering Publications, London. pp.351-368.
- [28] B. Tomkins (1968) Fatigue crack propagation -an analysis, *Phil. Mag.* **18**, pp.1041-1066.
- [29] S. Suresh, and R. O. Ritchie (1984) Propagation of short fatigue cracks. *Inter. Metals Rev.* **29**, pp.445-476.
- [30] D. L. Davidson, and J. Lankford (1985) Experimental mechanics of fatigue crack growth: the effect of crack size. *Eshelby memorial symposium -- Fundamentals of deformation and fracture* (ed. B. A. Bilby, K. J. Miller and J. R. Willis), p.559. Cambridge University Press.
- [31] M. F. Carlson and R. O. Ritchie (1977) On the effect of prior Austenite grain size on near-threshold fatigue crack growth. *Scripta Metall.* **11**, pp.1113-1118.
- [32] G. R. Yoder, L. A. Cooley and T. W. Crooker (1983) A critical analysis of grain-size and yield-strength dependence of near-threshold fatigue crack growth in steels. ASTM STP 791 (ed. J. C. Lewis and G. Sines), pp.I-348-I-365.

Appendix A

The system equilibrium equation for the dislocations is :

$$\int_{-1}^1 \frac{f(\zeta')}{\zeta - \zeta'} d\zeta' + \frac{P(\zeta)}{A} = 0 \quad (\text{A.1})$$

$$\text{with } P(\zeta) = \begin{cases} \tau & |\zeta| < n \\ \tau - \tau_0 - k' \left(\frac{bc}{2w} \int_{-1}^1 \zeta f(\zeta) d\zeta \right)^q & |\zeta| \geq n \end{cases} \quad (\text{A.2})$$

where $0 \leq q \leq 1$.

(A.1) is a singular integral equation of the Cauchy type. When $k'=0$, it represents the case for constant friction stress, of which the solution has been obtained [1] and fully discussed in [4]. There are two kinds of solutions to (A.1) depending on whether a bounded, or unbounded end condition is considered; both solutions can be expressed by a unified form [4].

Observe that the integral term in (A.2) will finally yield a function of n and $R_\tau = \tau/\tau_0$, but independent of position variable ζ , one can rewrite (A.2) as:

$$P(\zeta) = \begin{cases} \tau & |\zeta| < n \\ \tau - \tau_f(n) & |\zeta| \geq n \end{cases} \quad (\text{A.3})$$

where

$$\tau_f(n) = \tau_0 + k' \left(\frac{bc}{2w} \int_{-1}^1 \zeta f(\zeta) d\zeta \right)^q \quad (\text{A.4})$$

From (A.1) and (A.3), the solution of (A.1) can be easily obtained from that for the constant friction stress τ_0 [2], with the replacement of τ_0 by τ_f as:

$$f(\zeta) = \frac{\tau_f(n)}{\pi^2 A} \left[\cosh^{-1} \left(\left| \frac{1-n\zeta}{n-\zeta} \right| \right) - \cosh^{-1} \left(\left| \frac{1+n\zeta}{n+\zeta} \right| \right) \right] + \frac{\tau_f(n)\zeta}{\pi^2 A(1-\zeta)^{1/2}} \left[2 \sin^{-1} n + \pi \left(\frac{\tau}{\tau_f(n)} - 1 \right) \right] \quad (\text{A.5})$$

Note that

$$\begin{aligned}
& \int_{-1}^1 \zeta \cosh^{-1} \left(\left| \frac{1-n\zeta}{n-\zeta} \right| \right) d\zeta \\
&= \lim_{\varepsilon \rightarrow 0} \left[\int_{-1}^{n-\varepsilon} \zeta \cosh^{-1} \left(\frac{1-n\zeta}{n-\zeta} \right) d\zeta + \int_{n+\varepsilon}^1 \zeta \cosh^{-1} \left(\frac{1-n\zeta}{-n+\zeta} \right) d\zeta \right] \\
&= \frac{1}{2} \pi n \sqrt{1-n^2} \\
& \int_{-1}^1 \zeta \cosh^{-1} \left(\left| \frac{1+n\zeta}{n+\zeta} \right| \right) d\zeta = \int_1^{-1} (-\zeta) \cosh^{-1} \left(\left| \frac{1-n\zeta}{n-\zeta} \right| \right) d(-\zeta) \\
&= -\frac{\pi}{2} n \sqrt{1-n^2} \\
& \int_{-1}^1 \frac{\zeta^2}{\sqrt{1-\zeta^2}} d\zeta = \frac{\pi}{2}
\end{aligned}$$

One has:

$$\begin{aligned}
\int_{-1}^1 \zeta f(\zeta) d\zeta &= \int_{-1}^1 \left\{ \zeta \cdot \frac{\tau_f}{\pi^2 A} \left[\cosh^{-1} \left(\left| \frac{1-n\zeta}{n-\zeta} \right| \right) - \cosh^{-1} \left(\left| \frac{1+n\zeta}{n+\zeta} \right| \right) \right] \right. \\
&\quad \left. + \frac{\tau_f \zeta^2}{\pi^2 A (1-\zeta)^{1/2}} \left[2 \sin^{-1} n_i + \pi \left(\frac{\tau}{\tau_f} - 1 \right) \right] \right\} d\zeta \\
&= \frac{\tau_f}{\pi A} \left(\frac{\pi \tau}{2 \tau_f} - I_n \right)
\end{aligned}$$

$$\text{where } I_n = \frac{\pi}{2} - n \sqrt{1-n^2} - \sin^{-1} n \quad (\text{A.7})$$

therefore from (A.4), τ_f should satisfy the following equation :

$$\tau_f = \tau_o + k \left(\frac{bc}{2w} \frac{\tau_f}{\pi A} \left(\frac{\pi \tau}{2 \tau_f} - I_n \right) \right)^q \quad (\text{A.8})$$

Introducing the following parameters:

$$V = \left(\frac{k'}{\tau_o} \right)^{\frac{1}{q}} \frac{c \tau_o \kappa}{2wG} \quad (\text{A.9})$$

$$h = \tau_f / \tau_o \quad (\text{A.10})$$

(A.8) can be simplified as :

$$h = 1 + \left[V (\pi R_\tau - 2 I_n h) \right]^q \quad (\text{A.11})$$

$$\text{or } (h-1)^{1/q} = V (\pi R_\tau - 2 I_n h) \quad (\text{A.12})$$

when $q=1$, the linear hardening case should be recovered; in fact (A.12) with $q=1$ gives:

$$h = \frac{1 + \pi V R_\tau}{1 + 2 I_n V} = \frac{1 + \pi R_\tau p \kappa}{1 + 2 I_n p \kappa} \quad (\text{A.13})$$

$$\text{where } p = \frac{k' c \tau_0}{\tau_0 2Gw} = \frac{k' c}{2Gw}$$

(A.13) is identical to the results given in [21] for the linear hardening material.

When $0 < q < 1$, a general solution of (A.11) or (A.12) for h as a function of n and R_τ can be obtained using a numerical approach. However, for some special values of q , the derivation of an explicit expression of h is possible. Specially when $q=0.5$, which corresponds to a parabolic hardening, (A.12) becomes:

$$(h-1)^2 = V(\pi R_\tau - 2I_n h) \quad (\text{A.14})$$

$$\text{with } V = \left(\frac{k'}{\tau_0}\right)^2 \frac{c k \tau_0}{2WG} = \frac{k'^2 c k}{2W\tau_0 G} = \frac{k'}{\tau_0} p k \quad (\text{A.15})$$

Solving the equation gives:

$$h = 1 - I_n V + \sqrt{I_n^2 V^2 + V(\pi R_\tau - 2I_n)} \quad (\text{A.16})$$

Another branch of solution with negative square root has been omitted due to the fact that h should not be less than unity. From (A.7) it is easily shown that $0 \leq I_n \leq 2/\pi$, therefore with $R_\tau = \tau/\tau_0 > 1$, the term inside the square root, $I_n^2 V^2 + V(\pi R_\tau - 2I_n)$, is always positive which satisfies the physical condition of $h \geq 1$ and real.

In order to study the general properties of h , (A.16) is rewritten as:

$$(h-1+I_n V)^2 = I_n^2 V^2 + V(\pi R_\tau - 2I_n) \quad (\text{A.17})$$

Taking partial derivative of the above expression on both sides with respect to I_n , gives:

$$2(h-1+I_n V) \left(\frac{\partial h}{\partial I_n} + V \right) = 2I_n V^2 - 2V I_n$$

Rearranging the above gives:

$$\frac{\partial h}{\partial I_n} = -\frac{(h-1)+I_n}{(h-1)+I_n V} \cdot V \quad (\text{A.18})$$

while according to (A.7),

$$\frac{dI_n}{dn} = \frac{d}{dn} \left(\frac{\pi}{2} - n\sqrt{1-n^2} - \sin^{-1} n \right) = -2\sqrt{1-n^2} \quad (\text{A.19})$$

is obtained, therefore

$$\frac{\partial h}{\partial n} = \frac{\partial h}{\partial I_n} \frac{dI_n}{dn} = \frac{(h-1) + I_n}{(h-1) + I_n V} \cdot V \cdot 2\sqrt{1-n^2} \geq 0 \quad (\text{A.20})$$

Due to the fact that $h > 1, V > 0, \pi/2 \geq I_n \geq 0$.

Also from (A.16),

$$\frac{\partial h}{\partial R_\tau} = \frac{V\pi}{2\sqrt{I_n^2 V^2 + V(\pi R_\tau - 2I_n)}} > 0 \quad (\text{A.21})$$

(A.20) and (A.21) state that the hardening function h increases monotonically with increasing n , or increasing R_τ .

The situation $R_\tau = \tau/\tau_0 < 1$ might occur in some cases, such as in corrosion fatigue, or when some pre-crack or notch already exists. Due to the occurrence of pits induced by the corrosion environment which gives rise to local stress concentrations, and due to the severe reduction in barrier strength in the presence of aggressive environmental attack, fatigue crack growth may be activated and accumulate at load levels well below the conventional fatigue limit, leading to final failure. For such cases, the load ratio $R_\tau = \tau/\tau_0 < 1$, and the bounded solution will operate, with the second (singular) term in the unified solution in (A.5) equating to zero. Similar arguments can be made about the strain hardening effect, and crack growth law. For completeness and conciseness, the final results for $R_\tau < 1$ are listed below without a detailed derivation:

$$\tau_f = h\tau_0 \quad (\text{A.22})$$

$$\text{where } h = 1 + J_n V + \sqrt{J_n^2 V + 2J_n V} \quad (\text{A.23})$$

$$J_n = n\sqrt{1-n^2} \quad (\text{A.24})$$

V is the same as in (A.15).

It can also be proved that for $R_\tau < 1$,

$$\frac{\partial h}{\partial n} = \frac{\partial h}{\partial J_n} \frac{dJ_n}{dn} = \frac{hV}{\sqrt{J_n^2 V^2 + 2J_n V}} \cdot \frac{1}{\sqrt{1-n^2}} > 0 \quad (\text{A.25})$$

$$\text{while } \frac{\partial h}{\partial R_\tau} = 0 \quad (\text{A.26})$$

therefore the hardening function h increases monotonically with increasing n , while it is independent of load ratio R_τ .

To summarise, the parabolic strain hardening effect can be characterised by :

$$\tau_f = h\tau_o$$

$$h = \begin{cases} 1 - I_n V + \sqrt{I_n^2 V^2 + V(\pi R_\tau - 2I_n)} & \text{for } R_\tau \geq 1 \\ 1 + J_n V + \sqrt{J_n^2 V^2 + 2J_n V} & \text{for } R_\tau < 1 \end{cases} \quad (\text{A.27})$$

where I_n is given by (A.7), J_n by (A.24), and V by (A.15).

Table 5.1 The final major pit length, H_c , the initially pit size, H_o , the dissolution rate, B , and incubation time, t_o , obtained from tests at different stress amplitudes.

Specimen	τ (MPa)	t_o (Seconds)	$(1/B)^3$	H_c (μm)	H_o (μm)	pit
B10	112			60		pit1
TC13	207.4	55010	0.1251	35	0	pit1
TC18	306.6	1904	0.1186	32	0	pit6
TC5	364.3	865	0.1991	27	9	pit1
C4	371.1	225	0.1318	25	12	pit2
TC6	462.9	25	0.05139	16	3	pit1

Table 5.2 The parameters for major pit growth, obtained from Equations (5.3), (5.4) and (5.4), for various stress amplitudes in 0.6 M NaCl solution at pH=6.5, and frequency=5Hz.

Specimen	τ (MPa)	t_o (Second)	$(1/B)^3$	H_c (μm)	H_o (μm)
B10	112.0	679760	0.16937	57	0
TC13	207.4	43610	0.15113	41	0
TC11	216.5	33502	0.14938	40	0
TC7	251.8	11987	0.14256	36	0
TC3	273.5	6395	0.13839	33	0
TC10	304.6	2597	0.13240	30	0
TC2	305.9	2492	0.13213	30	0
TC18	306.5	2449	0.13201	30	0
TC5	364.3	465	0.12099	24	0
C4	371.1	373	0.11953	24	0
TC6	462.9	200	0.10231	18	0

Table 5.3 Stress concentration factor, K_t , for an ellipsoidal cavity of circular cross-section in an infinite body in tension, $\nu = 0.3$, $K_t = \sigma_{\max}/\sigma$ [10] *

E'/E	0	1/4	1/3	1/2	1
K_t (a/b=1)	2.47	1.85	1.74	1.44	1
K_t (a/b=0.5)	2.05	1.68	1.58	1.37	1

* a is the minimum diameter of the ellipsoid, b is the maximum radius,
Cavity contains material having modulus of elasticity E' perfectly bonded to body material having modulus of elasticity E

Table 5.4 Maximum stress concentration factor, K_{to} , around the major pit at its final length under various stress amplitudes

Specimen	τ (MPa)	K_{to}
B10	112.0	2.05
TC13	207.4	2.05
TC11	216.5	2.05
TC7	251.8	2.05
TC3	273.5	2.05
TC10	304.6	1.75
TC2	305.9	1.75
TC18	306.5	1.75
TC5	364.3	1.5
C4	371.1	1.5
TC6	462.9	1.5

Table 5.5 Parameters for the modelling

Parameters	in a 0.6 M NaCl solution	in air
Shear modulus G , MPa	81500	81500
Poisson's ratio ν	0.3	0.3
Burgers vector b , m	0.248E-09	0.248E-09
Grain size D , m	0.300E-04	0.300E-04
Ini. fric. (shear) τ_o , MPa	338.4	338.4
Fat. limit (shear) τ_{FL} , MPa	98	457.5
Ini. fric. (tensile) σ_o , MPa	617	617
Fat. limit (tensile) σ_{FL} , MPa	179	650
Slip band width w , m	0.100E-05	0.100E-05
D/w	30	30
r_o , m	0.100E-06	0.100E-06
G/k'	815	815
Strain hardening law	parabolic hardening	linear hardening
Crack initiation site	grain boundary	grain interior
Screw or edge dislocation	edge dislocation	edge dislocation

Table 5.6 Corrosion fatigue crack transition from stage-I growth to stage-II growth for different stress amplitudes in a 0.6 M NaCl solution, frequency of 5Hz, free potential.

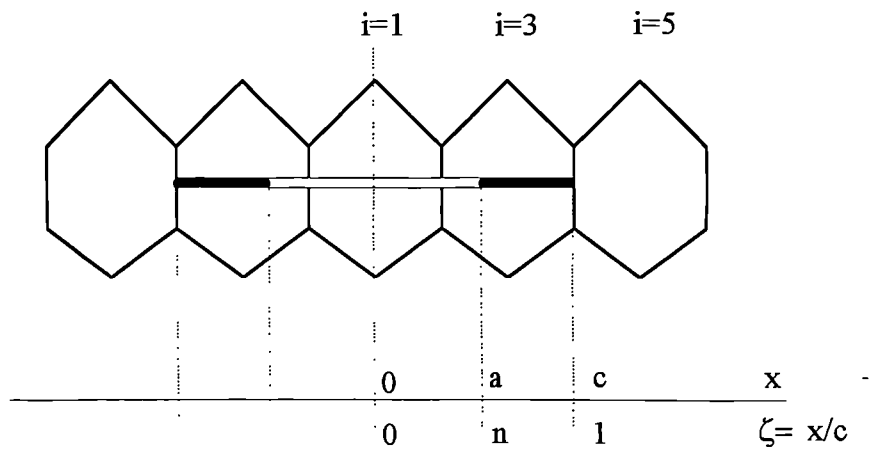
Specimen	τ (MPa)	Transition from stage-I crack to stage-II crack at
B10	112.0	2 grain diameter
TC13	207.4	2 grain diameter
TC11	216.5	2 grain diameter
TC7	251.8	2 grain diameter
TC3	273.5	2 grain diameter
TC10	304.6	2 grain diameter
TC2	305.9	2 grain diameter
TC18	306.5	2 grain diameter
TC5	364.3	2 grain diameter
C4	371.1	2 grain diameter
TC6	462.9	6 grain diameter

Table 5.7 Fatigue life predictions using the modified N-R model (Equation (5.62) with $m=1.9$ and $\alpha = 7514.4$) together with experimental results (in a 0.6 M NaCl solution, pH=6.5, frequency =5Hz, at room temperature)

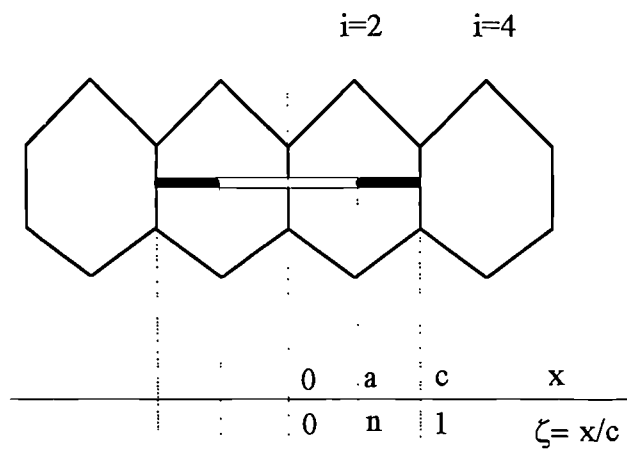
Specimen	τ (MPa)	N_{pit}	N_{crack}	N_{prdt}	N_{expt}
B10	112.0	3555631	3481428	7037059	6500000
TC13	207.4	270130	627289	897419	870500
TC11	216.5	215312	550731	766043	795000
TC7	251.8	93191	352414	445605	553000
TC3	273.5	56841	284636	341477	310500
TC10	304.6	30854	200373	231227	259500
TC2	305.9	30297	197695	227992	192000
TC18	306.5	30066	196272	226338	205000
TC5	364.3	10687	118912	129599	174320
C4	371.1	10127	110788	120915	132100
TC6	462.9	3483	52120	55603	73800

Table 5.8 Fatigue life predictions using the modified N-R model (Equation (5.62) with $m=3.5$ and $\alpha = 7797.7 \times 10^{11}$) together with experimental results (in air)

Test	τ (MPa)	N_{pit}	N_{crack}	N_{prdt}	N_{expt}
1	463	0	6279354	6279354	4850800
2	504	0	339043	339043	577000
3	515	0	254209	254209	376000
4	535	0	165309	165309	173000
5	553	0	66304	66304	66300
6	566	0	49619	49619	47126
7	610	0	18528	18528	16200
8	620	0	7163	7163	7000
9	671	0	2146	2146	2500



(a) crack initiates from grain interior



(b) crack initiates from grain boundary

Figure 5.1 Schematic representation of the crack, slip band and a zone simulating the locked dislocation across the grain boundary

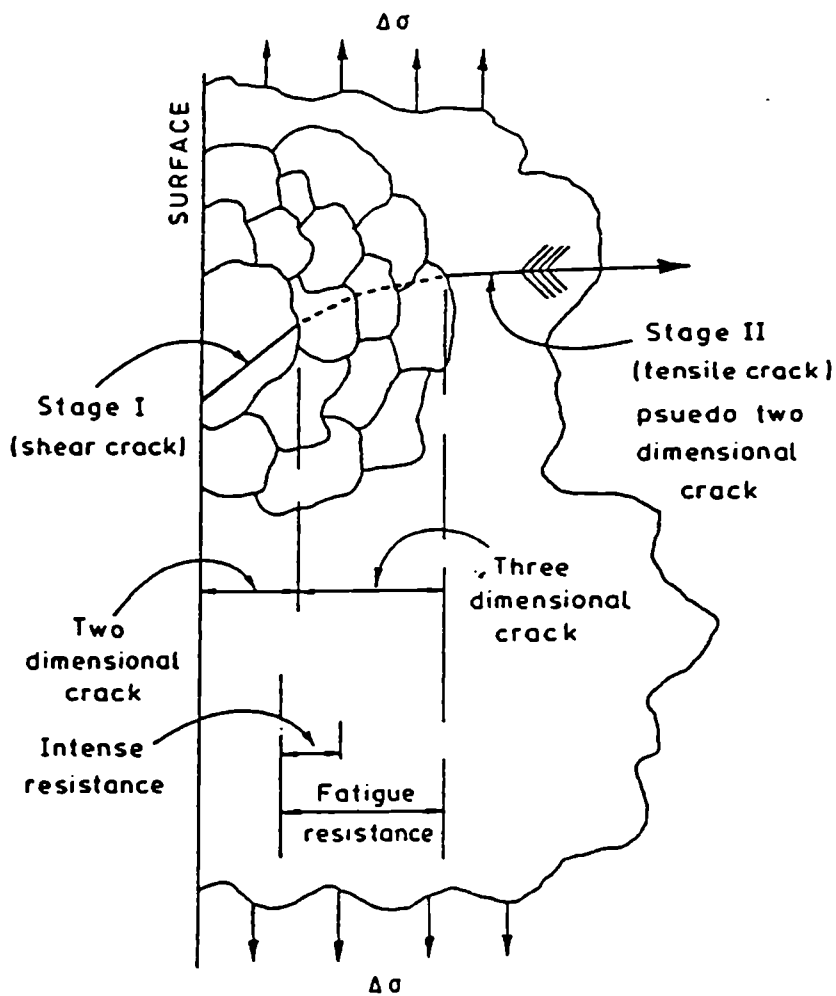


Figure 5.2 Fatigue resistance indicated in terms of the difficulty of an initial stage-I shear crack becoming a stage-II tensile crack. (After Miller [18])

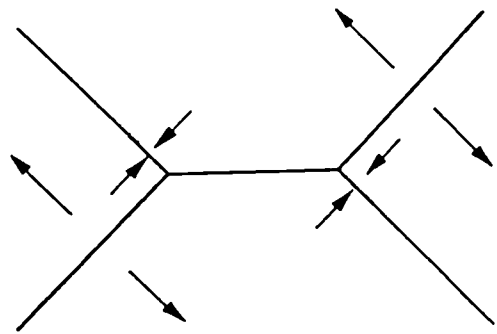
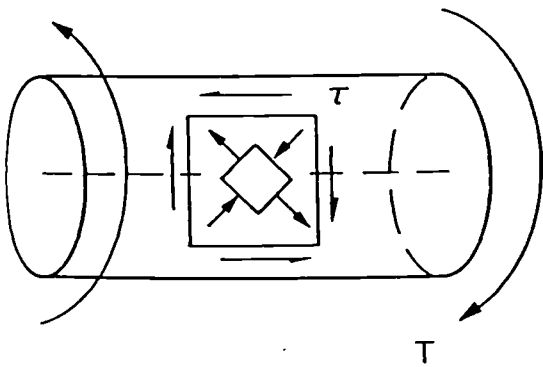
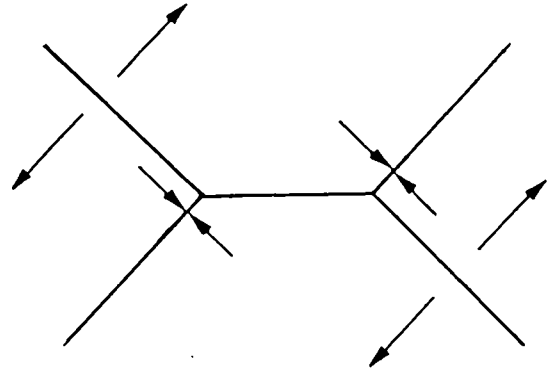
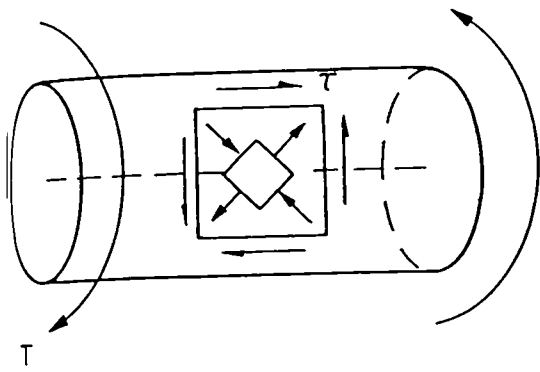


Figure 5.3 Schematic of shear stress and cracking systems (stage-I cracking and stage-II cracking) in torsion.

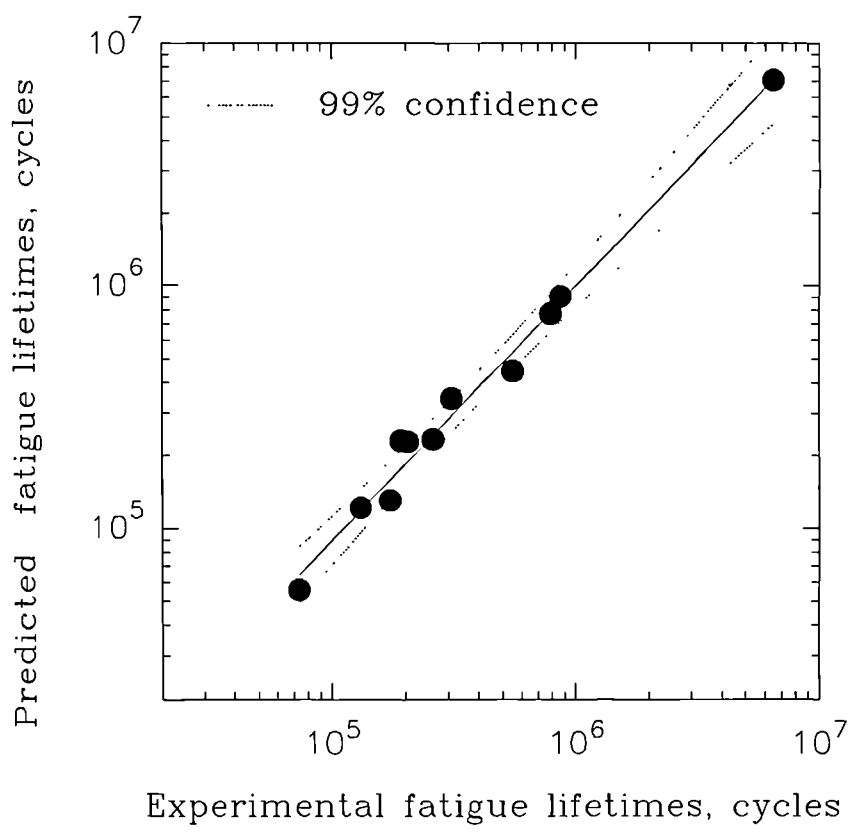
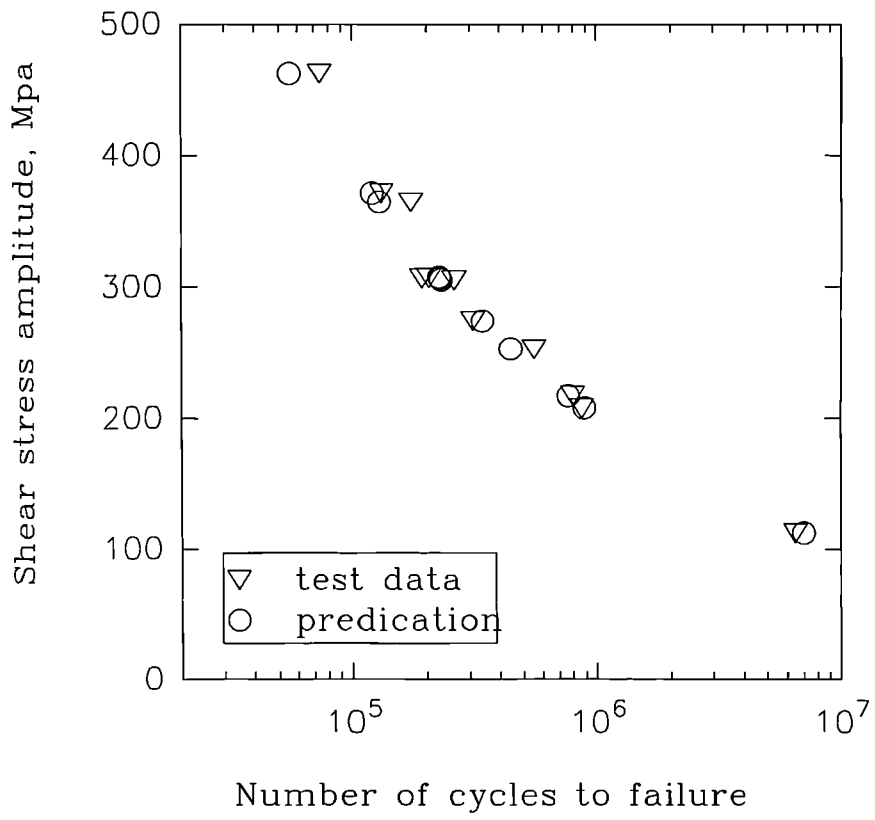


Figure 5.4 Comparison between experimental and predicted fatigue lifetimes, (a) Corrosion fatigue lifetimes

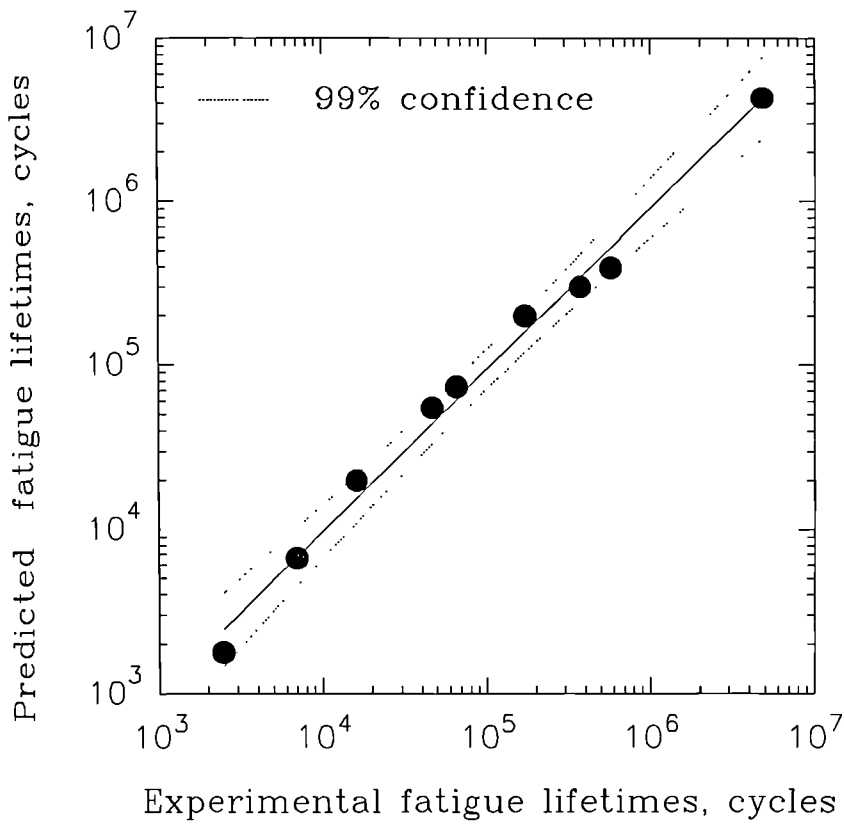
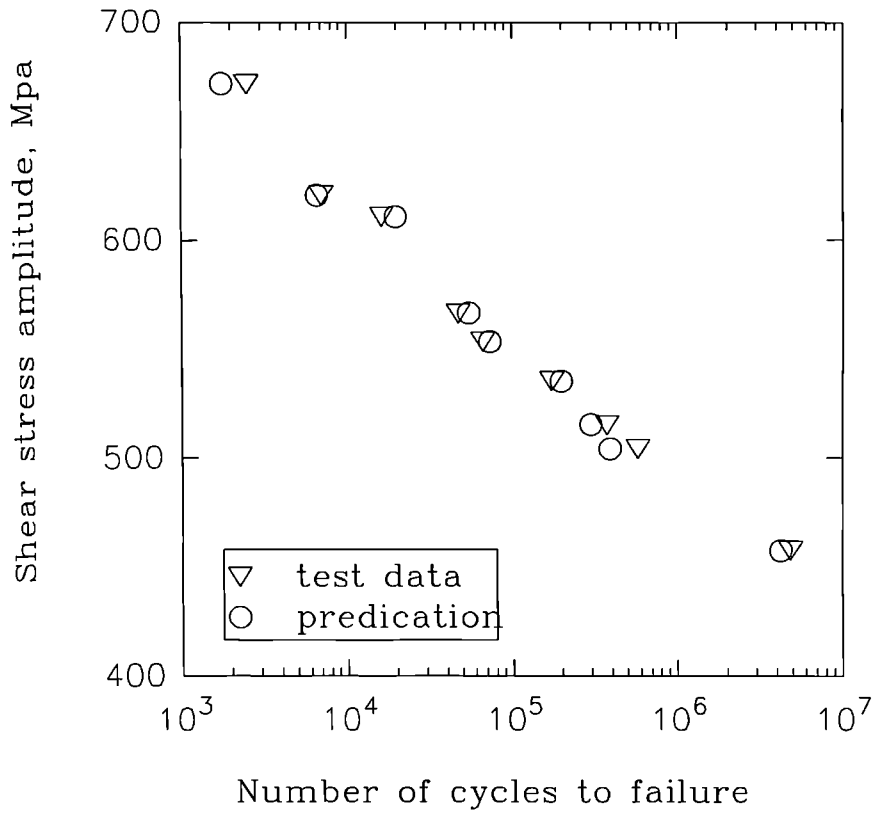


Figure 5.4 Comparison between experimental and predicted fatigue lifetimes, (b) Fatigue lifetimes in Air

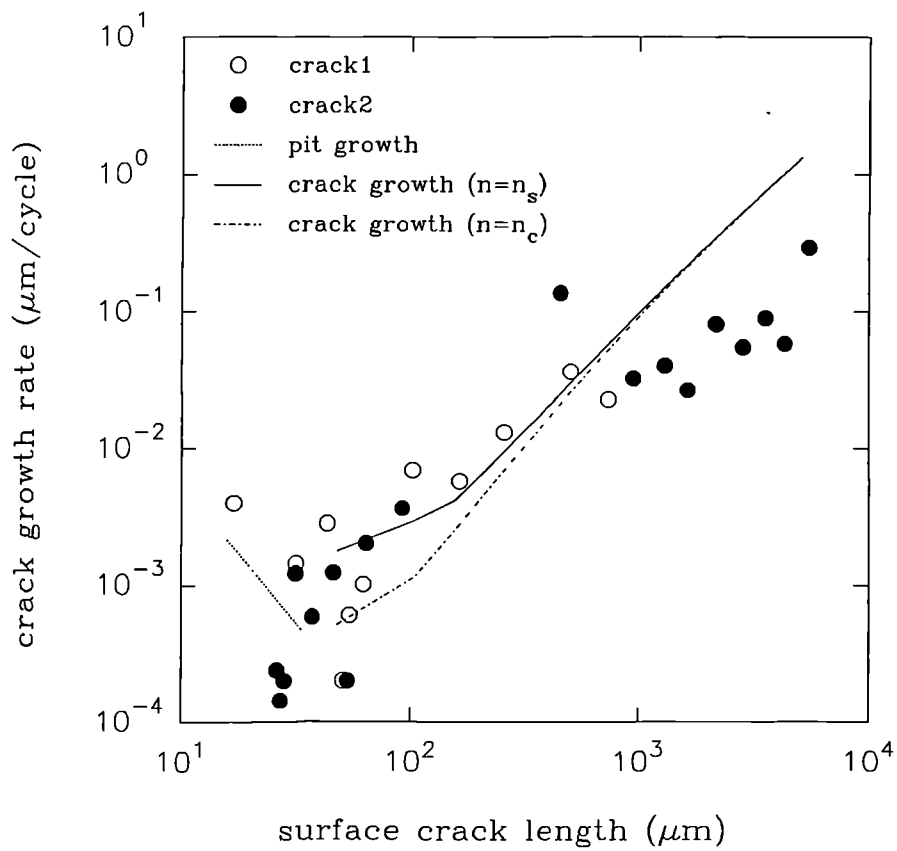
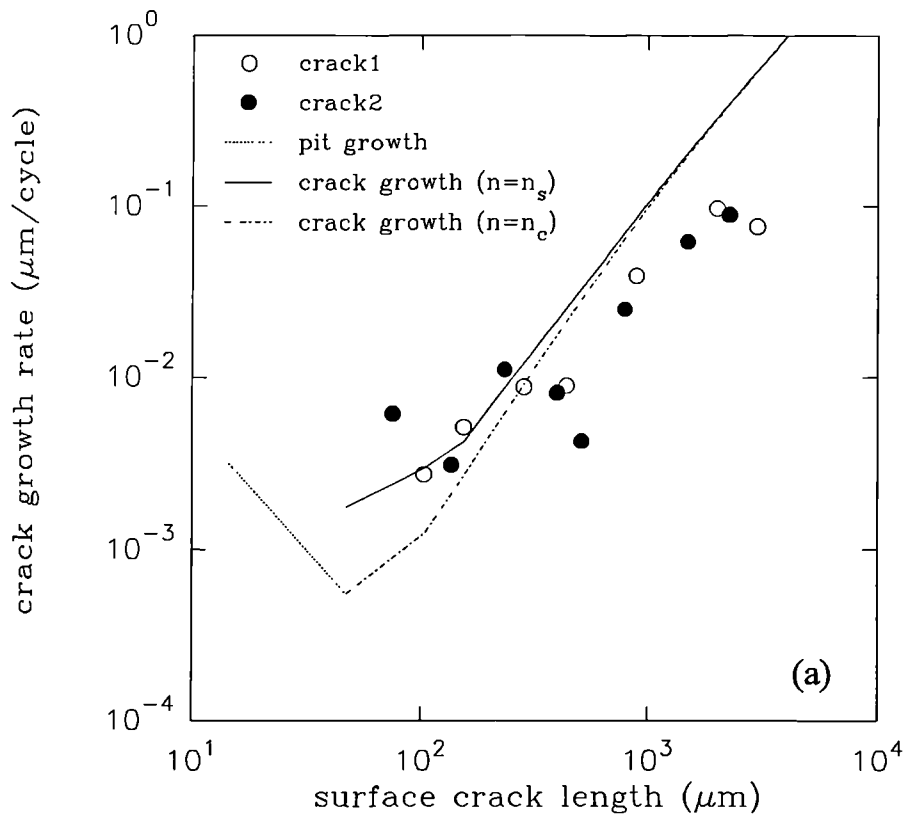


Figure 5.5 Comparison between experimental and predicted corrosion fatigue crack growth rates. (a) Specimen C4, $\Delta\tau=742\text{MPa}$. (b) Specimen TC5, $\Delta\tau=728\text{MPa}$

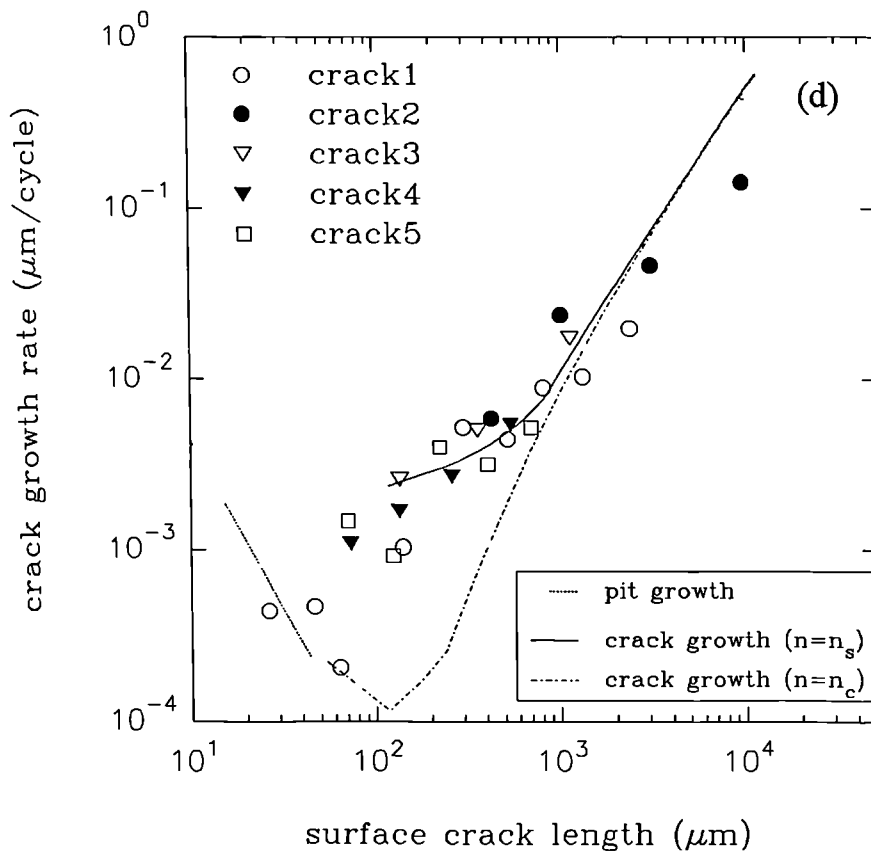
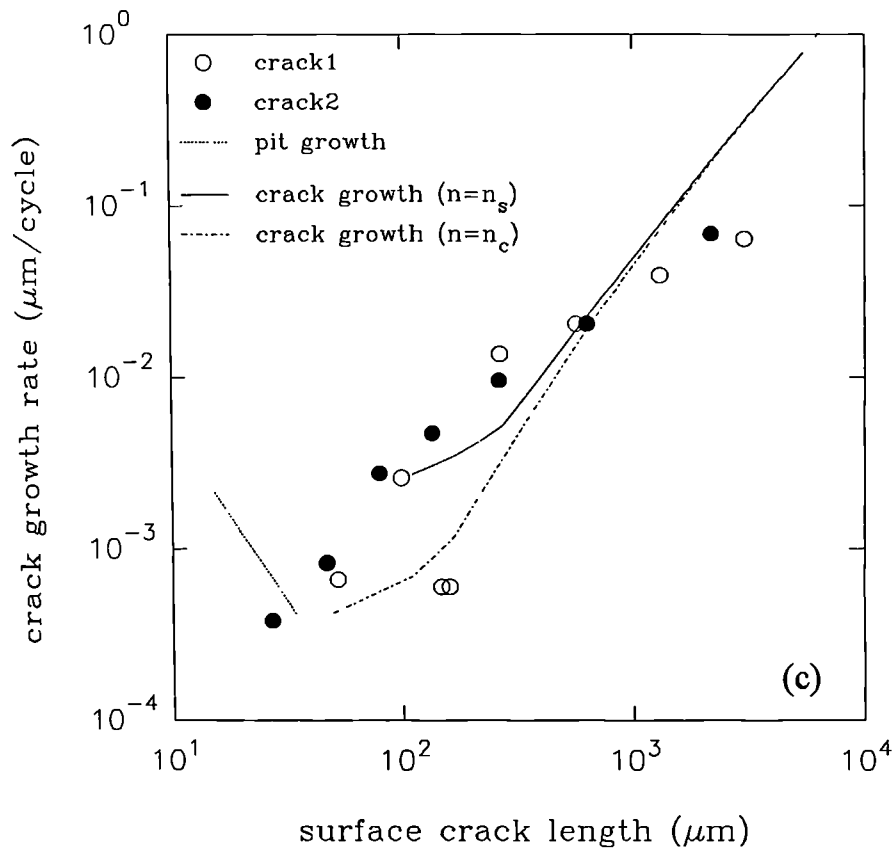


Figure 5.5 Comparison between experimental and predicted corrosion fatigue crack growth rates. (c) Specimen TC18, $\Delta\tau=613$ MPa (d) Specimen TC13, $\Delta\tau=415$ MPa

Chapter 6 Discussion

Since most discussion concerning the experimental and modelling work has been addressed in the relevant chapters previous to the section, only a few final points will be highlighted here which are central to the question as to why corrosion fatigue cracks can grow under a stress level well below the "in-air" fatigue limit and cause failure. Conclusions are then drawn from the present work in Chapter 7 together with some suggestions about further work.

6.1. Pit initiation time, t_0

In corrosion fatigue pits are usually found at the origin of the fracture surface of industrial machinery components as well as on test specimens. This implies that the pit initiation is the trigger for fatigue crack initiation. Therefore, the quantitative evaluation of pitting will make it possible to predict the corrosion fatigue crack initiation life. A formula of the following form (Equation (5.9) in Chapter 5) has been used to characterise pit growth.

$$N_{\text{pit}} = f \left(t_0 + (H_c - H_0)^3 \left(\frac{1}{B} \right)^3 \right) \quad (6.1)$$

here

N_{pit} = the number of cycles for pit to grow to a critical size

H_c = the critical pit size

H_0 = the initial defect size

B = a constant related to the solution dissolution rate

t_0 = the incubation time for pit formation

The physical meaning of t_0 , which was observed to increase with increasing stress levels, can be explained as following.

In uncracked components subjected to low cycle fatigue, general plasticity quickly roughens the surface from which a crack usually forms, propagates first along a slip plane (stage I), and then changes to a direction normal to the tensile axis.

The mechanism for high cycle fatigue is, however, different. When the stress is below general yielding, most of the life is taken up in developing a dominant crack. Although there is no general plasticity, local plasticity occurs whenever there is a notch, scratch, or change of section which gives rise to a stress concentration. A crack ultimately initiates in the zone of one of those stress concentrations and propagates, slowly at first, or intermittently depending on the crack size, microstructure and loading level, and then faster, until the component fails.

For low stress levels, much time will be spent on the stage I growth in the most favourably oriented grain in an inert environment. Because of the inhomogeneous nature of multi-grain orientations, the local strain concentration preferentially occurs at the grain which has an orientation for easy movement of dislocations. When the local strain accumulates to a value higher than a critical value, persistent slip bands form along the maximum shear plane in the grain (or subgrain) depending upon the microstructural texture of the material. The time for slip band formation depends on the level of the local strain, which is (under normal uniaxial loading conditions) proportional to the applied stress. The lower the applied stress level, the longer will be the time spent on slip band formation.

In corrosion fatigue, the applied stress level is usually lower than the fatigue limit in air and the overall strain is small. However, the local strain may be intensified by the corrosion process. In other words, strain localization can be expected to be enhanced by pit formation i.e. the notch effect.

At low applied stress levels, it is worth noting that not all pits can further develop to become a crack. Some pits had a greater possibility to become the initiation site of the major crack than other pits, particularly those that formed at a later stage.

For example, when specimen TC13 was exposed in 0.6M NaCl solution under a stress range of 415 MPa, a few pits appeared quickly on the central section of the specimen surface due to electro-chemical cell formation at the local sites of chemical inhomogeneity. However, it was found that they maintained the same size after 250000 cycles, and became dormant. Subsequently the major pit initiated after 271300 cycles ($N_p / N_f = 0.36$) from which the major crack developed after a further 47700 cycles and propagated in stage I. In comparison, some of the prior pits were still dormant but some developed to produce a small stage I crack which did not become the major crack.

Hence it can be explained that those pits appearing in the early stage of the corrosion fatigue process were predominantly the result of electro-chemical reactions at sites of chemical inhomogeneity on the specimen surface; these sites not necessarily being the favourite locations for primarily slip band formation. If the pits were induced by a combination of mechanical and electro-chemical effects, essentially by a local strain concentration at a grain with favourable orientation for primary slip band formation, more time t_0 would be needed for them to form the slip band at a lower strain level. Consequently, these 'more dangerous' pits would appear later, and subsequently became the initiation site for the major crack.

It is apparent that pit nucleation is affected by a combination of mechanical and electro-chemical effects. The mechanical factor is affected by local strain concentrations that develop primarily at grains favourably oriented in relation to the maximum shear stress plane, for the easy glide of dislocations. At high stress levels, the major pit can form

quickly. At lower applied stress levels, however, the major pit is observed to appear later. This physical procedure explains the existence of the term t_0 in Equation (6.1).

It follows that during corrosion fatigue, early surface defects, such as pits or other local defects, could be classified into two kinds: One is induced by an electro-chemical reaction which appears at an early stage, but becomes dormant, or non-propagating. The other is induced essentially by a local strain concentration at a favourable grain for primary slip band formation with the assistance of a chemical reaction; these latter kind of defects are found to form relatively late, and depend on the strain level. Eventually the major crack develops from the second kind and propagates, leading to specimen failure.

6.2. Effective size of the stress concentration around a pit

Once the pit forms, it will grow along the surface and in the depth, thus creating a surface notch of semicircular or elliptical shape. Consequently, a stress concentration develops around the pit.

Equation (5.10) provided a simple way to evaluate the stress concentration as a function of the distance from the pit, re-written here:

$$K_t = (K_{t0} - 1) \left(\frac{H_c}{2r} \right)^2 + 1 \quad (r \geq H_c / 2) \quad (6.2)$$

where K_{t0} is the maximum stress concentration at the edge of the pit, H_c is the critical pit size which varies with the applied stress range, r is the distance from the original pit centre, and K_t is the stress concentration factor.

The effective field of the stress concentration around the pit depends on r , the distance from the original pit centre to the location of interest. With increasing r , K_t will decrease asymptotically towards unity. For a given K_{t0} and H_c , a reasonable value of 1.05 for K_t

with a corresponding $r = r_c$ is used to assess the effective concentration zone; when $r > r_c$, the stress concentration can be regarded as negligible because K_t is very close to unity.

Table 6.1 The effect field of stress concentration around a pit under different stress levels

Specimen	τ MPa	K_t	Hc/2 μm	r_c μm (for $K_t = 1.05$)	Major crack length at final stage I μm
B10	112.0	2.05	28.5	130.6	58
TC13	207.4	2.05	20.5	93.9	56
TC11	216.5	2.05	20	91.6	—
TC7	251.8	2.05	18	82.4	—
TC3	273.5	2.05	16.5	75.6	—
TC10	304.6	1.75	15.5	60.0	—
TC2	305.9	1.75	15.5	60.0	—
TC18	306.5	1.75	15.5	60.0	58
TC5	364.3	1.5	12	37.9	54
C4	371.1	1.5	11.5	36.4	67
TC6	462.9	1.5	9	28.5	335

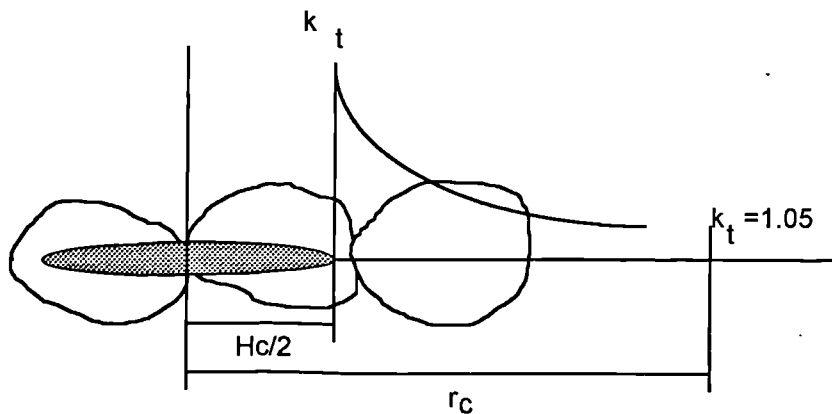
From experimental results, three cases were recognised:

Case A: $r_c > 60 \mu\text{m}$, i.e. larger than two prior austenite grain diameters. Once the pit formed, stage II cracking would initiate at the pit root immediately and grow in the direction perpendicular to the maximum tensile stress until failure of the specimen. It should be pointed out that direct growth of a stage II crack from the pit does not imply a shorter time for crack initiation and a faster crack propagation; in contrast, the time for pitting and crack initiation is much longer than the other two cases discussed below. A

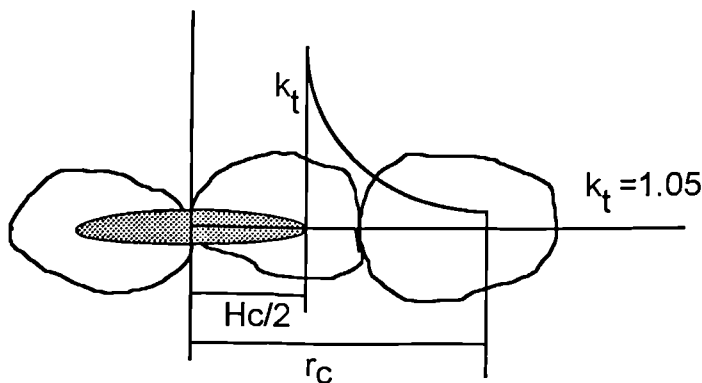
larger r_c comes from the fact that H_c at lower stresses is larger due to a prolonged electro-chemical reaction. Case A is normally associated with low or medium stress levels.

Case B: $30 \mu\text{m} < r_c \leq 60 \mu\text{m}$, i.e. between one and two prior austenite grain diameters. A stage I crack would initiate from the pit and propagate for a short distance (about one grain size when measured as half surface crack length) along the maximum shear stress plane, and then develop into a stage II crack perpendicular to the maximum tensile stress direction until failure. This case is usually associated with a medium stress level.

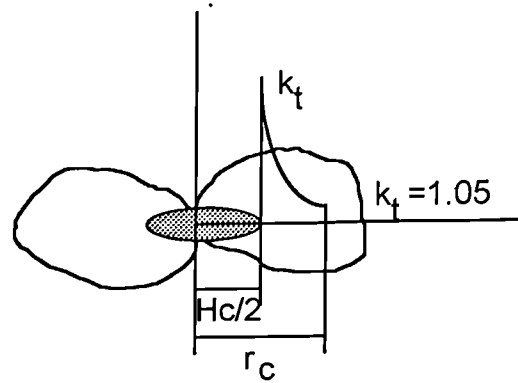
Case C: $r_c \leq 30 \mu\text{m}$, i.e. less than one prior austenite grain diameter. A stage I crack would initiate from a pit and propagate for a distance of several grain sizes along the maximum shear stress plane, then develop into a stage II crack perpendicular to the maximum tensile stress direction until failure of the specimen. This is the situation at a high stress level.



Case A



Case B



Case C

Figure 6.1 Schematic diagram of the three cases for the effective size of the stress concentration around a pit

The observations illustrate the significance of pit size and the associated effective stress concentration zone on crack initiation and its transition to a stage II crack. At high stress levels, cracks form and grow, promoted mainly by mechanical effects, while at lower stress level corrosion-induced defects play a vital role in the early stage of crack initiation and growth.

Environment assisted pit formation, above certain size, together with the appropriate applied load level, substantially reduces the barrier strength, shortens the stage I growth period, permits premature stage II growth, and hence eliminates the fatigue limit.

6.3. The effect of crack blunting

Once a crack is initiated in corrosion fatigue, blunting will occur more readily than in an inert environment, predominantly due to the dissolution process [1]. In a way similar to pitting, crack blunting by corrosion will assist the crack to cross grain boundaries, reduce

the final stage I crack length or eliminate the stage I crack growth process and, in effect, reduce the barrier resistance to fatigue crack growth.

The grain boundary acts as a barrier to crack propagation for a number of reasons:

- a) it constrains crack tip plasticity.
- b) the slip planes in the grain ahead of the defect may be unfavourably oriented for slip compared to those in the current grain.
- c) the slip planes in two adjacent grains are unlikely to intersect on a line lying in the grain boundary, consequently the crack in the next grain will require to be stepped in order to be continuous with the crack in the previous grain.
- d) the constraint provided by the surrounding material at the crack tip renders slip more difficult in the next grain.

For a blunted crack, the mode I elastic stress field equations were derived by Creager and Paris [2] as:

$$\begin{aligned}
 \sigma_x &= \frac{K_I}{\sqrt{2\pi r}} \cos \frac{\theta}{2} \left(1 - \sin \frac{\theta}{2} \sin \frac{3\theta}{2} \right) - \frac{K_I}{\sqrt{2\pi r}} \left(\frac{\rho}{2r} \right) \cos \frac{3\theta}{2} \\
 \sigma_y &= \frac{K_I}{\sqrt{2\pi r}} \cos \frac{\theta}{2} \left(1 + \sin \frac{\theta}{2} \sin \frac{3\theta}{2} \right) + \frac{K_I}{\sqrt{2\pi r}} \left(\frac{\rho}{2r} \right) \cos \frac{3\theta}{2} \\
 \tau_{xy} &= \frac{K_I}{\sqrt{2\pi r}} \sin \frac{\theta}{2} \cos \frac{\theta}{2} \cos \frac{3\theta}{2} - \frac{K_I}{\sqrt{2\pi r}} \left(\frac{\rho}{2r} \right) \sin \frac{3\theta}{2}
 \end{aligned} \quad \left(r \geq \frac{\rho}{2} \right) \quad (6.3)$$

The stress singularity term diminishes due to the fact that r cannot be less than $\rho/2$ as a result of blunting. While the tip singularity diminishes, the overall opening stress level σ_y within the notch region ($r \sim \rho$) flattens, but raises in the region further away from the crack tip as compared with a sharp crack, because of the addition of the second term and, from the Dugdale plasticity slit model, the notch plasticity zone will *spread further* ahead of the crack tip. Although strictly speaking a large deformation formulation is required to study the crack blunting effect near the tip process zone, the above simplified argument still indicates the general trend.

Hydrogen adsorption can be enhanced in the extended plastic zone (induced by crack-blunting), leading to the decohesion of material in the crack tip. As a result, the crack growth rate increases.

Also, by blunting the crack at a grain boundary the conditions experienced by the new grain become more like those of a tip of a notch rather than a sharp crack, and it becomes easier to re-initiate the crack in the new grain. This can be described in term of a reduction in the constraint at the crack tip or, in term of coping with the misfit between the two slip planes, the new crack requires fewer (though larger) steps to accommodate the misfit.

However, the pure 'geometric' effect of blunting will reduce the crack growth rate because the singularity diminishes at the crack tip. In an aggressive environment the total effect of crack blunting is a compromise of the above factors, and turns out to assist the crack growth in the present tests.

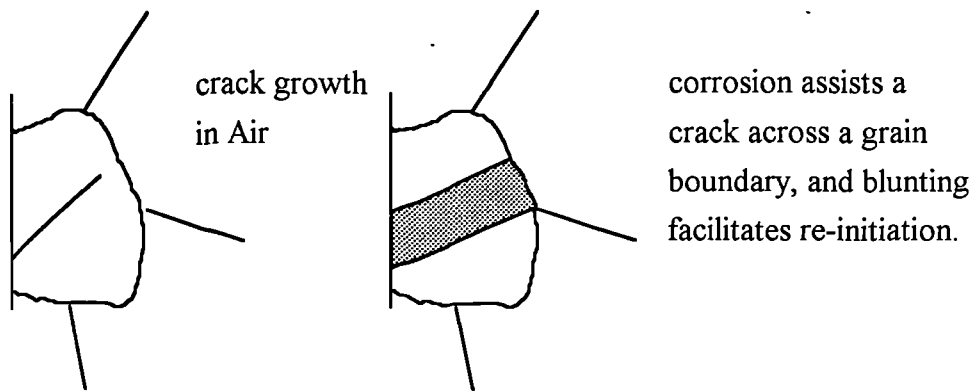


Figure 6.2 Schematic view of blunting facilitating crack across a grain boundary [1]

6.4. The effect of triaxial stress

In addition to crack tip blunting, hydrogen embrittlement may occur during corrosion fatigue.

Hydrogen embrittlement is the consequence of diffusion of hydrogen to locations ahead of the crack. The increased hydrogen concentration at this location assists cracking; microcracks linking up with the main crack. This effect is closely related to the three-dimensional expansion of the crystal lattice due to hydrostatic stress.

In the elastic stress fields of cracks the three principal stresses are not equal, even in plane strain. By splitting the triaxial stress state into a deviatoric and a hydrostatic component, the hydrostatic stresses of the crack tip field for different loading modes can be obtained as:

$$\begin{aligned}
 \text{Mode I:} \quad \sigma_h &= \frac{2(1+\nu)K_I}{3\sqrt{2\pi r}} \cos\left(\frac{\theta}{2}\right) && \text{plane strain} \\
 \text{Mode II:} \quad \sigma_h &= -\frac{2(1+\nu)K_{II}}{3\sqrt{2\pi r}} \sin\left(\frac{\theta}{2}\right) && \text{plane strain} \\
 \text{Mode III:} \quad \sigma_h &= 0
 \end{aligned} \tag{6.4}$$

therefore, for a mode I tensile crack σ_h reaches a maximum directly ahead of the crack tip. For mode II loading, there exists both a compressive hydrostatic state and a tensile hydrostatic state in different locations ahead of the crack, which reverses when the stress is reversed in the cycle. Hence the hydrostatic stress is always zero on the ligament directly ahead of the crack tip ($\theta = 0$). For mode III loading, there is no hydrostatic stress component.

In summary, when the crack is growing in mode I, there exists a tensile hydrostatic state around the tip region giving rise to volume dilatation which is favoured for hydrogen diffusion and hence embrittlement. When the crack is growing in mode II or mode III, no volume dilatation will occur directly ahead of the crack tip which will discourage the hydrogen embrittlement process.

Bearing in mind that stage I growth is a mixture of mode II and mode III cracking when considering a three dimensional configuration, while stage II growth is a mode I crack, the expression (6.4) states clearly that mode I stage II growth will be the most favourite path for a hydrogen-embrittlement controlled crack growth mechanism. This is in good agreement with the observed experimental phenomenon namely that corrosion fatigue crack growth, for the present material, always tended to grow in the stage II, opening mode, as compared with the in-air fatigue data for the same material where a stage I shearing mode lasted much longer, even up to a crack length of tens of millimetres [3]. Once the stage II crack formed in corrosion fatigue, crack growth continued in the direction perpendicular to the maximum tensile stress, giving rise to very straight crack paths (usually with two branches perpendicular to each other).

6.5. Corrosion fatigue resistance of a high strength steel

The fatigue resistance of an inadequately-machined component can be reduced by having rough surface finishes, inclusions and pits. Miller [4] has indicated that if surface grooves are deeper than the barrier dimension d , or inclusions are large in comparison to grain size, they can reduce fatigue resistance by two mechanisms: (a) by permitting an easy bridge between the stage I and stage II crack growth phase and, (b) by themselves cracking in a manner that permits the immediate growth of a stage II crack in the bulk material.

Further to the above, for a high strength steel when subjected to fully reversed torsional fatigue in an aggressive environment, it is necessary to take into account both the original defect size and its associated effective stress concentration size.

As observed from experiments, if the total stress concentration effective size is less than one grain size when the overall stress level is high, a stage I crack will initiate from the pit, and propagate along the shear stress planes. Alternatively, when the stress is low, the

effective stress concentration size is larger than one grain, and so the local stress level at the first grain boundary (assisted by environmental attack) will be increased sufficiently to overcome the microstructural barrier, hence a stage II crack will propagate immediately from the pit. At the same time, the combined effects of dissolution and hydrogen degradation by hydrogen diffusing into the maximum stress triaxiality zone will assist the process of crack tip decohesion and promote cracking in the direction perpendicular to the maximum tensile stress.

6.6. Fatigue strength

The conventional fatigue limit has two fundamental aspects, a stress range level below which the material will not fail regardless of the number of loading cycles, and a distance which represents the distance of the longest non-propagating crack that can be stopped by a microstructural barrier in a given material texture. If the applied stress level can not overcome the strongest barrier, the crack will become a non-propagation crack, and accordingly the applied stress level will be termed as a fatigue limit. In an aggressive environment, fatigue strength rather than fatigue limit is reported, which is the stress to which the metal can be subjected for a specified number of cycles to failure.

In an aggressive environment, however, the strength of microstructural barriers, i.e. grain boundaries, strengthening particles, precipitates, or phase interfaces, could be substantially reduced since the electro-chemical reaction preferentially occurs in those sites due to chemical and physical inhomogeneities. As a consequence, the first few barriers, which might be very effective in an inert environment, may be removed by dissolution, and the crack may grow to the next grain along the maximum shear stress plane without much difficulty. When the crack growth is at the transition phase from stage I to stage II, however, it has to grow in both the radial and tangential direction across several grains of various sizes and crystallographic orientations and hence has a 3-dimensional

configuration. Accordingly, the difficulty of an initial stage I crack becoming a stage II crack will increase, and the crack growth rate will be dramatically decreased.

From the respective da/dN versus average crack length a (Figure 4.8(b), (c), and (d), and Figure 4.28(a), (b) and (c)) under both free potential and cathodic polarisation in a 0.6M NaCl solution, it was found that the most profound slowing down of crack growth always occurred at the transition from stage I to stage II crack growth. This suggests that in an aggressive environment, the strongest barrier is associated with the stage I - stage II transition and an intense fatigue resistance will be experienced for a crack developing from a two dimensional configuration towards a three dimensional one (see Figure 5.2).

If the local stress at the initial stage I crack tip is below a critical value for the stage I-to-stage II transition, the crack can not change into stage II, and will subsequently become a non-propagating crack. There was evidence of such a non-propagating crack on the surface of specimen TC13, at $\Delta\tau=415$ MPa, in a 0.6M NaCl solution, with the length of 200 μ m along the shear stress plane, see Figure 4.3(b).

It is therefore suggested that the fatigue strength (at a specified number of cycles, usually in the range of 10^6 to 10^8 cycles) in corrosion fatigue of a metallic material can be the critical stress level below which crack growth cannot overcome the strongest barrier (corresponding to the transition from stage I to stage II crack growth). Such a stress level for the fatigue strength of BS251A58 steel in corrosion fatigue is 98 MPa for 10^7 cycles to failure at a frequency of 5Hz.

The combined electro-chemical/mechanical effects of dissolution, hydrogen degradation, and crack tip blunting and decohesion in corrosion fatigue lead to the weakening and eventual elimination of the microstructural barrier to crack growth translating from stage I to stage II. Reflected in a crack growth map, the microstructure threshold d and the

mechanical threshold a_{th} join together, and the gap between them, which exists in the case of in-air fatigue, vanishes, as illustrated in Figure 6.3.

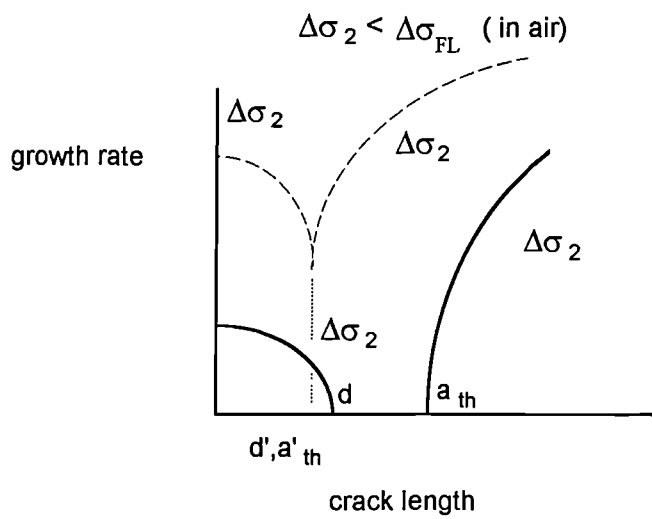


Figure 6.3 The important phase of defect extension (dashed line) in an aggressive environment i.e. the surmounting of the microstructural barrier and the linking of the two fatigue thresholds at a stress level below the in-air fatigue limit.

References

- [1] R. A. Markfield and P. Haritopoulos (1990) The role of corrosion in the initiation and growth of corrosion fatigue cracks, *Environment Assisted Fatigue*, EGF7, Edited by P.Scott, Mechanical Engineering Publications, London , pp.381-393.
- [2] M. Creager and P. C. Paris (1967) Elastic field equations for blunt cracks with reference to stress corrosion cracking, *Inter. J. Fract. Mech.*, **3**, pp.247-252.
- [3] Hafeez Ur Rehman (1991) The Influence of microstructural variables on the growth of short fatigue cracks in a high strength steel. *Ph.D thesis*, University of Sheffield.
- [4] K. J. Miller (1993) Two thresholds of fatigue behaviour , *Fatigue Frac. Engng. Mater. Struct.* **16**, No. 9, pp.931-939.

Chapter 7 Conclusions

7.1 Conclusions

Based on an experimental and theoretical study of the corrosion fatigue behaviour of a high strength BS251A58 steel, having a yield strength around 1400 MPa, the following conclusions are made:

1. The fatigue strength of BS251A58 steel, subjected to 10^7 cycles in a 0.6M NaCl solution, at pH6 and at a frequency of 5Hz, is 98 MPa, and is significantly lower than the value of the fatigue limit in air, i.e. 457.5 MPa.
2. Corrosion fatigue crack propagation in the high strength BS251A58 steel can be described sequentially in terms of corrosion-induced pits, microcracks from pits, cracks in stage I (shear type cracks), and cracks in stage II (tensile cracks).
3. The number of cycles in the stage I-to-stage II transition, in relation to the whole fatigue life, varies from 20% to 60%, increasing as the applied load decreases.
4. Crack coalescence may occur in both the stage I and stage II regimes. In the stage I regime, microcracks with an effective tip-to-tip distance less than 1 to 2 prior austenite grains will coalesce, while those with distances greater than 2 to 3 prior austenite grains will change to stage II propagation. In the stage II regime, crack coalescence occurs after about 70% of the fatigue life N_f .

5. The lower the cycling frequency, the shorter will be the corrosion fatigue life. The combination of a high stress level and a low frequency can eliminate the in-air-fatigue microstructural barrier effect.

6. Cathodic polarisation ($E = -1280\text{mv (SCE)}$) can prevent the surface of the specimen from pitting, delay the stage I-to-stage II transition, and decelerate the early stage II crack growth rate. However, as a stage II crack grows, cathodic polarisation will accelerate the crack growth rate.

7. In a 0.6M NaCl solution, the final stage I crack length increases from $50\mu\text{m}$ to $300\mu\text{m}$ with increasing cyclic shear stress range (from 224 MPa to 926 MPa). This distance equals approximately 2 to 10 prior austenite grain diameters. The final stage I crack length is much longer under cathodic polarisation than for a free corrosion potential under the same stress range. There is no significant frequency effect on the final stage I crack length when the frequency is in the range of 2Hz to 12.5Hz at the stress range of approximately 400 MPa.

8. The dislocation based Navarro-de los Rios model was employed in the present study to describe crack growth behaviour and to predict fatigue life. The pit growth behaviour, the crack transition from stage I-to-stage II, and a parabolic strain hardening law, were incorporated into the model to reflect more closely the actual fatigue behaviour of the material. The validity of the model was justified by the good agreement achieved between predictions based on the model and the experimental results.

7.2 Suggestions for future work

1. Local stress states and mixed-mode cracking in corrosion fatigue should be further studied to provide a clear picture of stage I crack growth and the transition from stage I to stage II cracking.
2. Crack tip chemical reactions should be investigated, and so should the interaction between mechanical and electrochemical effects, in relation to corrosion fatigue resistance.